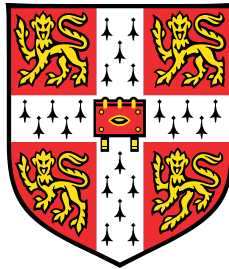


# Geometry and Hydrodynamics of Swimming with a Bundle of Bacterial Flagella



**Maria Tatulea-Codrean**

Department of Applied Mathematics and Theoretical Physics  
University of Cambridge

This dissertation is submitted for the degree of  
*Doctor of Philosophy*

Trinity College

June 2021



## **Declaration**

This thesis is the result of my own work and includes nothing which is the outcome of work done in collaboration except as declared in the Preface and specified in the text. I further state that no substantial part of my thesis has already been submitted, or, is being concurrently submitted for any such degree, diploma or other qualification at the University of Cambridge or any other University or similar institution except as declared in the Preface and specified in the text. It does not exceed the prescribed word limit for the relevant Degree Committee.

The subjects, ideas and approaches of this dissertation are the result of many discussions with my supervisor, Prof. Eric Lauga. Despite this, I will exercise nosism throughout.

Maria Tatulea-Codrean

June 2021



# Geometry and Hydrodynamics of Swimming with a Bundle of Bacterial Flagella

Maria Tatulea-Codrean

Microscopic-scale swimming has been a very active area of research in the last couple of decades. The interest in this topic has been driven partly by experimental advances, which have allowed scientists to observe the motion of microorganisms with unprecedented detail, partly by the great potential for applications (e.g., in the biomedical sciences and biomimetic engineering), and partly by a desire to understand the fundamentals of life starting from unicellular organisms.

Flagellar propulsion is the most common form of locomotion amongst unicellular organisms. On the one hand, eukaryotic organisms have flexible flagella which they undulate in a remarkable variety of patterns - from the whip-like motion of a spermatozoon tail, to the breast-stroke pattern of biflagellate algae such as *Chlamydomonas*, down to the metachronal waves formed by thousands of cilia on the surface of a *Paramecium*. On the other hand, bacteria are equipped with corkscrew-shaped flagella, which they can rotate rigidly in viscous fluids to generate forward motion.

In this thesis, we consider the role played by the number of flagella in the swimming of multi-flagellated bacteria, for which the model organism is *Escherichia coli*. The work presented here is theoretical and consists mainly of asymptotic calculations (usually exploiting a small parameter that represents the aspect ratio of flagellar filaments), assisted or verified by numerical simulations. We use two well-established theories for the hydrodynamics of slender filaments, namely resistive-force theory (RFT) for the analytical calculations and slender-body theory (SBT) for the numerical simulations.

The first part of the thesis, comprising three chapters, deals with the geometric aspects of having multiple helical filaments in close proximity to one another. We derive geometric constraints on the rate of synchronisation between rotating helical filaments as they come together to form a bundle, as well as the geometric constraints on the entanglement of a pair of helical filaments. Our results suggest that bacterial flagella are typically too few, and hence anchored too far apart on the cell body, to be able to form tangled bundles based on their intrinsic, undeformed geometry alone.

The next three chapters of the thesis focus on the hydrodynamic interactions (HIs) between flagellar filaments, and the effect that HIs have on the synchronisation and the propulsive capacity of a bundle of parallel filaments. We first derive an asymptotic theory for the HIs between rigid filaments separated by a distance larger than their contour length. Next, using this theory, we propose a novel analytical model for the synchronisation of

elastically tethered rotating helices. Remarkably, we find that there is an optimum strength of the elastic compliance which minimises the time scale for synchronisation, and that the flagellar filament, although more rigid than the hook, may play a more important role in the synchronisation of bacterial flagella and stability of flagellar bundles rotating in-phase.

In the final chapter on hydrodynamics we investigate how the hydrodynamic drag and thrust associated with a bundle of parallel helical filaments depend on the number of filaments. Remarkably, our findings reveal that the torque-speed relationship of the bacterial flagellar motor plays an important role in the swimming of multiflagellated bacteria. Because HIs within a circular bundle of filaments reduce the hydrodynamic resistance of each filament to rotation about its own axis, the bacterial flagellar motors actuating the bundle transition from the high-load to the low-load regime at a critical number of filaments within the biologically relevant range, which leads to a peak in the swimming speed followed by a monotonic decay with increasing number of filaments.

To my loving parents, Marinela and Ionel,  
and my brother, Alexandru.

—

Părinților mei, Marinela și Ionel, și fratelui meu, Alexandru,  
cu cel mai mare drag din lume.



## Acknowledgements

First and foremost, I am immensely grateful to my supervisor, Prof. Eric Lauga, who has been a mentor, teacher and inspiration to me since my very first term in Cambridge as an undergraduate. I am especially grateful for his patient guidance and support, for the many inspiring scientific discussions we have had, and for the opportunities he has offered me to work on challenging problems in a very exciting field of research. I have always been amazed by Eric's unwavering enthusiasm for science, and the way that he channels that enthusiasm to motivate his students. His encouraging comments have lifted my spirits in so many of our meetings, and they have helped me reach the finish line in this four-year marathon. The many great lessons that I have learnt from him during this time have shaped the researcher I am today, and I take them forward with me on this academic journey.

I have been extremely fortunate to be part of such a large and active research group studying biological fluid mechanics and biophysics in the Department of Applied Mathematics and Theoretical Physics. It has been a privilege to work alongside so many brilliant scientists, many of whom have helped me on my research journey over the past four years. I would like to thank particularly Prof. Raymond Goldstein and Prof. Timothy Pedley for their scientific advice and many interesting discussions and questions, which prompted me to reflect more deeply on my research and ultimately improved my work. I am also very grateful to all the past and present members of Eric's and Ray's group: Alex Chamolly, Debasish Das, Justas Dauparas, Gabriele de Canio, Masha Dvoriashyna, Christian Esparza-López, Panayiota Katsamba, Lyndon Koens, Maciej Lisicki, Yi Man, Ivan Tanasijevic, Albane Théry, Sumit Birwa, Francesco Boselli, George Fortune, Michael Gomez, Anne Herrmann, Pierre A. Haas, Stephanie Höhn, Julius Kirkegaard, Mazi Jalaal, Kyriacos Leptos, Hélène de Maleprade, Nuno Miguel Oliveira, François Peaudecerf, Praneet Prakash and Kirsty Wan. I thank them for sharing their knowledge of mathematical methods and biology with me, for organising the seminars and social events that brought the groups together, and generally for providing a fun and exciting environment to work in. I would like to thank Masha Dvoriashyna and Anne Herrmann, in particular, for reading and providing very helpful comments on drafts of this dissertation.

One of the best things about being a student member of Trinity College has been to be a part of a large community of mathematicians, which cover amongst them an impressive breadth and calibre of mathematical expertise. I would like to thank especially my college academic contact, Prof. John Lister, for his friendly and approachable nature, for many interesting scientific and casual conversations, and for providing honest feedback on my research. I am also grateful to my undergraduate Director of Studies, Dr. David Skinner, who gave me crucial encouragement without which I may have never embarked on the journey of research. I would also like to thank Prof. Imre Leader, Prof. David Tong, Prof. John Hinch, Prof. Harvey Reall, Dr. Tom Fisher and my supervisor, Eric, for the opportunity to perform undergraduate admissions interviews alongside them, which I thoroughly enjoyed. I would also like to thank Dr. Ailsa Keating for providing a platform to meet and exchange ideas with many exciting researchers, by organising events for women mathematicians in Cambridge.

There are many other people who have helped with my journey over the past years. I would like to thank my Trinity College tutor, Prof. Adrian Poole, my tutorial secretary, Mrs Lynn Clift, and the rest of the tutorial staff for their support and especially for their help during the pandemic. My spirits have been kept high by the Chaplains, Olga and John, through services and events in the chapel. I am grateful to Olga in particular for organising the Women's Bible Study.

I would also like to thank my friends from near and far, without whom my time as a PhD student would have been a lot less exciting: Irene and Matthew, Katya and Will, Diana and Jędrzek, Matthew, Mabel, Andreea, Minji, Anda, Adeline, Katy, Esther, Johan, Michal, and all the members of the Women's Bible study group. Particular thanks go to my cousin Andreea and her family, who have supported me since the time when I was interviewing for admission at Cambridge.

I am also grateful to the friendly communities in Cambridge that have welcomed me in passing during my PhD: the First and Third Boat Club, the Cambridge University Dancers' Club, and the Cambridge University Science Improv society. My time as a PhD student would not have been as fun without the activities that they organise and the chance to meet interesting people from across the university.

For those who know me well, it will be no surprise that I will end by thanking the gardeners. All the gardeners of Cambridge, for lifting up my spirits with their beautiful gardens that I admire most every day. Amongst them are Janet and Alan Windle, who shared their beautiful garden with our Bible study group during the pandemic. I am extremely grateful to my best friend and boyfriend, Georg, for the many motivating conversations that we have had about work and life in the past five years, often as we were walking through the gardens of Cambridge, and for his love, support and encouragement on this journey.

Next, I would like to thank all the gardeners in my family starting with my grandparents, who regularly remind me of my roots through their loving care and support. I am especially grateful to my big brother, Alexandru, for accompanying me on some of the most daunting and exciting journeys of my life, including my first trip to Scotland and the journey of writing this dissertation. I am so very grateful to my parents, Marinela and Ionel, who nurtured me while I was growing in their garden, and who have supported and loved me in every way possible in the years since. I am forever grateful for their trust and support in letting me follow my dreams, however difficult that has been at times on all of us. And finally, I praise and thank the greatest Gardener for His protection over me, and for the light He shines on all the things and people that I love most.



# Table of contents

<b>List of figures</b>	<b>xix</b>
<b>List of tables</b>	<b>xxiii</b>
<b>Nomenclature</b>	<b>xxv</b>
<b>1 Introduction</b>	<b>1</b>
1.1 Basics of flagellar propulsion at low Reynolds number . . . . .	3
1.1.1 Purcell’s scallop theorem . . . . .	3
1.1.2 Strategies for escaping Purcell’s scallop theorem . . . . .	5
1.1.3 Swimming with a helical propeller . . . . .	6
1.2 The bacterial flagellum . . . . .	8
1.2.1 The flagellar filament . . . . .	8
1.2.2 The hook . . . . .	10
1.2.3 The rotary motor . . . . .	11
1.3 Bacterial multiflagellarity . . . . .	13
1.3.1 Run-and-tumble motility . . . . .	14
1.3.2 Swimming speed of multiflagellated bacteria . . . . .	15
1.4 Objective of the thesis . . . . .	16
1.5 Structure of the thesis . . . . .	17
<b>2 Mathematical background</b>	<b>21</b>
2.1 Geometry of helical filaments . . . . .	21
2.1.1 Description of a helical filament with arbitrary orientation . . . . .	22
2.1.2 Macnab’s original study in helical geometry . . . . .	25
2.2 Hydrodynamics of flagellar filaments . . . . .	28
2.2.1 Fundamental solution of the Stokes equations . . . . .	28
2.2.2 Flows around rigid bodies . . . . .	29
2.2.3 Resistive-force theory . . . . .	30

2.2.4	Slender-body theory . . . . .	32
2.2.5	Hydrodynamic resistance matrix . . . . .	33
2.3	Conclusion . . . . .	34
<b>3</b>	<b>Geometrical intertwinement of bacterial polymorphic shapes</b>	<b>35</b>
3.1	Motivation . . . . .	35
3.2	Geometrical modelling . . . . .	36
3.2.1	Locus of relative position between filaments . . . . .	36
3.2.2	Possible states of intertwinement . . . . .	37
3.2.3	Definition of winding number . . . . .	38
3.2.4	Physical interpretation of transitions . . . . .	38
3.2.5	The case of irrational pitch ratio . . . . .	40
3.3	Application to bacterial polymorphic shapes . . . . .	41
3.4	Conclusion . . . . .	42
<b>4</b>	<b>Geometrical constraints on the tangling of helical filaments</b>	<b>43</b>
4.1	Motivation . . . . .	43
4.2	Geometrical modelling . . . . .	44
4.2.1	Definition of tangled bundle . . . . .	46
4.2.2	Kinematic perspective of tangling . . . . .	46
4.2.3	Geometrical constraints for a perfect helix . . . . .	49
4.2.4	Effect of tapering . . . . .	52
4.3	Comparison with experimental measurements . . . . .	54
4.3.1	Single cell results . . . . .	54
4.3.2	Population level results . . . . .	55
4.4	Discussion of extensions and limitations . . . . .	57
4.5	Conclusion . . . . .	60
	Appendix 4.A Calculation of cross-sectional shape . . . . .	62
	Appendix 4.B Sources of experimental data . . . . .	67
<b>5</b>	<b>Geometrical constraints on the bundling of helical filaments</b>	<b>71</b>
5.1	Motivation . . . . .	71
5.2	Geometrical modelling . . . . .	72
5.2.1	Kinematic model of bundling . . . . .	72
5.2.2	Intersections between two helices . . . . .	74
5.2.3	Critical phase difference . . . . .	77
5.3	Application to bacterial flagellar bundling . . . . .	78

5.3.1	Dominant geometrical constraint in a circular bundle . . . . .	78
5.3.2	Constraints on the rate of synchronisation . . . . .	80
5.3.3	Constraints on the motor torque difference . . . . .	81
5.4	Conclusion . . . . .	83
<b>6</b>	<b>Asymptotic theory of hydrodynamic interactions between slender filaments</b>	<b>85</b>
6.1	Introduction . . . . .	85
6.1.1	Previous work . . . . .	86
6.1.2	Current approach . . . . .	87
6.2	Asymptotic expansion for hydrodynamic interactions . . . . .	88
6.2.1	Geometrical setup . . . . .	89
6.2.2	Hydrodynamic setup . . . . .	90
6.2.3	Asymptotic series formulation . . . . .	93
6.2.4	Leading-order dynamics . . . . .	94
6.2.5	First-order correction . . . . .	95
6.2.6	Second-order correction . . . . .	97
6.2.7	Force moments for second-order correction . . . . .	99
6.2.8	Evaluating coefficients in the series expansion . . . . .	101
6.3	Validation of asymptotic expansion . . . . .	103
6.3.1	Computational method for hydrodynamic interactions . . . . .	103
6.3.2	Relative errors . . . . .	105
6.3.3	Time evolution of forces and torques . . . . .	108
6.4	Application to helical pumps . . . . .	113
6.4.1	Problem specification . . . . .	113
6.4.2	Computational results . . . . .	114
6.4.3	Asymptotic theory . . . . .	117
6.4.4	Forces and torques parallel to axis of rotation . . . . .	118
6.4.5	Forces and torques perpendicular to axis of rotation . . . . .	122
6.4.6	Deducing the dynamics of the second filament . . . . .	124
6.4.7	Interpretation of results . . . . .	124
6.4.8	Outlook: circular array of helical pumps . . . . .	128
6.5	Discussion . . . . .	129
6.5.1	Summary of results . . . . .	129
6.5.2	Advantages and limitations . . . . .	131
6.5.3	Potential applications . . . . .	132
Appendix 6.A	Calculating the leading-order resistance matrix from RFT . . . . .	133
Appendix 6.B	Calculating force moments from RFT . . . . .	138

Appendix 6.C	Useful integrals . . . . .	141
Appendix 6.D	Validation of computational method . . . . .	142
<b>7</b>	<b>Hydrodynamic synchronisation of rotating bacterial flagella</b>	<b>149</b>
7.1	Introduction . . . . .	149
7.1.1	Synchronisation of eukaryotic flagella . . . . .	150
7.1.2	Synchronisation of bacterial flagella . . . . .	151
7.1.3	Current approach . . . . .	151
7.2	Mathematical modelling . . . . .	152
7.2.1	Minimal setup for synchronisation . . . . .	152
7.2.2	Hydrodynamic interactions . . . . .	154
7.2.3	Governing equations . . . . .	156
7.2.4	Intrinsic kinematics of a single helical filament . . . . .	157
7.2.5	Multiple scales analysis . . . . .	159
7.2.6	Kinematic perturbation due to hydrodynamic interactions . . . . .	161
7.2.7	Evolution of phase difference . . . . .	163
7.2.8	Time scale for synchronisation . . . . .	164
7.2.9	Unequal driving torques . . . . .	165
7.3	Physical mechanism for synchronisation . . . . .	167
7.3.1	Preliminary considerations . . . . .	167
7.3.2	Intrinsic dynamics of a helical filament . . . . .	167
7.3.3	Dynamics of synchronisation . . . . .	170
7.4	Numerical simulations . . . . .	172
7.4.1	Computational method . . . . .	172
7.4.2	Comparison with theory . . . . .	174
7.4.3	Extracting the time scale for synchronisation . . . . .	175
7.4.4	Variation of parameters . . . . .	176
7.5	Biophysical insights . . . . .	178
7.5.1	Time scale for synchronisation . . . . .	178
7.5.2	Comparison of different polymorphic forms . . . . .	178
7.5.3	Optimal elastic tethering strength . . . . .	183
7.6	Signs of multisynchrony in the near-field . . . . .	186
7.7	Discussion . . . . .	188
Appendix 7.A	Resistance matrix coefficients obtained from RFT . . . . .	191
Appendix 7.B	Derivation of solvability condition . . . . .	192
Appendix 7.C	Series expansion of inverse resistance matrices . . . . .	194

---

<b>8</b>	<b>Hydrodynamics of multiflagellar propulsion</b>	<b>199</b>
8.1	Motivation . . . . .	199
8.2	Theoretical model . . . . .	201
8.2.1	Geometric and hydrodynamic setup . . . . .	201
8.2.2	Extended resistance matrix for a circular bundle of filaments . . . . .	203
8.2.3	Average resistance coefficients . . . . .	204
8.2.4	Computational method for hydrodynamic interactions . . . . .	205
8.3	Results and biophysical insights . . . . .	206
8.3.1	Hydrodynamic resistance of a bundle of flagellar filaments . . . . .	206
8.3.2	Swimming speed of a multiflagellated bacterium . . . . .	209
8.4	Conclusion . . . . .	212
<b>9</b>	<b>Summary and perspectives</b>	<b>215</b>
	<b>References</b>	<b>219</b>



# List of figures

1.1	Principles of swimming at low Reynolds number . . . . .	4
1.2	Essential features of the bacterial flagellar filament. . . . .	9
1.3	Essential features of the bacterial flagellar motor. . . . .	12
1.4	Run-and-tumble motility of peritrichous bacteria. . . . .	15
2.1	Illustration of the key geometrical parameters for a helical filament with arbitrary orientation. . . . .	23
2.2	Diagram explaining the geometrical intertwinement of two parallel and identical helices. . . . .	26
3.1	Diagram explaining the geometrical intertwinement of two parallel helices with different amplitudes and pitches, and opposite chiralities. . . . .	37
3.2	The locus of the relative distance between two intertwining filaments with rational pitch ratio. . . . .	39
3.3	The locus of the relative distance between two intertwining filaments with irrational pitch ratio. . . . .	41
3.4	The phase space of possible intertwinement between the normal shape flagellar filament and any other helical shape. . . . .	42
4.1	Bundling of flagellar filaments on a swimming bacterium. . . . .	45
4.2	Geometry of tangling for two identical helices, each tapered near their anchoring point. . . . .	48
4.3	Steps for computing the tangling threshold of two perfect helices. . . . .	50
4.4	Geometrical constraints on the tangling of two tapered helices. . . . .	53
4.5	Predictions of our geometrical model for tangling for a single cell. . . . .	56
4.6	Predictions of our geometrical model for tangling in a population of cells with variability in cell body size. . . . .	58
4.7	The cross-sectional shape of a helical filament in the “focal plane”. . . . .	65

5.1	Minimal model of bundling with rotational symmetry about the central axis of the bundle. . . . .	73
5.2	Setup for calculating the intersections between two rotating helices with their axes tilted towards the centre of the bundle. . . . .	75
5.3	Application of geometrical results to a circular bundle of flagellar filaments.	79
5.4	Constraints imposed by geometry during the bundling process. . . . .	81
5.5	Constraints imposed by geometry on a bundle in equilibrium. . . . .	82
6.1	Geometrical setup for the problem of hydrodynamic interactions between slender filaments. . . . .	89
6.2	Relative error between the asymptotic theory for hydrodynamic interactions and the computational method. . . . .	107
6.3	Comparison between computations and the asymptotic theory with RFT/SBT coefficients. Part 1 - small inter-filament separation. . . . .	109
6.4	Comparison between computations and the asymptotic theory with RFT/SBT coefficients. Part 2 - large inter-filament separation. . . . .	110
6.5	Comparison between computations and the asymptotic theory with SBT coefficients calculated to first and second order corrections. Part 1 - small inter-filament separation. . . . .	111
6.6	Comparison between computations and the asymptotic theory with SBT coefficients calculated to first and second order corrections. Part 2 - large inter-filament separation. . . . .	112
6.7	Average forces and torques exerted by a rotating helix due to the hydrodynamic interactions with a second helix rotating in parallel. . . . .	115
6.8	Variance over time in the forces and torques exerted by a rotating helix due to the hydrodynamic interactions with a second helix rotating in parallel. . .	116
6.9	Average forces and torques due to the hydrodynamic interactions between two helical pumps. . . . .	120
6.10	Variance in forces and torques due to the hydrodynamic interactions between two helical pumps. . . . .	121
6.11	Physical mechanism for the reduction in pumping force due to hydrodynamic interactions. . . . .	125
6.12	Basic principles of hydrodynamic interactions between helical pumps. . . .	129
6.13	Validation of computational method via tests on a prolate spheroid. . . . .	143
6.14	Validation of computational method via tests on a semi-circular filament. . .	144
6.15	Validation of computational method via tests on a helical filament. . . . .	145

---

6.16	Validation of computational method via tests on two helical filaments interacting hydrodynamically. . . . .	146
6.17	Numerical self-convergence tests for a helical filament. . . . .	147
7.1	Geometric and dynamical setup for our investigation of bacterial flagellar synchronisation. . . . .	153
7.2	Intrinsic dynamics of a rotating horseshoe in the absence of hydrodynamic interactions. . . . .	169
7.3	Physical mechanism for the synchronisation of two hydrodynamically-coupled rotating horseshoes. . . . .	171
7.4	In-phase synchronisation of two hydrodynamically-coupled helices. . . . .	174
7.5	Effect of the variation of parameters on the time scale for synchronisation. . . . .	177
7.6	Comparative analysis of the different polymorphic forms in the context of synchronisation. . . . .	182
7.7	Optimum actuation dynamics for synchronisation in the far field. . . . .	184
7.8	Numerical observations of multisynchrony in hydrodynamically-coupled helical filaments rotating nearby. . . . .	187
8.1	Geometrical and kinematic setup for investigating the hydrodynamics of a circular bundle of filaments. . . . .	202
8.2	Total drag, thrust and torque on a circular bundle of hydrodynamically-coupled filaments. . . . .	207
8.3	Deficit in drag, thrust and torque on an individual filament operating inside a circular bundle. . . . .	209
8.4	Dynamics of a swimming multiflagellated bacterium according to a minimal model consisting of a spheroidal cell body with “dry” coupling to a circular bundle of helical filaments which are hydrodynamically-coupled to each other. . . . .	211



# List of tables

4.1	Parameters used in our geometrical model for tangling. Part 1 - <i>Escherichia coli</i> data sets. . . . .	68
4.2	Parameters used in our geometrical model for tangling. Part 2 - <i>Salmonella typhimurium</i> and <i>Bacillus subtilis</i> data sets. . . . .	69
7.1	Geometric, dynamic, and kinematic parameters relevant to the synchronisation of bacterial flagella. . . . .	179



# Nomenclature

## Roman Symbols

$A_{if}^{\text{fcb}}, B_{if}^{\text{fcb}}, D_{ij}^{\text{fcb}}$  effective resistance coefficients for a filament in a circular bundle

**A, B, D** constituent blocks of the resistance matrix for an individual helix

$A_{ij}, B_{ij}, D_{ij}$  components of the resistance matrix for an individual helix

$A_{\parallel}$  hydrodynamic resistance of a prolate spheroid to translation along its major axis

$D_{\parallel}$  hydrodynamic resistance of a prolate spheroid to rotation about its major axis

$c$  eccentricity of a spheroid

$c_{\parallel}, c_{\perp}$  parallel and perpendicular drag coefficients

**C** cross-interaction resistance matrix

$\mathbf{C}_{j \rightarrow k}^{\text{cb}}$  cross-interaction resistance matrix between filaments  $j$  and  $k$  in a circular bundle

$e$  Euler's number

$\mathbf{e}_1^{(k)}, \mathbf{e}_2^{(k)}, \mathbf{e}_3^{(k)}$  body-fixed frame of unit vectors of filament  $k$

$\mathbf{e}_1, \mathbf{e}_2, \mathbf{e}_3$  body-fixed frame of unit vectors

$\mathbf{e}_x, \mathbf{e}_y, \mathbf{e}_z$  laboratory frame of unit vectors

**F** force exerted by a rigid body on the fluid

$h$  height along the helical axis

$K$  ratio between rotation time scale and elastic relaxation time scale

$k$  elastic tethering strength

---

$L$	contour length of the filament
$N$	number of helical turns
$p$	helical pitch
$\mathbf{p}$	vector of three orientation angles for the filament
$\mathbf{Q}$	rotation matrix
$R$	helical amplitude
$\mathbf{r}(s)$	position of filament centreline
$\mathbf{r}^{(k)}(s)$	centreline of filament $k$ , relative to laboratory frame
$\mathbf{r}_k(s)$	centreline of filament $k$ , relative to body-fixed frame
Re	Reynolds number
$s$	arc length along filament
$\mathbf{S}$	self-induced resistance matrix
$\mathbf{S}_k^{\text{cb}}$	self-induced resistance matrix of filament $k$ in a circular bundle
$t$	fast time scale of rotation
$T_0$	constant driving torque applied by the motor
$\mathbf{T}$	torque exerted by a rigid body on the fluid
$\hat{\mathbf{t}}(s)$	unit tangent along the filament
$\hat{\mathbf{t}}_k(s)$	unit tangent along filament $k$
$T_{\text{stall}}$	stall torque of bacterial motor
$t_{\text{sync}}$	time scale for synchronisation
$\mathbf{U}$	linear velocity of a rigid body
$\mathbf{u}(s)$	velocity of filament centreline
$\mathbf{u}_\infty$	background flow
$\mathbf{x}_k$	position of body-fixed frame relative to laboratory frame

**Greek Symbols**

$\alpha, \beta, \gamma, \delta, \zeta, \eta$  dummy variables, defined locally in each chapters as needed

$\chi$  spin angle

$\Delta\Phi$  absolute phase difference, non-parallel filaments

$\Delta\phi$  phase difference, parallel filaments

$\varepsilon$  cross-sectional radius of the filament

$\lambda_p$  ratio of helical pitches

$\lambda_R$  ratio of helical amplitudes

$\mu$  dynamic viscosity of the fluid

$\nu$  phase lag of sideways displacement for an elastically-tethered rotating helix

$\Omega_0$  intrinsic angular speed of the helix

$\Omega_{\text{body}}$  angular velocity of the cell body

$\mathbf{\Omega}$  angular velocity of a rigid body

$\Omega_{\text{knee}}$  knee value of angular speed

$\Phi$  absolute phase angle, non-vertical filament

$\phi$  azimuthal/phase angle

$\pi$  Archimedes' constant

$\psi$  pitch angle of the helix

$\rho$  amplitude of sideways displacement for an elastically-tethered rotating helix

$\rho_{\text{fluid}}$  density of the fluid

$\sigma$  chirality of the helix

$\tau$  slow time scale of synchronisation

$\theta$  polar/tilt angle

$\xi$  circumferential angle around the helical axis

**Other Symbols**

$\langle \dots \rangle$  average over period of rotation

$\tilde{\cdot}$  dimensional equivalent of the quantity underneath the tilde sign

**Acronyms / Abbreviations**

BFM bacterial flagellar motor

CCW counter-clockwise

CW clockwise

HIs hydrodynamic interactions

RFT resistive-force theory

SBT slender-body theory

# Chapter 1

## Introduction

*“I want to take you into the world of very low Reynolds number – a world which is inhabited by the overwhelming majority of the organisms in this room.” – E.M. Purcell*

We might wonder where the great Edward M. Purcell found himself as he said these words in a 1976 lecture at Harvard University [170]. Was he in a room full of vials and jars that vastly outnumbered the members of his audience? Surprisingly, the audience themselves made his statement possible. An average-sized adult human body harbours an incredible  $3.8 \times 10^{13}$  bacterial cells and only  $3.0 \times 10^{13}$  human cells, according to recently revised estimates by Sender et al. [189].<sup>1</sup> So what Purcell is referring to, in this quote, is the vast number of micro-organisms present in the lecture theatre and in every other room. These micro-organisms are wriggling their way through life at low Reynolds number under physical constraints that we, humans, have outgrown due to the large size of our bodies. We say “outgrown” because even human life starts at low Reynolds number, with a micrometer-sized spermatozoon making its way towards an egg cell.

The next question we might ask ourselves is why Purcell, a Nobel laureate, would give an entire lecture on the swimming of micro-organisms at low Reynolds number, and why the study of micro-organisms is worthwhile in general. For some, the desire to understand the fundamentals and origins of life is sufficient motivation. For others, the study of micro-organisms is important for biomedical applications such as fertility treatments [55, 186], microfluidic diagnostic tools [122], and targeted drug delivery to cancerous tissues [80, 183]. Micro-organisms are also crucial for carbon storage in the ocean [36, 104] and for the survival of ecosystems [202], as they are the bottom link of the food chain. Finally, an almost too

---

<sup>1</sup>At the time when Purcell gave this lecture, the ratio was thought to be closer to 10:1 in favour of bacterial cells [135].

obvious reason to study micro-organisms is that they transmit a host of diseases that we would like to cure, prevent or even eradicate [13].

As suggested by the wide range of applications in the previous paragraph, the study of micro-organisms has not been limited to a single discipline. Microbiologists, ecologists, biochemists, engineers, physicists, and mathematicians alike have contributed to our understanding of the topic. For as long as people have known about microscopic life, they have tirelessly catalogued it [86, 125, 126, 182], poked it [98], and watched it go about its business [40, 61, 195, 209]. In the last few decades, people have also constructed simplified models of micro-organisms and simulated their behaviour using computers [83, 96, 107, 158].

The theoretical work of modelling and simulating micro-organisms has been, for the most part, the pursuit of physicists and mathematicians. Our work as theorists is possible thanks to experimental advances in microscopy over the last couple of decades, which have allowed scientists to track and observe the movement of micro-swimmers with unprecedented detail [45, 46, 61, 209]. Interest in this area of research has also been spurred by the prospect of discovering new physics in active systems of micro-organisms, which are inherently out of equilibrium [144, 174].

It would be impossible to discuss all of microscopic life in one dissertation – we focus on bacteria. Nor would it be possible to discuss all aspects of bacterial life in detail. Out of the seven functions of living things, i.e. movement, sensitivity, respiration, nutrition, growth, reproduction and excretion, we focus on movement or motility.

The majority of motile bacteria use flagella as a means of propulsion [15]. Flagella in general, i.e. both in bacteria and eukaryotes, are long and slender appendages protruding from the cell body in relatively small numbers, in contrast to eukaryotic cilia which are shorter and cover the cell body like a carpet [14]. Since we approach the topic of bacterial motility from the perspective of applied mathematics rather than evolutionary or cell biology, the research presented in this dissertation consists of minimal models for the swimming of multiflagellated bacteria, focused on the geometric and hydrodynamic description of flagellar bundles. For a broader discussion of bacterial hydrodynamics, beyond models of a single swimming cell or a flagellar bundle, we refer the reader to the review article by Lauga [121].

This introductory chapter is intended as a guide for newcomers into the world of “low Reynolds number”, to provide them with the physical intuition to navigate it. We start by explaining the basic physical principles of flagellar propulsion, and then steer the reader towards the topic of this dissertation by providing them with some biological background on what the bacterial flagellum is, and what it means for bacteria to have multiple flagella. In the final two sections, we discuss the overarching goal of our research and we review the structure of the thesis.

## 1.1 Basics of flagellar propulsion at low Reynolds number

The Reynolds number<sup>2</sup> is a dimensionless parameter that tells us the relative importance of inertial and viscous forces in a fluid. It is defined by the formula  $Re = \rho_{\text{fluid}}UL/\mu$ , where  $\rho_{\text{fluid}}$  is the density of the fluid,  $U$  is the speed of the flow,  $L$  is a characteristic length scale, and  $\mu$  is the dynamic viscosity of the fluid. For a swimming organism, the characteristic length scale is the size of the body, so the smaller the organism, the smaller the Reynolds number. The bacteria that we are interested in have a cell body size of a few micrometers,  $L \approx 2 \mu\text{m}$ , and they swim at a speed around  $U = 30 \mu\text{m s}^{-1}$ . In water at  $20^\circ\text{C}$  this leads to a Reynolds number on the order of  $Re \sim 6 \times 10^{-5}$ , meaning that bacteria feel the effect of viscous forces from the fluid thousands of times more strongly than they feel inertial forces.

The fact that viscous forces dominate over inertial effects has deep repercussions on the swimming of micro-organisms at low Reynolds number. Their movement is essentially instantaneous - as soon as they stop actuating their flagella, the viscosity of the surrounding fluid grinds them down to a halt. Purcell [170] estimated that a swimming bacterium would coast for only 0.001% of its body length after it stopped moving its flagella. Evidently, this is an organism that does not know much about inertia. Its motion depends only on the instantaneous rate at which the flagella are moving, and not on their past history of actuation.

The second important property of low Reynolds number hydrodynamics is that rigid bodies respond linearly to the forces applied on them [115]. If the micro-organism applies twice as much force to its swimming appendages, they move at twice the speed. Combined with the previous property of instantaneity, this leads to a fundamental result usually referred to as Purcell's scallop theorem, which says that a time-reciprocal swimming gait cannot lead to net motion at zero Reynolds number.

### 1.1.1 Purcell's scallop theorem

The scallop, illustrated in Fig. 1.1 (a), is the classic example of a swimmer with only one degree of freedom: the opening angle of its shell,  $\theta$ . Because the scallop moves through a time-reciprocal sequence of geometries as it opens up its shell and closes it back up, the centre of mass returns to its initial position at the end of the swimming gait – if the scallop lives in the world of low Reynolds number. This statement can be written down mathematically using the two properties of instantaneity and linearity introduced earlier.

The vertical speed,  $\dot{z}(t)$ , of the scallop in Fig. 1.1 (a) is linearly proportional to the instantaneous rate at which the shell opens,  $\dot{\theta}(t)$ . The factor of proportionality between the

<sup>2</sup>Osborne Reynolds (1842-1912) famously studied the transition between laminar and turbulent flows in pipes and classified the two categories of flows according to the number which now bears his name [179].

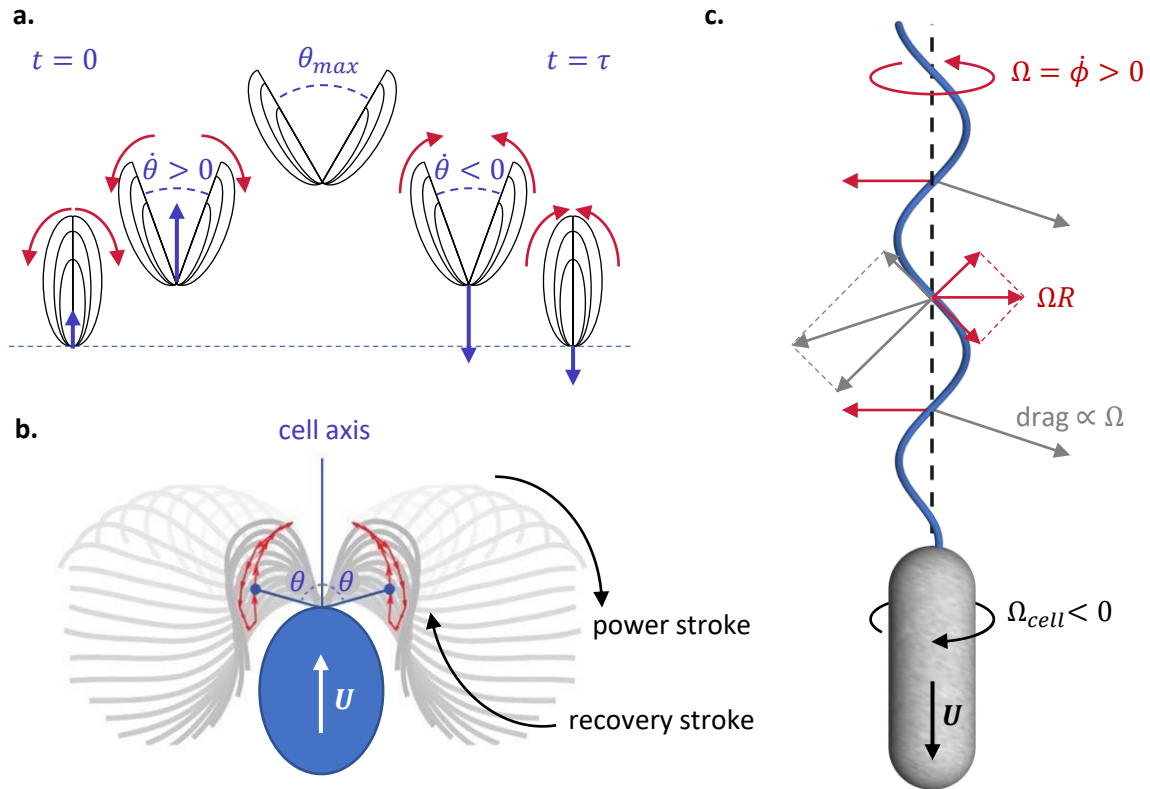


Fig. 1.1 Principles of swimming at low Reynolds number. (a) Purcell's scallop theorem, demonstrated by a time series of instantaneous shapes. A swimmer with a time-reciprocal swimming gait cannot generate sustained motion at low Reynolds number, since it moves up and down by the same amount during the power and recovery stroke. (b) Breaststroke swimming of *Chlamydomonas reinhardtii*. Having flexible flagella allows eukaryotic cells to swim persistently in one direction, by modulating the shapes of the power and the recovery stroke, which results in a non-reciprocal gait. Diagram adapted with permission from Wan et al. [221]. (c) Sketch of a swimming bacterium with one flagellum. By continuously rotating a left-handed helical propeller in the counter-clockwise (CCW) direction, bacteria are able to push their bodies forward. The local velocity of the rotating filament relative to the fluid is horizontal everywhere on the figure, while the drag exerted by the fluid on the filaments has a negative vertical component due to the anisotropic drag on a slender rod (i.e. the drag perpendicular to the filament is larger than the drag parallel to it). By integrating the drag exerted by the fluid along the length of the helix, we deduce that the rotating propeller experiences a net force in the downward vertical direction. If the cell is free to move, it swims downwards and rotates in the opposite sense to the propeller, in order to balance the forces and torques exerted by the fluid on the entire bacterium.

two is a parameter,  $\zeta_{\text{scallop}}(\theta(t))$ , that encapsulates the instantaneous shape of the scallop but not its past history. Therefore, the vertical speed is  $\dot{z}(t) = \zeta_{\text{scallop}}(\theta(t))\dot{\theta}(t)$ , and the net displacement of the scallop over one period of motion is

$$z(\tau) - z(0) = \int_0^\tau \frac{dz}{dt} dt = \int_0^\tau \zeta_{\text{scallop}}(\theta(t)) \frac{d\theta}{dt} dt = \int_{\theta(0)}^{\theta(\tau)} \zeta_{\text{scallop}}(\theta) d\theta. \quad (1.1)$$

This is identically zero because the limits of integration are the same, since the scallop returns to the same geometry at the end,  $\theta(0) = \theta(\tau) = 0$ . Even if the scallop closes its shell faster than it opens it, there can be no net displacement because there is no inertia. This is a prime example of how the world of low Reynolds number escapes our physical intuition from the high Reynolds number world.

### 1.1.2 Strategies for escaping Purcell's scallop theorem

One way to generate a non-reciprocal swimming gait is to have more than one degree of freedom, for instance by having a body with multiple moving parts. An abstract realisation of this is Purcell's three-link swimmer [170] whose motion has been characterised theoretically [6], or more generally an  $N$ -link swimmer [4]. In the limit of very many and very short links, coupled elastically to one another, this strategy becomes equivalent to having a flexibly deforming body or flagellum. Eukaryotic cells such as *Chlamydomonas reinhardtii*, illustrated schematically in Fig. 1.1 (b), use this strategy for locomotion. In the case of *Chlamydomonas*, the flagella move further away from the cell body during the downward power stroke compared to the upward recovery stroke. This allows the alga to pull itself up by a greater amount during the power stroke, leading to net motion along the axis of the cell, in the direction of the beating flagella.

An alternative way to satisfy the constraint of non-reciprocal motion, without using flexible flagella, is to stick with a rigid propeller that has only one degree of freedom, but to make that degree of freedom rotational. This is the solution used by bacteria, which possess a specialised motor that can rotate a helical propeller around its own axis, as shown in Fig. 1.1 (c). The rotational degree of freedom means that the cell can return to the same configuration and be ready for another cycle of motion, without the degree of freedom itself returning to the same value. If  $\phi$  is the angle by which the propeller has rotated around its own axis, we follow the same argument as for the scallop to find that there is a net displacement over one period of rotation of the propeller,

$$z(\tau) - z(0) = \int_0^{2\pi} \zeta_{\text{rotating propeller}}(\phi) d\phi, \quad (1.2)$$

because the limits of integration are now different,  $\phi(0) = 0$  and  $\phi(\tau) = 2\pi$ . By continuously rotating a helical propeller, the bacterium is able to generate net motion of its centre of mass within the constraints of low Reynolds number hydrodynamics.

### 1.1.3 Swimming with a helical propeller

We now go into more detail about the physical mechanism that allows a continuously rotating propeller to push the cell forward. The fundamental reason why a rotating helical filament generates a net thrust along its axis is that, at low Reynolds number, the viscous drag on a slender rod is anisotropic. To be more specific, the force required to translate a slender rod perpendicular to its axis is roughly twice as large as the force needed to translate the same rod along its axis.

In order to explain the forces acting on the helical propeller, we use the approximation that the filament is locally straight at every point along its centreline. This is a reasonable approximation since the curvature of bacterial flagellar filaments is much larger than the thickness of the filaments. Then, at every point along the filament, we decompose the velocity of the filament relative to the fluid into components parallel and perpendicular to the filament centreline, as shown in Fig. 1.1 (c). Due to the anisotropy of the drag on a slender rod, we deduce that the local drag on the helical filament has a negative component in the vertical direction (on the figure) at every point along the helix. When integrated along the length of the filament, the horizontal components of the drag lead to a net torque exerted by the fluid against the direction of rotation of the filament, while the vertical components add up to a net thrust along the axis of the filament. Under normal operating conditions, bacteria rotate left-handed filaments in the CCW direction, which leads to a net thrust in the negative  $z$  direction - see Fig. 1.1 (c). Hence, bacteria are pushed forward by the flagella rotating at the back of the cell, in contrast to organisms like *Chlamydomonas* which are pulled by the flagella in front of them - see Fig. 1.1 (b).

To determine the speed at which the bacterium moves, it is necessary to consider the force balance on the entire cell along the direction of motion. If the bacterium swims freely, i.e. there is no external force applied to it, then the thrust provided by the helical propeller due to rotation must balance out the drag on the filament and the drag on the cell body due to translation, written in order as

$$B\Omega + AU + A_{\text{body}}U = 0. \quad (1.3)$$

Note that we have exploited the linearity of low Reynolds number flow when writing down the force balance equation, by introducing the linear coefficients of proportionality,  $B$ ,  $A$  and

$A_{\text{body}}$ , between the forces and the velocities. Furthermore, there is no contribution to the force balance from the rotation of the cell body, because the cell body is not chiral like the propeller.<sup>3</sup> The equation for vertical force balance is easily inverted to obtain the swimming speed of the cell in terms of the angular velocity of the propeller,

$$U = -\frac{B\Omega}{A + A_{\text{body}}}. \quad (1.4)$$

Likewise, by considering the torque balance on the cell in the vertical direction, we determine the angular velocity of the cell as approximately

$$\Omega_{\text{body}} \approx -\frac{D\Omega}{D_{\text{body}}}, \quad (1.5)$$

where  $D$  and  $D_{\text{body}}$  are positive coefficients of proportionality between the angular velocity and the torque exerted by the propeller and the cell, respectively. The approximation comes from neglecting the torque due to the translation of the filament, which turns out to be much smaller than the torque due to its rotation, for a typical bacterial flagellum. Because bacteria have large bodies compared to the helical amplitude of their propeller, the resistance of the cell body to rotation is much larger than the resistance of the helical filament, so  $\Omega_{\text{body}} \ll \Omega$ . Hence, the cell body counter-rotates with respect to the helical propeller at a much lower angular velocity [40].

In this section, we have considered a minimal model of a bacterium that swims by rotating a helical propeller in order to illustrate two important concepts: the way in which thrust is generated from the anisotropic drag on a slender filament, and the way in which the swimming speed and rotation rate of the cell are selected via a force and torque balance on the entire organism. The minimal model does not include hydrodynamic interactions between the cell body and the propeller, and does not take into account the details of how the propeller is actuated and connected to the cell body. To improve our modelling of the swimming bacterium, we need to understand the organism in more depth, starting with the organelle used for swimming – the bacterial flagellum.

---

<sup>3</sup>Some bacteria like *Spirillum volutans* have a helicoidal cell body as well as helical propellers, but here we focus on bacteria with cell bodies shaped like a spheroid or a cylinder with rounded poles.

## 1.2 The bacterial flagellum

The bacterial flagellum is an organelle used primarily for locomotion [152] and is made up of three components: a specialised molecular motor embedded in the cell wall, a helical flagellar filament that acts as a propeller, and a short and flexible hook that joins the motor to the flagellar filament. Unlike eukaryotic flagella, which are actively stretched and contracted along their entire length by dynein motors [15], bacterial flagella are actuated passively through the rotation of the molecular motor at the basal end of the flagellum.

A convincing case for the argument that bacteria swim by rotating their flagellar filaments was made in 1973 by Berg and Anderson [10]. Prior to that, there was a debate between the idea that bacterial flagellar filaments rotate rigidly around their axis, and the alternative suggestion that a helical wave propagates down a flexible flagellar filament, similar to the motion of a spermatozoon tail. The two mechanisms cannot be distinguished purely based on a two-dimensional video recording of a swimming bacterium, since they both appear as sinusoidal waves propagating away from the cell body. Berg and Anderson [10] brought further physical arguments based on experimental evidence that motile bacteria become immobilised when either flagellar antibodies or bacteriophages are added to the aqueous solution. Berg and Anderson [10] demonstrated that the action of both flagellar antibodies and bacteriophages on the flagellar filaments would only prevent the bacteria from swimming if the mechanism by which bacteria swim is the rigid rotation of its flagellar filaments.

### 1.2.1 The flagellar filament

The bacterial flagellar filament is a very long and thin structure, with a typical contour length of around 7  $\mu\text{m}$  [209], and a cross-sectional diameter of only 24 nm for the species that we are interested in [222]. Flagellar filaments are made up of a single protein called flagellin and can be reconstituted *in vitro* through a process of polymerisation, if flagellar fragments are added as nucleation sites to a solution of flagellin monomers [5]. In live bacteria, it has been shown via fluorescent staining with multiple dyes that flagellar filaments continue to grow from the distal end of the filament [178, 210]. It has been suggested that the way in which bacteria manage to assemble flagellar filaments outside the cell body, where there is no power source, is through an injection-diffusion mechanism [90, 178]. This means that flagellin is produced inside the cell body and injected into the inner channel of the flagellum by a structure called a type III secretion system [139], after which the flagellin diffuses to the end of the filament and polymerises onto the existing scaffold.

An essential feature of flagellar filaments is their helical shape, visible in the images of live *Escherichia coli* cells reproduced in Fig. 1.2 (a-d), which were captured with a

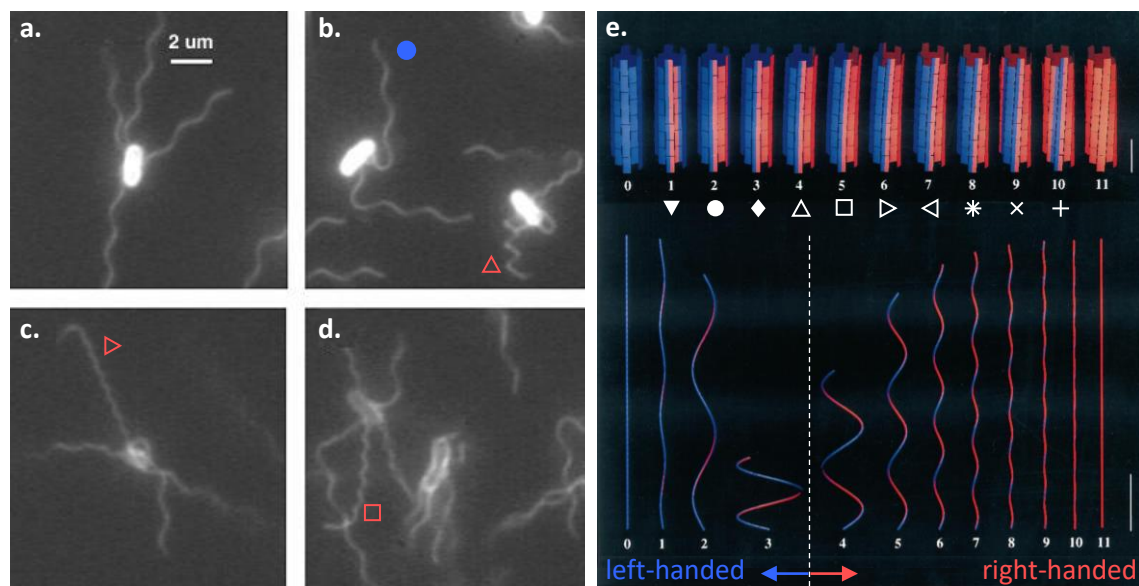


Fig. 1.2 Polymorphic shapes of the bacterial flagellar filament. (a-d) *Escherichia coli* cells with multiple flagella observed through a fluorescence microscope. The flagellar filaments assume multiple polymorphic shapes: (a) normal, (b) normal, semicoiled, curly I, (c-d) normal, curly I, curly II. Labels correspond to the classification in (e). Images adapted with permission from Turner et al. [209]. Copyright 2000 American Society for Microbiology. (e) The full set of polymorphic forms predicted by a theoretical model of the internal structure of the filament [81]. The flagellar filament is straight when the eleven protofilaments in its composition are all in the L-type configuration (blue) or in the R-type configuration (red). Ten helical shapes are observed in between, identified by a polymorphic number from 1 to 10. The most common are the normal (poly. no. 2), semicoiled (poly. no. 4), curly I (poly. no. 5) and curly II (poly. no. 6). Figure adapted with permission from Hasegawa et al. [81]. Copyright 1998 Elsevier.

fluorescence microscope by Turner et al. [209]. The shape most commonly assumed by the flagellar filaments of multi-flagellated bacteria is a left-handed helix called the “normal” shape, labelled by a blue circle in Fig. 1.2 (b). Three right-handed helical shapes are also identifiable in Fig. 1.2 (b-d) and they are named semicoiled (upward triangle), curly I (square) and curly II (rightward triangle). The full spectrum of helical shapes that bacterial flagellar filaments can assume is dictated by the internal structure of the filament and has been predicted by theoretical models [20, 81] - see Fig. 1.2 (e).

Using Fig. 1.2 (e) as a visual aid, we now seek to explain the existence of a discrete set of helical shapes for the flagellar filaments of bacteria. Flagellin, the protein in the composition of the flagellar filament, assembles into 11 protofilaments that run along the centreline of the filament, and each protofilament is made up of molecular subunits that take one of two

stable conformations with slightly different lengths. When all the protofilaments are in the L-type (blue) or the R-type (red) conformation the filament is straight, with the protofilaments wrapping around the axis of the filament either in a left-handed or a right-handed sense - see top row of Fig. 1.2 (e). In between the straight configurations are ten stable helical shapes identified by a polymorphic number which is equal to the number of R-type protofilaments. Note that the protofilaments in the R-type conformation, which is shorter, run along the inside of the helical shape, as seen in Fig. 1.2 (e). The overall chirality of the flagellar filament is determined by the relative number of protofilaments in the L-type and R-type conformation, with polymorphic number between 1 and 3 being left-handed helices, and polymorphic numbers between 4 and 10 being right-handed helices. The shapes and mechanical stability of the polymorphic forms were first explained theoretically by Calladine [20] based on the discrete packing of flagellin subunits. More recently, a continuum rod model has been proposed by Srigiriraju and Powers [199, 200] that captures the essential mechanical features of bacterial polymorphism.

During a tumbling event<sup>4</sup>, the change in the motor torque applied to the flagellar filament can cause the filament to snap between different minima in the elastic energy landscape associated with its multiple polymorphic shapes [217]. Transitions between the polymorphic shapes can also be triggered *in vitro* by changes in pH and temperature [106] or by applying an external flow to the filaments [31, 88]. The mechanical conditions for polymorphic transformations have been determined via controlled force-extension measurements by Darnton and Berg [39]. Between polymorphic transformations, the flagellar filament deforms elastically with a bending stiffness much larger than that of the hook (see §1.2.2).

The bending stiffness of the flagellar filament has been estimated from controlled force-extension measurements by Darnton and Berg [39], and from the slight changes observed between the helical shape of stationary versus rotating flagellar filaments by Darnton et al. [40]. The elastic deformation of a helical filament due to an external flow has been studied theoretically by Kim and Powers [112], while the deformation and buckling of a rotating helical filament has been investigated with macroscopic scale models by Jawed et al. [101].

### 1.2.2 The hook

The flagellar hook is a short polymeric structure made up of a different protein, which connects the flagellar filament to the molecular motor. Compared to the flagellar filament, the hook is both shorter and much more flexible, with a contour length of 59 nm and a bending rigidity of  $1.6 \times 10^{-4}$  pN  $\mu\text{m}^2$  measured in *Escherichia coli* by Sen et al. [188]. The typical

---

<sup>4</sup>Tumbling will be discussed later in the context of bacterial multiflagellarity.

flagellar filament has a length around 7  $\mu\text{m}$  and bending rigidity around 3.5 pN  $\mu\text{m}^2$  [39]. For this reason, the hook is often modelled as a point joint allowing the flagellar filament to rotate freely around its anchoring point.

Despite its small size, the hook plays an important role in the mechanism by which bacteria with a single flagellum change swimming direction. When the bacterium swims forward, the hook is under compression due to the thrust exerted on it by the helical propeller. Eventually, the hook buckles under the mechanical stress and the flagellar filament is flicked to one side of the cell, leading to a change in orientation. This strategy for changing orientation was observed in the swimming pattern of the marine bacterium *Vibrio alginolyticus* by Son et al. [195].

In bacteria with multiple flagella, like *Escherichia coli*, the hook allows flagellar filaments to come together at the back of the cell and form a bundle. Theoretical models have suggested that multi-flagellated bacteria are able to systematically choose a swimming direction due to an elastohydrodynamic instability, made possible by the low bending rigidity of the hook [97, 180]. Meanwhile, experiments using hook-length variants of *Salmonella enterica* have revealed that the length of the hook is optimised for maximal stability of the flagellar bundle [198].

### 1.2.3 The rotary motor

The bacterial flagellar motor (BFM) is a rotary stepping motor powered by a flux of protons or sodium ions across the cytoplasmic membrane [148]. The energy lost by the ions as they go down an electrochemical gradient from the outside to the inside of the cell is used up by the mechanical work done in rotating the central shaft of the motor. The internal structure of the BFM is depicted in Fig. 1.3 (a). The torque generating units called “stators” are bound to the cell wall, while the cytoplasmic ring called the “rotor” is free to rotate relative to the stators. Mechanistic models for the BFM have proposed that each step of the motor is the result of a conformational change in the stator unit, powered by the free energy released by a passing ion [143].

One important feature of the BFM, depicted in Fig. 1.3 (b), is the relationship between the angular speed and the torque applied by the BFM to an external load (e.g. the flagellar filament). The distinctive feature of the torque-speed curve is that the torque is roughly constant in the high-load regime, and then decreases linearly with angular speed in the low-load regime. Bacterial flagella typically operate in the high-load regime, so the torque exerted by the BFM on the flagellar filament is, to a good approximation, constant.

Theoretical modelling of the internal dynamics of the BFM has suggested that the two regimes are determined by a balance between waiting times and moving times of the motor

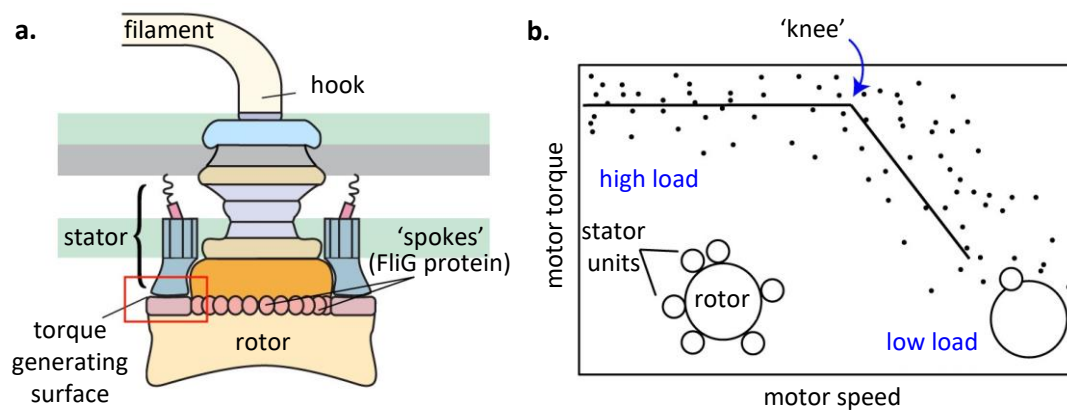


Fig. 1.3 Essential features of the bacterial flagellar motor. (a) The flagellar filament is connected through a short and flexible hook to a rotary motor embedded in the cell wall. The most important structural units of the bacterial flagellar motor (BFM) are the “rotor” ring which, as the name suggests, is free to rotate in the cytoplasm, and the torque-generating “stator” units bound to the cell wall. (b) The torque-speed relationship of the BFM exhibits a high-load regime where the torque is approximately constant, and a low-load regime when where the torque decreases linearly with the rotation speed. There is evidence that the BFM recruits more stator units as the external load increases; the saturation of stator units is partially responsible for the plateau in torque in the high-load regime. Figure adapted with permission from Nirody et al. [161]. Copyright 2019 The Royal Society.

[160, 161, 227]. In the low-load regime, the time spent waiting for a new ion to arrive is much longer than the time it takes for the motor to make one step, so the dynamics of the motor are kinetically-limited. In the high-load regime, the motor takes longer to perform each step due to the large hydrodynamic resistance of the external load, so the motor is mechanically-limited. There is also experimental evidence that the recruitment of additional stator units by the BFM as the load increases contributes to the existence of the plateau region, since motors with a single stator unit do not exhibit such a pronounced plateau[134]. For more information about the BFM, including details of how the torque-speed relationship is measured in practice, we refer the reader to a comprehensive review article by Sowa and Berry [196].

As a final note, we mention that the motor plays an important role in the navigation of motile bacteria by allowing them to change swimming direction, as previously hinted at in our discussion of the flagellar hook. This change in swimming direction is achieved by stochastic reversals in the direction of rotation of the BFM [109, 140].

In this section, we have provided some biological background on the structure and mode of actuation of the bacterial flagellum, placing particular emphasis on the helical polymorphic shapes of the flagellar filament, and the torque-speed relationship of the bacterial flagellar

motor. These two features are essential for the theoretical models and results presented in this dissertation. The helical shape of the flagellar filament is the underpinning of the three chapters on geometry, while the torque-speed relationship is crucial for the dynamics of synchronisation and propulsion discussed in the chapters on hydrodynamics.

### 1.3 Bacterial multiflagellarity

Now that we are equipped with a basic understanding of what the bacterial flagellum is, we turn to the idea of multiflagellarity. The model organism for multi-flagellated bacteria is *Escherichia coli*, to which we henceforth refer simply as *E. coli*. For a cross-disciplinary introduction to the topic including the physiology, biochemistry and genetics of *E. coli*, we refer the reader to a classic text by Berg [9]. Here, we focus on the physics and, in particular, the fluid mechanics of *E. coli* and other multi-flagellated bacteria like it.

*E. coli* is a peritrichous bacterium, meaning that the flagella are distributed uniformly around the cell body. As seen in Fig. 1.2 (a-d), the cell typically has between three and five flagella [208], slightly less than the average of six flagella owned by *Salmonella typhimurium* [91] and much less than the twenty-six flagella of *Bacillus subtilis* [156]. One obvious question to ask at this point is why the number of flagella varies between different species of bacteria.

While we do not wish to dwell on evolutionary aspects of multiflagellarity, we briefly mention that in the *Atlas of bacterial flagellation*, Leifson [125] writes that: “The available evidence indicates that bacterial evolution is from polar monotrichous organisms to peritrichous organisms and, finally, to atrichous organisms.” Monotrichous refers to bacteria with a single flagellum placed at one end of the cell (polar), while atrichous refers to bacteria without flagella. Leifson [125] goes on to suggest that the flagellation patterns of bacteria may be linked to locomotion in different environments, with monotrichous bacteria more commonly found in fresh and sea water, and peritrichous bacteria more commonly found in soil and denser media. Bacteria are known to lose their flagella when placed in nutrient-rich environments, either by becoming parasitic or being cultured in the laboratory. A more recent discussion of the mechanisms by which bacteria regulate the number and location of their flagella can be found in Schuhmacher et al. [187].

In the rest of this section, we focus on the consequences of having multiple flagella, rather than the reasons for it. We are particularly interested in the mechanical aspects of swimming with multiple flagella, which is the unifying theme of this dissertation.

### 1.3.1 Run-and-tumble motility

Peritrichous bacteria explore their environment using a strategy called run-and-tumble, where they swim in straight lines (“runs”) interrupted by short intervals of reorientation (“tumbles”). During a run, the flagellar filaments gather at the back of the cell body and rotate together in a bundle [209], or multiple bundles in the case of highly-flagellated bacteria like *B. subtilis* [155]. As the cell swims forward, the body of the bacterium rotates in a CCW direction to balance the torque on the bacterium, as previously discussed in §1.1.3. These counter-rotations of the cell body are known to contribute to the wrapping of the flagellar filaments around each other to form a bundle [1, 168].

The bundling and unbundling process can be seen in fluorescence microscopy images of *E. coli* in Fig. 1.4 (a). Tumbling events are triggered by a reversal in the direction of rotation of at least one motor, followed by the dispersal of the bundle and the reorientation of the cell. The stages of run-and-tumble are summarised diagrammatically in Fig. 1.4 (b). Note that one of the flagellar filaments in the diagram changes its helical amplitude and pitch during the tumble, since polymorphic transformations are known to accompany tumbling events [40, 209].

The swimming and tumbling statistics of *E. coli* are well understood, having been measured experimentally by Darnton et al. [40] and in a follow-up study by Turner et al. [208]. To get a sense of the time scales, we mention that bacteria typically spend around 1 s swimming in a straight line, while the tumbling event is much shorter around 0.1 s. Both the initiation of the tumbling event and the reorientation angle are stochastic effects, so bacteria essentially explore their environment via a random walk. This can be seen in Fig. 1.4 (c) from the trajectory of *E. coli* cells tracked by Berg and Brown [11]. By modulating the duration of run intervals in response to changing chemical signals, peritrichous bacteria are able to bias their random walk towards favourable environmental conditions [8, 11]. This process is called chemotaxis and is essential for cells that need to find nutrients or escape harmful substances.

Experimental observations by Najafi et al. [156], where they analyse the swimming trajectories of *B. subtilis* mutants with fewer or more flagella than the wild-type, have revealed that the number of flagella affects all aspects of run-and-tumble motility: the instantaneous speed of the cells, the duration of run intervals, and the change in orientation angle between runs. We say a few more words below about how the swimming speed varies with the number of flagella, since this question will be the focus of one of our later chapters.

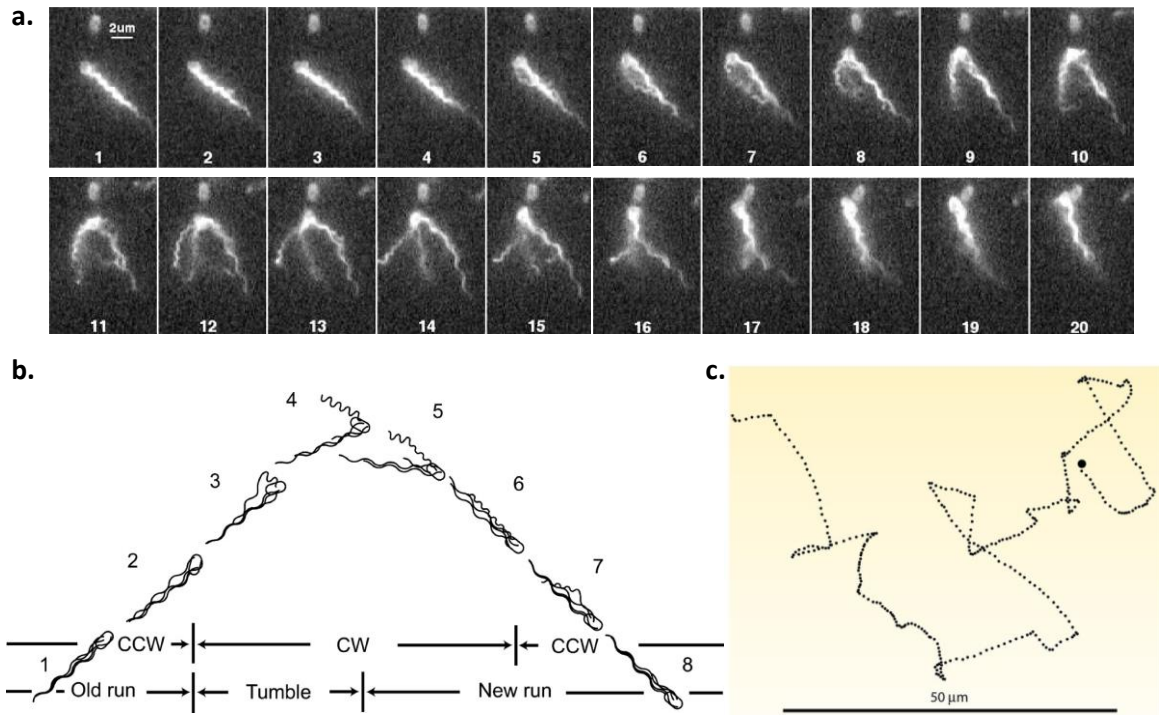


Fig. 1.4 Run-and-tumble motility of peritrichous bacteria. (a) Images of a motile *E. coli* cell, tracked with a fluorescence microscope, demonstrate that the flagellar filaments are able to unbundle (top row) and then rejoin the bundle at the back of the cell body (bottom row). Images adapted with permission from Turner et al. [209]. Copyright 2000 American Society for Microbiology. (b) Sketch of run-and-tumble motility. Two intervals of swimming in a straight line (“runs”) are interrupted by a tumbling event when one of the motors reverses from CCW to CW rotation. The tumble is often accompanied by polymorphic transformations in some flagellar filaments. Figure reprinted with permission from Darnton et al. [40]. Copyright 2007 American Society for Microbiology. (c) Random walk trajectory of a bacterium performing run-and-tumble. Figure reprinted with permission from Stocker and Seymour [202] with permission, original content. Copyright 2012 American Society for Microbiology. Original content reproduced with permission from Berg and Brown [11]. Copyright 1972 Nature Publishing Group.

### 1.3.2 Swimming speed of multiflagellated bacteria

In §1.1.3 we calculated the swimming speed of a cell with a single helical propeller, based on a force balance argument along the direction of motion. This result can be extended to the case of a multi-flagellated bacterium, following Nguyen and Graham [158], by including in the force balance equation the thrust and drag on multiple helical propellers,

$$N_f B \Omega + N_f A U + A_{\text{body}} U = 0, \quad (1.6)$$

where  $N_f$  is the number of flagellar filaments propelling the cell. We rearrange this expression to find the swimming speed of a bacterium with multiple flagella as

$$U = -\frac{N_f B \Omega}{N_f A + A_{\text{body}}}. \quad (1.7)$$

According to this simple argument, which does not include hydrodynamic interactions with the cell body or between the filaments themselves, the absolute swimming speed of the cell increases linearly as  $|U| \sim N_f B \Omega / A_{\text{body}}$  for very small number of flagella, and then reaches a plateau,  $|U| \rightarrow B \Omega / A$ , when the number of filaments is sufficiently large. In this simplified model, the speed of the bacterium is limited by the intrinsic speed of its individual helical propellers, i.e. the speed  $B \Omega / A$  at which a force-free helical filament would move if some external mechanism imposes on it a constant angular velocity  $\Omega$ .

The purpose of this simple calculation is to highlight that the swimming speed of the cell is not directly proportional to the number of flagella, but bounded above by the intrinsic properties of the propellers. The sublinear gain in swimming speed is surprising when contrasted with the expected linear increase in energetic cost, based on a general understanding of how the flagella are assembled and operated [9].

## 1.4 Objective of the thesis

As evidenced by our discussion from the previous section, the reason why bacteria have multiple flagella is an open question. While flagellation patterns may be an environmental adaptation [125], the variation of flagellar numbers within the class of peritrichous bacteria may have nothing to do with constraints related to motility. On the other hand, there is theoretical and experimental evidence that the number of flagella does influence the motility of multi-flagellated cells [107, 156, 158]. Setting aside evolutionary and physiological considerations, the purpose of this dissertation is to advance our physical understanding of multiflagellar motility, focusing on the dynamics of a bundle of bacterial flagella.

The global objective of this dissertation is to understand how bacterial flagellar filaments interact with each other as they rotate together in a bundle, and what this means for the operation of the bundle and the swimming of the cell. The interactions between flagella may be of a hydrodynamic nature, meaning that the flagellar filaments are coupled to each other through the entrainment of the fluid around them, or they may be “dry” interactions such as excluded volume effects. The latter interactions are intrinsically linked to the helical geometry of flagellar filaments, which dictates how much a filament can deviate from its current position before it collides with another filament in the bundle.

In this dissertation, we investigate both the hydrodynamic and geometrical interactions between bacterial flagella using the mathematical tools at our disposal, which will be discussed in more depth in Chapter 2. For the geometrical side of the investigation, we use concepts from classical and vector geometry, while the hydrodynamic calculations are handled using asymptotic methods that exploit a separation of scales between parameters [84], e.g. the separation between the cross-sectional radius of a flagellar filament and its length [69, 79, 105, 132], or the separation between the frequency of rotation of the filaments and their rate of synchronisation.

Synchronisation does, in fact, provide the connective tissue between the two parts of this dissertation. As previously found by Macnab [138] and further developed in Chapter 5 of this thesis, the helical geometry of flagellar filaments requires that the filaments synchronise in phase with each other in order for the bundle to operate smoothly. Since the rotary motors actuating the filaments work independently of each other, this requirement for synchronisation must be satisfied by other means. One mechanism considered in the literature, and further developed in Chapter 7 of this thesis, is that rotating bacterial flagella synchronise through hydrodynamic interactions [171, 175–177].

## 1.5 Structure of the thesis

Aside from the current introductory chapter, this thesis is structured into

- one chapter of mathematical background (Chapter 2),
- three chapters on the geometry of flagellar bundles (Chapters 3,4,5),
- three chapters on the hydrodynamics of flagellar filaments (Chapters 6,7,8),
- and a final chapter with future directions for research (Chapter 9).

Below we provide more detail on the six chapters of the thesis that contain novel research results, highlighting the questions that each chapter addresses.

In Chapter 3, we investigate the geometrical intertwinement of flagellar filaments with different polymorphic shapes. While Macnab [138] found that the left-handed geometry of the normal polymorphic form is incompatible with the right-handed wrapping imposed by hydrodynamics effects, it is not known whether normal shape filaments could intertwine in a right-handed sense with different polymorphic forms. Our findings suggest that the polymorphic transformations to the right-handed semicoiled and curly I/II shapes during a tumbling event may contribute to the filaments rejoining the bundle at the start of a new run,

by allowing the right-handed filaments to wrap around the bundle in the direction dictated by hydrodynamics.

In Chapter 4, we consider the geometrical constraints on the tangling of anchored helical filaments as they come together to form a bundle. In this context, tangling is regarded as a mistake in the bundling process, since tangled bundles cannot be actuated smoothly by the rotary motors. It is not fully understood how bacteria are able to robustly form coherent bundles despite the uncoordinated actuation of multiple rotary motors. By comparing the theoretical predictions of our geometrical model with experimental measurements of the geometry of flagellar filaments and the cell body, we find that the intrinsic geometry of flagellar filaments makes tangling very unlikely. This suggests that the bundling process is robust, despite the lack of control over the individual positions of the filaments. This chapter is based on a manuscript written in collaboration with my supervisor, Eric Lauga, and published in *Scientific Reports* [206]. Modifications have been made to the text and the figures so that the style and notation of this chapter is consistent with the rest of the dissertation.

In Chapter 5, we investigate the geometrical requirement for synchronisation during the bundling of continuously rotating filaments. The idea of this chapter is to identify how much coordination is needed so that the flagellar filaments do not collide with each other. The longer-term research goal of this chapter is to compare the amount of synchronisation required by geometry with the rate of synchronisation induced by hydrodynamic interactions. The balance between the two determines the operational constraints on the bundle, such as the critical number of filaments or the critical variation in motor torque to ensure smooth operation. Furthermore, this chapter serves as motivation for our work on the elasto-hydrodynamic synchronisation of bacterial flagella in Chapter 7.

In Chapter 6, we develop an asymptotic theory for the hydrodynamic interactions (HIs) between rigid filaments separated by a distance greater than their contour length. The purpose of this theory is to provide an analytical basis for understanding the physical principles that govern the HIs between rotating helical filaments, as a minimal model for bacterial flagella. Our asymptotic calculations are based on the well-established methods of resistive-force theory (RFT) [69, 79, 132] and slender-body theory (SBT) [105, 108, 131], combined with an asymptotic series expansion of the Oseen tensor [115].<sup>5</sup> We validate our theory using numerical computations that involve a Galerkin method solution of the SBT equations with full HIs between the filaments, and then we apply the theory to the case of two helical pumps rotating in parallel. The technical content of this chapter is used as a foundation for the next two chapters on synchronisation and propulsion. This chapter is based on a

---

<sup>5</sup>These fundamental concepts in low Reynolds number hydrodynamics will be introduced in Chapter 2.

manuscript written in collaboration with my supervisor, Eric Lauga, which has been accepted for publication by *Physical Review Fluids* [207]. Modifications have been made to the text in order to avoid repetition with the rest of the dissertation.

In Chapter 7, we address the important issue of synchronisation between rotating bacterial flagella. While several analytical models have been proposed for the synchronisation of beating eukaryotic flagella, the synchronisation of rotating bacterial flagella is less well understood. Since bacterial flagella are fundamentally different from eukaryotic flagella in terms of their actuation, shape and rigidity, it is expected that different analytical models are required. In this chapter, we propose a reduced model of the bacterial flagellum which incorporates the salient features of the organelle, and we use the method of multiple scales [84] to rigorously coarse-grain the equations of motion into an evolution equation for the phase difference between two rotating helical filaments. When the filaments are sufficiently far apart, HIs generically lead to in-phase synchronisation.

Remarkably, we find that the rate of elastohydrodynamic synchronisation between two bacterial flagella is maximised at an intermediate value of elastic compliance, in contrast to previous studies on eukaryotic flagella where the rate of synchronisation has been observed to increase monotonically with increased elastic compliance. The surprising implication of our results is that the elastic compliance provided by the flagellar filament, although much more rigid than the hook, may contribute more to the synchronisation of bacterial flagella. The crucial role of elastic compliance is also manifested in the emergence of multisynchrony when the rotating filaments are sufficiently close together, as captured by our numerical simulations. This novel result is of great relevance to the stability of flagellar bundles, and the onset of unbundling events in multiflagellated bacteria.

In Chapter 8, we investigate how the swimming speed of a multi-flagellated bacterium varies with the number of flagella. We first determine how the propulsive force exerted by the bundle and the hydrodynamic drag on the bundle depend on the number of filaments and the radius of the bundle. Next, to calculate the swimming speed of the cell, we incorporate the hydrodynamic resistance of the bundle into the force and torque balance on the entire bacterium, together with the torque-speed relationship of the BFM, but without HIs between the bundle and the cell body. Notably, we find that the swimming speed is affected in an essential way by the torque-speed relationship of the BFM, leading to a peak in swimming velocity at an optimum number of flagella. This optimum number is within the range observed in experiments.



# Chapter 2

## Mathematical background

In this chapter, we introduce the notation and mathematical methods used in the rest of the dissertation. The first section focuses on geometry and the second on hydrodynamics. First, we introduce the notation used for describing helical filaments of arbitrary orientation, and we review the original study in helical geometry by Macnab [138], which serves as inspiration for our work on the geometry of flagellar bundles. Next, we provide a brief historical perspective on the hydrodynamic modelling of microorganisms, and we introduce the methods used in this dissertation to model the hydrodynamics of flagellar filaments, namely resistive-force theory (RFT) and slender-body theory (SBT).

### 2.1 Geometry of helical filaments

Nature builds a fascinating range of structures and shapes: one of them is the helix. On macroscopic scales, helices can emerge from the differential growth of tissues, with examples including the tendrils of climbing plants and the horns of spiral-horned antelopes [58, 89]. At the microscopic level, many molecules and polymers assume a helical structure [149], most famous being the DNA double-helix [224]. As discussed in §1.2.1, helical shapes also emerge in the self-assembly of bacterial flagellar filaments due to the L-type and R-type binding of molecular subunits [81].

The first to recognise the importance of geometrical constraints on the bundling of bacterial flagella was the biologist Robert M. Macnab, who derived the conditions for geometrical intertwinement of two parallel identical helices, and verified the implications of the geometrical model through experiments with a dry macroscopic-scale model of a rotating bundle [138].

To lay the groundwork for the rest of this dissertation, and in particular the next three chapters on geometry, we first introduce the notation for describing a helical filament with

arbitrary orientation. Once this notation is established, we review the geometrical argument proposed by Macnab [138] and discuss its physical implications for the actuation of flagellar filaments in bundles.

### 2.1.1 Description of a helical filament with arbitrary orientation

A vertical helical filament is shown in Fig. 2.1 (a). The helical geometry of the filament can be described either by a helical amplitude,  $R$ , and pitch,  $p$ , or alternatively by the pitch angle,  $\psi$ , defined as the constant angle that the helix makes with the central axis of the filament, and the number of helical turns of the filament,  $N$ . The conversion between the two descriptions is given by

$$\psi = \tan^{-1} \left( \frac{2\pi R}{p} \right), \quad N = \frac{L}{\sqrt{(2\pi R)^2 + p^2}}, \quad (2.1)$$

or in the other direction,

$$R = \frac{L \sin \psi}{2\pi N}, \quad p = \frac{L \cos \psi}{N}, \quad (2.2)$$

where  $L$  is the contour length of the filament. The cross-sectional radius of the filament,  $\epsilon$ , is much smaller than the contour length,  $L$ . As discussed in §1.2.1, flagellar filaments have an aspect ratio of about 1:300.

#### Centreline and tangent vector

With respect to a body-fixed frame of unit vectors,  $\{\mathbf{e}_1, \mathbf{e}_2, \mathbf{e}_3\}$ , we write the helical centreline of the filament in terms of the arc length,  $s$ ,

$$\mathbf{r}(s) = R \cos \left( \frac{2\pi N s}{L} \right) \mathbf{e}_1 + \sigma R \sin \left( \frac{2\pi N s}{L} \right) \mathbf{e}_2 + s \cos \psi \mathbf{e}_3. \quad (2.3)$$

The unit vectors  $\{\mathbf{e}_1, \mathbf{e}_2, \mathbf{e}_3\}$  are fixed to the entire rigid filament and hence independent of the arc length,  $s$ . The vector  $\mathbf{e}_3$  points along the axis of the cylindrical envelope that contains the helix, while the vector  $\mathbf{e}_1$  points through the midpoint of the filament as seen in Fig. 2.1. The range covered by the arc length is either  $s \in (0, L)$  or  $s \in (-L/2, L/2)$ , as best suited for the calculations at hand. This will be indicated in each chapter as necessary. Note that the helix is left-handed if the chirality parameter is negative,  $\sigma = -1$ , or right-handed if  $\sigma = +1$ .

By taking a derivative with respect to arc length, we find the unit tangent to the centreline to be

$$\hat{\mathbf{t}}(s) = -\sin \psi \sin \left( \frac{2\pi N s}{L} \right) \mathbf{e}_1 + \sigma \sin \psi \cos \left( \frac{2\pi N s}{L} \right) \mathbf{e}_2 + \cos \psi \mathbf{e}_3. \quad (2.4)$$

Note that the tangent vector makes a constant angle  $\psi$  with the axis of the filament,  $\mathbf{e}_3$ .

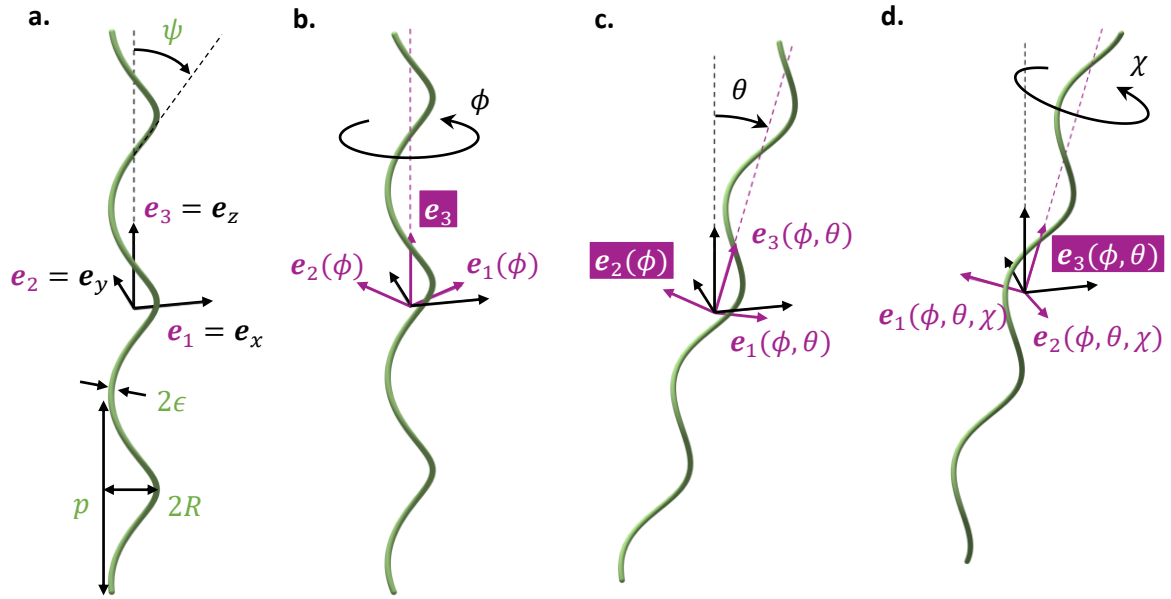


Fig. 2.1 Key geometrical parameters for a helical filament with arbitrary orientation. The filament has helical amplitude,  $R$ , pitch,  $p$ , and cross-sectional radius,  $\varepsilon$ . The tangent to the helix makes a constant angle,  $\psi = \tan^{-1}(2\pi R/p)$ , with the axis of the filament,  $\mathbf{e}_3$ . (a) When the body-frame vectors  $\{\mathbf{e}_1, \mathbf{e}_2, \mathbf{e}_3\}$  are aligned with the laboratory frame  $\{\mathbf{e}_x, \mathbf{e}_y, \mathbf{e}_z\}$ , the three orientation angles  $(\phi, \theta, \chi)$  are identically zero. An arbitrary orientation is obtained by rotating the filament through (b) an angle  $\phi$  around the axis  $\mathbf{e}_3 = \mathbf{e}_z$ , (c) an angle  $\theta$  around the new axis  $\mathbf{e}_2(\phi)$ , and (d) an angle  $\chi$  around the new axis  $\mathbf{e}_3(\phi, \theta)$ .

The helical centreline may be parameterised in other ways than through the arc length. In some contexts, it is more natural to think of the height along the filament axis,  $h$ , or the circumferential angle around the axis,  $\xi$ . The equivalence between the three description is

$$\xi = \frac{2\pi Ns}{L} = \frac{2\pi h}{p}. \quad (2.5)$$

In the chapters on geometry, we predominantly use the description in terms of height and angle around the helical axis, while in the chapters on hydrodynamics we use the arc length.

### A note on dimensions

When we discuss the hydrodynamics of flagellar filaments, we rescale the variables in our problem in order to obtain a set of dimensionless equations. Therefore, in Chapters 6,7,8, we use a tilde to denote the dimensional equivalent of the quantity underneath the tilde sign, e.g.  $\tilde{R}$  is the helical amplitude of a flagellar filament in units of micrometers, while  $R$  is the dimensionless helical amplitude rescaled by an appropriate length scale. Since

the expressions from Eqs. (2.1)-(2.5) involve only geometrical parameters, they are valid regardless of the units in which we choose to express these parameters, so with or without tildes on top of the symbols  $R, p, L, \varepsilon, s$  and  $h$  (note that  $N$  and  $\psi$  are already dimensionless).

In purely geometrical problems, all the variables have units of length, so it is not necessary to rescale them. Therefore, in Chapters 3,4, 5 we do not make a distinction between symbols with or without a tilde sign. To avoid clutter, we use symbols without a tilde sign even when we refer to quantities that have dimensional units.

### Orientation of body-fixed frame

The three-dimensional orientation of a filament is given by a vector of three angles,  $\mathbf{p} = (\phi, \theta, \chi)$ , which we choose to define in the following way. The angles  $\phi$  and  $\theta$  are called the azimuthal and polar angles since they are the standard angles to describe the direction of the filament axis,  $\mathbf{e}_3(\phi, \theta)$ , in spherical polar coordinates. The third angle describes the rotation of the filament around its own axis,  $\chi$ , so we call it the spin angle.

The sequence of rotations that takes us from the laboratory frame  $\{\mathbf{e}_x, \mathbf{e}_y, \mathbf{e}_z\}$  to the body-fixed frame of vectors  $\{\mathbf{e}_1, \mathbf{e}_2, \mathbf{e}_3\}$  is outlined in Fig. 2.1 (b-d), and the resulting expressions for the body-frame unit vectors are

$$\mathbf{e}_1 = \cos \chi [\cos \theta (\cos \phi \mathbf{e}_x + \sin \phi \mathbf{e}_y) - \sin \theta \mathbf{e}_z] + \sin \chi [-\sin \phi \mathbf{e}_x + \cos \phi \mathbf{e}_y], \quad (2.6)$$

$$\mathbf{e}_2 = -\sin \chi [\cos \theta (\cos \phi \mathbf{e}_x + \sin \phi \mathbf{e}_y) - \sin \theta \mathbf{e}_z] + \cos \chi [-\sin \phi \mathbf{e}_x + \cos \phi \mathbf{e}_y], \quad (2.7)$$

$$\mathbf{e}_3 = \sin \theta (\cos \phi \mathbf{e}_x + \sin \phi \mathbf{e}_y) + \cos \theta \mathbf{e}_z. \quad (2.8)$$

These are obtained by first rotating the filament through an angle  $\phi$  about the  $\mathbf{e}_z$  axis, then tilting the filament axis by an angle  $\theta$  away from the vertical (equivalent to rotating by an angle  $\theta$  around the direction  $\mathbf{e}_2$ ), and finally rotating through an angle  $\chi$  about the axis of the filament,  $\mathbf{e}_3(\phi, \theta)$ .

### Multiple filaments

In the case of multiple filaments, the centreline of the  $k$ th filament with respect to the laboratory frame is given by

$$\mathbf{r}^{(k)}(s) = \mathbf{x}_k + \mathbf{r}_k(s), \quad (2.9)$$

where  $\mathbf{x}_k$  is the position of the body-fixed frame relative to the laboratory frame, and  $\mathbf{r}_k(s)$  is the position of the filament centreline relative to the body-fixed frame,

$$\mathbf{r}_k(s) = R \cos \left( \frac{2\pi N s}{L} \right) \mathbf{e}_1^{(k)} + \sigma R \sin \left( \frac{2\pi N s}{L} \right) \mathbf{e}_2^{(k)} + s \cos \psi \mathbf{e}_3^{(k)}. \quad (2.10)$$

The unit vectors  $\{\mathbf{e}_1^{(k)}, \mathbf{e}_2^{(k)}, \mathbf{e}_3^{(k)}\}$  depend implicitly on the orientation of the filament,  $\mathbf{p}_k = (\phi_k, \theta_k, \chi_k)$ . The corresponding tangent vector is  $\hat{\mathbf{t}}_k(s)$ .

### Definition of phase angle

Since both the azimuthal angle,  $\phi$ , and the spin angle,  $\chi$ , correspond in their own ways to rotations about the axis of the filament (see Fig. 2.1 (b) and (d)), we define the phase angle for a filament with arbitrary orientation to be

$$\Phi = \phi + \chi. \quad (2.11)$$

Thus, in problems where we have two non-parallel filaments, the phase difference between them is defined as

$$\Delta\Phi = \Phi_2 - \Phi_1 = \Delta\phi + \Delta\chi. \quad (2.12)$$

Note that, for vertical helices, both  $\phi$  and  $\chi$  correspond to rotation about the vertical axis. In this dissertation, whenever the setup of the problem involves only vertical filaments, we take  $\chi = 0$  without loss of generality, and we refer to  $\phi$  as the phase angle and  $\Delta\phi$  as the phase difference between the filaments.

Now that we have established the notation, we are ready to review the geometrical arguments brought by Macnab [138] on the topic of helical bundles.

### 2.1.2 Macnab's original study in helical geometry

The setup from the original study is illustrated in Fig. 2.2 (a). Since the filaments are parallel,  $\theta = 0$ , the spin angle  $\chi$  is redundant. Therefore, the configuration of the filaments is described by only two parameters: the distance between the axes of the helices,  $d$ , and the phase difference,  $\Delta\phi = \phi_2 - \phi_1$ . These are indicated on the horizontal projection of the filament centrelines in Fig. 2.2 (b).

If the distance between the axes is smaller than a critical value,

$$d < d_c = 2R \sin\left(\frac{\Delta\phi}{2}\right), \quad (2.13)$$

then the helices are intertwined in a direction consistent with their chirality - CCW for right-handed helices and CW for left-handed helices, as we view the filaments from the top. This can be seen by tracing the filaments in Fig. 2.2 (a) from the bottom to the top: filament B crosses over filament A and then underneath it, so the two are intertwined.

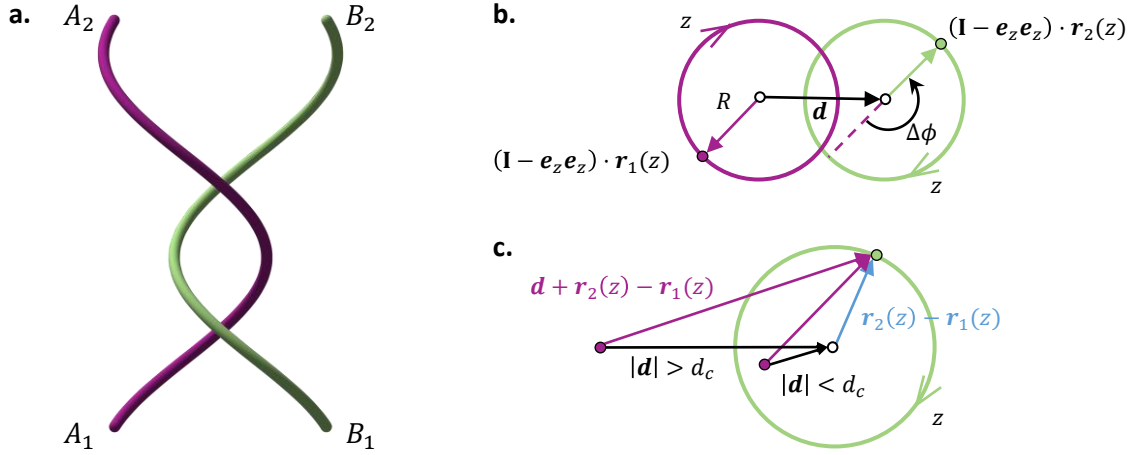


Fig. 2.2 Diagram explaining the geometrical intertwinement of two parallel and identical helices. (a) From a side view of the filaments, we see that filament B crosses over and then underneath filament A. The two filaments are said to be physically-interconnected or intertwined. If we place our thumbs on points  $A_1$  and  $B_1$ , our index fingers on  $A_2$  and  $B_2$ , and we try to pull the filaments apart, we find that it is not possible. (b) The conditions for intertwinement are determined from the relative position of one filament to another in the horizontal plane. The configuration is described by the directed distance between the axes of the filaments,  $\mathbf{d}$ , and the phase difference between the filaments,  $\Delta\phi$ . (c) The locus of points on filament B relative to filament A is a circle of radius  $2R \sin(\Delta\phi/2)$ . If the distance between the axes of the filaments is smaller than this radius, then filament B (filled green circle) revolves around filament A (filled purple circle, stationary) in a clockwise (CW) direction compatible with the left-handed geometry of the filaments.

### Derivation of critical distance

To derive the critical distance, we consider the position of one filament relative to the other in the horizontal plane (perpendicular to their axes). Using the parameterisation of the helical centreline introduced in §2.1.1, with filament orientations  $(\phi_1, \theta_1, \chi_1) = (0, 0, 0)$  and  $(\phi_2, \theta_2, \chi_2) = (\Delta\phi, 0, 0)$ , the position of filament B relative to filament A is

$$\mathbf{d} + \mathbf{r}_2(z) - \mathbf{r}_1(z) = \mathbf{d} + R \cos\left(\frac{2\pi z}{p}\right) \begin{pmatrix} \cos \Delta\phi - 1 \\ \sin \Delta\phi \\ 0 \end{pmatrix} + \sigma R \sin\left(\frac{2\pi z}{p}\right) \begin{pmatrix} -\sin \Delta\phi \\ \cos \Delta\phi - 1 \\ 0 \end{pmatrix}. \quad (2.14)$$

Note that for vertical filaments the height along the filament axis,  $h$ , is the same as the  $z$  coordinate, and we have chosen to use the latter. This can be simplified to

$$\mathbf{d} + \mathbf{r}_2(z) - \mathbf{r}_1(z) = \mathbf{d} + 2R \sin\left(\frac{\Delta\phi}{2}\right) \left[ \cos\left(\frac{2\pi z}{p}\right) \mathbf{e}_\phi\left(\frac{\Delta\phi}{2}\right) - \sigma \sin\left(\frac{2\pi z}{p}\right) \mathbf{e}_r\left(\frac{\Delta\phi}{2}\right) \right], \quad (2.15)$$

where  $\mathbf{e}_r$  and  $\mathbf{e}_\phi$  are the standard radial and azimuthal vectors in cylindrical polar coordinates. The expression in the square brackets corresponds to a unit circle traversed CCW or CW with increasing  $z$  if the helices are right-handed ( $\sigma = +1$ ) or left-handed ( $\sigma = -1$ ). Hence, the curve  $\mathbf{d} + \mathbf{r}_2(z) - \mathbf{r}_1(z)$  is a circle of radius  $2R \sin(\Delta\phi/2)$  around the position  $\mathbf{d}$ . If  $|\mathbf{d}| = d < 2R \sin(\Delta\phi/2)$ , filament B circles around filament A in a direction consistent with its chirality. If filament B is further away,  $d > d_c$ , then the filaments are not intertwined. The distinction is illustrated in Fig. 2.2 (c).

### Physical implications

It is important to note that left-handed helices only intertwine in the CW direction, and right-handed helices only in the CCW direction. Their intrinsic geometry does not allow it otherwise. The flagellar filaments of a bacterium are typically in the normal shape, which is left-handed. While the bacterium swims in a straight line, the filaments rotate CCW in order to propel the cell forward, and the cell body counter-rotates CW to balance the torque. Therefore, hydrodynamic interactions between the rotating filaments and the counter-rotations of the cell body both impose a right-handed intertwining on the filaments forming the bundle. Macnab's conclusion is that, in order to minimise the elastic energy stored in the bundle, the flagellar filaments must be coaxial, in phase, and minimally distorted around each other in a right-handed sense. This hypothesis is corroborated by experiments with a dry macroscopic model [138].

The second observation made by Macnab relates to the time evolution of the bundle. The result of Eq. (2.15) concerns the intertwining of two stationary helices as we scan over their length. By replacing the vertical dependence,  $2\pi z/p$ , with a time dependence on the frequency of rotation,  $\Omega_0 t$ , one can reinterpret these results to be about the intertwining of two rotating filaments over time. In Fig. 2.2 (b-c), we replace the vertical coordinate,  $z$ , by the time coordinate,  $t$ , and we find that two parallel helices separated by a distance  $d < d_c(\Delta\phi)$  intertwine indefinitely around each other in a left-/right-handed sense if they are rotating CW/CCW with a fixed phase difference  $\Delta\phi$ . This becomes an issue when we consider that flagella are anchored to the rotary motors embedded in the cell wall, which do not move relative to one another. Twist inevitably builds up between the tops of the filaments,

which are rotating around each other, and the anchoring points which are fixed. The large bending stiffness of flagellar filaments supports only a limited amount of elastic deformation, so the bundle eventually jams. Hence, Macnab concluded that out-of-phase bundles are not compatible with the continuous actuation of flagella by the rotary motors. Synchronisation between the filaments is needed in order to ensure the smooth actuation of the bundle.

## 2.2 Hydrodynamics of flagellar filaments

The mathematical study of microorganism hydrodynamics started in the 1950s with the pioneering work of Taylor [204], who proposed a two-dimensional swimming sheet model for the locomotion of spermatozoa and derived an energetic argument for the in-phase synchronisation of two nearby swimming sheets. Gray and Hancock [69, 79] followed shortly afterwards with two papers in which they model the tail of a swimming spermatozoon as a wave propagating down a slender infinite filament. Theirs is the first application of a “slender-body theory”, a class of mathematical methods for calculating hydrodynamic forces on slender filaments, which will be discussed later in this section.

By the 1970s, flagellar hydrodynamics was already considered a “significant field” for the application of mathematics and Lighthill [131] was invited to give a lecture on the topic at the Rensselaer Polytechnic Institute. The transcript of this lecture has become a classical text in the field of low Reynolds number hydrodynamics, much like the lecture given by Purcell [170] two years later, and referenced in the Introduction. From amongst the growing body of theoretical work of that decade, we mention two papers by Higdon [82, 83], who was able to derive the optimal length of a flagellum by including in the calculations the hydrodynamic interactions between the filament and the cell body.

In later decades, as the field grew and benefited from advancements in experimental observations [209], the references become too numerous to do them justice. We conclude here our brief historical perspective of the field of micro-swimmer hydrodynamics, and we proceed with introducing the mathematical methods used in this dissertation.

### 2.2.1 Fundamental solution of the Stokes equations

At very low Reynolds number, the motion of the fluid around a swimming microorganism is well described by the incompressible Stokes equations [115],

$$-\nabla p + \mu \nabla^2 \mathbf{u} + \mathbf{f} = 0, \quad \nabla \cdot \mathbf{u} = 0, \quad (2.16)$$

where we make an exception to our usual notation to denote the external force density on the fluid,  $\mathbf{f}$ , and the scalar pressure field,  $p$ .<sup>1</sup> The Stokes equations are linear and time-independent, which is consistent with the properties of linearity and instantaneity mentioned in our discussion of Purcell's scallop theorem in §1.1.

The fundamental solution of the Stokes equations is the flow generated by a point force of strength  $\mathbf{F}$  located at the origin,

$$\mathbf{u}_{\text{Stokeslet}}(\mathbf{r}) = \frac{\mathbf{I} + \hat{\mathbf{r}}\hat{\mathbf{r}}}{8\pi\mu r} \cdot \mathbf{F} = \mathbf{J}(\mathbf{r}) \cdot \mathbf{F}, \quad (2.17)$$

where  $r = |\mathbf{r}|$ . The flow  $\mathbf{u}_{\text{Stokeslet}}$  is evidently called a Stokeslet, while  $\mathbf{J}(\mathbf{r})$  is referred to as the Oseen tensor. Since the Stokes equations are linear, any derivative of the Stokeslet is also a solution of Eqs. (2.16) in a domain excluding the origin. General solutions can be obtained from a superposition of fundamental singularities, i.e. the Stokeslet from Eq. (2.17) and its derivatives, with the condition that the output is linear in the input parameters [115].

## 2.2.2 Flows around rigid bodies

Since the hydrodynamic study of swimming bacteria involves the motion of the cell body and its flagella, it is useful to have solutions for the flows around rigid bodies in motion.

For simple body shapes such as a sphere, the flow outside the body can be written as a finite sum of fundamental singularities. For instance, the flow outside a rigid sphere with radius,  $a$ , and linear velocity,  $\mathbf{U}$ , is expressed as the sum of a Stokeslet and a source dipole,

$$\mathbf{u}_{\text{sphere}}(\mathbf{r}; \mathbf{U}) = \frac{3a}{4} \left( \frac{\mathbf{I} + \hat{\mathbf{r}}\hat{\mathbf{r}}}{r} \right) \cdot \mathbf{U} + \frac{a^3}{4} \left( \frac{\mathbf{I} - 3\hat{\mathbf{r}}\hat{\mathbf{r}}}{r^3} \right) \cdot \mathbf{U}, \quad (2.18)$$

where  $\mathbf{r}$  is the position relative to the centre of the sphere. This expression is clearly linear in the input parameter – the velocity of translation of the sphere,  $\mathbf{U}$ . The same sphere rotating with angular velocity  $\boldsymbol{\Omega}$  generates a flow

$$\mathbf{u}_{\text{sphere}}(\mathbf{r}; \boldsymbol{\Omega}) = \frac{a^3 \boldsymbol{\Omega} \times \mathbf{r}}{r^3}, \quad (2.19)$$

which is also called a rotlet and is the antisymmetric part of the first derivative of the stokeslet.

For general body shapes, the flow can be expressed as a surface integral of singularities, rather than a finite sum. This is called the boundary integral formulation of Stokes flows and involves the convolution of the boundary conditions for surface traction with the Green's

<sup>1</sup>Eq. (2.16) is the only place where we use  $p$  to denote the pressure, not the helical pitch of the filament, and  $\mathbf{f}$  to denote the body force on the fluid, not the force density along a filament centreline.

function from Eq. (2.16), as well as the convolution of the boundary conditions for velocity with the stress tensor associated with the Stokeslet solution [169]. The convolution is taken as a surface integral over the boundary of the fluid domain, in this case the surface of the cell body. In other words, the flow outside an arbitrarily-shaped body may be described by a surface distribution of fundamental singularities.

The central idea of flagellar hydrodynamics is to exploit the large aspect ratio of swimming appendages. Instead of a surface integral of singularities, the flows generated by the motion of slender filaments can be approximated by a distribution of flow singularities along the centreline of the filament [115]. This leads to a generic class of “slender-body theories” for the hydrodynamics of thin filaments. In this dissertation, we make a distinction between the earlier “slender-body theories” which are logarithmically correct [32, 69, 79, 132], and the later “slender-body theories” which are algebraically correct [105, 108, 131]. Henceforth, we refer to the first group of theories as resistive-force theory (RFT) and the second group as slender-body theory (SBT).

### 2.2.3 Resistive-force theory

In earlier theories of flagellar hydrodynamics, the flow created by a moving slender filament is approximated by a line distribution of Stokeslets along the centreline of the filament. Below, we provide a sketch of the asymptotic calculation behind RFT, to illustrate why the resistance coefficients depend logarithmically on the aspect ratio.

Suppose we have a slender filament with centreline,  $\mathbf{r}(s)$ , and cross-sectional radius,  $\varepsilon$ , such that points on the surface of the filament,  $\mathbf{r}(s) + \mathbf{r}_\varepsilon$ , lie at a short perpendicular distance away from the centreline,  $|\mathbf{r}_\varepsilon| = \varepsilon$ . The filament moves with prescribed velocity,  $\mathbf{u}(\mathbf{r}(s) + \mathbf{r}_\varepsilon)$ , and we wish to represent the flow generated by the motion of the filament using a line distribution of Stokeslets along the filament centreline. If  $\mathbf{f}(s)$  is the unknown density of Stokeslets, then the no-slip condition on the surface of the filament requires that

$$\mathbf{u}(\mathbf{r}(s) + \mathbf{r}_\varepsilon) = \int_{-L/2}^{+L/2} \frac{\mathbf{I} + \hat{\mathbf{R}}_\varepsilon(s, s') \hat{\mathbf{R}}_\varepsilon(s, s')}{8\pi\mu |\mathbf{R}_\varepsilon(s, s')|} \cdot \mathbf{f}(s') ds', \quad (2.20)$$

where  $\mathbf{R}_\varepsilon(s, s') = \mathbf{r}(s) + \mathbf{r}_\varepsilon - \mathbf{r}(s')$  is the distance between a point  $s'$  on the centreline and the point at which we are applying the no-slip condition.

The integral in Eq. (2.20) is then evaluated asymptotically in the limit of small filament thickness,  $\varepsilon \ll L$ , by splitting the domain of integration into different regions. The inner region,  $|s - s'| = \mathcal{O}(\varepsilon)$ , brings only an  $\mathcal{O}(1)$  contribution to the integral, while the dominant logarithmic contribution comes from an outer region  $\mathcal{O}(\varepsilon) \ll |s - s'| \ll \mathcal{O}(L)$ , where  $L$  is a

length scale over which the tangent to the centreline does not change very much (i.e. on the order of the radius of curvature of the filament). In this region, the filament is approximated to leading order by a straight rod with  $|\mathbf{R}_\varepsilon(s, s')| \approx |s - s'|$  and  $\hat{\mathbf{R}}_\varepsilon(s, s') \approx \hat{\mathbf{t}}(s)$ . By using this locally straight approximation to evaluate the Oseen tensor, and also Taylor expanding the velocity and force density, we deduce that the leading-order asymptotic behaviour of Eq. (2.20) is given by

$$\mathbf{u}(\mathbf{r}(s)) \approx \frac{(\mathbf{I} + \hat{\mathbf{t}}(s)\hat{\mathbf{t}}(s)) \cdot \mathbf{f}(s)}{8\pi\mu} \int_{-\mathcal{O}(L')}^{s-\mathcal{O}(\varepsilon)} + \int_{s+\mathcal{O}(\varepsilon)}^{\mathcal{O}(L')} \frac{ds'}{|s-s'|}. \quad (2.21)$$

We invert this equation using the identity  $(\mathbf{I} + \hat{\mathbf{t}}\hat{\mathbf{t}})^{-1} = \mathbf{I} - \frac{1}{2}\hat{\mathbf{t}}\hat{\mathbf{t}}$  to obtain the leading-order solution for the force density in terms of the prescribed velocity of the centreline,

$$\mathbf{f}(s) \approx \frac{4\pi\mu}{\ln(\mathcal{O}(L')/\mathcal{O}(\varepsilon))} \left[ (\mathbf{I} - \hat{\mathbf{t}}\hat{\mathbf{t}}) + \frac{1}{2}\hat{\mathbf{t}}\hat{\mathbf{t}} \right] \cdot \mathbf{u}(\mathbf{r}(s)). \quad (2.22)$$

Since the error in Eq. (2.21) is of  $\mathcal{O}(1)$ , the error in the force density from Eq. (2.22) is of  $\mathcal{O}(\ln(L'/\varepsilon)^{-2})$ . Therefore, RFT is valid in the limit of exponentially small filament thickness.

This sketch of the asymptotic calculation behind RFT was presented for two reasons. First, to justify the emergence of the logarithmic dependence, and secondly to demonstrate the origin of the anisotropic Stokes drag on a slender rod, since the force density from Eq. (2.22) is twice as large when  $\mathbf{u} \perp \hat{\mathbf{t}}$  than when  $\mathbf{u} \parallel \hat{\mathbf{t}}$ . Recall that in §1.1.3 of the introduction, we used the anisotropy of the drag to illustrate how a rotating helical propeller generates a net thrust and hence propels the body of the bacterium forward.

The question that remains open in our sketch of RFT is the most appropriate choice for the length scale  $L'$ . As we will shortly see, different choices for this length scale lead to different drag coefficients on the filament.

In RFT, the linear relationship between the local force density and the velocity of the filament centreline is expressed generically as

$$\mathbf{f}(s) = [c_\perp(\mathbf{I} - \hat{\mathbf{t}}\hat{\mathbf{t}}) + c_\parallel\hat{\mathbf{t}}\hat{\mathbf{t}}] \cdot [\mathbf{u}(\mathbf{r}(s)) - \mathbf{u}_\infty(\mathbf{r}(s))], \quad (2.23)$$

where  $c_\perp$  and  $c_\parallel$  are the perpendicular and parallel drag coefficients on the filament, and the velocity of the centreline is now taken relative to the background flow at the position of the centreline,  $\mathbf{u}_\infty(\mathbf{r}(s))$ . Note that  $\mathbf{f}(s)$  is the force density exerted *by* the filament *on* the fluid, so the drag coefficients  $c_\perp$  and  $c_\parallel$  are positive, since the velocity of the filament relative to the fluid is in the same direction as the force exerted on the fluid (and opposite to the viscous force exerted by the fluid on the filament).

The drag coefficients derived by Gray and Hancock [69, 79] are

$$c_{\perp} = 4\pi\mu \left( \ln \left( \frac{L}{\varepsilon} \right) + \frac{1}{2} \right)^{-1}, \quad c_{\parallel} = 2\pi\mu \left( \ln \left( \frac{L}{\varepsilon} \right) - \frac{1}{2} \right)^{-1}. \quad (2.24)$$

The calculation for these drag coefficients goes one step beyond the sketch provided above, by including the  $\mathcal{O}(1)$  contributions to the asymptotic expansion of the integral in Eq. (2.20). Hence, the drag coefficients are calculated up to and including order  $\mathcal{O}(\ln(L/\varepsilon)^{-2})$ . Implicitly, the calculation of Gray and Hancock uses the length of the filament as the length scale  $L'$  from our previous sketch of the solution.

A separate set of drag coefficients was derived by Lighthill [132] specifically for the purpose of modelling the hydrodynamics of helical filaments. In terms of the number of helical turns of the filament,  $N$ , Lighthill's drag coefficients are equivalent to

$$c_{\perp} = 4\pi\mu \left( \ln \left( \frac{0.18L}{N\varepsilon} \right) + \frac{1}{2} \right)^{-1}, \quad c_{\parallel} = 2\pi\mu \left( \ln \left( \frac{0.18L}{N\varepsilon} \right) \right)^{-1}, \quad (2.25)$$

although Lighthill [132] derived them in the limit of an infinitely long helix, so  $L/N \equiv p/\cos\psi$ . Intuitively, we recognise from the above expressions that the typical length scale on which a helical filament can be approximated as a straight rod is not the entire contour length of the filament, but a fraction of the length of one helical turns,  $L/N$ .

## 2.2.4 Slender-body theory

Algebraically-accurate asymptotic theories for the hydrodynamics of slender filaments were later developed by Johnson [105], Keller and Rubinow [108], Lighthill [131]. By including further singularities along the centreline of the filament, specifically Stokeslets and source dipoles, Johnson [105] obtained a Fredholm integral equation of the second kind for the force density,  $\mathbf{f}(s)$ , in terms of the relative velocity of the centreline

$$\begin{aligned} 8\pi\mu [\mathbf{u}(\mathbf{r}(s)) - \mathbf{u}_{\infty}(\mathbf{r}(s))] &= \int_{-L/2}^{+L/2} \left[ \frac{\mathbf{I} + \hat{\mathbf{R}}_0(s, s')\hat{\mathbf{R}}_0(s, s')}{|\mathbf{R}_0(s, s')|} \cdot \mathbf{f}(s') - \frac{\mathbf{I} + \hat{\mathbf{t}}(s)\hat{\mathbf{t}}(s)}{|s' - s|} \cdot \mathbf{f}(s) \right] ds' \\ &+ \left[ \left( 2\ln \left( \frac{L}{\varepsilon} \right) + 1 \right) \mathbf{I} + \left( 2\ln \left( \frac{L}{\varepsilon} \right) - 3 \right) \hat{\mathbf{t}}(s)\hat{\mathbf{t}}(s) \right] \cdot \mathbf{f}(s), \end{aligned} \quad (2.26)$$

where  $\mathbf{R}_0(s, s') = \mathbf{r}(s) - \mathbf{r}(s')$  is the distance between two points on the centreline. This calculation of the force density is accurate to  $\mathcal{O}((\varepsilon/L)^2 \ln(L/\varepsilon))$ . Note that the result of Eq. (2.26) is correct for filaments with a specific cross-sectional radius,  $r_{\varepsilon}(s) = \varepsilon\sqrt{1 - (2s/L)^2}$ , that vanishes quadratically at the ends.

In recent decades, SBT has become a very popular framework for analysing the hydrodynamics of flagellar propulsion [42, 111, 133, 142, 197] and of suspensions of fibers [19, 147, 185, 205]. Amongst others, SBT has been used to quantify the hydrodynamic interactions between helical filaments rotating side-by-side [111] and to determine the optimal bacterial polymorphic shape for swimming [197]. In terms of theoretical developments, SBT has been extended to “slender-ribbon theory” [117], and it has also been shown that SBT can be derived directly from the boundary integral formulation of Stokes flows [118].

### 2.2.5 Hydrodynamic resistance matrix

Another very useful concept for our hydrodynamic calculations is the idea of a resistance matrix. Since the Stokes equations are linear, the relationship between the dynamics of the filament (force,  $\mathbf{F}$ , and torque,  $\mathbf{T}$ , exerted *by* the filament *on* the fluid) and the kinematics of the filament (linear and angular velocity,  $\mathbf{U}$  and  $\mathbf{\Omega}$ , of the filament relative to a stationary fluid) can be expressed as a linear system,

$$\begin{pmatrix} \mathbf{F} \\ \mathbf{T} \end{pmatrix} = \begin{pmatrix} \mathbf{A} & \mathbf{B} \\ \mathbf{B}^T & \mathbf{D} \end{pmatrix} \begin{pmatrix} \mathbf{U} \\ \mathbf{\Omega} \end{pmatrix}, \quad (2.27)$$

where the matrix in the middle is called the “grand resistance matrix”. The reciprocal theorem of Stokes flow tells us that the resistance matrices  $\mathbf{A}$  and  $\mathbf{D}$  are symmetric, while the minimum dissipation theorem says that  $\mathbf{A}$ ,  $\mathbf{D}$  and the grand resistance matrix are positive definite [115].

In general, the matrices  $\mathbf{A}$ ,  $\mathbf{B}$  and  $\mathbf{D}$  depend on the shape, size and orientation of the rigid body. For a sphere of radius,  $a$ , the resistance matrices are isotropic

$$\mathbf{A}_{\text{sphere}} = 6\pi\mu a\mathbf{I}, \quad \mathbf{B}_{\text{sphere}} = \mathbf{0}, \quad \mathbf{D}_{\text{sphere}} = 8\pi\mu a^3\mathbf{I}. \quad (2.28)$$

For a spheroid with major axis length,  $l$ , and minor axis length,  $w$ , the resistance coefficients are different for motion parallel or perpendicular to the major axis of the spheroid. By placing a line of singularities between the two foci of the spheroid, Chwang and Wu [26] determined that the hydrodynamic resistance of a prolate spheroid to translation,  $A_{\parallel}$ , or rotation,  $D_{\parallel}$ , along its major axis are

$$A_{\parallel} = \frac{8\pi\mu l c^3}{-2c + (1 + c^2) \log\left(\frac{1+c}{1-c}\right)}, \quad (2.29)$$

$$D_{\parallel} = \frac{4\pi\mu l^3 c^3 (1 - c^2)}{3(2c + (1 - c^2) \log\left(\frac{1+c}{1-c}\right))}, \quad (2.30)$$

where  $c = \sqrt{1 - w^2/l^2}$  is the eccentricity of the spheroid. The resistance coefficients for translation and rotation perpendicular to the major axis of a spheroid are also available in closed-form solutions Chwang and Wu [26], but  $A_{\parallel}$  and  $D_{\parallel}$  are of greater interest to us for the purpose of modelling the swimming of a bacterium along its axis.

Note that there is no coupling between rotational and linear degrees of freedom for axisymmetric shapes such as a spheroid ( $\mathbf{B}_{\text{spheroid}} = \mathbf{0}$ ), but chiral objects such as a helix are capable of generating forces through rigid-body rotation. This is the fundamental principle by which rotating helical propellers generate motion. In Chapter 7, we will derive expressions for the resistance matrix of a helical filament using the method of RFT introduced above.

## 2.3 Conclusion

In this chapter, we have provided the necessary mathematical background for the calculations presented in this dissertation. In the first section, we introduced the notation that will be used to describe a helical filament of arbitrary orientation, and we gave an overview of the original study in helical geometry by Macnab [138]. This type of geometrical analysis will be extended in the next three chapters, each of them addressing a specific question about the bundling of bacterial flagellar filaments: (i) can polymorphic transformations contribute to the re-bundling of flagellar filaments at the end of a tumble? (Chapter 3), (ii) how is it that bacteria always form tangle-free bundles without having precise control over the position of the filaments? (Chapter 4), and (iii) how much synchronisation is necessary between the filaments in order for the bundle to rotate smoothly (Chapter 5)?

On the hydrodynamics front, we have provided a brief historical perspective on the growth of micro-swimmer hydrodynamics as a field of research, paying particular attention to developments in the modelling of flagellar hydrodynamics, which is one of the two focal points of this dissertation (the other being the geometry of flagellar filaments). In the chapters on hydrodynamics, we will be using resistive-force theory (RFT) as an analytical tool for understanding the hydrodynamic interactions between flagellar filaments, while slender-body theory (SBT) will be used to obtain more accurate numerical results.

Another numerical framework for modelling micro-swimmer hydrodynamics that we have not discussed in this chapter is the method of regularised Stokeslets. A comparative analysis between the method of regularised Stokeslets, SBT, and RFT with both Hancock's and Lighthill's drag coefficients was carried out by Rodenborn et al. [181].

## Chapter 3

# Geometrical intertwinement of bacterial polymorphic shapes

In this chapter, we consider the possible states of intertwinement between bacterial flagellar filaments with different polymorphic shapes, which are represented by helices with different pitches and amplitudes. We focus in particular on the intertwinement between two helices with opposite chiralities, since bacterial flagellar filaments often exhibit a mixture of left-handed shapes (normal) and right-handed shapes (semicoiled, curly I and II) during a tumbling event. Using a similar geometrical framework as Macnab [138], we find that the the intrinsic geometry of normal-semicoiled and normal-curly I/II pairs is compatible with the CCW intertwinement imposed by hydrodynamic effects, without the filaments having to undergo elastic deformations.

### 3.1 Motivation

The question of intertwinement between two non-identical helices is relevant to the swimming of multiflagellated bacteria because their filaments often undergo polymorphic transformations during a tumble, usually progressing from the left-handed normal shape through a series of right-handed shapes called semicoiled, curly I and curly II, or a subset of these [209]. A diagram of the different polymorphic shapes is available in the introduction, Fig. 1.2 (b).

While two left-handed helices can only intertwine CW, due to their intrinsic chirality, it is expected that a pair of a left-handed and a right-handed helix could intertwine either CW or CCW depending on their relative geometries and positions. This idea is connected to the issue identified by Macnab [138] and discussed in §2.1.2, namely that hydrodynamic effects

due to the CCW rotation of the filaments are incompatible with the intrinsic left-handed geometry of normal filaments.

## 3.2 Geometrical modelling

Since left-handed normal filaments coexist with right-handed polymorphic shapes during tumbling events, we want to understand the possible states of intertwinement between a left- and a right-handed helix.

### 3.2.1 Locus of relative position between filaments

The setup consists of a right-handed helix with amplitude  $R_1$  and pitch  $p_1$ , and a left-handed helix with amplitude  $R_2$  and pitch  $p_2$ , shown in Fig. 3.1 (a). We introduce the dimensionless parameters

$$\lambda_R = \frac{R_1}{R_2}, \quad \lambda_p = \frac{p_1}{p_2}, \quad (3.1)$$

which represent the amplitude and pitch of the right-handed helix relative to the left-handed one. For irrational pitch ratio,  $\lambda_p$ , the two-helix ensemble never repeats in the vertical direction, while for rational  $\lambda_p = n/m$ , with coprime integers  $n$  and  $m$ , the ensemble has a vertical period  $P = np_2 = mp_1$ .

As in §2.1.2, we consider the relative position of the two filaments in the horizontal plane. The position of filament B relative to filament A is given by

$$\mathbf{d} + \mathbf{r}_2(z) - \mathbf{r}_1(z) = \mathbf{d} + R_2 \begin{pmatrix} \cos\left(\frac{2\pi z}{p_2} - \Delta\phi\right) - \lambda_R \cos\left(\lambda_p^{-1} \frac{2\pi z}{p_2}\right) \\ -\sin\left(\frac{2\pi z}{p_2} - \Delta\phi\right) - \lambda_R \sin\left(\lambda_p^{-1} \frac{2\pi z}{p_2}\right) \\ 0 \end{pmatrix}. \quad (3.2)$$

Using the simplifying notation  $\xi = 2\pi z/p_2$ , we write

$$(\mathbf{r}_2(z) - \mathbf{r}_1(z)) \cdot \mathbf{e}_x = R_2 [\cos(\xi - \Delta\phi) - \lambda_R \cos(\lambda_p^{-1} \xi)], \quad (3.3)$$

$$(\mathbf{r}_2(z) - \mathbf{r}_1(z)) \cdot \mathbf{e}_y = R_2 [-\sin(\xi - \Delta\phi) - \lambda_R \sin(\lambda_p^{-1} \xi)]. \quad (3.4)$$

The curve described by Eqs. (3.3)-(3.4) is a hypotrochoid, an example of which is shown in Fig. 3.1 (c). A hypotrochoid is formally defined as the curve traced out by a fixed point attached to a smaller circle that rolls on the inside of a larger circle [123]. We find that

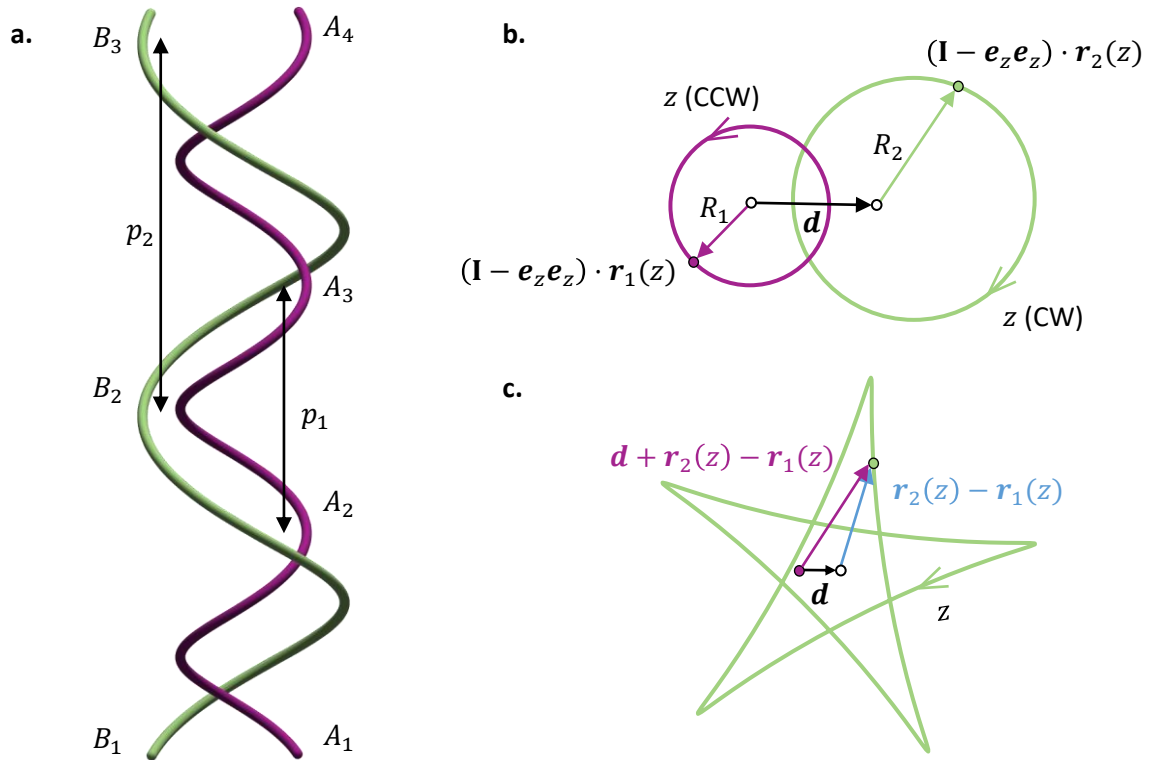


Fig. 3.1 Diagram explaining the geometrical intertwinement of two parallel helices with different pitches and amplitudes, and opposite chiralities. (a) From a side view of the filaments, we see that the left-handed filament B turns around filament A twice in the CW direction. (b) The conditions for intertwinement are determined from the relative position of one filament to another in the horizontal plane. (c) The locus of points on filament B relative to filament A is a hypotrochoid with  $n + m$  extremities, if  $\lambda_p = n/m$ . Here,  $n = 2$  and  $m = 3$ .

the same family of curves arises naturally from the relative position between two parallel non-identical helices.<sup>1</sup>

### 3.2.2 Possible states of intertwinement

The intertwinement between the filaments is determined by following the path traced out by  $\mathbf{d} + \mathbf{r}_2(z) - \mathbf{r}_1(z)$  in the direction of increasing  $z$ , indicated by a purple arrow in Fig. 3.1 (c). In this example, the vector  $\mathbf{d}$  lies in the inner-most region of the hypotrochoid, and the green curve makes two full CW turns around it. This corresponds to the ensemble illustrated in Fig. 3.1 (a), where the pair of helices have pitch ratio  $\lambda_p = 2/3$  and the left-handed filament B turns around filament A twice in the CW direction. Further examples of hypotrochoids for

<sup>1</sup>The spirograph, named the “Toy of the Year” in 1967, can be used to draw hypotrochoids and epitrochoids (for the latter, the smaller circle rolls on the outside of the larger circle). If the original study in helical geometry reinvented the wheel, see Eq. (2.15), then in this section we have reinvented the spirograph.

the case of rational pitch ratio  $\lambda_p = 2/3$  are provided in Fig. 3.2. The number of extremities of the hypotrochoid is equal to  $m + n$ , where  $m$  and  $n$  are coprime integers such that  $\lambda_p = n/m$ , giving a five-point hypotrochoid when  $\lambda_p = 2/3$ .

For fixed  $\lambda_p < 1$ , the family of curves has three distinct regimes shown in Fig. 3.2 (a), (b) and (c) in order of increasing  $\lambda_R$ . In the regimes (a) and (c), the curve circles CW or CCW, respectively, around every point inside the hypotrochoid. In the intermediate regime (b), the curve may circle either CW or CCW depending on the distance vector  $\mathbf{d}$ . The transition points between the regimes correspond to the creation of petal-shaped CCW regions at the extremities (when  $\lambda_R = \lambda_p$ , see Fig. 3.2 (d)) and (c) the loss of the star-shaped CW region through a pinching off at the centre (when  $\lambda_R = 1$ , see Fig. 3.2 (e)).

### 3.2.3 Definition of winding number

The intertwinement of two non-identical filaments can be described by a winding number  $\Gamma$  defined as

$$\Gamma = \frac{1}{2\pi} \int_0^P \frac{d\gamma}{dz} dz, \quad (3.5)$$

where  $P = np_2 = mp_2$  is the vertical period of the ensemble, and  $\gamma$  is the angle that the curve  $\mathbf{d} + \mathbf{r}_2(z) - \mathbf{r}_1(z)$  makes with the  $x$  axis,

$$\gamma(z) = \tan^{-1} \left( \frac{(\mathbf{d} + \mathbf{r}_2(z) - \mathbf{r}_1(z)) \cdot \mathbf{e}_y}{(\mathbf{d} + \mathbf{r}_2(z) - \mathbf{r}_1(z)) \cdot \mathbf{e}_x} \right). \quad (3.6)$$

The winding number is positive or negative if the intertwinement is in the right-handed (CCW) or left-handed (CW) direction, respectively. In Fig. 3.2 we indicate the winding number next to different positions of the vector  $\mathbf{d}$ . The winding number ranges from  $-n$  to  $+m$  because, in the laboratory frame, the left-handed filament turns CW  $n$  times and the right-handed filament turns CCW  $m$  times over one period of the two-helix ensemble.

### 3.2.4 Physical interpretation of transitions

The transition at  $\lambda_R = 1$  is clearly related to the helical amplitude of one filament being smaller or larger than the other. To understand the transition at  $\lambda_R = \lambda_p$ , we consider the pitch angle  $\psi = \tan^{-1}(2\pi R/p)$  that the tangent to the filament makes with the  $z$  axis (also defined in §2.1). We observe that

$$\frac{\tan \psi_2}{\tan \psi_1} = \frac{\lambda_p}{\lambda_R}, \quad (3.7)$$

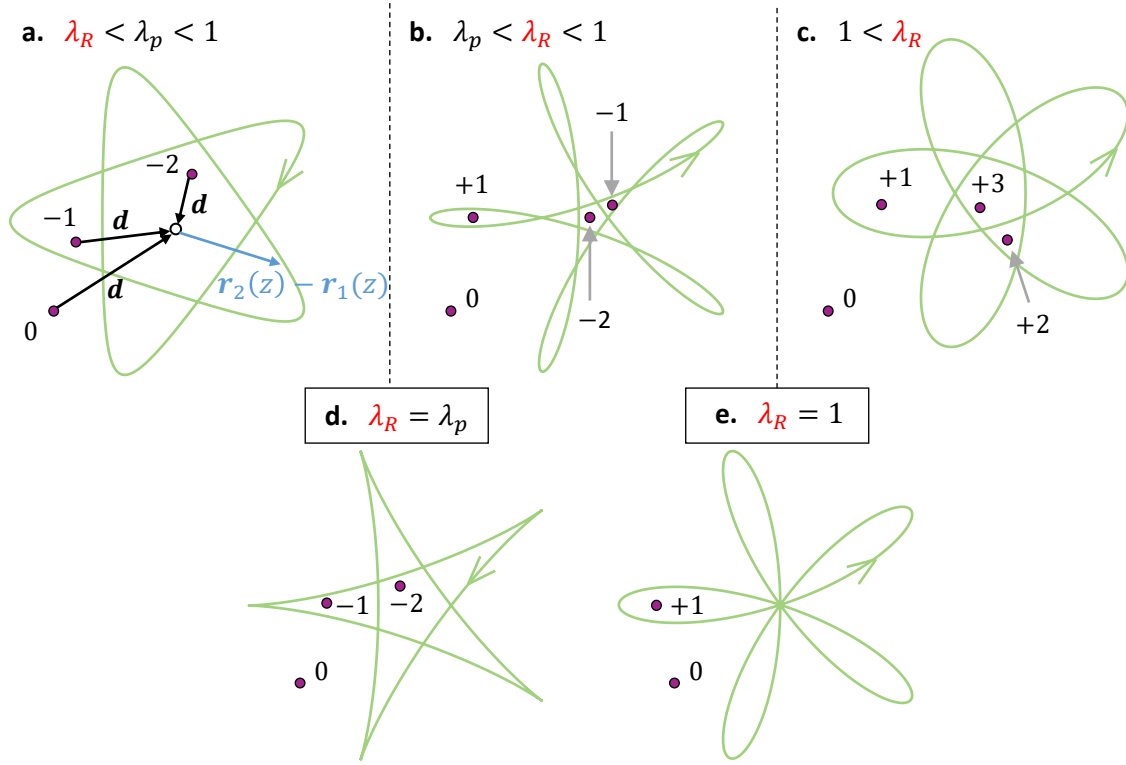


Fig. 3.2 Locus of filament B relative to filament A for varying amplitude ratios,  $\lambda_R = R_2/R_1$ , and fixed pitch ratio  $\lambda_p = 2/3$ . Hypotrochoid curves arise as solutions of Eqs. (3.3)-(3.4). The distance vector,  $\mathbf{d}$ , is shown explicitly only in (a), while in the other panels we indicate only its starting point (purple dot) to avoid cluttering the diagram. The winding number defined in Eq. (3.5) is indicated next to a range of possible distance vectors,  $\mathbf{d}$ , and takes values between  $-n$  and  $+m$  for  $\lambda_p = n/m$ .

so the transition at  $\lambda_R = \lambda_p$  has to do with the pitch angle of one filament being smaller or larger than the other one. The larger the pitch angle, the more coiled is the helix.

In the case  $\lambda_R < \lambda_p < 1$ , from Fig. 3.2 (a), the left-handed filament is both larger in amplitude ( $R_2 > R_1$  if  $\lambda_R < 1$ ) and more coiled ( $\psi_2 > \psi_1$  if  $\lambda_R < \lambda_p$ ) than the right-handed filament. These two features mean that only CW intertwinement is possible between the two filaments.

At the other end of the spectrum,  $\lambda_p < 1 < \lambda_R$ , from Fig. 3.2 (c), the right-handed filament has the dominant geometry (both larger in amplitude and more coiled) so it always imposes the CCW intertwinement compatible with its nature.

In the intermediate regime, Fig. 3.2 (b), the left-handed filament is larger in amplitude but the right-handed filament is more coiled, so the direction of intertwinement depends on their relative position. The winding number is  $\Gamma = -n$  in the central region of the hypotrochoid, because that corresponds to placing the right-handed filament with smaller amplitude inside

the larger left-handed filament (see Fig. 3.1 (a)). In the petal-shaped regions on the edge of the hypotrochoid, the right-handed filament is placed further away and the cylindrical domains of the two helices overlap only slightly. The right-handed filament winds around the left-handed filament once per period ( $\Gamma = +1$ ), when the left-handed filament happens to make an excursion inside the cylindrical domain that the right-handed filament is tightly coiled around.

Note that any statement of the form “the left-handed filament intertwines in a CW direction around the right-handed filament for some given amplitude ratio  $\lambda_R$  and pitch ratio  $\lambda_p$ ” has a mirror-image equivalent in the statement “the right-handed filament intertwines in a CCW direction around the left-handed filament for some given amplitude ratio  $\lambda_R^{-1}$  and pitch ratio  $\lambda_p^{-1}$ ”. This equivalence can be deduced by placing a vertical mirror next to any two-helix ensemble and observing the mirror image of the ensemble, in which the helices have opposite chiralities to the original ones, so the amplitude and pitch ratios become the inverse of their original values. Furthermore, any CW intertwinement becomes CCW intertwinement. In this way, the physical interpretations of the three regimes (a), (b) and (c) that we have discussed above for the case of pitch ratio  $\lambda_p < 1$  can be extended to the case  $\lambda_p > 1$ .

### 3.2.5 The case of irrational pitch ratio

Beyond the fact that *in vivo* measurements of the flagellar shapes are inevitably accompanied by experimental uncertainty, there is nothing in the internal structure of the flagellar filament to suggest that the pitches of flagellar filaments come in integer multiples of a fundamental unit [81]. Indeed, when comparing flagellar filament shapes against each other, we find that the pitch ratio is not a rational number. However, two-helix ensembles with irrational pitch ratio  $\lambda_p$  lack periodicity in the vertical direction, so the curve traced out by  $\mathbf{d} + \mathbf{r}_2(z) - \mathbf{r}_1(z)$  never closes in on itself. To illustrate what happens as the pitch ratio approaches an irrational number, we consider the case where  $\lambda_p$  is the ratio of two larger integers,  $\lambda_p = 21/31$ . This should be, in theory, very close to the previously considered case  $\lambda_p = 2/3$ .

In Fig. 3.3, we recognise the three regimes previously identified for ratios of smaller integers. If we consider a sequence of rational  $\lambda_p$  tending towards some irrational value, the space between the inner region of the curve and the exterior progressively gets filled up by points on the locus of  $\mathbf{d} + \mathbf{r}_2(z) - \mathbf{r}_1(z)$ , so it is not possible to determine the winding number at every point in space. However, the qualitative distinction between the regimes  $\lambda_R < 1$ ,  $\lambda_p < \lambda_R < 1$  and  $\lambda_R > 1$  remains the same, and this is the result we use in order to compare the bacterial polymorphic shapes.

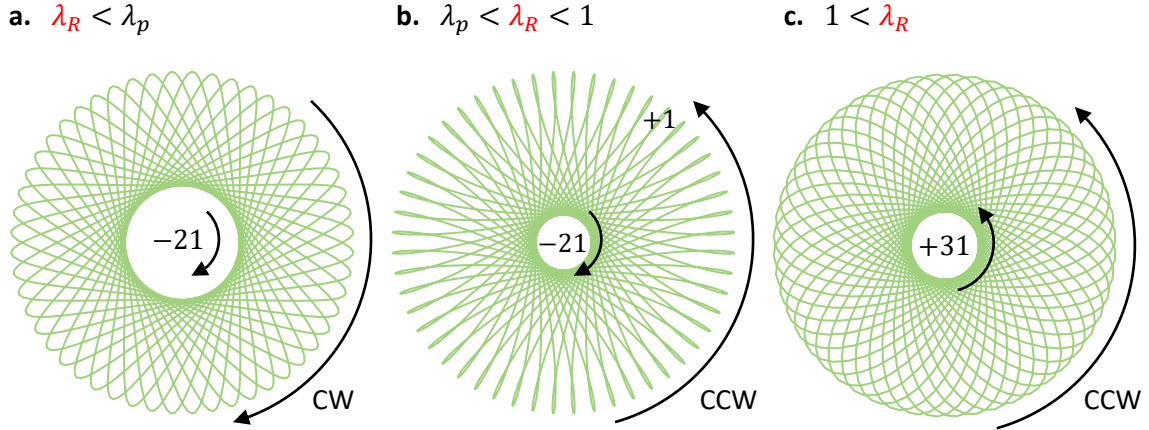


Fig. 3.3 Hypotrochoids for pitch ratio  $\lambda_p = 21/31$ . The filaments can intertwine (a) only CW, (b) both CW and CCW, and (c) only CCW depending on the ratio of their helical amplitudes.

### 3.3 Application to bacterial polymorphic shapes

We summarise the information from the previous section by drawing a phase space in the  $(\lambda_R, \lambda_p)$  plane. For  $\lambda_p < 1$  we have identified the boundaries between different regions to be the lines  $\lambda_R = 1$  and  $\lambda_R = \lambda_p$ . These regions can be extended to  $\lambda_p > 1$  by reflecting the two-helix ensemble in a vertical mirror, which switches the chirality of the filaments and therefore sends  $\lambda_p \mapsto \lambda_p^{-1}$  and  $\lambda_R \mapsto \lambda_R^{-1}$ .

In Fig. 3.4 we show the phase space of possible intertwining between a normal flagellar filament and another helical geometry. The other polymorphic forms are overlaid as symbols onto the diagram, with multiple data points coming from different sources of experimental measurements and theoretical predictions for the polymorphic shapes [21, 59, 81, 88, 106, 209]. All data comes from peritrichous bacteria, either *Escherichia coli* or *Salmonella typhimurium*.

We observe that the normal-semicoiled, normal-curly I and normal-curly II pairs that occur naturally during a tumbling event all have the possibility of intertwining in the CCW direction. At the end of a tumbling event, as the flagellar filaments rejoin the bundle, the filaments resume their CCW rotation and the cell body rotates CW to balance out the total torque on the bacterium. Therefore, hydrodynamic effects impose a CCW intertwining on the flagellar filaments, which is compatible with the intertwining allowed by the intrinsic geometry of normal-semicoiled and normal-curly I/II pairs, without the need for elastic deformations. In contrast, the intrinsic geometry of a normal filament paired with any other polymorphic shape does not allow CCW intertwining, as visible on Fig. 3.4.

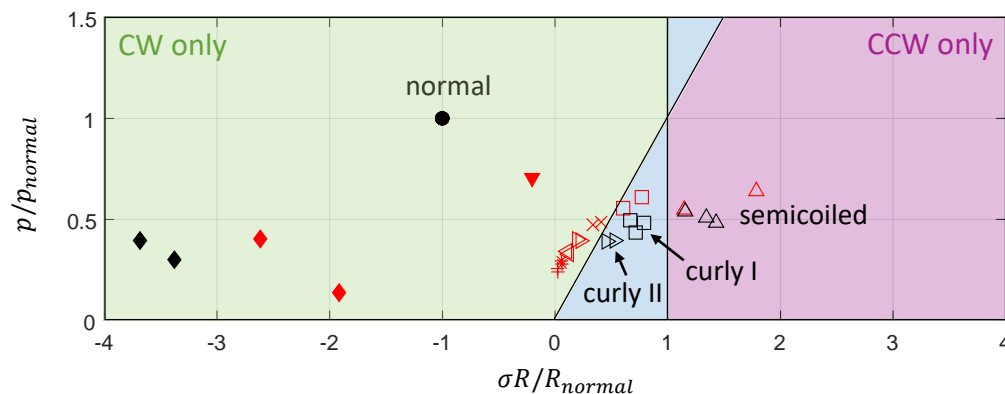


Fig. 3.4 The phase space of possible intertwinement (green - CW only, purple - CCW only, blue - both) between a normal shape filament and a second filament with pitch  $p$ , amplitude  $R$ , and chirality  $\sigma$ . The overlaid symbols correspond to the shapes of bacterial polymorphic forms (see Fig. 1.2 (b)), with experimental measurements shown in black and theoretical predictions in red. Filled and empty symbols represent left- and right-handed shapes, respectively, according to the same legend as in Fig. 1.2 (b). Symbols not annotated on the diagram:  $\blacktriangledown$  hyperextended,  $\blacklozenge$  coiled,  $\triangleleft$  polymorphism number 7,  $*$  polymorphism number 8,  $+$  polymorphism number 9,  $\times$  polymorphism number 10.

### 3.4 Conclusion

The findings presented in this chapter suggest that the polymorphic transformation of flagellar filaments during a tumbling event may play a role in the formation of bundles with a right-handed twist. It is not clear from experimental observations whether the polymorphic transformation from semicoiled and curly I/II back to the normal shape happens before or after the filaments rejoin the bundle [209]. If the transformation happened afterwards, then the CCW intertwinement of the filaments would be facilitated by the fact that the semicoiled and curly I/II shapes are right-handed and have a larger pitch angle than the normal shape. Additionally, the helical amplitude of semicoiled is larger than that of normal, making it especially easy for a semicoiled filament to wrap CCW around a normal filament. To establish more firmly the link between the observations made in this chapter and the CCW intertwinement of the flagellar filaments in practice, it would be necessary to investigate a dynamical model similar to the one considered by Lee et al. [124].

# Chapter 4

## Geometrical constraints on the tangling of helical filaments

In this chapter, we consider the geometrical constraints on the formation of tangled bundles of filaments using a kinematic model of tangling with rotational symmetry. The question of how bacteria are able to form tangle-free bundles, despite the uncoordinated actuation of multiple rotary motors, is not fully understood. By comparing the theoretical predictions of our geometrical model with experimental measurements of the flagellar shape and number, we find that the intrinsic geometry of flagellar filaments makes tangling very unlikely. This suggests that bundling is robust against the lack of control over the individual positions of the filaments as they bundle.

### 4.1 Motivation

As discussed in §1.3 of the introduction, run-and-tumble behaviour lies at the heart of motility for peritrichous bacteria. It is known that the initial stage of bundling is enabled by an elasto-hydrodynamic instability of the hook [97, 180], and from there onwards both the counter-rotation of the cell-body [1, 168] and the hydrodynamic interactions between the filaments [49, 57, 100, 175, 176, 223] contribute to the synchronisation of the filaments and formation of the bundle. Computational studies have investigated the effect of the number of flagella on the motility of the cell [158], as well as the role played by polymorphic transformations [124] and mismatched motor torques [177] in the bundling and unbundling process. Experiments using scale models have provided further insights into the bundling mechanism [113, 114].

Evidently, the ability of a peritrichous bacterium to bundle and unbundle its flagella is crucial for its mobility [172]. However, the cell has no control over the exact position of individual filaments whilst bundling, so it is intriguing that a passive process can reliably lead to ordered bundles. One potential problem is the helical geometry of the filaments which may intertwine around each other, as highlighted by Macnab [138] and discussed in §2.1.2. Yet neither experiments, nor computational studies have reported cases of tangled bundles. Despite the helical structure of flagella and the stochastic fluctuations in the torque applied by motors, it appears that tangling is always prevented thanks to hydrodynamic interactions between the filaments, their elastic deformations, as well as the shape and arrangement of flagellar filaments over the cell body. In this chapter we aim to isolate and better understand the effect of one of those agents – what can geometry on its own, without the mechanics, tell us about the issue of tangling?

In this chapter, we show that the geometrical constraints imposed by the intrinsic helical shape of bacterial flagella are incompatible with the formation of tangled bundles, therefore increasing the robustness of the bundling process. The underlying assumption of this study is that the dynamics of the filaments is quasi-steady, so that we may neglect elastic deformations and focus on the kinematics that can be achieved with the filaments in their intrinsic helical shape, as if they were perfectly rigid. Inspired by experimental observations, we consider the proximal to distal coming together of the filaments as they are being swept behind the cell body (see Fig. 4.1 (a)) and we ask what are the possible bundles that can be obtained in this way (see Fig. 4.1 (b)). We define a bundle to be the final configuration where all filaments are aligned with the cell body axis, and in particular we are interested in the possibility of forming a tangled bundle in which the filaments are physically interconnected. It can be shown that a bundle of three or more parallel helices cannot be physically interconnected if no pair of helices is intertwined. Therefore, it is sufficient to consider the pairwise tangling of flagella within the bundle. Under the quasi-steady assumption, we establish the theoretical conditions under which a pair of rigid helical filaments may tangle, and then compare these constraints with experimental data collected from the literature. Our results suggest that bacterial flagella are too straight and too far apart to form tangled bundles based on their intrinsic, undeformed geometry alone.

## 4.2 Geometrical modelling

We begin by clarifying our definition of a tangled bundle, and then propose a kinematic model for the tangling of two helical filaments in which they are placed symmetrically about the midline between their anchoring points. We first derive the geometrical constraints for

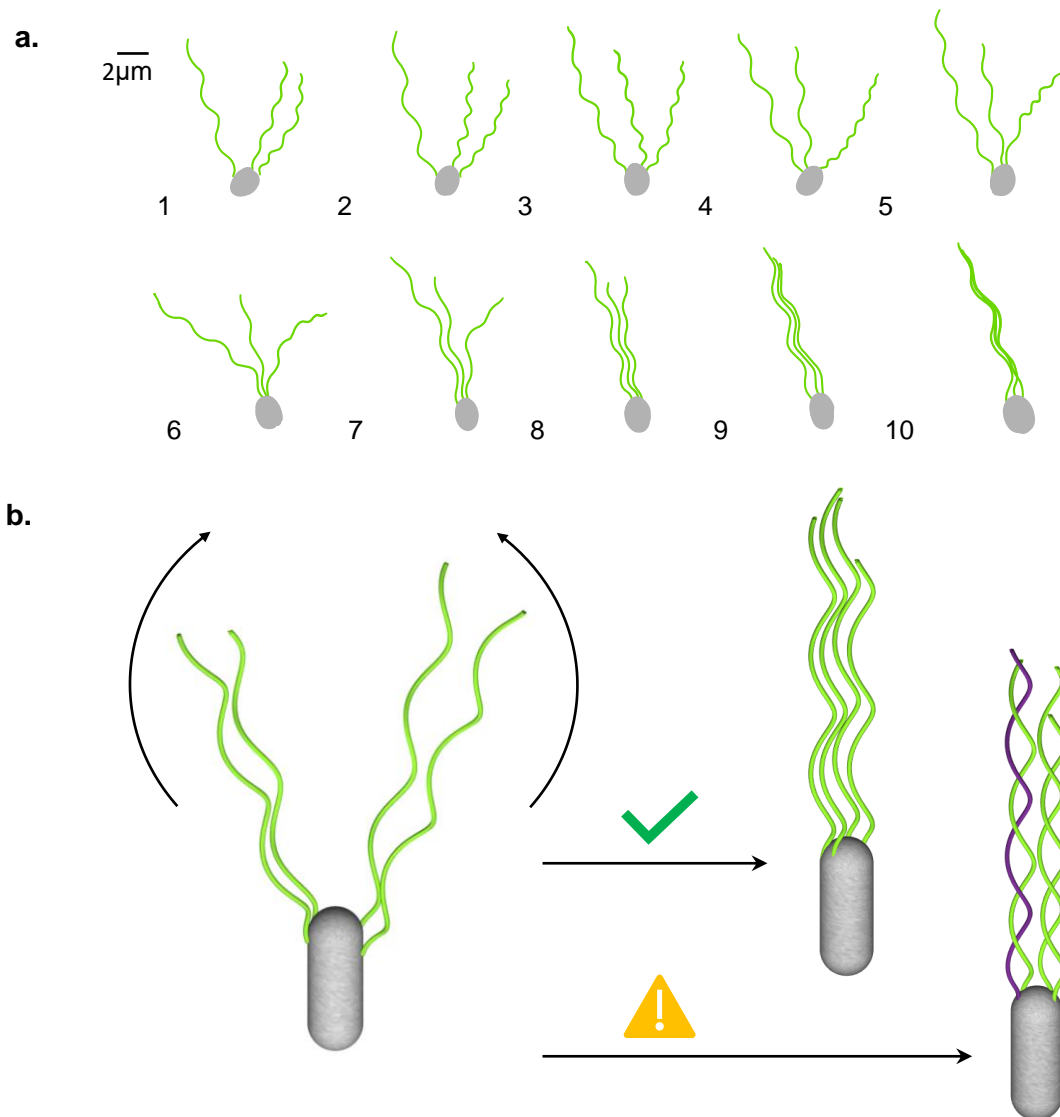


Fig. 4.1 Bundling of flagellar filaments on a swimming bacterium. (a) Sketch of flagellar filaments rejoining a bundle from the proximal to the distal end of the filaments. Based on images of fluorescently labelled *E. coli* in Turner, Ryu & Berg (2000) *J. Bacteriol.*, **182**, 2793–2801 [209]. (b) Sketch of the problem, illustrating the possible outcomes of the bundling process. An ordered bundle can rotate continuously and propel the cell forward, whereas a tangled bundle cannot fulfill this purpose. One flagellar filament is drawn in a different colour to highlight that it revolves around the other filament – the two are said to be intertwined.

two helices of constant amplitude, and then we discuss the effect of tapering at the base of the filaments.

### 4.2.1 Definition of tangled bundle

We define a tangled bundle as a configuration of helical filaments with axes parallel to each other, where at least one pair of filaments are intertwined around each other. The condition for a pair of helices to be intertwined was first derived by Macnab [138] and reviewed in §2.1.2. Two parallel identical helices of helical amplitude  $R$  are intertwined (or tangled) if the distance between the helical axes is less than

$$d_c = 2R \sin(\Delta\phi/2), \quad (4.1)$$

or alternatively if the phase difference between the helices, taken without loss of generality to be in the interval  $[0, \pi)$ , is greater than

$$\Delta\phi_c = 2 \sin^{-1}(d/2R). \quad (4.2)$$

As we scan two intertwined filaments along their helical axes (from bottom to top in Fig. 4.1 (b)), we observe that each filament revolves around the other in the same direction as the handedness of the helix (left-handed in Fig. 4.1 (b)). Macnab [138] also considered the case when the parallel helices are anchored to a pair of fixed points (i.e. the location of the rotary motors). Given the rigidity of flagellar filaments, two tangled flagella cannot be rotated continuously by the motors, as happens during a run, due to an overwinding of the filaments around each other and an unsustainable build-up of torsion. Since a peritrichous bacterium could not swim with a bundle of tangled flagella, what restrictions are there on the shape and number of flagella in order to prevent tangling?

### 4.2.2 Kinematic perspective of tangling

We consider the tangling process in purely kinematic terms, i.e. as a series of configurations through which the filaments move in order to reach their final state, without considering the forces necessary to achieve this path dynamically. The only physical barrier guiding the tangling process is the condition that the two rigid structures cannot overlap at any snapshot in time. With this view in mind, we note that it is not possible to entangle two helical filaments by keeping them parallel and changing their phase difference, since they are physical objects that cannot cut through each other when the phase difference reaches  $\Delta\phi_c$ . Therefore, if flagella on a real bacterium were ever to form a tangled bundle, they would have to follow a

sequence of non-parallel configurations. This could happen at the end of the tumble, when the flagella come back together.

In order to describe such behaviour, we begin by introducing the parameters that allow us to represent non-parallel helices. Since the hook is much shorter and much more flexible than the filament, we model the flagellum as being anchored to a fixed location by a universal point joint. We assume that the helices are tapered near their anchoring point, meaning that the helical amplitude,  $\tilde{R}(h) = R - R \exp(-h^2/h_{\text{tapering}}^2)$ , is a function of the height along the axis,  $h$ , as previously modelled by Higdon [83]. This ensures that the filament is tangent to the helical axis at the anchoring point.

In the body frame  $\{\mathbf{e}_1, \mathbf{e}_2, \mathbf{e}_3\}$  of the helical filament, its centreline is described by

$$\mathbf{r}(h) = \tilde{R}(h) \cos\left(\frac{2\pi h}{p}\right) \mathbf{e}_1(\phi, \theta, \chi) + \sigma \tilde{R}(h) \sin\left(\frac{2\pi h}{p}\right) \mathbf{e}_2(\phi, \theta, \chi) + h \mathbf{e}_3(\phi, \theta), \quad (4.3)$$

according to the notation introduced in §2.1.1. Because we later treat the spin angle  $\chi$  as a dependent variable to be solved for, it is convenient to adsorb the spin angle into the trigonometric functions and have unit vectors dependent on  $(\phi, \theta)$  alone. Therefore, we introduce the unit vectors

$$\mathbf{e}'_1(\phi, \theta) = \mathbf{e}_1(\phi, \theta, 0), \quad \mathbf{e}'_2(\phi, \theta) = \mathbf{e}_2(\phi, \theta, 0), \quad (4.4)$$

and we rewrite the centreline of the filament as

$$\mathbf{r}(h) = \tilde{R}(h) \cos\left(\frac{2\pi h}{p} + \sigma \chi\right) \mathbf{e}'_1(\phi, \theta) + \sigma \tilde{R}(h) \sin\left(\frac{2\pi h}{p} + \sigma \chi\right) \mathbf{e}'_2(\phi, \theta) + h \mathbf{e}_3(\phi, \theta). \quad (4.5)$$

The helical axis of the filament,  $\mathbf{e}_3$ , is parallel to the radial unit vector  $\mathbf{e}_r(\theta, \phi)$  in standard spherical polar coordinates. The two vectors spanning the plane orthogonal to the helical axis are  $\mathbf{e}'_1 = \mathbf{e}_\theta(\theta, \phi)$  and  $\mathbf{e}'_2 = \mathbf{e}_\phi(\phi)$ , i.e. the unit vectors in the directions of increasing inclination angle,  $\theta$ , and increasing azimuthal angle,  $\phi$ , respectively.

Now consider a pair of filaments anchored to two fixed points separated by a distance  $d$ . In the kinematic perspective, where we are only interested in the space occupied by the filaments at each moment in time, we can adaptively change our frame of reference  $\{\mathbf{e}_x, \mathbf{e}_y, \mathbf{e}_z\}$  such that the anchoring points remain fixed and the direction  $\mathbf{e}_x$  is always given by the line between the two anchoring points, despite the cell-body counter-rotations that may be observed in a stationary frame. Henceforth it is assumed that we are in a frame where the anchoring points, and hence the distance  $d$ , are fixed.

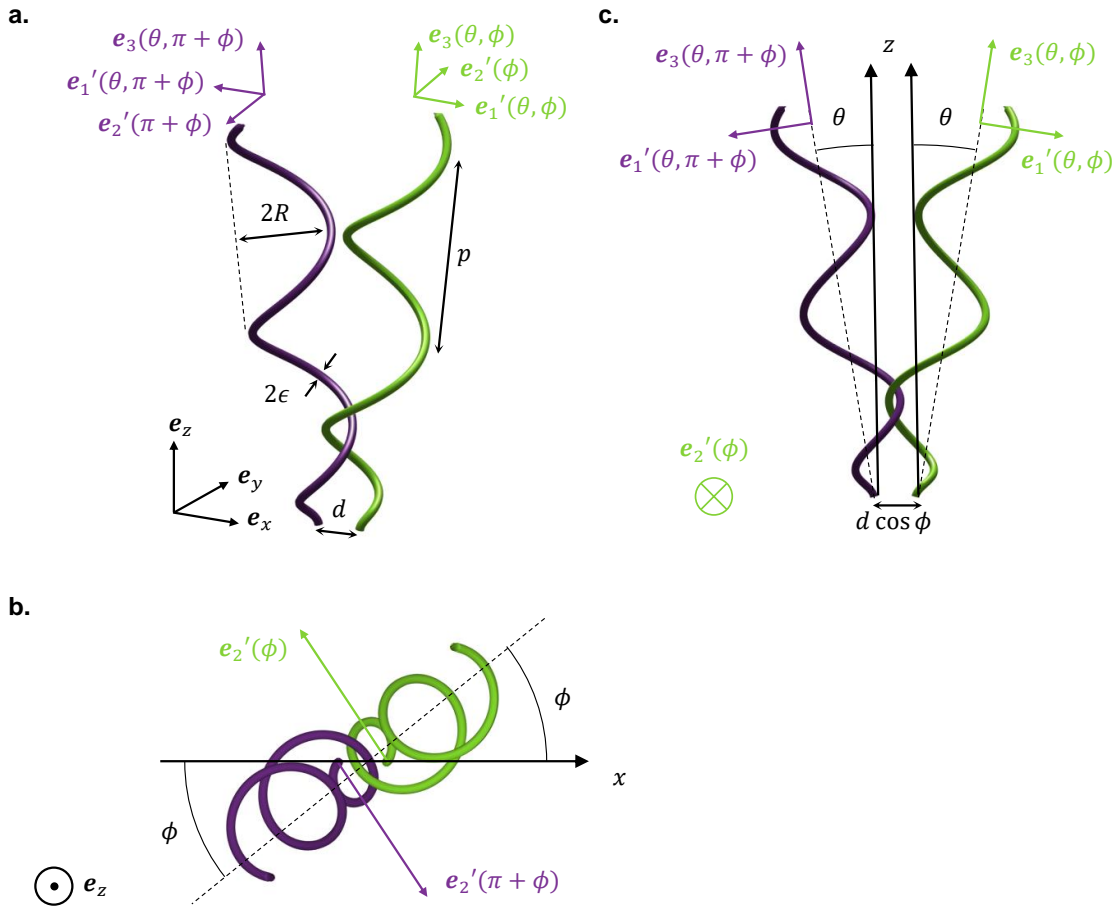


Fig. 4.2 Geometry of tangling for two identical helices, each tapered near their anchoring point. (a) The easiest way to tangle two identical, rigid and helical filaments is to arrange them symmetrically about the midline between their anchoring points, which are a distance  $d$  apart. In this case, one helix has configuration  $(\phi, \theta, \chi)$ , while the second has configuration  $(\phi + \pi, \theta, \chi)$ , obtained by rotating the first filament through an angle  $\pi$  about the midline between their anchoring points. (b) Top view of (a), with  $e_z$  pointing out of the page. (c) Side view of (a), with  $e_2$  pointing into the page.

Suppose we wanted to bring the two flagella from a configuration where they are not intertwined (e.g. pointing away from each other, as they would be at the end of a tumble) into a tangled bundle. Intuitively, the easiest way to achieve this is to arrange the helices symmetrically about the midline between their anchoring points at every step of the way, because this gives them space to circle around each other and intertwine, without blocking each other's way. This can be achieved by placing one helix in the configuration  $(\phi, \theta, \chi)$  and the second in the configuration  $(\phi + \pi, \theta, \chi)$ , so that the helices are an image of one another under a rotational symmetry through angle  $\pi$  about the midline between their anchoring

points, as illustrated in Fig. 4.2. If tangling is not possible under these conditions, then it is not possible at all.

In this symmetric configuration, the problem of intertwining two helices around each other becomes equivalent to intertwining one helix around a fixed vertical line of zero thickness, which represents the midline between the anchoring points of the two original helices. This is depicted in Fig. 4.3 (a). In our setup, the midline is the  $z$ -axis, and the helix is anchored to the  $xy$ -plane at a distance  $d/2$  away from it along the  $x$ -axis. Despite having zero thickness the vertical line has material properties, i.e. the filament cannot cross this line, because it would have to cross through its mirror image filament on the other side of the midline.

Since we want to determine the threshold where tangling is no longer possible, we must look at the limiting case where there is only enough space to tangle if the helical filament is touching the line of zero thickness, as seen in Fig. 4.3 (a). The trajectory of the filament as it tangles around the line can be characterised uniquely by a pair of coordinates  $(h, \phi)$  indicating the contact point and the azimuthal angle over which the helical axis is inclined. In keeping with experimental observations illustrated in Fig. 4.1, we consider the problem as the contact point,  $h$ , slides up from the proximal to the distal end of the helix. As this happens, the portion of the helical filament below  $h$  will gradually envelop the vertical line, until we reach a deadlock (for videos of the tangling process, see online supplementary material [206]). At a certain critical height  $h_{\text{crit}}$ , not only will the outside of the filament be in contact with the line at  $h_{\text{crit}}$ , by design, but the inside of the filament will also make contact with the line at height  $h_{\text{crit}} - p$ . Since the vertical line has material properties, any further increase of  $h$  will lead to an overlap, so we cannot go beyond this point. This constraint is a consequence of the helical geometry of the filament and applies equally well to a helix of constant amplitude, so we start by deriving the threshold in the case of a perfect helix.

### 4.2.3 Geometrical constraints for a perfect helix

We may calculate the critical point analytically, as a function of the azimuthal angle  $\phi$  at which the helical axis is inclined, by taking a cross-section in the plane spanned by  $\mathbf{e}_z$  and  $\mathbf{e}'_2(\phi) \wedge \mathbf{e}_z$ , which we call the “focal plane” – see Fig. 4.3 (a), (b). Recall that we are interested in finding the point of contact between the helix and the vertical  $z$ -axis. If one imagines keeping the azimuthal angle,  $\phi$ , fixed and varying the incline angle,  $\theta$ , in order to find the special value  $\hat{\theta}(\phi, h)$  at which the helix is tangent to the  $z$ -axis at point  $h$  along the helix, then the cylindrical envelope containing the helix will be “sliced” by the  $z$ -axis along the plane normal to  $\mathbf{e}'_2(\phi) = (-\sin \phi, \cos \phi, 0)$  going through the origin, which explains our choice of focal plane. If we impose the further condition that the filament is tangent to the line

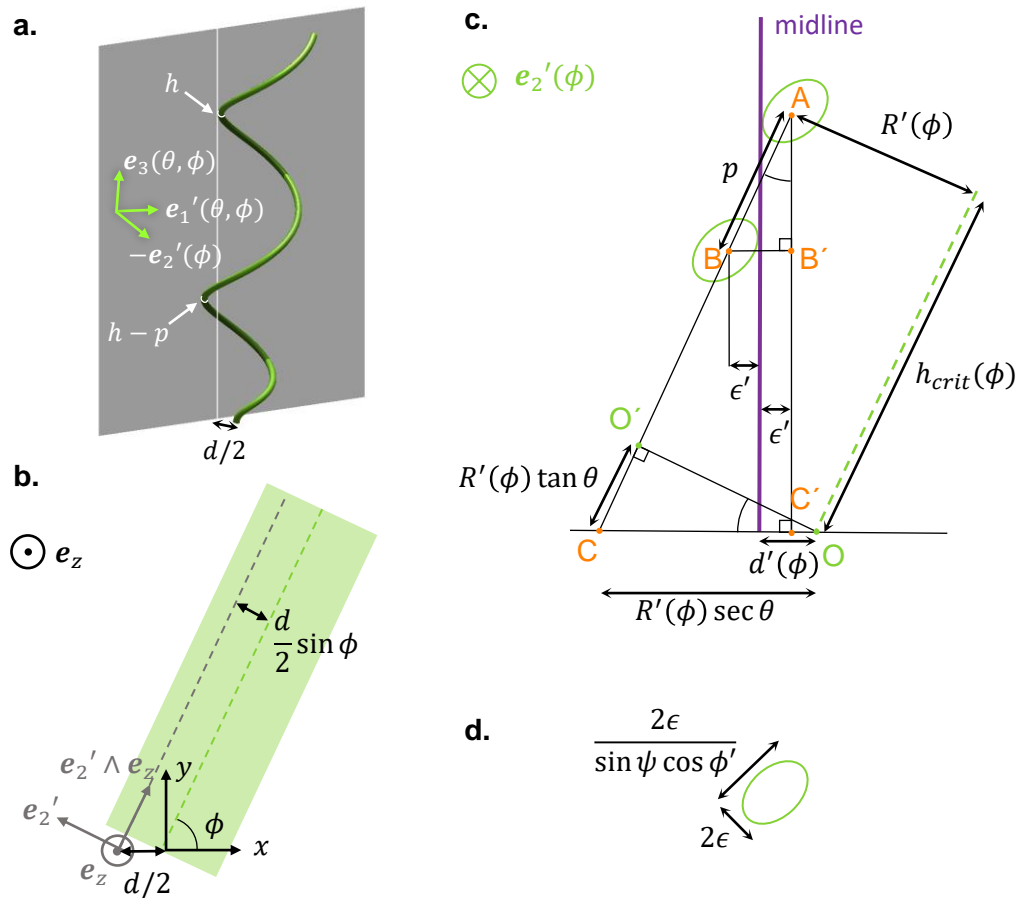


Fig. 4.3 Computing the tangling threshold for two perfect helices. (a) In a symmetric configuration, the problem reduces to that of a rigid helical filament intertwining around a fixed vertical line of zero thickness (white). In the limiting case, tangling can be achieved by bringing the filament in contact with the line at point  $h$  along the helix, and sliding this contact point up. Tangling cannot proceed past the point  $h = h_{\text{crit}}$  where the exterior of the filament is in contact with the line at  $h$ , by design, but the filament makes contact with the line again on the interior at  $h - p$ . To locate this critical point we take a cross-section in the plane normal to  $\mathbf{e}'_2(\phi)$ , indicated in this figure by a shaded screen, which we call the “focal plane”. (b) Projection onto the  $xy$ -plane. The projection of the cylindrical envelope containing the helix is shown in light green. The direction of the vector  $\mathbf{e}'_2 \wedge \mathbf{e}_z = (\cos \phi, \sin \phi, 0)$  is parallel to the projection on the  $xy$ -plane of the helical axis and lies at a distance  $d \sin \phi / 2$  away from it. The focal plane is normal to the vector  $\mathbf{e}'_2(\phi) = (-\sin \phi, \cos \phi, 0)$  and goes through the origin, denoted by a grey dot. The helix is anchored to the  $xy$ -plane at a distance  $d/2$  away from the origin along  $x$ . (c) Sketch (not to scale) of the cross-section in the focal plane through a perfect helix of constant amplitude. The projection of the helical axis on the focal plane is drawn as a dashed light green line. The outline of the helical filament is also drawn in light green around the points A and B at heights  $h_{\text{crit}}$  and  $h_{\text{crit}} - p$  along the helical axis, respectively, and is tangent to the vertical midline drawn in dark purple. The dimensions of the elliptical cross-section are shown separately in (d).

at  $h - p$  as well, we can determine the critical point  $h_{\text{crit}}(\phi)$ , and the critical incline angle  $\theta_{\text{crit}}(\phi) = \hat{\theta}(\phi, h_{\text{crit}}(\phi))$ .

The resulting geometric problem is sketched in Fig. 4.3 (c). The projected distance between the anchoring point and the  $z$ -axis is

$$d'(\phi) = \frac{d \cos \phi}{2}, \quad (4.6)$$

and the projected distance between the filament centreline and the helical axis is

$$R'(\phi) = R \cos \phi', \quad \phi' = \sin^{-1} \left( \frac{d \sin \phi}{2R} \right). \quad (4.7)$$

The angle  $\phi'$  measures the offset between the focal plane and the axis of the filament.

The quantity that requires more careful consideration is the horizontal distance  $\varepsilon'$  between the filament centreline and the  $z$ -axis. It can be shown that for small filament thickness,  $\varepsilon \ll R, p$ , the intersection of the helical filament with the focal plane is well approximated by an ellipse with minor axis  $2\varepsilon$  and major axis  $2\varepsilon / \sin \psi \cos \phi'$ , where  $\psi = \tan^{-1}(2\pi R/p)$  is the pitch angle of the helix - see Fig. 4.3 (d). The major axis of the ellipse makes an angle  $\theta + \tan^{-1}(\sin \phi' \tan \psi)$  with the  $z$ -axis. The tilting of the ellipse away from the vertical direction is partly due to the inclination angle  $\theta$  applied to the entire helix, and partly due to the offset  $\phi'$  between the focal plane and the helical axis, the latter effect being enhanced by the amount of sloping in the helical filament, as measured by  $\psi$ . The full calculation of the cross-sectional shape is given in Appendix 4.A. All these factors combined lead to a horizontal distance of approximately

$$\varepsilon'(\theta, \phi) \simeq \varepsilon \sqrt{1 + \frac{\sin^2(\theta + \tan^{-1}(\sin \phi' \tan \psi))}{\tan^2(\sin^{-1}(\cos \phi' \sin \psi))}} \quad (4.8)$$

between the filament centreline and the  $z$ -axis.

The multiple lengths in the problem can be linked together through the similarity of triangles  $\triangle ABB'$  and  $\triangle ACC'$ , from which we derive

$$\sin \theta = \frac{2\varepsilon'(\theta, \phi)}{p} = \frac{R'(\phi) \sec \theta - d'(\phi) + \varepsilon'(\theta, \phi)}{R'(\phi) \tan \theta + h_{\text{crit}}(\phi)}. \quad (4.9)$$

The first part of Eq. (4.9) will only be satisfied by a specific value of  $\theta = \theta_{\text{crit}}$  dependent on  $\phi$ , for which we can solve in the limit of small thickness  $\varepsilon \ll R, p$  using Eq. (4.8), to find that

$$\theta_{\text{crit}}(\phi) \simeq \frac{2\varepsilon}{p} \sqrt{1 + \frac{\sin^2(\tan^{-1}(\sin \phi' \tan \psi))}{\tan^2(\sin^{-1}(\cos \phi' \sin \psi))}}. \quad (4.10)$$

Then, by rearranging the second part of Eq. (4.9), we obtain the critical height

$$h_{\text{crit}}(\phi) = \frac{p}{2} - \frac{d'(\phi)}{\sin \theta_{\text{crit}}(\phi)} + \frac{R'(\phi)}{\tan \theta_{\text{crit}}(\phi)}, \quad (4.11)$$

with  $d'(\phi)$ ,  $R'(\phi)$  and  $\theta_{\text{crit}}(\phi)$  defined in Eqs. (4.6), (4.7) and (4.10). The condition from Eq. (4.11) restricts trajectories in  $(\phi, h)$  coordinate space, as shown in Fig. 4.4. Because of this constraint, the tangling of a perfect helix around a fixed material line, or equivalently of two identical perfect helices around each other, is only possible for filaments shorter than  $\max_{\phi} h_{\text{crit}}(\phi) = h_{\text{crit}}(\pi)$ .

#### 4.2.4 Effect of tapering

Beyond the case of helices with constant amplitude, tapering imposes further constraints on the  $(\phi, h)$  trajectory of the filament due to interactions near the anchoring point. The theoretical threshold for tangling from Eq. (4.11) is valid for a perfect helix with constant amplitude,  $R$ , meaning that the bottom end is not properly anchored to the point where the helical axis meets the  $xy$ -plane. Its locus is a sphere of radius  $R$  around that point. If we wanted to intertwine the helix around the vertical line as much as possible, we could keep the azimuthal angle fixed at  $\phi = \pi$ , so that the helix is leaning towards the vertical line, and raise the contact point up to the global maximum of the constraint, which is  $\max_{\phi} h_{\text{crit}}(\phi) = h_{\text{crit}}(\pi)$ . As we do this, we must continuously decrease the spin angle  $\sigma\chi$ , for which we have the exact solution  $\hat{\chi}(\phi, h) = \sin^{-1}(d \sin \phi / 2R) - \sigma 2\pi h / p$ , while also decreasing the incline angle  $\hat{\theta}(\phi, h)$ . The motion this would generate is that of a helix being screwed around a fixed vertical line, which is possible because the bottom end of the helix is free to loop around the vertical line. A video illustrating this process is available in the online supplementary material of Ref. [206], but here we provide an explanation in words. During the screwing motion, each time the contact point covers an interval of length  $p$  above some arbitrary point  $h_0 + p/2$ , the point  $h_0$  loops around the vertical line once. This is because the incline angle  $\hat{\theta}(\phi, h) < \hat{\theta}(\phi, h_0)$  if  $h > h_0$ , so the vertical line already lies inside the cylindrical envelope of the helix up to the point  $h_0$ . Meanwhile, the point  $h_0$  revolves around

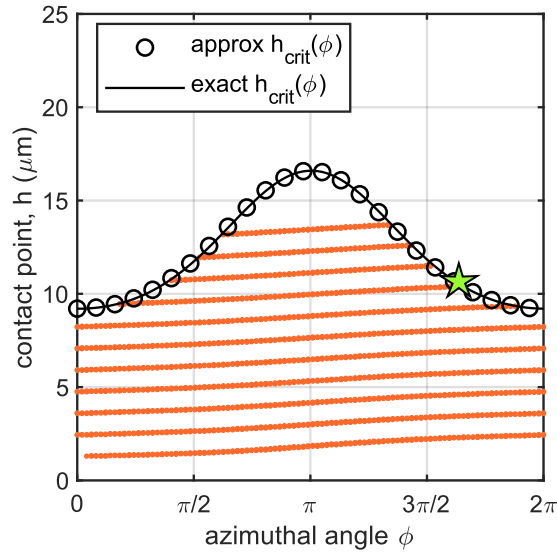


Fig. 4.4 Representative example of the coordinate space  $(\phi, h)$  of configurations. The curve  $h_{\text{crit}}(\phi)$  represents a constraint due to the helical shape of the filament. The approximate solution (circles) given by Eqs. (4.10) and (4.11) relies on a small  $\varepsilon$  approximation. This is verified by the exact solution (solid black) where we solve the transcendental equations for  $\varepsilon'(\theta, \phi)$  and  $\theta_{\text{crit}}(\phi)$  iteratively. The sloping orange lines represent additional constraints due to the tapering of the helix and its anchoring to a fixed point, and they are computed numerically.

this cylindrical envelope once every time the spin angle  $\hat{\chi}(\phi, h)$  covers a period of  $2\pi$ , which happens each time the contact point  $h$  covers an interval of length  $p$ .

Suppose we wanted to follow the same strategy (i.e. keep  $\phi$  fixed and increase  $h$ ) with a tapered helix that is anchored to a fixed point. Then every time the contact point goes up by one helical pitch, the filament would have to intersect the vertical line. This is because the bottom end of the anchored helix is fixed relative to the vertical line, but there exists some point  $h_0$  higher up the filament which loops around the vertical line once. Since the filament is a continuous curve between these two points, then it must intersect the vertical line in the process. These intersections can be determined numerically, with results shown as dotted orange lines in Fig. 4.4, and represent physical constraints to the motion of the filament.

In order to complete tangling up to the highest possible point along the helix, we must navigate the coordinate space  $(\phi, h)$  in such a way as to avoid hitting any physical constraints. We may work our way up between the sloping lines shown in Fig. 4.4 and around the  $\phi$ -periodic domain until we reach the constraint  $h = h_{\text{crit}}(\phi)$ . The maximum height up to which two helices can tangle around one another is found numerically to be  $h_{\text{crit}}^* = h_{\text{crit}}(\phi^*)$ , where  $\phi^*$  is a consequence of tapering. This threshold depends on all the parameters in our model,

namely the geometry of the flagellum described by  $(p, R, \varepsilon)$ , and the distance,  $d$ , between the two anchoring points.

### 4.3 Comparison with experimental measurements

What are the implications of these results for the morphology of real bacteria? For a single cell, with a given cell body size and a given number of flagella, the possibility of forming tangled bundles will be determined by the shape of those flagella. If one were to design a robotic micro-swimmer resembling peritrichous bacteria, one could consider a continuous parameter space for the helical shape of propellers, whereas in real bacteria the shape belongs to a discrete set of polymorphic forms. On the other hand, if the shape of the filament is assumed to be one of the polymorphic forms, the possibility of forming tangled bundles in a population of cells with stochastic variations in morphology will be determined by the relation between cell body size and number of flagella, which affects how closely together the flagella are packed. We address both of these points in the next two subsections, using parameter values taken from the biological literature.

#### 4.3.1 Single cell results

We start by considering a single cell of fixed dimensions, and we allow for isometric variations in the shape of the helical flagellum (i.e. continuously varying pitch and radius, at constant integrated length). Any helical filament of fixed length  $L$  can be described by a pair of coordinates  $R/L$ , the helical radius relative to the length of the filament, and  $\psi = \tan^{-1}(2\pi R/p)$ , the pitch angle. The coordinate space  $(R/L, \psi)$  can be divided into two regions where the pair of filaments may or may not tangle, according to whether the theoretical threshold,  $h_{\text{crit}}^*(p, R, \varepsilon, d)$ , is greater or less than the full height of the filament,  $h_{\text{end}}(p, R, L)$ . The boundary between these two regions depends on  $d/L$ , the distance between the anchoring points relative to the length of the filaments, which is our control parameter.

In order to choose realistic values for  $d/L$ , we note that the expected minimum distance between any two flagella on a bacterium will depend on the size of the cell body and the number of flagella. Modelling the cell body as a capsule (i.e. a cylinder with two hemispherical caps) of length,  $l$ , and width,  $w$ , we compute the expected minimum distance between any two rotary motors,  $d_{\text{min}}(N_f, l, w)$ , by simulating 10,000 random arrangements of  $N_f$  motors on the cell body sampled from a uniform distribution over a capsule (this sample size is sufficient to make our estimate for  $d_{\text{min}}$  accurate to within 1%). The expected minimum distance is then scaled by the mean length of a flagellum reported in the literature.

Our theoretical predictions for a single cell, using the average cell body size and average length of flagella for the bacterial strain *E. coli* AW405 [40, 209], are shown in Fig. 4.5 (a). As the number of flagella increases and the relative separation between them decreases, the region where filaments could, in theory, form a tangled bundle occupies increasingly more of the parameter space, as expected.

The four most common polymorphic forms, depicted in Fig. 4.5 (b), are indicated as discrete points in the continuous parameter space of Fig. 4.5 (a). We observe that normal form, the most common of the polymorphic forms, does not enter the region where the formation of tangled bundles is possible until the number of flagella is greater than or equal to six. This compares favourably with the average number of flagella for *E. coli* AW405 quoted in the literature, which is between three and four flagella [209]. From the phase space we also deduce that the shape of semicoiled form is the most susceptible to tangling. Finally we note that, at a typical number of three or four flagella [209], all four polymorphic forms lie in the region where the rigid geometry of the flagellar filaments should not allow the formation of tangled bundles.

### 4.3.2 Population level results

We now consider stochastic variations in the shape of the cell body and the length of flagella, but keep the helical shape of the filaments constant. We model the cell body as a capsule, as before, and we generate a sample of 500 cells with independent normally distributed body lengths,  $l$ , and widths,  $w$ , with means and variances taken from the literature. For each of these cells, we compute the expected minimum distance between any two rotary motors,  $d_{\min}(N_f, l, w)$ , by randomly placing  $N_f$  motors on the cell body (distributed either uniformly or according to a known asymmetric distribution [166]) and averaging over 10,000 realisations of motor placements. The flagellar filaments attached to these motors have a given geometry  $(p, R, \varepsilon)$  corresponding to one of the bacterial polymorphic forms found in nature, but their length is a random variable, sampled either from an experimentally measured distribution [91] or from a log-normal distribution if only the mean and variance are available in the literature. For each simulated cell we compute the theoretical threshold,  $h_{\text{crit}}^*(p, R, \varepsilon, d_{\min}(N_f, l, w))$ , and compare this with the length of the simulated filaments to determine if, for that number of motors, we would expect any two flagella to be sufficiently near each other to form a tangled bundle. This allows us to predict the maximum number of flagella that the cell may have without running the risk of tangling.

Our theoretical predictions, based on parameter values taken from the literature [3, 39, 40, 54, 59, 88, 91–93, 106, 128, 208, 209, 222], are shown in Fig. 4.6 (circles and triangles) alongside the real number of flagella counted in experiments (diamonds), for the three most

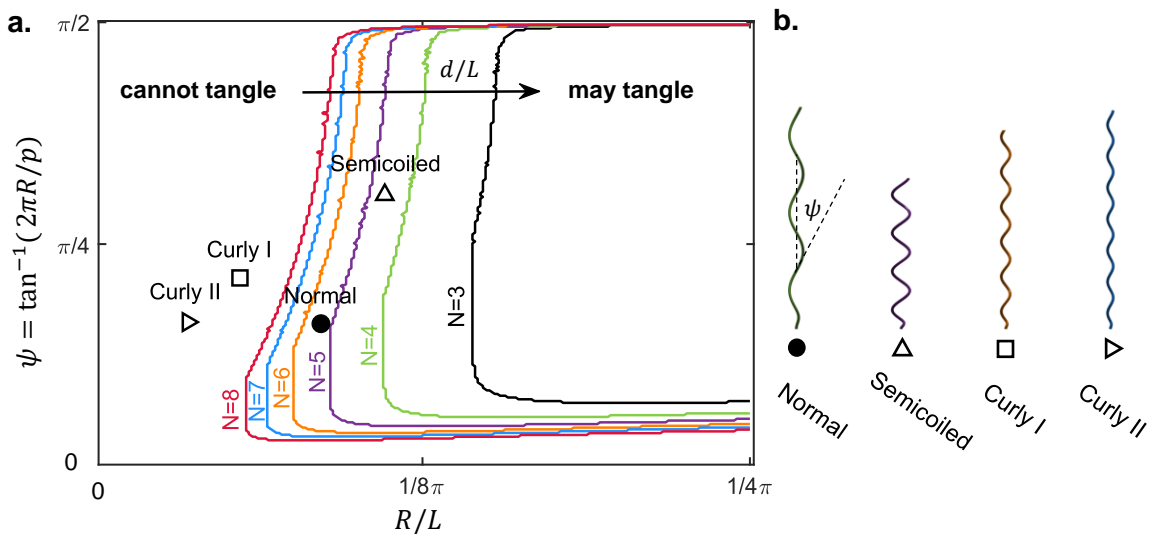


Fig. 4.5 Single cell results. (a) Phase space for an identical pair of isometric filaments with constant length,  $L$ , and helical shape described by  $(R/L, \psi)$ . Each boundary is labelled with an integer number of flagella,  $N_f$ , and corresponds to a different partitioning of the phase space into two regions. The boundary for a given  $N_f$  is obtained using a distance between the anchoring points equal to the expected minimum distance between any pair of flagella, when there are  $N_f$  flagella distributed uniformly across the cell surface. To the left of each boundary, our theoretical model predicts that no pair amongst the  $N_f$  flagella should be close enough to form a tangled bundle, while to the right of the boundary the closest pair of flagella may be able to form a tangled bundle. The values of the control parameters  $(L, \epsilon, l, w)$  are representative of the bacterial strain *E. coli* AW405 [40]. (b) Isometric filaments in the shape of the four polymorphic forms most commonly seen in bacteria.

widely studied species of peritrichous bacteria: *E. coli*, *S. typhimurium* and *B. subtilis* (see Appendix 4.B for data sources). For our theory, we use the two most common polymorphic forms that the bacterial flagellum can take, namely the left-handed “normal” form used in runs (circles) and the right-handed “semicoiled” form used in tumbles (triangles) [39]. The empty symbols represent an estimate based on a non-uniform arrangement of molecular motors over the cell body, according to distributions reported in the literature for *E. coli* and *B. subtilis* [76, 166] (no equivalent data was available for *S. typhimurium*). These estimates are always slightly lower than those for a uniform distribution, because the effective distance between flagella is reduced when the molecular motors are crowded towards one pole of the cell, which makes tangling more likely. However, the relative difference between the two estimates is very small because the asymmetry in motor distribution is not very pronounced.

Remarkably, we find that the theoretical thresholds in Fig. 4.6 are always above, or less than one below, the real number of flagella observed in experiments. This close agreement strongly suggests that the morphologies of the flagellar filaments and of the cell body in the strains we have considered make it unlikely for flagella to form tangled bundles under a quasi-steady motion without elastic deformations. We note that two other polymorphic forms (curly I and II) are sometimes observed in the flagellar bundles of swimming bacteria [209], but they are so slender that the corresponding theoretical thresholds are much higher than for normal and semicoiled flagella, as evidenced in Fig. 4.5. Hence, preventing their tangling does not appear to impose strong physical constraints on the cell.

## 4.4 Discussion of extensions and limitations

There are two geometrical aspects which we have not included in the present study. Firstly, the setup described in Fig. 4.2 consists of filaments anchored to a pair of fixed points in free space. Although we model the geometry of the cell body in order to determine the typical spacing between filaments, the surface of the cell body is not included as a physical constraint in our configuration space from Fig. 4.4. However, we note that the typical distance between flagella before their intrinsic geometry allows them to tangle in free space is between  $0.1 \mu\text{m}$  for curly and  $0.5 \mu\text{m}$  for semicoiled, whereas at the poles of the cell the radius of curvature is around  $0.35 - 0.6 \mu\text{m}$  depending on the strain. Hence, the effect of surface curvature will be most important for semicoiled flagella attached to smaller cells, since the surface could then be bulging out between the anchoring points at an angle as high as  $46^\circ$  from the horizontal, while the helical filament of semicoiled makes an angle of approximately  $35^\circ$  with the horizontal. In this case, the steric interactions between the filaments and the cell body surface will depend greatly on the details of the tapering of the helix near the anchoring

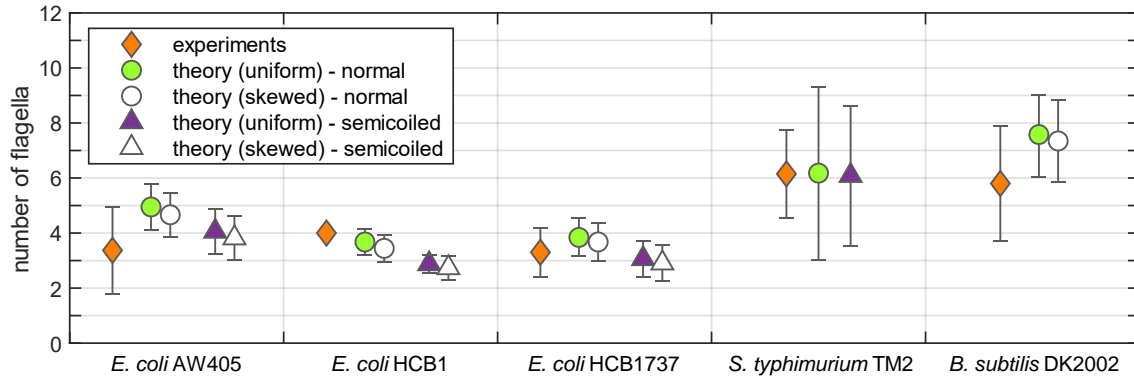


Fig. 4.6 Comparison between theoretical predictions and experimental data for three peritrichous species of bacteria: *E. coli*, *S. typhimurium* and *B. subtilis*. Our predicted critical number of normal flagella (circles) and semicoiled flagella (triangles) is compared against the real number of flagella counted in experiments (diamonds). For the filled circles and triangles we have assumed that flagella are uniformly distributed over the cell body, while for the empty symbols we have used a non-uniform distribution that is skewed towards one pole of the cell (for *E. coli* and *B. subtilis*, this data was available in the literature [76, 166]; no equivalent data was available for *S. typhimurium*). The error bars represent one standard deviation.

point. For normal flagella, the cell body surface would be raised at an angle of at most  $34^\circ$  to the horizontal near the anchoring point, even on the smallest cells we have considered, whereas the filament of normal flagella makes an angle of  $61^\circ$  to the horizontal. Hence, the presence of the curved surface will have very little effect on the tangling of normal flagella, and even less so for curly I and II.

The second aspect of the geometry which we have neglected is that the shape of the filament can change dynamically while the cell tumbles due to polymorphic transformations which propagate from the proximal to the distal end of the filament [39, 124, 209]. The angle between sections of the filament in different polymorphic states is given by Hotani's rule [87]. This aspect of the geometry requires a fully dynamical model including the elasticity of the filament and the hydrodynamic load that triggers the transformation, and goes beyond the scope and purpose of the current study.

Furthermore, our modelling approach is purely kinematic and neglects a number of important dynamical factors. On one hand, elastic deformations might allow the entanglement of longer filaments than we have predicted but, on the other hand, thermal fluctuations would increase the effective thickness of the filaments, thereby decreasing the likelihood of tangling. The finite length of the hook is another element of complexity that cannot be addressed in our simple model, because it would introduce further degrees of freedom. The end of the

filament would no longer have to be anchored to a fixed point, but could hover within a small distance (the length of the hook) away from the true location of the molecular motor, which is fixed. When the filaments are being swept behind the cell body, the effective distance between the proximal ends of the filaments could be reduced, making it easier to form a tangled bundle.

Hydrodynamic interactions play a very important role in the formation of stable bundles since they favour the synchronisation of flagella, leading to helical filaments rotating in phase with one another [175]. The clockwise rotation of normal flagella, together with the counter-rotation of the cell body, lead to a right-handed wrapping of the filaments inside the bundle, as seen in experiments [113] and computations [1, 100]. This kind of wrapping is made possible by the elastic deformation of the filaments and is different to the left-handed tangling considered in this article, which is the only one allowed by the left-handed intrinsic geometry of the normal flagellum [138]. Simulations have shown that, if hydrodynamic interactions are switched off, the bundle comes apart because the filaments are not geometrically interconnected due to the right-handed wrapping [100]. In this article we have focused instead on the tangling which arises from the intrinsic geometry of the filaments (left-handed for normal flagella, and right-handed for the others) because it is the one that hinders the continuous actuation of the filaments during a run and the dispersal of the filaments during a tumble.

Our kinematic model for tangling is based on the idea that the set of hydrodynamically feasible paths is a subset of all possible geometries of motion. Thus, we have shown that hydrodynamics is not essential to prevent tangling in the quasi-steady regime – geometry imposes sufficient restrictions to avoid the formation of tangled bundles. If we relax the quasi-steady approximation, the set of possible geometries of motion will expand greatly since the shape of the filament could undergo arbitrary elastic deformations. Then tangling will (obviously) always be theoretically possible within the set of all possible geometries of motion. It is therefore necessary to identify the filament kinematics that are also dynamically feasible given the background flow conditions and the input of the rotary motors. Such a wide range of dynamic conditions is computationally inexhaustible, which is where our model can provide a stepping stone for further studies and narrow down the search. Based on the intrinsic geometry of the filaments, we have identified the kinematics that leads to tangling. Videos illustrating the tangling process are available online in the supplementary material of Ref. [206]. We have compared this kinematics to the typical frequency of rotation of bacterial motors and identified that the motors would have to switch the direction of rotation one hundred times per second and spend an equal amount of time rotating in either direction, whereas in real bacteria the motors only switch the direction of rotation once per second

and spend the vast majority of the time rotating clockwise [40]. The qualitative difference between the kinematics that leads to tangling and that of real flagella is a further argument for the robustness of the bundling process.

## 4.5 Conclusion

The number of flagella is a fundamental control parameter for peritrichous bacteria, and its connection to bacterial spreading and speed of locomotion has been previously investigated [107, 156, 158]. In the current study, our kinematic model for tangling allows us to examine whether the number of flagella could be linked to the robustness of bundling. By comparing the thresholds from our theoretical model with the real number of flagella counted in experiments, we deduce that the intrinsic geometry of flagellar filaments should not allow the formation of tangled bundles. This is consistent across the four most common polymorphic forms of the bacterial flagellum, and across three different strains of *E. coli* and one strain of *S. typhimurium* for which we could test a consistent set of data. We note that in the case of *B. subtilis*, the geometrical constraints identified in this chapter and presented in the last column of Fig. 4.6 are only suitable for the shorter mutant DK2002 [208], which is equipped with fewer flagella. In contrast, the wild-type and highly-flagellated strains of *B. subtilis* can have up to forty flagella with only a slight increase in cell body size (less than 50%), meaning that the constraints imposed by the intrinsic geometry of flagella are not sufficient to rule out tangling. The thresholds predicted by our model for the wild-type strain DS9540 [208] were of approximately nine normal flagella or thirty curly flagella, compared to experimental measurements of twenty-six derived from a basal body count [76].

For *E. coli* and *S. typhimurium*, we can formulate our conclusion either in terms of the helical geometry of the polymorphic forms, which appears to be too slender to allow tangling (Fig. 4.5), or in terms of the relative spacing between motors, which appears to be too wide to allow tangling (Fig. 4.6). Alternatively, we can think about the space of configurations as being partitioned into different regions by the physical constraint that the filaments cannot overlap (Fig. 4.4). Using parameter values from the experimental literature, our theoretical model suggests that tangled bundles are isolated in configuration space from the state in which flagella typically find themselves at the end of a tumble (see Fig. 4.1 (b)). Since tangled bundles are physically inaccessible, this means that the bundling process is more robust against the lack of coordination between molecular motors and the inability of the bacterium to control the individual trajectory of each filament.

Our results bring a new perspective on the ability of peritrichous bacteria to passively form coherent, tangle-free bundles of flagella that can be continuously actuated during a run

and easily taken apart during the tumble. At one extreme, we know that straight flagella could not intertwine, but they would also not be able to propel the cell forward in a viscous fluid. It appears that the polymorphic forms most commonly adopted by bacterial flagella are sufficiently coiled to be efficient propellers [197] but also sufficiently slender to avoid tangling.

This chapter is a reprint of Tătulea-Codrean, M. & Lauga, E. (2020) *Sci. Rep.* **10**, 8406. The dissertation author was the primary investigator and author of this paper. Modifications were made to the text and figures to avoid overlap in content with the introduction, and to make the notation consistent with the rest of the dissertation.

## Appendix 4.A Calculation of cross-sectional shape

In this appendix, we determine the cross-sectional shape of the helical filament as it intersects the focal plane - see Fig. 4.3. For our analytical model we only consider perfect helices with constant helical amplitude,  $R$ , while tapering is handled numerically. As in the main manuscript, we parameterise the helical centreline by  $h$ , such that

$$\mathbf{r}(h) = r \cos\left(\frac{2\pi h}{p}\right) \mathbf{e}_1 - r \sin\left(\frac{2\pi h}{p}\right) \mathbf{e}_2 + h \mathbf{e}_3 + \frac{d}{2} \mathbf{e}_x. \quad (4.12)$$

Without loss of generality, we present the calculations for a left-handed helix with  $\sigma = -1$  and spin angle  $\chi = 0$ , so that  $\mathbf{e}'_1 = \mathbf{e}_1$  and  $\mathbf{e}'_2 = \mathbf{e}_2$ . Varying the spin angle does not change the cross-sectional shape of the filament in the focal plane.

The tangent vector to the centreline is

$$\hat{\mathbf{t}}(h) = -\sin \psi \sin\left(\frac{2\pi h}{p}\right) \mathbf{e}_1 - \sin \psi \cos\left(\frac{2\pi h}{p}\right) \mathbf{e}_2 + \cos \psi \mathbf{e}_3, \quad (4.13)$$

where  $\psi = \tan^{-1}(2\pi R/p)$  is the pitch angle of the helix. Similarly, we have the normal and the binormal vectors

$$\hat{\mathbf{n}}(h) = -\cos\left(\frac{2\pi h}{p}\right) \mathbf{e}_1 + \sin\left(\frac{2\pi h}{p}\right) \mathbf{e}_2, \quad (4.14)$$

$$\hat{\mathbf{b}}(h) = -\cos \psi \sin\left(\frac{2\pi h}{p}\right) \mathbf{e}_1 - \cos \psi \cos\left(\frac{2\pi h}{p}\right) \mathbf{e}_2 - \sin \psi \mathbf{e}_3. \quad (4.15)$$

Assuming that the filament has a circular cross-section of radius  $\varepsilon$ , the outside surface of the filament can be parameterised by two variables  $(h, \zeta)$  in the following way

$$\mathbf{r}_\varepsilon(h, \zeta) = \mathbf{r}(h) + \varepsilon (\cos \zeta \hat{\mathbf{n}}(h) + \sin \zeta \hat{\mathbf{b}}(h)). \quad (4.16)$$

The intersection between the filament surface and the focal plane will be given by the points that satisfy

$$\mathbf{r}_\varepsilon(h, \zeta) \cdot \mathbf{e}_2 = 0, \quad (4.17)$$

by construction of the focal plane. This can be rearranged into

$$(R - \varepsilon \cos \zeta) \sin\left(\frac{2\pi h}{p}\right) + \varepsilon \sin \zeta \cos \psi \cos\left(\frac{2\pi h}{p}\right) = -\frac{d}{2} \sin \phi. \quad (4.18)$$

Using double angle formulae, we can find the solution to the above equation as a one-parameter family of points  $s = h^*(\zeta)$  that satisfy

$$h^*(\zeta) = \frac{p}{2\pi} \left[ \sin^{-1} \left( \frac{-\frac{d}{2} \sin \phi}{\sqrt{(R - \varepsilon \cos \zeta)^2 + (\varepsilon \sin \zeta \cos \psi)^2}} \right) - \tan^{-1} \left( \frac{\varepsilon \sin \zeta \cos \psi}{R - \varepsilon \cos \zeta} \right) \right]. \quad (4.19)$$

Inverse trigonometric functions are multivalued, and the solutions correspond to different intersections between the helix and the focal plane. In this case, the inverse tangent must always be evaluated in an interval with positive cosine, since  $R - \varepsilon \cos \zeta > 0$  for all  $\zeta$ . There are two possible values for the inverse sine which correspond to the helix intersecting the focal plane twice per helical turn – once on the left of the helical axis and once on the right, see Fig. 4.3 (a). We continue our calculations with the branch of solutions where the inverse sine is evaluated in the interval  $(\pi/2, 3\pi/2)$ , because this describes the cross-sectional shape seen in Fig. 4.3 (c). The other branch of solutions would give the intersections of the helix with the focal plane on the other side of the helical axis, but these are not shown in Fig. 4.3 (c) because they are not important for the model.

With this in mind, we can Taylor expand Eq. (4.19) for  $\varepsilon \ll R$  to give

$$h^*(\zeta) = \frac{p}{2\pi} \left[ \pi + \phi' + \frac{\varepsilon}{r} \tan \phi' \cos \zeta - \frac{\varepsilon}{r} \cos \psi \sin \zeta + \mathcal{O} \left( \left( \frac{\varepsilon}{r} \right)^2 \right) \right], \quad (4.20)$$

where we have used the notation  $\phi' = \sin^{-1}(d \sin \phi / 2R)$  from Eq. (4.7).

The outline of the filament in the focal plane is simply the locus of points  $\mathbf{r}_\varepsilon(h^*(\zeta), \zeta)$ . We begin by computing this shape in terms of coordinates along the vectors  $\{\mathbf{e}_1, \mathbf{e}_3\}$  which span the focal plane and are perpendicular and, respectively, parallel to the helical axis. Using Eqs. (4.12)-(4.16) and the orthonormality of the basis  $\{\mathbf{e}_1, \mathbf{e}_2, \mathbf{e}_3\}$  we deduce that

$$\mathbf{r}(h^*(\zeta), \zeta) \cdot \mathbf{e}_1 = (R - \varepsilon \cos \zeta) \cos \left( \frac{2\pi h^*}{p} \right) - \varepsilon \cos \psi \sin \zeta \sin \left( \frac{2\pi h^*}{p} \right), \quad (4.21)$$

$$\mathbf{r}(h^*(\zeta), \zeta) \cdot \mathbf{e}_3 = h^*(\zeta) - \varepsilon \sin \psi \sin \zeta. \quad (4.22)$$

Substituting the approximate expression for  $h^*(\zeta)$  from Eq. (4.20), we get that

$$\mathbf{r}(h^*(\zeta), \zeta) \cdot \mathbf{e}_1 \approx -R \cos \phi' + \frac{\varepsilon}{\cos \phi'} \cos \zeta, \quad (4.23)$$

$$\mathbf{r}(h^*(\zeta), \zeta) \cdot \mathbf{e}_3 \approx \frac{p(\phi' + \pi)}{2\pi} - \frac{\varepsilon}{\sin \psi} \sin \zeta + \frac{\varepsilon \tan \phi'}{\tan \psi} \cos \zeta. \quad (4.24)$$

The first term in each equation represents the leading-order position of the centreline, while the other terms are an approximation to first order in  $\varepsilon/r$  of the cross-sectional shape of the filament in the focal plane. After some lengthy algebra, we can manipulate the first-order terms into the form

$$\varepsilon \cos(\zeta - \zeta_0) \begin{pmatrix} \cos \eta \\ -\sin \eta \end{pmatrix} - \frac{\varepsilon}{\sin \psi \cos \phi'} \sin(\zeta - \zeta_0) \begin{pmatrix} \sin \eta \\ \cos \eta \end{pmatrix}, \quad (4.25)$$

where we have introduced the simplifying notation

$$\zeta_0 = \cot^{-1}(\cot \phi' \cos \psi), \quad (4.26)$$

$$\eta = \tan^{-1}(\sin \phi' \tan \psi). \quad (4.27)$$

By writing the first-order terms in this form, we can clearly see that the parameter  $\zeta$  traces out an ellipse with principal axes parallel to the two column vectors appearing in Eq. (4.25). Therefore, the right-hand side of Eqs. (4.23)-(4.24) is an exact parameterisation of an ellipse centred at  $-R \cos \phi' \mathbf{e}_1 + p(\phi' + \pi)/2\pi \mathbf{e}_3$  with minor axis length,  $2\alpha$ , and major axis length,  $2\beta$ , given by

$$\alpha = \varepsilon, \quad \beta = \frac{\varepsilon}{\sin \psi \cos \phi'}. \quad (4.28)$$

The major axis of the ellipse is inclined at an angle  $\eta$  to the helical axis, as it is parallel to the vector  $\sin \eta \mathbf{e}_1 + \cos \eta \mathbf{e}_3$  and  $\mathbf{e}_3$  is the direction of the helical axis, as seen in Fig. 4.7 (a). Using Eqs. (4.13) and (4.20), we can deduce that the major axis is approximately parallel to  $(\mathbf{I} - \mathbf{e}_2 \mathbf{e}_2) \cdot \hat{\mathbf{t}}(h^*)$ . Therefore, the cross-sectional shape of the helical filament is stretched out along the projection of the vector tangent to the centreline onto the focal plane. This is intuitively what we expect.

Next, we compute the distance (in the focal plane) between the filament centreline and the  $z$ -axis, denoted  $\varepsilon'(\theta, \phi)$ . We need to consider the outline of the filament in coordinates along the vectors  $\{\mathbf{e}_2 \wedge \mathbf{e}_z, \mathbf{e}_z\}$  which span the focal plane. To a first-order approximation this will be an ellipse with minor axis length,  $2\alpha$ , and major axis length,  $2\beta$ , which is inclined at an angle  $\theta + \eta$  to the  $z$ -axis. This is because the major axis of the ellipse makes an angle  $\eta$  with the helical axis, which makes an angle  $\theta$  with the  $z$ -axis, as seen in Fig. 4.7 (b).

Consider the general problem of finding the horizontal extremes of an ellipse with minor axis length,  $2\alpha$ , and major axis length,  $2\beta$ , inclined at an angle  $\theta + \eta$  to the vertical. In Cartesian coordinates  $(X, Y)$  relative to the centre of the ellipse, where the  $Y$ -axis is the

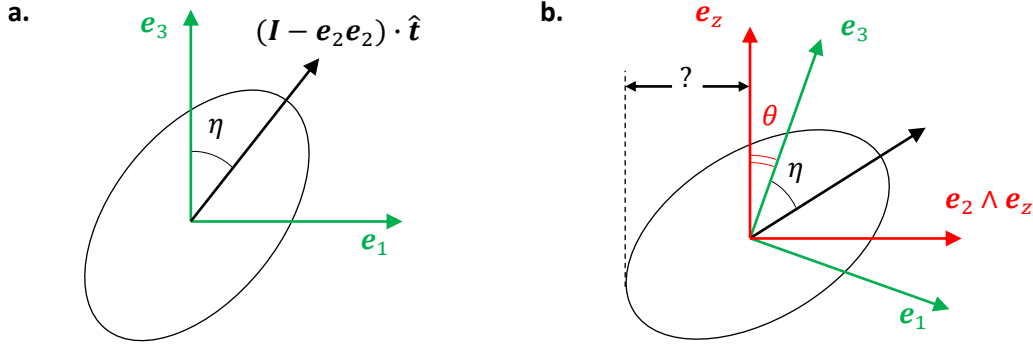


Fig. 4.7 To a first-order approximation in  $\varepsilon/R$ , the cross-sectional shape of the helix in the focal plane is an ellipse. (a) The major axis of the ellipse is parallel to the projection on the focal plane of the tangent vector to the helical centreline. (b) The major axis is inclined at an angle  $\eta$  to the helical axis,  $\mathbf{e}_3$ , which is in turn inclined at an angle  $\theta$  to the vertical,  $\mathbf{e}_z$ . We want to determine the horizontal distance between the extremes of the ellipse and the  $z$ -axis.

vertical, the ellipse is described parametrically by

$$\begin{pmatrix} X(\zeta) \\ Y(\zeta) \end{pmatrix} = a \cos \zeta \begin{pmatrix} \cos(\theta + \eta) \\ -\sin(\theta + \eta) \end{pmatrix} + b \sin \zeta \begin{pmatrix} \sin(\theta + \eta) \\ \cos(\theta + \eta) \end{pmatrix}. \quad (4.29)$$

The horizontal extreme points on the ellipse are the turning points of  $X(\zeta)$ , so we consider

$$\frac{dX}{d\zeta} = -\alpha \sin \zeta \cos(\theta + \eta) + \beta \cos \zeta \sin(\theta + \eta) = 0, \quad (4.30)$$

which is solved by  $\zeta^*$  that satisfies

$$\sin \zeta^* = \frac{\beta \sin(\theta + \eta)}{\sqrt{\alpha^2 \cos^2(\theta + \eta) + \beta^2 \sin^2(\theta + \eta)}}, \quad (4.31)$$

$$\cos \zeta^* = \frac{\alpha \cos(\theta + \eta)}{\sqrt{\alpha^2 \cos^2(\theta + \eta) + \alpha^2 \sin^2(\theta + \eta)}}. \quad (4.32)$$

Therefore, the horizontal extremes of the ellipse are at a distance

$$X(\zeta^*) = \sqrt{a^2 \cos^2 \beta + b^2 \sin^2 \beta} \quad (4.33)$$

from the vertical.

Using Eqs. (4.28) and (4.27) to substitute our values for  $\alpha$  and  $\beta$ , we deduce that

$$\varepsilon'(\theta, \phi) = \varepsilon \sqrt{\cos^2(\theta + \tan^{-1}(\sin \phi' \tan \psi)) + \frac{\sin^2(\theta + \tan^{-1}(\sin \phi' \tan \psi))}{(\sin \psi \cos \phi')^2}}. \quad (4.34)$$

Finally, if we write the denominator of the second term as  $\sin^2(\sin^{-1}(\sin \psi \cos \phi'))$ , we can simplify the expression for  $\varepsilon'(\theta, \phi)$  to the form given in Eq. (4.8),

$$\varepsilon'(\theta, \phi) = \varepsilon \sqrt{1 + \frac{\sin^2(\theta + \tan^{-1}(\sin \phi' \tan \psi))}{\tan^2(\sin^{-1}(\sin \psi \cos \phi'))}}, \quad (4.35)$$

where we remind the reader that  $\phi' = \sin^{-1}(d \sin \phi / 2r)$  is an implicit function of  $\phi$ .

## Appendix 4.B Sources of experimental data

Tables 4.1 and 4.2 contain a systematic collection of sources from which we gathered the values of our input parameters: the helical geometry ( $p, R$ ) of polymorphic shapes, the cell body size ( $l, w$ ), the length,  $L$ , and thickness,  $\varepsilon$ , of filaments. Our theoretical model for tangling takes these inputs and produces an estimate for the critical number of flagella above which the bacterium may run the risk of tangling. This output must likewise be compared with the number of flagella observed experimentally, also given in Tables 4.1 and 4.2.

We selected strains for which the data could be gathered from as few sources as possible. For each strain we strived to compile a coherent database of compatible sources, preferably coming from the same research group in the same time period. From papers investigating the growth and shape of bacterial flagellar filaments it was possible to gather comprehensive data about the helical geometry of the polymorphic shapes, whereas papers focusing on the speed of locomotion or tumbling frequency often quoted the size of the cell body, and the number and length of flagella.

For *S. typhimurium* we used Ref. [92] for the pitch and radius of most polymorphic forms because it had the closest links with Ref. [91], from which we took the distributions of filament length and number of flagella. However, this reference did not contain measurements for the semicoiled form, so we tested our theory using measurements from three other experimental groups [59, 88, 106]. There was no significant difference between the results obtained with the three different sets of data.

For the dimensions of the cell body, Ref. [93] only provides measurements for the cell length of *S. typhimurium*, but in conjunction with Ref. [54] we were able to make a reasonable estimate for the cell width.

Because the imaging techniques required for measuring the thickness of slender flagellar filaments are fundamentally different from the imaging techniques for visualising the entire ensemble of bacterial cell bodies and flagella, it was necessary to use different sources for the filament radius, which were separate from the rest of the database. Ref. [222] only provides measurements of the flagellar filament radius for *S. typhimurium* and *B. subtilis*. However, according to Ref. [3], the flagellin in the composition of *E. coli* flagella is very similar in size to that of *S. typhimurium* flagella (497 vs. 489 amino acids) so we assume that the filament radius of the two bacterial species are the same.

Parameter	Symbol	<i>E. coli</i> AW405		<i>E. coli</i> HCB1		<i>E. coli</i> HCB1737	
		value	source	value	source	source	value
Helical diameter	$2R$						
normal		0.35	[40]	0.35	[40]	0.35	[40]
semicoiled		0.50	[209]	0.50	[209]	0.50	[209]
curly I		0.25	[209]	0.25	[209]	0.25	[209]
curly II		0.16	[209]	0.16	[209]	0.16	[209]
Helical pitch	$p$						
normal		2.3	[40]	2.3	[40]	2.3	[40]
semicoiled		1.1	[209]	1.1	[209]	1.1	[209]
curly I		1.0	[209]	1.0	[209]	1.0	[209]
curly II		0.9	[209]	0.9	[209]	0.9	[209]
Filament radius	$\varepsilon$	0.012	[222]	0.012	[222]	0.012	[222]
Filament length	$L$	$7.1 \pm 1.8$	[40]	$5.3 \pm 0.1$	[128]	$6.3 \pm 1.8$	[208]
Cell body length	$l$	$2.5 \pm 0.6$	[40]	$1.7 \pm 0.1$	[128]	$2.0 \pm 0.5$	[208]
Cell body width	$w$	$0.88 \pm 0.09$	[40]	$0.8 \pm 0.1$	[128]	$0.7 \pm 0.1$	[208]
Number of flagella	$N_f$	$3.37 \pm 1.59$	[40]	4	[128]	$3.3. \pm 0.9$	[208]

Table 4.1 Geometric parameters used in our theoretical model for tangling, with references to experimental measurements on *E. coli*. All parameters are given in units of  $\mu\text{m}$ , except for the number of flagella.

Parameter	Symbol	<i>S. typhimurium</i> TM2		<i>B. subtilis</i> DK2002	
		value	source	value	source
Helical diameter	$2R$				
normal		0.50	[92]	2.06	[59]
semicoiled		0.52	[88]	–	–
curly I		0.36	[92]	0.42	[59]
curly II		0.16	[92]	–	–
Helical pitch	$p$				
normal		2.2	[92]	0.91	[59]
semicoiled		1.24	[88]	–	–
curly I		1.1	[92]	0.18	[59]
curly II		0.92	[92]	–	–
Filament radius	$\epsilon$	0.012	[222]	0.006	[222]
Filament length	$L$	(†)	[91]	$9.0 \pm 2.0$	[208]
Cell body length	$l$	$3.8 \pm 0.9$	[93]	$5.0 \pm 1.7$	[208]
Cell body width	$w$	$1.2 \pm 0.15$	est.	$1.2 \pm 0.1$	[208]
Number of flagella	$N_f$	$6.2 \pm 1.6$	[91]	$5.8 \pm 2.1$	[208]

Table 4.2 Geometric parameters used in our theoretical model for tangling, with references to experimental measurements on *S. typhimurium* and *B. subtilis*. All parameters are given in units of  $\mu\text{m}$ , except for the number of flagella. (†) We extracted the full distribution of filament lengths from the histograms published in Iino [91].



# Chapter 5

## Geometrical constraints on the bundling of helical filaments

In order for flagellar filaments to rotate continuously as they form a bundle, without colliding into each other, the bundle must be sufficiently synchronised. In this chapter, we investigate the amount of synchronisation required by the helical geometry of flagellar filaments, using a kinematic model of bundling with rotational symmetry around the axis of the bundle. Finally, we apply our geometrical results to two questions relevant to the bundling of bacterial flagella: the critical rate of synchronisation in a bundle that is converging due to hydrodynamic effects, and the critical torque difference between motors in a bundle that has reached an equilibrium state.

### 5.1 Motivation

When they come together to form a bundle, bacterial flagellar filaments rotate continuously under the actuation of independent motors. As the distance between the filaments decreases, there is an increased possibility of collisions due to the rotation of the filaments. One way to ensure a smooth operation of the bundle is for the filaments to synchronise with each other. This could be induced by direct hydrodynamic interactions between the filaments [175], or due to the filaments being coupled to the motion of the cell body. The latter mechanism has not been demonstrated for bacteria, but there is evidence of this effect contributing to flagellar synchronisation in swimming algae [62]. In this chapter, we do not consider the dynamics that lead to synchronisation, but focus on the requirements imposed by the helical geometry of the filaments.

For parallel filaments, the level of synchronisation imposed by geometrical constraints is known from the original study by Macnab [138]. The result of Eq. (2.13) can be reinterpreted as an expression for the critical phase difference,

$$\Delta\phi_c = 2 \sin^{-1} \left( \frac{d}{2R} \right). \quad (5.1)$$

When  $\Delta\phi$  reaches the critical value, the centrelines of the two filaments intersect. For very slender filaments such as bacterial flagella, this is a good approximation for the phase difference at which two rotating filaments collide with each other.

Here, we wish to extend Eq. (5.1) to filaments that are inclined with respect to each other, like the flagellar filaments forming a bundle. Theoretical studies have suggested that the earliest stage of bundling is enabled by an elasto-hydrodynamic instability of the hook [180], after which the dominant hydrodynamic effect comes from the flow induced by the motion of the cell body, to be replaced by direct hydrodynamic interactions between the filaments only in the final stages of bundling [23]. Motivated by these observations, we consider a minimal kinematic model of bundling, where the filaments get dragged behind the cell body at the same rate from all sides. As in the previous chapter on the geometrical constraints for tangling, the kinematic model does not take into account the hydrodynamic forces and torques acting on the filaments. We only consider the constraints imposed by the helical shape of flagellar filaments as the filaments move through a sequence of geometries of motion consistent with the general understanding of bundling from experiments and theory.

## 5.2 Geometrical modelling

To keep the problem analytically tractable, we consider a system with rotational symmetry around the bundle, where the axes of  $N_f$  helical filaments are anchored to fixed and evenly spaced out points around a circle. The filaments join the bundle at the same rate,  $\dot{\theta}$ .

### 5.2.1 Kinematic model of bundling

The setup depicted in Fig. 5.1 consists of  $N_f$  helical filaments, labelled  $k = 1, \dots, N_f$ , whose axes are anchored at regularly spaced points around a circle,

$$\mathbf{x}_k = R_b \cos \left( \frac{2\pi k}{N_f} \right) \mathbf{e}_x + R_b \sin \left( \frac{2\pi k}{N_f} \right) \mathbf{e}_y. \quad (5.2)$$

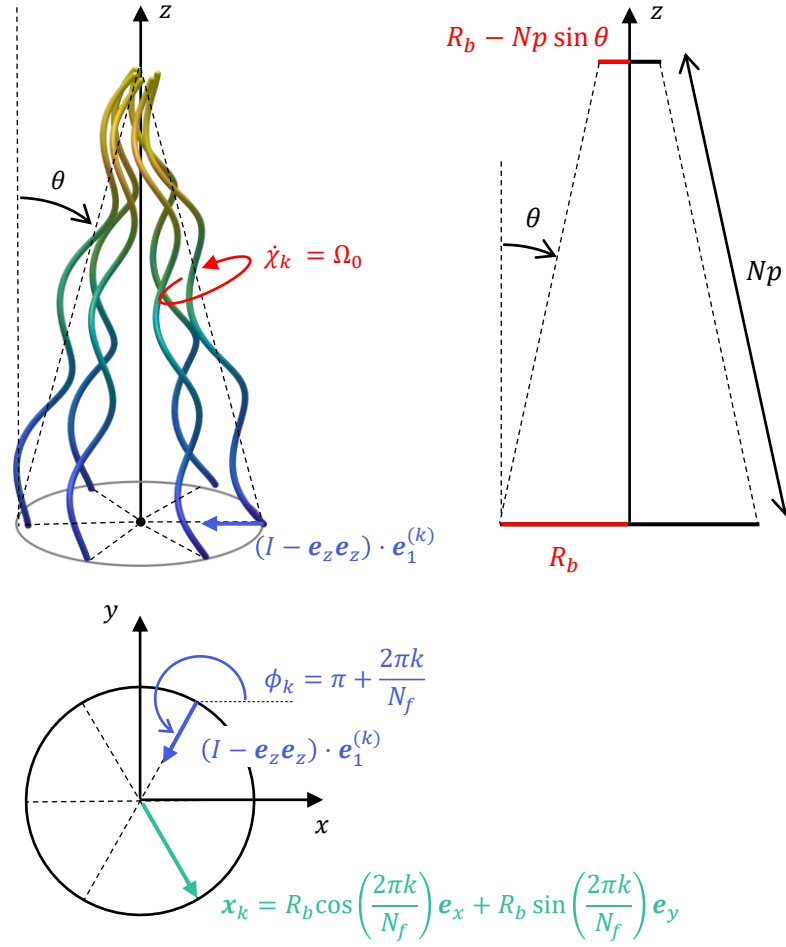


Fig. 5.1 Minimal model of bundling with rotational symmetry about the central axis of the bundle (here, the  $z$ -axis). The axes of the helical filaments are anchored around a circular base of radius,  $R_b$ , at regularly spaced intervals of angle,  $2\pi/N_f$ . All the filaments are tilted directly towards the central axis of the bundle by the same angle,  $\theta$ . The colour gradient indicates the proximity of the filaments to each other.

The filaments are tilted directly towards the central axis of the bundle, so that the azimuthal angle,  $\phi_k$ , for each filament is given by

$$\phi_k = \pi + \frac{2\pi k}{N_f}, \quad (5.3)$$

and the tilt angle is positive,  $\theta_k = \theta \geq 0$ . The centreline of the helical filament, starting from the anchoring point  $\mathbf{x}_k$ , is then given by

$$\mathbf{r}^{(k)}(\xi) = \mathbf{x}_k + R \cos(\xi) \mathbf{e}_1^{(k)} + R \sin(\xi) \mathbf{e}_2^{(k)} + \frac{p\xi}{2\pi} \mathbf{e}_3^{(k)}, \quad (5.4)$$

according to the notation introduced in §2.1.1. Note that the filaments are implicitly right-handed ( $\sigma = +1$ ). A bundle with left-handed filaments is simply the mirror image of the problem we consider here, and the final results are identical.

The modelling assumptions for the kinematics of the filaments are that

$$\dot{\theta}_k = \dot{\theta} > 0, \quad (5.5)$$

$$\chi_k(t) = \Omega_0 t + \Delta\chi_k, \quad (5.6)$$

meaning that the filaments join the bundle at the same unknown rate,  $\dot{\theta}$ , and they rotate about their own axes at a constant angular velocity  $\Omega_0$ ,

We are interested in bundles that converge towards the central axis, so with  $\theta$  being positive. Furthermore, we require that the tilt angle be bounded above by the value

$$\theta < \theta_{\max} = \sin^{-1} \left( \frac{R_b}{Np} \right), \quad (5.7)$$

such that the axes of the helices do not cross over each other. If the axes cross, the helices always collide even for zero phase difference. The quantity we want to compute is the critical phase difference between the filaments such that they can rotate continuously without collisions.

### 5.2.2 Intersections between two helices

The condition that the bundle operates smoothly, without collisions, is to a good approximation the same as requiring that the centrelines of any two filaments do not intersect. Hence, we solve for the intersection of two helices separated by an arbitrary angle  $2\alpha$  around the circular base of the bundle. This setup is shown in Fig. 5.2 (a). Without loss of generality, we choose the  $x$ -axis to be the perpendicular bisector of the line connecting the two anchoring points, such that

$$\mathbf{x}_{\pm} = R_b (\cos \alpha \mathbf{e}_x \pm \sin \alpha \mathbf{e}_y), \quad (5.8)$$

and the azimuthal angles are

$$\phi_{\pm} = \pi \pm \alpha. \quad (5.9)$$

We also choose the time  $t = 0$  such that the angles of rotation about the filament axis are

$$\chi_{\pm}(t) = \Omega_0 t \pm \beta. \quad (5.10)$$

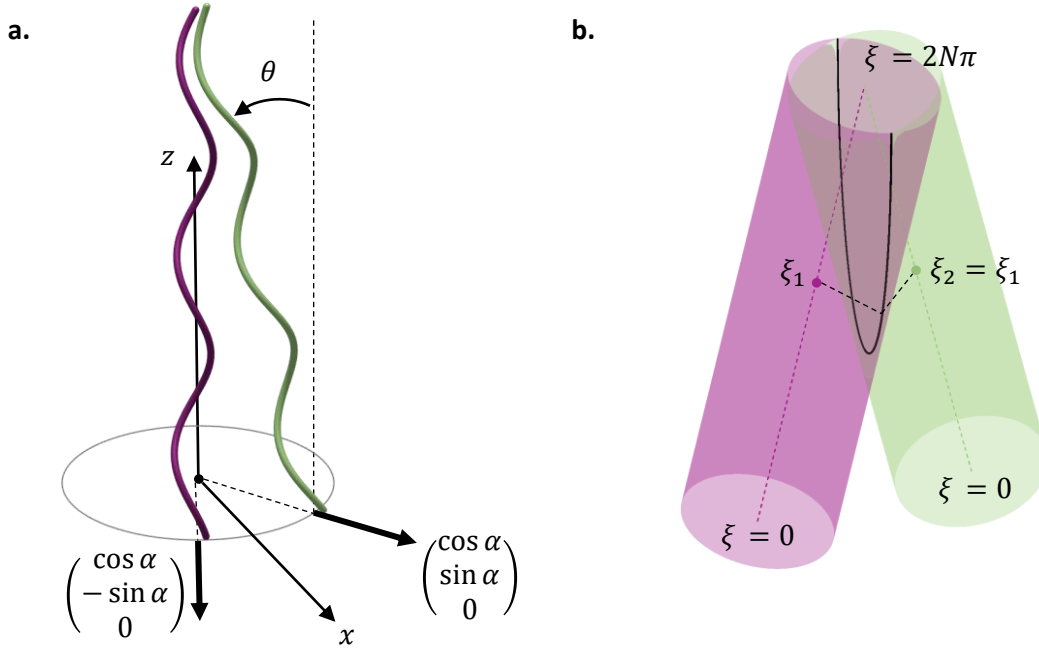


Fig. 5.2 Setup for calculating the intersections between two inclined helices. (a) The  $x$  axis is chosen as the bisector of the arc connecting the two anchoring points, to exploit symmetry in the calculations. (b) The domains of revolution of the two helices are cylinders which intersect along a family of points with equal coordinates along the axes of the two helices (for  $\theta < \theta_{\max}$ ).

Hence, the centrelines of the two filaments are given by

$$\mathbf{r}^{(\pm)}(\xi, t) = R_b (\cos \alpha \mathbf{e}_x \pm \sin \alpha \mathbf{e}_y) + R \cos(\xi) \mathbf{e}_1(\phi_{\pm}, \theta(t), \chi_{\pm}(t)) + R \sin(\xi) \mathbf{e}_2(\phi_{\pm}, \chi_{\pm}(t)) + \frac{p\xi}{2\pi} \mathbf{e}_3(\phi_{\pm}, \theta(t), \chi_{\pm}(t)), \quad (5.11)$$

with body-frame unit vectors  $\{\mathbf{e}_1, \mathbf{e}_2, \mathbf{e}_3\}$  defined in the Introduction §2.1.1.

We look for intersections between the two filaments by solving the equation  $\mathbf{r}^{(+)}(\xi_1, t) = \mathbf{r}^{(-)}(\xi_2, t)$  for the time-dependent coordinates  $\xi_{1,2}(t)$  along the axes of the filaments. The locus of points covered by a rotating helical is a cylinders. Hence, a necessary condition for  $\mathbf{r}^{(+)}(\xi_1, t) = \mathbf{r}^{(-)}(\xi_2, t)$  is that the points lie on the intersection of the two domains of revolution of the helices, shown in Fig. 5.2 (b). For  $\theta < \theta_{\max}$ , the points of intersection have the same coordinate,  $\xi_1 = \xi_2$ , along the axes of the two cylinders. For  $\theta > \theta_{\max}$ , there is a second family of solutions where  $\xi_1 \neq \xi_2$ , but we do not consider this regime in which the rotating filaments collide even for zero phase difference. Hence, we need to solve the equation  $\mathbf{r}^{(+)}(\xi, t) = \mathbf{r}^{(-)}(\xi, t)$  for the point of intersection  $\xi(t)$ .

Using Eqs. (2.6)-(2.8) to determine the  $z$  components of the units vectors  $\{\mathbf{e}_1, \mathbf{e}_2, \mathbf{e}_3\}$ , we derive the condition for  $\mathbf{e}_z \cdot \mathbf{r}^{(+)}(\xi, t) = \mathbf{e}_z \cdot \mathbf{r}^{(-)}(\xi, t)$  to be

$$-R \sin \theta \cos(\xi + \chi_+) + \frac{p \cos \theta}{2\pi} \xi = -R \sin \theta \cos(\xi + \chi_-) + \frac{p \cos \theta}{2\pi} \xi, \quad (5.12)$$

from which we deduce that

$$\cos(\xi + \chi_+) = \cos(\xi + \chi_-), \quad \sin(\xi + \chi_+) = -\sin(\xi + \chi_-). \quad (5.13)$$

Note that this automatically satisfies the matching condition for the  $x$  components,  $\mathbf{e}_x \cdot \mathbf{r}^{(+)}(\xi, t) = \mathbf{e}_x \cdot \mathbf{r}^{(-)}(\xi, t)$ , since

$$\begin{aligned} R \cos \theta \cos \phi_+ \cos(\xi + \chi_+) - R \sin \phi_+ \sin(\xi + \chi_+) + \frac{p \sin \theta}{2\pi} \cos \phi_+ \xi = \\ R \cos \theta \cos \phi_+ \cos(\xi + \chi_-) + R \sin \phi_+ \sin(\xi + \chi_-) + \frac{p \sin \theta}{2\pi} \cos \phi_+ \xi. \end{aligned} \quad (5.14)$$

Furthermore, from Eq. (5.13), we deduce that

$$\sin(\xi + \Omega_0 t) = 0, \quad \cos(\xi + \Omega_0 t) = \pm 1. \quad (5.15)$$

The choice of sign correspond to the two branches seen in Fig. 5.2 (b), where the two cylinders intersect symmetrically on either side of the plane spanned by their axes,  $\mathbf{e}_3^{(+)}$  and  $\mathbf{e}_3^{(-)}$ .

Without loss of generality, we continue our analysis with the branch  $\cos(\xi + \Omega_0 t) = 1$  which, using the definition of  $\chi_{\pm}$  from Eq. (5.10), leads to

$$\frac{1}{2} (\cos(\xi + \chi_+) + \cos(\xi + \chi_-)) = \cos \beta, \quad (5.16)$$

$$\frac{1}{2} (\sin(\xi + \chi_+) - \sin(\xi + \chi_-)) = \sin \beta. \quad (5.17)$$

Using Eqs. (2.6)-(2.8) to determine the  $y$  components of the units vectors  $\{\mathbf{e}_1, \mathbf{e}_2, \mathbf{e}_3\}$ , we derive the condition for  $\mathbf{e}_y \cdot \mathbf{r}^{(+)}(\xi, t) = \mathbf{e}_y \cdot \mathbf{r}^{(-)}(\xi, t)$  to be

$$\begin{aligned} R_b \sin \alpha + R \cos \theta \sin(\phi_+) \cos(\xi + \chi_+) + R \cos(\phi_+) \sin(\xi + \chi_+) + \frac{p \xi}{2\pi} \sin \theta \sin(\phi_+) = \\ -R_b \sin \alpha - R \cos \theta \sin(\phi_+) \cos(\xi + \chi_-) + R \cos(\phi_+) \sin(\xi + \chi_-) - \frac{p \xi}{2\pi} \sin \theta \sin(\phi_+). \end{aligned} \quad (5.18)$$

By switching the notation to the height along the filament axis,  $h(t) = p\xi(t)/2\pi$ , and using Eqs. (5.9),(5.16),(5.17), we simplify the matching condition for the  $y$  components into

$$\sin \alpha (R_b - h(t) \sin \theta) = R \cos \theta \sin \alpha \cos \beta + R \cos \alpha \sin \beta, \quad (5.19)$$

which can be put in the form

$$\frac{\sin \alpha (R_b - h(t) \sin \theta)}{\sqrt{\cos^2 \alpha + \cos^2 \theta \sin^2 \alpha}} = R \sin (\beta + \tan^{-1} (\cos \theta \tan \alpha)). \quad (5.20)$$

The inverse tangent in the previous equation is to be taken in the interval  $(0, \pi/2)$ . We invert this expression to determine the angle  $\beta$  representing the fixed difference in rotation angles between the two filaments,

$$\beta = -\tan^{-1} (\cos \theta \tan \alpha) + \sin^{-1} \left( \frac{\tan \alpha (R_b - h(t) \sin \theta)}{R\sqrt{1 + \cos^2 \theta \tan^2 \alpha}} \right). \quad (5.21)$$

The inverse sine is to be taken in the interval  $(0, \pi/2)$ . If the above equation has a solution for time  $t$ , then the filaments collide at time  $t$  and height  $h(t)$  along the axis of the filament.

### 5.2.3 Critical phase difference

In the Introduction §2.1.1, we defined the absolute phase difference between two non-parallel filaments as  $\Delta\Phi = \Delta\phi + \Delta\chi = 2\alpha + 2\beta$ . Using our previous expression for  $\beta$ , this becomes

$$\Delta\Phi = 2\alpha - 2 \tan^{-1} (\cos \theta \tan \alpha) + 2 \sin^{-1} \left( \frac{\tan \alpha (R_b - h(t) \sin \theta)}{R\sqrt{1 + \cos^2 \theta \tan^2 \alpha}} \right). \quad (5.22)$$

To ensure that there are no collisions inside the bundle, there can be no solutions for any time  $t$ . Therefore,  $\Delta\Phi$  must be smaller than the minimal value of the right-hand side of Eq. (5.22) for all time. Since  $\theta > 0$ , the right-hand side achieves its minimal value when  $h(t) = h_{\max} = Np$ , the total height of the filament axis. As expected, the dominant geometrical constraint comes from the top ends of the filaments (i.e. those furthest away from the anchoring points,  $\mathbf{x}_{\pm}$ ), which are closer to each other than any other points along the filaments. Hence, we derive the critical phase difference

$$\Delta\Phi_c(\theta, \alpha) = 2\alpha - 2 \tan^{-1} (\cos \theta \tan \alpha) + 2 \sin^{-1} \left( \frac{\tan \alpha (R_b - Np \sin \theta)}{R\sqrt{1 + \cos^2 \theta \tan^2 \alpha}} \right), \quad (5.23)$$

which depends explicitly on the azimuthal spacing around the bundle,  $2\alpha$ , and the vertical tilt of the filaments,  $\theta$ .

The result of Eq. (5.23) is a generalisation of the critical condition identified by Macnab [138] for two parallel helices. In the limit  $\theta = 0$ , we recover

$$\Delta\Phi_c(0, \alpha) = 2 \sin^{-1} \left( \frac{R_b \sin \alpha}{R} \right) \quad (5.24)$$

which is equivalent to Eq. (5.1) since the length of the chord connecting the two anchoring points is  $d = 2R_b \sin \alpha$ .

### 5.3 Application to bacterial flagellar bundling

We now consider the implications of the geometrical constraint, Eq. (5.23), for the bundling of bacterial flagellar filaments. In Fig. 5.3 (a), we show the typical length scales for a bundle of bacterial flagellar filaments. In particular, the helical amplitude,  $R$ , corresponds to the normal polymorphic shape, and the diameter at the base of the bundle,  $2R_b$ , represents the width of a bacterial cell body. The results presented in Figs. 5.3, 5.4 and 5.5 are all based on these dimensional parameters.

#### 5.3.1 Dominant geometrical constraint in a circular bundle

Since  $Np \gg R_b$  in a typical bundle of normal-shape filaments, the tilt angle  $\theta < \theta_{\max} \ll 1$  is very small. Therefore, we expand the phase difference, Eq. (5.23), around  $\theta = 0$  to find

$$\Delta\Phi_c(\theta, \alpha) \sim 2 \sin^{-1} \left( \frac{R_b}{R} \left( 1 - \frac{\theta}{\theta_{\max}} \right) \sin \alpha \right) + \mathcal{O}(\theta^2). \quad (5.25)$$

The critical phase difference from Eq. (5.25) grows sub-linearly with the azimuthal spacing,  $\alpha$ , if the filaments are tilted sufficiently far away from the axis of the bundle,

$$\theta > \left( 1 - \frac{R}{R_b} \right) \theta_{\max} = \theta^*. \quad (5.26)$$

This can be seen in Fig. 5.3 (b) as well. The two regimes,  $0 < \theta < \theta^*$  and  $\theta > \theta^*$ , lead to different dominant constraints on the synchronisation of filaments placed in a circular bundle.

When  $0 < \theta < \theta^*$ , the diameter at the top of the bundle,  $2R_b - Np \sin \theta$ , is greater than the diameter of the helical filaments,  $2R$ , which means that the locus of points visited by any given filament does not overlap with the locus of the filament directly across from it in the circular bundle. In this regime, a sufficient condition for the bundle to rotate smoothly,

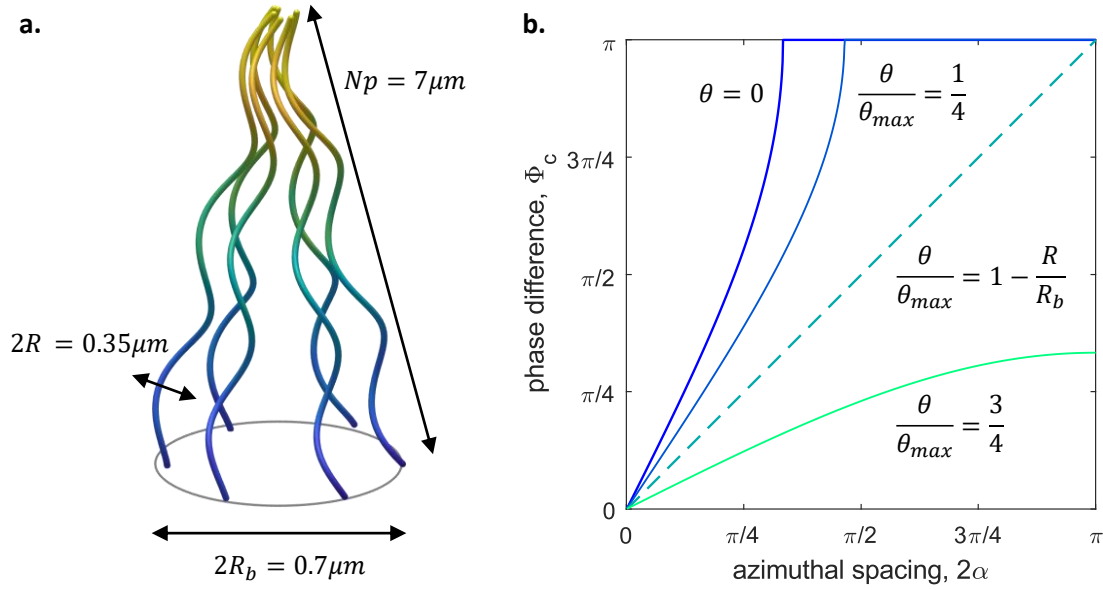


Fig. 5.3 Application of geometrical results to a circular bundle of flagellar filaments. (a) Typical dimensions of a bundle of normal-shaped flagellar filaments. (b) Critical phase difference as a function of the angular spacing between the filaments, for various degrees of convergence of the bundle.

without collisions, is that each filament keeps within the required phase difference to its nearest neighbour.

When  $\theta > \theta^*$ , the filaments on opposite sides of the circular bundles have overlapping domains of rotation, since the diameter at the top of the bundle is smaller than the diameter of the helical filaments. Indeed, the domains of rotation overlap between any given pair of filaments. Since  $\Delta\Phi_c(\theta, \alpha)$  grows sub-linearly with the azimuthal spacing,  $\alpha$ , it is not sufficient for each filament to keep within a phase difference  $\Delta\Phi_c(\theta, \pi/N_f)$  from its nearest neighbour. After  $k$  steps around the circular bundle, there may be a phase difference  $k\Delta\Phi_c(\theta, \pi/N_f) > \Delta\Phi_c(\theta, k\pi/N_f)$ . In this regime, it is necessary for the filaments to maintain a critical phase difference to all the other filaments in the bundle, not just their nearest neighbour.

With this in mind, we define an effective critical phase difference between two adjacent filaments as

$$\Delta\Phi_{\text{eff}}(\theta, N_f) = \min_{1 \leq k \leq N_f - 1} \left\{ \frac{1}{k} \Delta\Phi_c \left( \theta, \frac{k\pi}{N_f} \right) \right\}, \quad (5.27)$$

which depends crucially on the number of filaments,  $N_f$ , and the tilt angle,  $\theta$ . The minimum is achieved for  $k = 1$  if  $0 < \theta < \theta^*$ , and for  $k = \lfloor N_f/2 \rfloor$  if  $\theta^* < \theta < \theta_{\text{max}}$ . If every pair of adjacent filaments has a phase difference smaller than  $\Delta\Phi_{\text{eff}}(\theta, N_f)$ , then the bundle operates smoothly for any  $0 < \theta < \theta_{\text{max}}$ . Therefore, Eq. (5.27) is a sufficient, but not

necessary condition for the bundle to operate smoothly, since the phase difference may be distributed unevenly around the bundle. In an average sense, however,  $\Delta\Phi_{\text{eff}}(\theta, N_f)$  is a reasonable measure of the level of synchronisation imposed by geometrical constraints. We now use the effective phase difference to gain insights about two aspects of flagellar bundling: the necessary rate of synchronisation of an evolving bundle, and the critical motor torque difference in a stationary bundle.

### 5.3.2 Constraints on the rate of synchronisation of a converging bundle

We consider a bundle with a fixed number of filaments,  $N_f$ , and an unknown bundling rate  $\dot{\theta}$  coming from the hydrodynamics of the bundle and the cell - see Fig. 5.4 (a). By taking a time derivative of the critical phase difference, Eq. (5.27), we can relate the rate of bundling,  $\dot{\theta}$ , and the rate of synchronisation imposed by geometry,  $-\Delta\dot{\Phi}_{\text{eff}}$ , through the expression

$$-\frac{d\Delta\Phi_{\text{eff}}}{dt} = -\frac{\partial\Delta\Phi_{\text{eff}}}{\partial\theta} \frac{d\theta}{dt}. \quad (5.28)$$

The partial derivative of  $\Delta\Phi_{\text{eff}}$  with respect to  $\theta$  does not have a simple expression, so we do not provide it here, but it can be calculated and its qualitative features can be seen in Fig. 5.4 (b).

The phase difference imposed by geometry decreases rapidly with  $\theta$  at first, when the domains of adjacent filaments start to overlap (the start of the curves for  $N_f = 2$  and  $N_f = 4$  filaments). Afterwards, the geometrical constraint varies more slowly, until we cross over into the regime  $\theta > \theta^*$  when the domains of rotation of all the filaments in the bundle overlap. This imposes an additionally strong constraint on the synchronisation of the bundle, which is noticeable in the discontinuity of the slope at  $\theta/\theta_{\text{max}} = 1 - R/R_b = 0.5$ . For larger tilt angles, the effective phase difference decreases more slowly and reaches zero with a linear slope inversely proportional to the number of filaments,

$$\Delta\Phi_{\text{eff}}(\theta, N_f) \approx \frac{4Np}{N_f R} (\theta_{\text{max}} - \theta), \quad (5.29)$$

near  $\theta = \theta_{\text{max}}$ . The limiting behaviour is indicated in Fig. 5.4 (b) only for  $N_f = 2, 8$  to avoid overcrowding the diagram.

### Outlook

From Fig. 5.4 (b), we gain a general understanding of how the geometry of the filaments imposes increasingly higher constraints on their synchronisation as the bundling progresses.

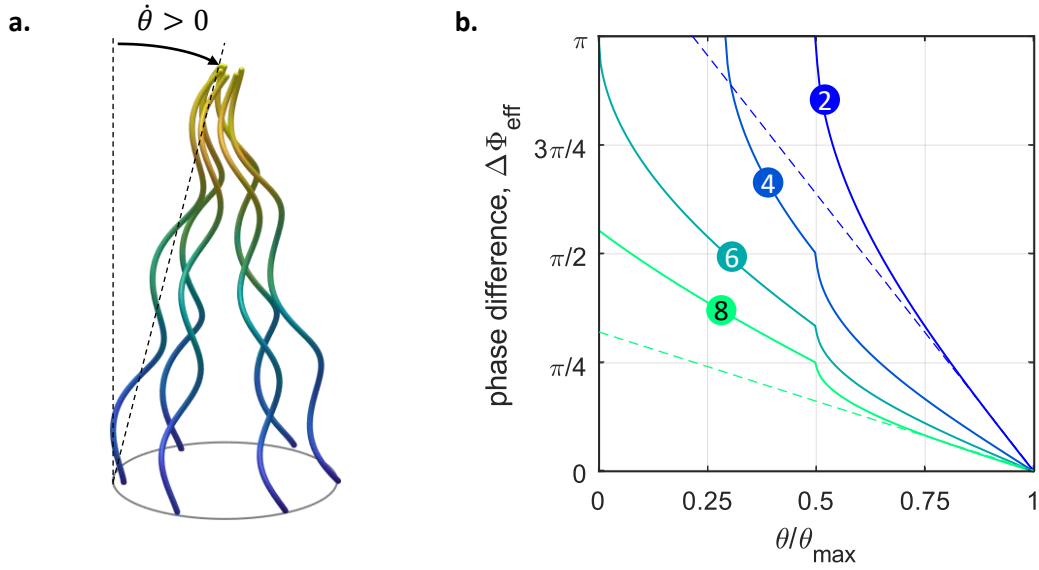


Fig. 5.4 Constraints imposed by geometry during the bundling process. (a) Sketch of a bundle converging at an unknown rate  $\dot{\theta}$  due to, for instance, hydrodynamics effects. (b) During the bundling process, the rate of change of  $\Delta\Phi_{\text{eff}}$  with respect to  $\theta$  determines the ratio between the bundling rate and the rate of synchronisation imposed by geometrical constraints. Solid lines are the result of Eq. (5.27), while the dashed lines are the result of Eq. (5.29). The number of filaments,  $N_f$ , is indicated on each line.

According to our kinematic model, all trajectories falling below  $\Delta\Phi = \Delta\Phi_{\text{eff}}(\theta, N_f)$  in the  $(\theta, \Delta\Phi)$  parameter space are permissible since, by definition, the effective phase difference is a sufficient condition to avoid collisions between the filaments. The exact trajectory  $(\theta(t), \Delta\Phi(t))$  in which the parameter space is traversed depends on the elasto-hydrodynamics of the hook and flagellar filaments and the flow around the cell body.

In principle, the geometrical results presented in this section can be combined with dynamical models for the rate of bundling,  $\dot{\theta}$ , and the rate of synchronisation,  $\Delta\dot{\Phi}$ , to determine the conditions under which the bundle operates smoothly, such as the maximum number of filaments (if there is one) for which the dynamics of the filaments are able to keep up with the constraints imposed by geometry as the bundling goes on.

### 5.3.3 Constraints on the motor torque difference in a stationary bundle

Another aspect worth considering is the fact that the motor torques driving the filaments vary due to biochemical noise - see Fig. 5.5 (a). As we discuss later in Chapter 7, hydrodynamically-coupled filaments driven at different torques tend to synchronise at a non-zero phase difference which depends on the magnitude of the torque difference, and the coupling between

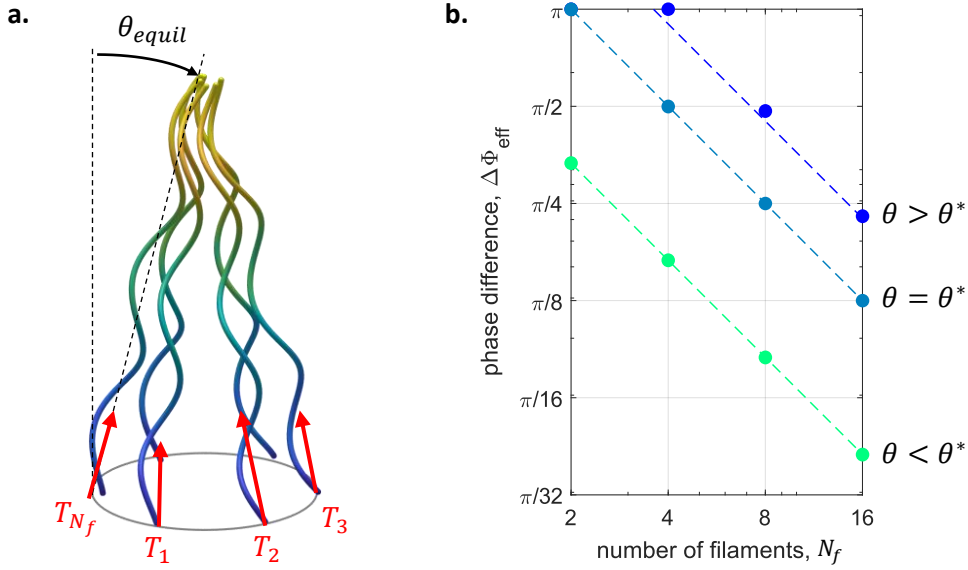


Fig. 5.5 Constraints imposed by geometry on a bundle in equilibrium. (a) Sketch of a stationary bundle ( $\dot{\theta} = 0$ ) in which the filaments are driven by variable torques applied to their axes. (b) The phase difference allowed by geometry (and hence the difference in torque magnitudes) decays like the inverse of the number of filaments. Filled circles are exact solutions from Eq. (5.27), while dashed lines are large  $N_f$  asymptotics from Eqs. (5.30)-(5.31).

filaments. This has been observed in numerical simulations of the hydrodynamic synchronization of rotating helical filaments [175, 177].

Using the effective phase difference,  $\Delta\Phi_{eff}(\theta, N_f)$ , from Eq. (5.27) as an indicator of the maximum torque difference compatible with geometrical constraints, we consider how these two quantities change with the number of filaments. We assume that the bundle has reached a steady configuration with  $\theta = \theta_{equil}$ , which could be due to a balance between hydrodynamic attraction and steric repulsion between the filaments, for instance.

We now determine the asymptotic behaviour of  $\Delta\Phi_{eff}(\theta, N_f)$  for a large number of filaments,  $N_f$ . In the regime  $0 < \theta < \theta^*$ , we expand  $\Delta\Phi_c(\theta, \alpha)$  from Eq. (5.23) near  $\alpha = \pi/N_f \ll 1$ , to obtain

$$\Delta\Phi_{eff}(\theta) \sim \frac{2\pi}{N_f} \left( 1 - \cos \theta + \frac{Np}{R} (\sin \theta_{max} - \sin \theta) \right), \quad (5.30)$$

as  $N_f \rightarrow \infty$ . Meanwhile, in the regime  $\theta^* < \theta < \theta_{max}$ , we expand  $\Delta\Phi_c(\theta, \alpha)$  near  $\alpha = \pi/2$ , to get

$$\Delta\Phi_{eff}(\theta) \sim \frac{4}{N_f} \sin^{-1} \left( \frac{Np(\sin \theta_{max} - \sin \theta)}{R \cos \theta} \right), \quad (5.31)$$

as  $N_f \rightarrow \infty$ . Importantly, the effective phase difference decays like the inverse of the number of filaments in both regimes.

### Outlook

The fast decay of the critical phase difference with number of filaments suggests that there may be a limit on the feasible number of filaments in a bundle, for a given amount of biochemical noise in the torques driving the rotation of the bundle. The geometrical results in this section can, in principle, be combined with electrostatic models for the repulsion between filaments and hydrodynamic models for their attraction, in order to determine the critical number of filaments. It is possible that the equilibrium tilt angle is not independent of the number of filaments, so the decay of  $\Delta\Phi_{\text{eff}}(\theta, N_f)$  with  $N_f$  may not be so rapid once we take into account the dependence on  $\theta_{\text{equil}}(N_f)$ .

## 5.4 Conclusion

In this chapter, we have proposed an extension of the original study in helical geometry by Macnab [138] and considered the critical phase difference between helices tilted at an angle to each other. The main geometrical results of this chapter are Eq. (5.23) for the critical phase difference between two filaments, and Eq. (5.27) for the effective critical phase difference in a circular bundle of  $N_f$  filaments. We have applied these geometrical results to two questions relevant to the bundling of bacterial filaments: the critical rate of synchronisation in a bundle that is converging due to hydrodynamic effects, and the critical torque difference between the motors in a bundle that has reached a steady state. In our discussion of these two problems, we have proposed routes for combining these geometrical results with dynamical models in order to deduce operational constraints for the bundle.

In the future, it will be possible to use these results for a comparative analysis of bacterial polymorphic shapes, since the geometrical results depend explicitly on the helical geometry of the flagellar filaments. The kinematic model can also be extended by adding a finite amount of CCW twist around the bundle, to incorporate the effect of the swirling flow induced by each filament, and also the counter-rotations of the cell body. The calculation for the intersection of two filaments would have to be modified, in this case, to allow for non-planar axes of the filaments.

Finally, we acknowledge that there are a number of limitations inherent to our geometrical approach of the question of bundling. The work presented in this chapter is based on a purely kinematic model, where we go through a sequence of plausible geometries of motion without modelling dynamical factors such as the hydrodynamic interactions between the filaments

[142, 207], the elastic deformations of both hook and filaments [101, 112], the torque-speed relationship of the BFM [160, 227], and the steric interactions with the cell body. Nevertheless, the geometrical necessity for synchronisation identified in this chapter serves as a motivation to further investigate the hydrodynamic synchronisation of rotating helical filaments in Chapter 7, after we have developed the necessary hydrodynamic machinery in Chapter 6.

## Chapter 6

# Asymptotic theory of hydrodynamic interactions between slender filaments

In this chapter, we lay the technical groundwork that allows us to investigate the important questions of synchronisation and propulsion in the next two chapters. We calculate the hydrodynamic interactions between two rigid filaments as an asymptotic series expansion in powers of  $L/d < 1$ , where  $L$  is the contour length of the filaments, and  $d$  is the distance between them. We validate our asymptotic expansion using a computational method based on SBT, and we apply our theoretical results to the case of two helical pumps rotating in parallel. In this final part, we focus on two questions: (i) is there any net attraction or repulsion between the helical pumps, and (ii) how do hydrodynamic interactions affect the pumping force and torque exerted by the helices?

The asymptotic series expansion will be used in later chapters as an analytical tool to understand the dynamics of helices interacting in the far field, while the computational method will allow us to extend our investigations to the near field.

### 6.1 Introduction

The microscopic world is filled with examples of rigid structures that interact with each other as they move through fluids. In the biological context, these can range from very dense systems such as bacterial swarms [41], where steric interactions are important, to regularly-spaced arrays of cilia, which can be coupled both hydrodynamically (through the fluid) [17] and elastically (through the cell membrane) [75, 220], down to dilute suspensions of planktonic bacteria and algae [94], where only hydrodynamic interactions prevail. Outside biology, hydrodynamic interactions are important in the dynamics of sedimentation and

the rheology of suspensions [48, 71, 137, 190], as well as the collective behaviour of synthetic active particles [144, 174]. For artificial devices such as diffusio- or electrophoretic swimmers, one must also consider long-range chemical interactions in addition to the hydrodynamics [184, 191, 213, 214].

Hydrodynamic interactions (HIs) represent a particular interest for research because, due to their long-range nature, they can give rise to collective behaviour in systems with a large number of active, self-propelled particles [53, 215]. A popular approach for studying active matter is to coarse-grain the system and postulate phenomenological equations based on symmetries, but it remains important to capture the microscopic origin of interactions between the particles. Therefore, the study of HIs between a small number of suspended bodies is the necessary link between understanding the dynamics of a single body in an unbounded fluid and that of a large collection of them.

On a microscopic length scale, the physics of the fluid is dominated by viscous dissipation, and inertia is negligible most of the time. Therefore, the interaction of micro-swimmers is usually a low Reynolds number problem, governed by the Stokes equations. Naturally, HIs are important in biology across all Reynolds numbers. For instance, they influence predator-prey interactions and sexual reproduction in small marine organisms such as copepods, which operate at low to intermediate Reynolds number [127]. HIs are also very important in schools of fish (usually high Reynolds number), where they give rise to stable swimming formations and affect endurance and propulsive efficiency [35, 164, 225]. At intermediate and high Reynolds number, however, the problem of HIs is usually approached with experimental and computational tools. In contrast, in the low Reynolds number limit, the linearity of the Stokes equations allows for exact analytical solutions if the geometry is simple enough, e.g. the interaction between two rigid spheres.

### **6.1.1 Previous work**

For rigid spheres at low Reynolds number, exact analytical solutions were found for the flow field around two spheres of arbitrary size but specified orientation [63, 103, 201], as well as around two identical spheres with arbitrary orientation [64, 218]. These exact solutions are possible either by exploiting a cylindrical symmetry in the problem [103, 201], or by using a bispherical coordinate system [63, 64, 218]. These classical analytical results were later confirmed by computational studies [34, 116, 228]. In addition to the exact solutions, there are also approximate analytical solutions for the interaction of two spheres sufficiently far apart [27, 56]. These solutions are expressed as series expansions in inverse powers of the distance between the spheres, and have the advantage of circumventing bispherical coordinates. For more than two spheres, the interactions become more complicated, but

researchers have studied this problem experimentally [102] and numerically [28], and have also made analytical progress in the form of a far-field theory [85].

For shapes more complex than a sphere, it is often necessary to approach the modelling problem with computational tools. In the biological context, full boundary-element method (BEM) simulations have been carried out to study the HIs between micromachines with spiral tails [157], uniflagellar bacteria swimming side by side [96], and spherical colonies of algae swimming near boundaries [95]. Other computational studies have considered the interactions between more abstract types of swimmers such as dumbbell-type [77] or squirmer-type pushers and pullers [68, 153]. One important question to consider when talking about HIs between microorganisms is whether there is any net attraction or repulsion between the swimmers, and if they settle into stable swimming patterns. These questions are also motivated by experimental observations of swimming bacteria and volvocine algae [47, 129].

In this chapter we focus on the HIs between slender filaments at low Reynolds number, in order to tackle the interactions between swimming appendages such as cilia and flagella, rather than entire microorganisms. If HIs between microorganisms are important for the stability of swimming patterns in groups of swimmers, then the HIs between swimming appendages are essential to single-cell behaviour. This includes questions such as the speed and state of flagellar synchronisation [17, 22, 111, 141, 176, 177], the emergence of swimming gaits [220] and metachronal waves [52, 73], and the propulsive capacity of an organism with multiple appendages [52, 158]. Much previous work in this area is computational [18, 22, 52, 111, 141, 158, 176, 177], but there has also been some analytical work on the HIs between nearby slender filaments [142], as well as experimental work on HIs between the beating cilia of live algae [17], and between rotating helices in macro-scale models of bacterial flagella [113, 114].

### 6.1.2 Current approach

We use the mathematical methods introduced in Chapter 2, namely resistive-force theory (RFT) and slender-body theory (SBT), to describe the HIs between two slender filaments separated by a distance,  $d$ , greater than the contour length of the filaments,  $L$ . In a similar way to previous studies on spheres [27, 56], we express the force distribution along each filament as a series expansion in inverse powers of  $d/L > 1$ . This uses principles from the method of reflections, where some contributions in the expansion correspond to hydrodynamic effects that have reflected back and forth between the filaments a number of times. The method of scattering has previously been employed in the theoretical study of suspensions of rods [137, 190], but these studies focus on the bulk rheology of a suspension of passive fibres,

whereas our current purpose is to derive analytical expressions for the specific HIs between two active slender filaments. Furthermore, the present study can handle helical and other shapes of filaments, while the aforementioned work was limited to straight rods.

Our final analytical results pertain specifically to rigid filaments, whose motion can be encapsulated in one mathematical object – the resistance matrix. For multiple filaments, it is the extended resistance matrix (see also Ref. [27]) that relates the full dynamics (forces and torques on all the filaments) to the full kinematics (the linear and angular velocities of all the filaments). We expand our solution for the extended resistance matrix up to and including second-order corrections in  $L/d < 1$ . This is motivated by our subsequent application to rotating helical pumps, where the net attraction or repulsion between the helices is only noticeable at second order. It is also at second order that the power of slender-filament methods like RFT and SBT comes into play. The first-order contribution of HIs is the same for slender filaments as it is for spheres or any rigid object that exerts a net force on the fluid. At second order, however, we have contributions not only from the flow that is reflected between the objects (which is the same for spheres), but also from expanding the shape of the filament centreline about its centre.

The chapter is divided into three central parts – the derivation, validation, and application of the theory for HIs between slender filaments. In §6.2 we derive analytical expressions for the extended resistance matrix of two arbitrarily-shaped rigid slender filaments, written as a series expansion up to second-order corrections in inverse distance. We then evaluate the coefficients in this series using both RFT and SBT, and in §6.3 we validate the asymptotic theory against numerical simulations based on SBT. Finally, in §6.4, we apply both theory and simulations to the case of two helical pumps rotating side by side in an infinite fluid. We perform a thorough investigation of the forces and torques exerted by the helical pumps, and derive analytical expressions that capture the qualitative effects of HIs with varying distance and phase difference between the helices. Based on our understanding of pairwise HIs between helical pumps, we then provide a perspective on the HIs within a circular array of helical pumps, and we conclude the chapter by discussing our results in a wider context in §6.5.

## 6.2 Asymptotic expansion for hydrodynamic interactions

In this section, we consider the HIs between two rigid slender filaments separated by a distance,  $d$ , greater than their contour length,  $L$ . We quantify the dynamics of the interacting filaments through an extended resistance matrix, for which we derive a series expansion solution up to second-order corrections in  $L/d < 1$ .

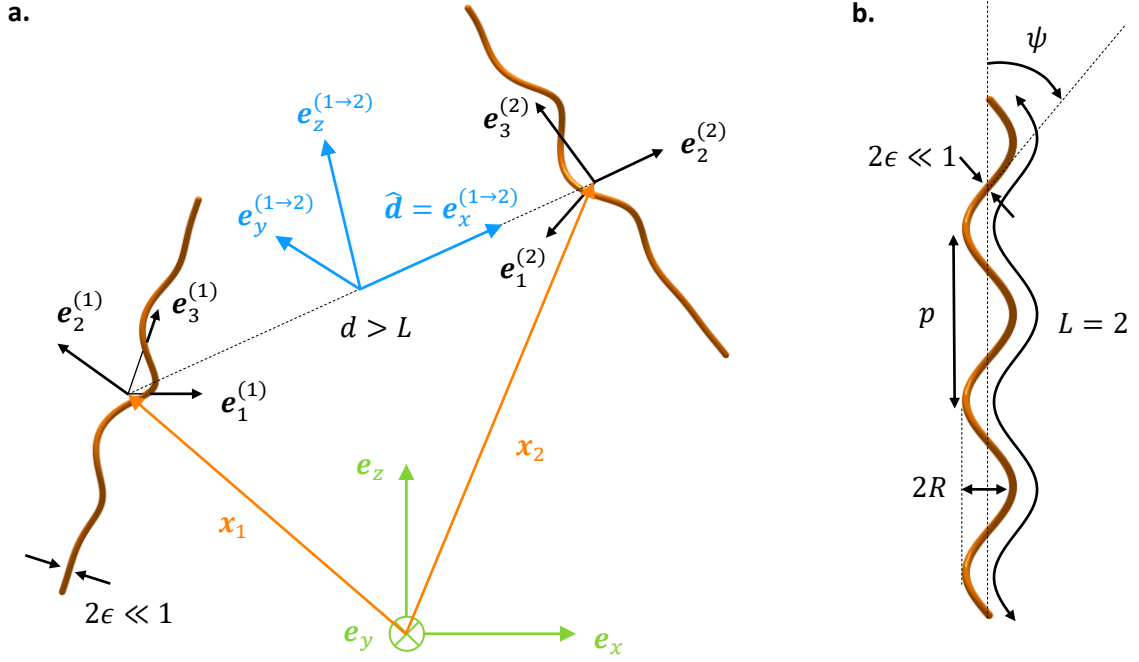


Fig. 6.1 Geometrical setup of the problem. (a) Two rigid filaments of dimensionless contour length  $L = 2$  interact with each other hydrodynamically as they move through a viscous fluid. Our asymptotic theory is valid for sufficiently large inter-filament separation,  $d > L$ , and in the limit of small filament thickness,  $\varepsilon \ll 1$ . We identify three useful coordinate systems: the laboratory frame (green), the interaction frame for a pair of filaments (blue), and the body frame for an individual filament (black). (b) Parameters describing the geometry of a helical filament, which we will use for the validation and application of our asymptotic theory.

### 6.2.1 Geometrical setup

We begin by sketching the setup of our hydrodynamic problem and introducing the mathematical notation. In Fig. 6.1 (a) we illustrate the different coordinate systems used in this chapter. First, there is the laboratory frame  $\{\mathbf{e}_x, \mathbf{e}_y, \mathbf{e}_z\}$  in usual Cartesian coordinates. Then there is a body-fixed frame for each filament, where the unit vectors  $\{\mathbf{e}_1^{(k)}, \mathbf{e}_2^{(k)}, \mathbf{e}_3^{(k)}\}$  are the same as those defined in §2.1.1 with an additional label,  $k$ , for the filament. The three-dimensional orientation of the filament is described by three angles, written compactly as an orientation vector  $\mathbf{p}_k = (\phi_k, \theta_k, \chi_k)$ . Relative to the body frame, we write the position of the centreline and the unit tangent along an arbitrarily-shaped filament as

$$\mathbf{r}_k(s) = x_1^{(k)}(s)\mathbf{e}_1^{(k)} + x_2^{(k)}(s)\mathbf{e}_2^{(k)} + x_3^{(k)}(s)\mathbf{e}_3^{(k)}, \quad (6.1)$$

$$\hat{\mathbf{t}}_k(s) = \frac{\partial x_1^{(k)}}{\partial s}\mathbf{e}_1^{(k)} + \frac{\partial x_2^{(k)}}{\partial s}\mathbf{e}_2^{(k)} + \frac{\partial x_3^{(k)}}{\partial s}\mathbf{e}_3^{(k)}, \quad (6.2)$$

where  $s$  is the arc length along the filament.

Finally there is a frame of interaction,  $\{\mathbf{e}_x^{(j \rightarrow k)}, \mathbf{e}_y^{(j \rightarrow k)}, \mathbf{e}_z^{(j \rightarrow k)}\}$ , defined for every pair of filaments  $j$  and  $k$  such that the unit vector  $\mathbf{e}_x^{(j \rightarrow k)}$  points from the origin of the body frame of filament  $j$  to that of filament  $k$ . This frame is useful for discussing interactions between three filaments or more, where there could be multiple pairwise interaction frames distinct from the absolute laboratory frame. However, in our discussion of interactions between two filaments, we may assume without loss of generality that the interaction frame is identical to the laboratory frame.

Our asymptotic theory is written in terms of dimensionless quantities. We measure lengths in units of  $\tilde{L}/2$  and viscosity in units of  $\tilde{\mu}$ , where  $\tilde{L}$  is the integrated length of the filament and  $\tilde{\mu}$  is the viscosity of the medium. This is equivalent to taking  $L = 2$  and  $\mu = 1$  in dimensionless terms. In these units, the cross-sectional radius of the filament,  $\varepsilon$ , and the centre-to-centre distance between the filaments,  $d$ , must satisfy  $\varepsilon \ll 1 < d$  in order for our theory to hold. We also note that, in our notation, the arc length falls in the interval  $s \in (-1, +1)$ , giving a total dimensionless length  $L = 2$  for the filament, and placing the midpoint of the filament at  $s = 0$ .

In Fig. 6.1 (b), we illustrate a filament geometry of particular interest - a helical filament with helical radius,  $R$ , and helical pitch,  $p$ . It is convenient to introduce the helix angle  $\psi = \tan^{-1}(2\pi R/p)$  and the number of helical turns  $N = L/\sqrt{(2\pi R)^2 + p^2}$ . In terms of these, the dimensionless radius of the helix is  $R = \sin \psi / (\pi N)$  and the pitch is  $p = 2 \cos \psi / N$ . As in §2.1.1, we write the centreline of helix  $k$  relative to the origin of the body-fixed frame as

$$\mathbf{r}_k(s) = R \cos(\pi N s) \mathbf{e}_1^{(k)} + \sigma R \sin(\pi N s) \mathbf{e}_2^{(k)} + s \cos \psi \mathbf{e}_3^{(k)}, \quad (6.3)$$

where  $s \in (-1, +1)$  is the arc length along the helix and  $\sigma = \pm 1$  is the chirality (negative for left-handed helices, positive for right-handed). We also write the unit tangent vector along the centreline as

$$\hat{\mathbf{t}}_k(s) = -\sin \psi \sin(\pi N s) \mathbf{e}_1^{(k)} + \sigma \sin \psi \cos(\pi N s) \mathbf{e}_2^{(k)} + \cos \psi \mathbf{e}_3^{(k)}. \quad (6.4)$$

The calculations in §6.2 are valid for filaments of arbitrary shape, but in later sections we focus on helical filaments for the purposes of validating and applying our analytical results.

## 6.2.2 Hydrodynamic setup

The goal is to find a relationship between the kinematics and the dynamics of the two filaments. This is generally quantified by an extended resistance matrix, which relates the

forces and torques exerted by the filaments to their linear and angular velocities, such that

$$\begin{pmatrix} \mathbf{F}_1 \\ \mathbf{T}_1 \\ \mathbf{F}_2 \\ \mathbf{T}_2 \end{pmatrix} = \begin{pmatrix} \mathbf{S}(\mathbf{x}_1, \mathbf{x}_2, \mathbf{p}_1, \mathbf{p}_2) & \mathbf{C}(\mathbf{x}_1, \mathbf{x}_2, \mathbf{p}_1, \mathbf{p}_2) \\ \mathbf{C}(\mathbf{x}_2, \mathbf{x}_1, \mathbf{p}_2, \mathbf{p}_1) & \mathbf{S}(\mathbf{x}_2, \mathbf{x}_1, \mathbf{p}_2, \mathbf{p}_1) \end{pmatrix} \begin{pmatrix} \mathbf{U}_1 \\ \boldsymbol{\Omega}_1 \\ \mathbf{U}_2 \\ \boldsymbol{\Omega}_2 \end{pmatrix}, \quad (6.5)$$

where the matrix  $\mathbf{S}$  stands for self-induced dynamics and the matrix  $\mathbf{C}$  represents cross-interactions between the filaments. We have made it explicit that the resistance matrix depends on the positions,  $\mathbf{x}_j$ , and orientations,  $\mathbf{p}_j$ , of the two filaments. Note that even the matrix  $\mathbf{S}$  for self-induced dynamics depends on the position of both filaments, because fluid disturbances induced by the motion of one filament will reflect off the second filament and travel back to the position where they originated. Because  $\mathbf{F}_j$  and  $\mathbf{T}_j$  are the forces and torques exerted by the filaments on the fluid, the resistance matrix is positive definite and, by the reciprocal theorem, also symmetric. In particular, this means that  $\mathbf{C}(\mathbf{x}_2, \mathbf{x}_1, \mathbf{p}_2, \mathbf{p}_1) = \mathbf{C}(\mathbf{x}_1, \mathbf{x}_2, \mathbf{p}_1, \mathbf{p}_2)^T$ .

Without loss of generality for the two filament case, we may define the laboratory frame to be centred on the first filament, so that  $\mathbf{x}_1 = 0$ . Thus, the resistance matrix only depends on the directed distance  $\mathbf{d} = \mathbf{x}_2 - \mathbf{x}_1$  so that

$$\begin{pmatrix} \mathbf{F}_1 \\ \mathbf{T}_1 \end{pmatrix} = \mathbf{S}(\mathbf{d}, \mathbf{p}_1, \mathbf{p}_2) \begin{pmatrix} \mathbf{U}_1 \\ \boldsymbol{\Omega}_1 \end{pmatrix} + \mathbf{C}(\mathbf{d}, \mathbf{p}_1, \mathbf{p}_2) \begin{pmatrix} \mathbf{U}_2 \\ \boldsymbol{\Omega}_2 \end{pmatrix}, \quad (6.6)$$

$$\begin{pmatrix} \mathbf{F}_2 \\ \mathbf{T}_2 \end{pmatrix} = \mathbf{S}(-\mathbf{d}, \mathbf{p}_2, \mathbf{p}_1) \begin{pmatrix} \mathbf{U}_2 \\ \boldsymbol{\Omega}_2 \end{pmatrix} + \mathbf{C}(-\mathbf{d}, \mathbf{p}_2, \mathbf{p}_1) \begin{pmatrix} \mathbf{U}_1 \\ \boldsymbol{\Omega}_1 \end{pmatrix}. \quad (6.7)$$

If the filaments are slender ( $\varepsilon \ll 1$ ), then we may represent the dynamics of filament  $k$  by a force density  $\mathbf{f}_k(s)$  along its centreline. We define an arclength-dependent drag tensor  $\boldsymbol{\Sigma}(s)$  which relates the force density to the relative velocity of the filament centreline through the expression

$$\mathbf{f}_k(s) = \boldsymbol{\Sigma}_k(s) \cdot [\mathbf{u}(\mathbf{r}_k(s)) - \mathbf{u}_\infty(\mathbf{r}_k(s))]. \quad (6.8)$$

In §6.2.8 we will return to the drag tensor and explain how to evaluate it using resistive-force theory (RFT) and slender-body theory (SBT). Until then, the derivation of the asymptotic series expansion is independent of which method we use to characterise the drag on an individual filament.

For a rigid filament, the velocity of the centreline is given by the rigid body motion

$$\mathbf{u}(\mathbf{r}_k(s)) = \mathbf{U}_k + \boldsymbol{\Omega}_k \times \mathbf{r}_k(s). \quad (6.9)$$

To make our notation more compact, we introduce a kinematics vector with six components made through the concatenation of the linear and angular velocities of the filament, i.e.  $(\mathbf{U}_k, \mathbf{\Omega}_k)$ . Then, using summation convention, we may write the velocity of the first filament's centreline as

$$u_i(\mathbf{r}_1(s)) = (\delta_{ij} + \varepsilon_{i,j-3,k}(\mathbf{r}_1(s))_k)(\mathbf{U}_1, \mathbf{\Omega}_1)_j, \quad (6.10)$$

where the index  $j$  is summed over from 1 to 6, while the other free indices run from 1 to 3 as usual, and the Kronecker delta and Levi-Civita symbol are understood to be identically zero if any index falls outside the normal range  $\{1, 2, 3\}$ .

Next, we consider the background flow at the position of the first filament, which is nothing more than the flow induced by the second filament. At distances much greater than the filament thickness,  $\varepsilon$ , the dominant flow induced by the second filament is the cumulative effect of a distribution of Stokeslets placed along its centreline, and represented by the force density  $\mathbf{f}_2(s)$ . Hence, we can express the background flow as

$$\mathbf{u}_\infty(\mathbf{r}_1(s)) = \frac{1}{8\pi\mu} \int_{-1}^{+1} \frac{\mathbf{I} + \hat{\mathbf{R}}_d(s, s')\hat{\mathbf{R}}_d(s, s')}{|\mathbf{R}_d(s, s')|} \cdot \mathbf{f}_2(s') ds', \quad (6.11)$$

where  $\mathbf{R}_d(s, s') = \mathbf{d} + \mathbf{r}_2(s') - \mathbf{r}_1(s)$  is the relative distance between a point  $s'$  on the centreline of the second filament and a point  $s$  on the centreline of the first filament. Note that  $\mu = 1$  in our dimensionless units, but was included for clarity. Higher-order singularities, such as the source dipoles included in computational studies [147, 205], decay at least as fast as the inverse cube of distance, and hence do not contribute to HIs at order  $\mathcal{O}(d^{-2})$ , which is as far as we go with the asymptotic series expansion in this chapter.

To obtain the total hydrodynamic force and torque exerted by the filament, we need to calculate force moments along the length of the filament, so that

$$\mathbf{F} = \int_{-1}^{+1} \mathbf{f}(s) ds, \quad \mathbf{T} = \int_{-1}^{+1} \mathbf{r}(s) \times \mathbf{f}(s) ds. \quad (6.12)$$

Using the compact notation introduced earlier, we can write an expression for the dynamics vector  $(\mathbf{F}_1, \mathbf{T}_1)$  of the first filament as

$$(\mathbf{F}_1, \mathbf{T}_1)_i = \int_{-1}^{+1} (\delta_{ij} + \varepsilon_{i-3,kj}(\mathbf{r}_1(s))_k)(\mathbf{f}_1(s))_j ds, \quad (6.13)$$

where the index  $i$  runs from 1 to 6, while the other indices are summed over from 1 to 3.

### 6.2.3 Asymptotic series formulation

Equations (6.8)-(6.11) define a coupled system of equations for the force densities on the two filaments, which we will solve in the regime  $d > L = 2$ . We write the force distribution along each filament as an asymptotic series expansion

$$\mathbf{f}_k(s) = \mathbf{f}_k^{(0)}(s) + d^{-1}\mathbf{f}_k^{(1)}(s) + d^{-2}\mathbf{f}_k^{(2)}(s) + \mathcal{O}(d^{-3}), \quad (6.14)$$

with the ultimate goal of calculating series expansions for the self-induced and cross-interaction resistance matrices in Eq. (6.6). We can write these as

$$\mathbf{S}(\mathbf{d}, \mathbf{p}_1, \mathbf{p}_2) = \mathbf{S}^{(0)}(\hat{\mathbf{d}}, \mathbf{p}_1, \mathbf{p}_2) + d^{-1}\mathbf{S}^{(1)}(\hat{\mathbf{d}}, \mathbf{p}_1, \mathbf{p}_2) + d^{-2}\mathbf{S}^{(2)}(\hat{\mathbf{d}}, \mathbf{p}_1, \mathbf{p}_2) + \mathcal{O}(d^{-3}), \quad (6.15)$$

$$\mathbf{C}(\mathbf{d}, \mathbf{p}_1, \mathbf{p}_2) = \mathbf{C}^{(0)}(\hat{\mathbf{d}}, \mathbf{p}_1, \mathbf{p}_2) + d^{-1}\mathbf{C}^{(1)}(\hat{\mathbf{d}}, \mathbf{p}_1, \mathbf{p}_2) + d^{-2}\mathbf{C}^{(2)}(\hat{\mathbf{d}}, \mathbf{p}_1, \mathbf{p}_2) + \mathcal{O}(d^{-3}), \quad (6.16)$$

where the matrices at each order only depend on the direction of separation,  $\hat{\mathbf{d}}$ , with all dependence on the magnitude of separation,  $|\mathbf{d}| = d$ , captured by the algebraic power of the given order. Because the leading order is given by the limit  $d \rightarrow \infty$ , where the filaments do not know of each other's presence, we deduce that

$$\mathbf{S}^{(0)}(\hat{\mathbf{d}}, \mathbf{p}_1, \mathbf{p}_2) = \mathbf{S}^{(0)}(\mathbf{p}_1), \quad \mathbf{C}^{(0)}(\hat{\mathbf{d}}, \mathbf{p}_1, \mathbf{p}_2) = \mathbf{0}. \quad (6.17)$$

In order to solve Eq. (6.8) as an asymptotic series, we need to expand the flow induced by the second filament in inverse powers of distance. The Stokeslets decay like  $1/|\mathbf{R}_d|$ , so we first write the magnitude of the relative distance as

$$|\mathbf{R}_d| = d \left( 1 + \frac{2\hat{\mathbf{d}} \cdot (\mathbf{r}_2(s') - \mathbf{r}_1(s))}{d} + \frac{|\mathbf{r}_2(s') - \mathbf{r}_1(s)|^2}{d^2} \right)^{1/2}. \quad (6.18)$$

Because all points on the filament centreline lie within a sphere of diameter  $L$  around the centre, we have  $|\mathbf{r}_2(s') - \mathbf{r}_1(s)| < L < d$ , so we can apply the binomial expansion to get

$$\frac{1}{|\mathbf{R}_d|} = \frac{1}{d} - \frac{\hat{\mathbf{d}} \cdot (\mathbf{r}_2(s') - \mathbf{r}_1(s))}{d^2} + \mathcal{O}(d^{-3}), \quad (6.19)$$

$$\hat{\mathbf{R}}_d = \hat{\mathbf{d}} + \frac{(\mathbf{I} - \hat{\mathbf{d}}\hat{\mathbf{d}}) \cdot (\mathbf{r}_2(s') - \mathbf{r}_1(s))}{d} + \mathcal{O}(d^{-2}). \quad (6.20)$$

Note that these binomial expansions is valid for any  $d > L$ , and higher accuracy can be obtained by including more terms in the series. Therefore, we can expand the induced flow

in Eq. (6.11) as

$$u_{\infty,i}(\mathbf{r}_1(s)) = \int_{-1}^{+1} (d^{-1}J_{ij}(\hat{\mathbf{d}}) + d^{-2}K_{ijp}(\hat{\mathbf{d}})(\mathbf{r}_2(s') - \mathbf{r}_1(s))_p + \mathcal{O}(d^{-3})) (\mathbf{f}_2(s'))_j ds', \quad (6.21)$$

where the second-rank tensor

$$J_{ij}(\hat{\mathbf{d}}) = \frac{\delta_{ij} + \hat{d}_i \hat{d}_j}{8\pi\mu} \quad (6.22)$$

represents the leading-order Stokeslet induced by the second filament, and the third-rank tensor

$$K_{ijp}(\hat{\mathbf{d}}) = \frac{\hat{d}_i \delta_{jp} + \hat{d}_j \delta_{ip} - \hat{d}_p \delta_{ij} - 3\hat{d}_i \hat{d}_j \hat{d}_p}{8\pi\mu} \quad (6.23)$$

represents higher-order moments of the force distribution along the second filament.

## 6.2.4 Leading-order dynamics

The induced flow, Eq. (6.21), makes no contributions to Eq. (6.8) at  $\mathcal{O}(1)$ . By using Eq. (6.10) to express the rigid-body motion of the filament, we find that the leading-order force distribution is given by

$$(\mathbf{f}_1^{(0)}(s))_i = (\boldsymbol{\Sigma}_1(s))_{ij} (\delta_{jk} + \varepsilon_{j,k-3,l}(\mathbf{r}_1(s))_l) (\mathbf{U}_1, \boldsymbol{\Omega}_1)_k. \quad (6.24)$$

Then, by using Eq. (6.13) to find the total force and torque exerted by the filament, and putting the result in the form of Eq. (6.6), we find that

$$S_{ij}^{(0)}(\mathbf{p}_1) = \int_{-1}^{+1} (\delta_{ik} + \varepsilon_{i-3,lk}(\mathbf{r}_1(s))_l) (\boldsymbol{\Sigma}_1(s))_{km} (\delta_{mj} + \varepsilon_{j-3,nm}(\mathbf{r}_1(s))_n) ds, \quad (6.25)$$

where the free indices  $i$  and  $j$  run from 1 to 6. but all others are summed over from 1 to 3. Note that the integral depends implicitly on the orientation  $\mathbf{p}_1$  of the filament through the filament centreline  $\mathbf{r}_1$  and the tensor  $\boldsymbol{\Sigma}_1$ .

The self-induced resistance matrix  $\mathbf{S}^{(0)}(\mathbf{p}_1)$  can be obtained, for any orientation  $\mathbf{p}_1$  of the filament, by applying a change of basis to the resistance matrix expressed in the body frame of the filament, which we denote by

$$\mathbf{S}_0 = \begin{pmatrix} \mathbf{A} & \mathbf{B} \\ \mathbf{B}^T & \mathbf{D} \end{pmatrix} \equiv \mathbf{S}^{(0)}(\mathbf{0}). \quad (6.26)$$

If  $\mathbf{Q}(\mathbf{p}_1)$  is the orthogonal matrix whose columns are the unit vectors  $\{\mathbf{e}_1^{(1)}, \mathbf{e}_2^{(1)}, \mathbf{e}_3^{(1)}\}$  defined in §2.1.1, then the self-induced resistance matrix for orientation  $\mathbf{p}_1$  is

$$\mathbf{S}^{(0)}(\mathbf{p}_1) = \begin{pmatrix} \mathbf{Q}(\mathbf{p}_1) & \mathbf{0} \\ \mathbf{0} & \mathbf{Q}(\mathbf{p}_1) \end{pmatrix} \begin{pmatrix} \mathbf{A} & \mathbf{B} \\ \mathbf{B}^T & \mathbf{D} \end{pmatrix} \begin{pmatrix} \mathbf{Q}(\mathbf{p}_1)^T & \mathbf{0} \\ \mathbf{0} & \mathbf{Q}(\mathbf{p}_1)^T \end{pmatrix}, \quad (6.27)$$

where we applied the change of basis to each three-by-three block of the resistance matrix.

### 6.2.5 First-order correction

Next, we analyse Eq. (6.8) at  $\mathcal{O}(d^{-1})$  using the expansion of the induced flow from Eq. (6.21). We find that the first-order correction to the force distribution is given by

$$(\mathbf{f}_1^{(1)}(s))_i = -(\boldsymbol{\Sigma}_1(s))_{ij} \int_{-1}^{+1} J_{jk}(\hat{\mathbf{d}}) (\mathbf{f}_2^{(0)}(s'))_k ds'. \quad (6.28)$$

Then, substituting the leading-order force density from Eq. (6.24), we find that

$$(\mathbf{f}_1^{(1)}(s))_i = -(\boldsymbol{\Sigma}_1(s))_{ij} J_{jk}(\hat{\mathbf{d}}) \int_{-1}^{+1} (\boldsymbol{\Sigma}_2(s'))_{kl} (\delta_{ij} + \varepsilon_{i,j-3,k}(\mathbf{r}_2(s'))_k) ds' (\mathbf{U}_2, \boldsymbol{\Omega}_2)_l. \quad (6.29)$$

Then, by using Eq. (6.13) to find the total force and torque exerted by the filament, and putting the result in the form of Eq. (6.6), we find that

$$S_{ij}^{(1)}(\hat{\mathbf{d}}, \mathbf{p}_1, \mathbf{p}_2) = 0, \quad (6.30)$$

and

$$C_{ij}^{(1)}(\hat{\mathbf{d}}, \mathbf{p}_1, \mathbf{p}_2) = - \int_{-1}^{+1} (\boldsymbol{\Sigma}_1(s))_{ik} (\delta_{kl} + \varepsilon_{k,l-3,m}(\mathbf{r}_1(s))_m) ds \\ \times J_{kn}(\hat{\mathbf{d}}) \int_{-1}^{+1} (\boldsymbol{\Sigma}_2(s'))_{np} (\delta_{pj} + \varepsilon_{p,j-3,q}(\mathbf{r}_2(s'))_q) ds'. \quad (6.31)$$

We recognise from Eq. (6.25) that these integrals are the first three columns and rows of the leading-order matrix for the first and second filament, respectively, so we can write the leading-order cross-interaction matrix as

$$C_{ij}^{(1)}(\hat{\mathbf{d}}, \mathbf{p}_1, \mathbf{p}_2) = -S_{ik}^{(0)}(\mathbf{p}_1) J_{kl}(\hat{\mathbf{d}}) S_{lj}^{(0)}(\mathbf{p}_2), \quad (6.32)$$

where the free indices  $i$  and  $j$  run from 1 to 6, but all others are summed over from 1 to 3. We can read this expression from right to left to understand its physical interpretation. At leading

order, the second filament induces a Stokeslet flow of strength  $(\mathbf{S}^{(0)}(\mathbf{p}_2))_{lj}(\mathbf{U}_2, \boldsymbol{\Omega}_2)_j$  (with  $l \in \{1, 2, 3\}, j \in \{1, 2, \dots, 6\}$ ), which gets carried over to the position of the first filament by the Oseen tensor  $J_{kl}(\hat{\mathbf{d}})/d$ . The first filament sees a uniform background flow at leading order and responds to it using its own self-induced resistance matrix  $(\mathbf{S}^{(0)}(\mathbf{p}_1))_{ik}$  (with  $i \in \{1, 2, \dots, 6\}, k \in \{1, 2, 3\}$ ), as if it was translating with a uniform velocity in the opposite direction to the background flow, hence the minus sign.

We note that directionality is lost at this order, because the tensor  $J_{ij}(\hat{\mathbf{d}})$ , defined in Eq. (6.22), is invariant under the transformation  $\hat{\mathbf{d}} \mapsto -\hat{\mathbf{d}}$ . All that matters at this order is the distance  $d$  between the two filaments. Furthermore,  $\mathbf{C}^{(1)}(\hat{\mathbf{d}}, \mathbf{p}_1, \mathbf{p}_2)^T = \mathbf{C}^{(1)}(-\hat{\mathbf{d}}, \mathbf{p}_2, \mathbf{p}_1)$ , so the reciprocal theorem is satisfied at this order.

The result can also be extended to non-identical filaments by incorporating information about the filament geometry. We can make this dependence explicit in our notation by writing  $\mathbf{S}^{(0)}(\mathbf{p}; \mathbf{g})$ , where the vector parameter  $\mathbf{g}$  encapsulates all information about the filament geometry. For the particular case of helical filaments, note from Eqs. (6.114)-(6.136) that our dimensionless  $S_{ij}^{(0)}$  depends explicitly on the helix angle  $\psi$ , the number of turns  $N$ , and implicitly on the slenderness parameter  $\varepsilon$  through the drag coefficients  $c_\perp$  and  $c_\parallel$ , hence  $\mathbf{g} = (\psi, N, \varepsilon)$  for a helix. Note also that, in our derivation of the dimensionless  $\mathbf{S}(\mathbf{n}; \mathbf{g})$  we had rescaled lengths by the filament length, so we would need to add this information back in if we wanted to consider filaments of different lengths.

Using tildes to denote dimensional quantities, we can write the leading-order self-induced resistance matrix as

$$\tilde{\mathbf{S}}^{(0)}(\mathbf{p}; \mathbf{g}, \tilde{L}) = \frac{\tilde{\mu}\tilde{L}}{2} \begin{pmatrix} \mathbf{I} & 0 \\ 0 & \mathbf{I}\tilde{L}/2 \end{pmatrix} \begin{pmatrix} \mathbf{Q}(\mathbf{p})\mathbf{A}(\mathbf{g})\mathbf{Q}(\mathbf{p})^T & \mathbf{Q}(\mathbf{p})\mathbf{B}(\mathbf{g})\mathbf{Q}(\mathbf{p})^T \\ \mathbf{Q}(\mathbf{p})\mathbf{B}(\mathbf{g})^T\mathbf{Q}(\mathbf{p})^T & \mathbf{Q}(\mathbf{p})\mathbf{D}(\mathbf{g})\mathbf{Q}(\mathbf{p})^T \end{pmatrix} \begin{pmatrix} \mathbf{I} & 0 \\ 0 & \mathbf{I}\tilde{L}/2 \end{pmatrix}, \quad (6.33)$$

and also the dimensional cross-interaction matrix as

$$\tilde{\mathbf{C}}_{ij}^{(1)}(\mathbf{d}, \mathbf{p}_1, \mathbf{p}_2; \mathbf{g}_1, \mathbf{g}_2, \tilde{L}_1, \tilde{L}_2) = -\tilde{S}_{ip}^{(0)}(\mathbf{p}_1; \mathbf{g}_1, \tilde{L}_1) \frac{(\delta_{pq} + \hat{d}_p \hat{d}_q)}{8\pi\tilde{\mu}\tilde{d}} \tilde{S}_{qj}^{(0)}(\mathbf{p}_2; \mathbf{g}_2, \tilde{L}_2). \quad (6.34)$$

The results in Eqs. (6.33) and (6.34) describe in full generality the far-field HIs between two filaments of arbitrary shape and orientation up to order  $\mathcal{O}(\tilde{d}^{-1})$ .

### 6.2.6 Second-order correction

We now begin to analyse Eq. (6.8) at  $\mathcal{O}(d^{-2})$  using the expansion of the induced flow from Eq. (6.21). We find that the second-order correction to the force distribution is given by

$$\begin{aligned} (\mathbf{f}_1^{(2)}(s))_i = & -(\boldsymbol{\Sigma}_1(s))_{ij} \int_{-1}^{+1} J_{jk}(\hat{\mathbf{d}})(\mathbf{f}_2^{(1)}(s'))_k ds' \\ & - (\boldsymbol{\Sigma}_1(s))_{ij} \int_{-1}^{+1} K_{jkp}(\hat{\mathbf{d}})(\mathbf{r}_2(s') - \mathbf{r}_1(s))_p (\mathbf{f}_2^{(0)}(s'))_k ds'. \end{aligned} \quad (6.35)$$

The first of these terms will contribute to the self-induced resistance matrix because  $\mathbf{f}_2^{(1)}$  is linear in the kinematics of the first filament, while the second of them will contribute to the cross-interaction matrix because  $\mathbf{f}_2^{(0)}$  is linear in the kinematics of the second filament.

After substituting the first-order force density from Eq. (6.29) into Eq. (6.35), we find that there is a contribution to  $\mathbf{f}_1^{(2)}(s)$  of the form

$$\begin{aligned} -(\boldsymbol{\Sigma}_1(s))_{ij} \int_{-1}^{+1} J_{jk}(\hat{\mathbf{d}})(-\boldsymbol{\Sigma}_2(s'))_{kl} J_{lm}(\hat{\mathbf{d}}) ds' \\ \times \int_{-1}^{+1} (\boldsymbol{\Sigma}_1(s''))_{mn} (\delta_{np} + \varepsilon_{n,p-3,q}(\mathbf{r}_1(s''))_q) ds'' (\mathbf{U}_1, \boldsymbol{\Omega}_1)_p. \end{aligned} \quad (6.36)$$

Then, using Eqs. (6.6) and (6.13) to bring the result to its final form, we deduce that

$$S_{ij}^{(2)}(\hat{\mathbf{d}}, \mathbf{p}_1, \mathbf{p}_2) = S_{ik}^{(0)}(\mathbf{p}_1) J_{kl}(\hat{\mathbf{d}}) S_{lm}^{(0)}(\mathbf{p}_2) J_{mn}(\hat{\mathbf{d}}) S_{nj}^{(0)}(\mathbf{p}_1), \quad (6.37)$$

where the free indices  $i$  and  $j$  run from 1 to 6, but all others are summed from 1 to 3. Note that this clearly satisfies the reciprocal theorem because both  $\mathbf{S}^{(0)}$  and the Oseen tensor are symmetric.

Physically, the result in Eq. (6.37) expresses the fact that the Stokeslet field produced by the first filament propagates with an  $\mathcal{O}(d^{-1})$  decay to the position of the second filament, where it produces a disturbance in the force. The  $\mathcal{O}(d^{-1})$  perturbation in the force exerted by the second filament gets reflected back to the first filament with the same  $\mathcal{O}(d^{-1})$  decay. This generates an  $\mathcal{O}(d^{-2})$  disturbance in the dynamics of the first filament that is self-induced (i.e. proportional to its own kinematics).

Similarly, after substituting the leading-order force density from Eq. (6.24) into Eq. (6.35), we find that there is a contribution to  $\mathbf{f}_1^{(2)}(s)$  of the form

$$\begin{aligned} & -(\boldsymbol{\Sigma}_1(s))_{ij} \int_{-1}^{+1} K_{jkl}(\hat{\mathbf{d}})(\mathbf{r}_2(s'))_l (\boldsymbol{\Sigma}_2(s'))_{km} (\delta_{mn} + \varepsilon_{m,n-3,p}(\mathbf{r}_2(s'))_p) ds' (\mathbf{U}_2, \boldsymbol{\Omega}_2)_n \\ & + (\boldsymbol{\Sigma}_1(s))_{ij} K_{jkl}(\hat{\mathbf{d}})(\mathbf{r}_1(s))_l \int_{-1}^{+1} (\boldsymbol{\Sigma}_2(s'))_{km} (\delta_{mn} + \varepsilon_{m,n-3,p}(\mathbf{r}_2(s'))_p) ds' (\mathbf{U}_2, \boldsymbol{\Omega}_2)_n. \end{aligned} \quad (6.38)$$

We introduce the notation

$$P_{ij}(\hat{\mathbf{d}}, \mathbf{p}_2) = \int_{-1}^{+1} K_{ikl}(\hat{\mathbf{d}})(\mathbf{r}_2(s'))_l (\boldsymbol{\Sigma}_2(s'))_{km} (\delta_{mj} + \varepsilon_{m,j-3,n}(\mathbf{r}_2(s'))_n) ds' \quad (6.39)$$

for the second-rank tensor appearing in Eq. (6.38), and rewrite this contribution as

$$\left[ -(\boldsymbol{\Sigma}_1(s))_{ij} P_{jn}(\hat{\mathbf{d}}, \mathbf{p}_2) + (\boldsymbol{\Sigma}_1(s))_{ij} K_{jkl}(\hat{\mathbf{d}})(\mathbf{r}_1(s))_l S_{kn}^{(0)}(\mathbf{p}_2) \right] (\mathbf{U}_2, \boldsymbol{\Omega}_2)_n \quad (6.40)$$

with the help of Eq. (6.25). Finally, we integrate the force density as per Eq. (6.13) to find the correction to the total force and torque due to the kinematics of the second filament. Using the fact that  $K_{jkl}(\hat{\mathbf{d}}) = K_{kjl}(\hat{\mathbf{d}})$  (follows directly from the definition in Eq. (6.23)), we deduce that the  $\mathcal{O}(d^{-2})$  correction to the cross-interaction matrix is

$$C_{ij}^{(2)}(\hat{\mathbf{d}}, \mathbf{p}_1, \mathbf{p}_2) = -S_{ik}^{(0)}(\mathbf{p}_1) P_{kj}(\hat{\mathbf{d}}, \mathbf{p}_2) + P_{ik}^T(\hat{\mathbf{d}}, \mathbf{p}_1) S_{kj}^{(0)}(\mathbf{p}_2), \quad (6.41)$$

where the free indices  $i$  and  $j$  run from 1 to 6, but  $k$  is summed from 1 to 3. Note that this also satisfies the reciprocal theorem, according to which  $\mathbf{C}(\hat{\mathbf{d}}, \mathbf{p}_1, \mathbf{p}_2)^T = \mathbf{C}(-\hat{\mathbf{d}}, \mathbf{p}_2, \mathbf{p}_1)$  because  $P_{ij}(-\hat{\mathbf{d}}, \mathbf{p}_2) = -P_{ij}(\hat{\mathbf{d}}, \mathbf{p}_2)$  (follows directly from the definitions of  $K_{ijp}$  and  $P_{ij}$  in Eqs. (6.23) and (6.39), respectively).

The final result for  $C_{ij}^{(2)}(\hat{\mathbf{d}}, \mathbf{p}_1, \mathbf{p}_2)$ , given by Eq. (6.41), involves a new quantity that we have not calculated explicitly yet – the tensor  $P_{ij}$ , defined in Eq. (6.39). In contrast, the expressions for  $C_{ij}^{(1)}(\hat{\mathbf{d}}, \mathbf{p}_1, \mathbf{p}_2)$  and  $S_{ij}^{(2)}(\hat{\mathbf{d}}, \mathbf{p}_1, \mathbf{p}_2)$  (Eqs. (6.32) and (6.37), respectively) have the advantage that they involve only the leading-order resistance matrices  $S_{ij}^{(0)}(\mathbf{p}_1)$  and  $S_{ij}^{(0)}(\mathbf{p}_2)$ . These can be easily calculated from RFT or SBT since they are nothing more than the resistance matrix for an isolated filament. Our final task is to show that the tensor  $P_{ij}(\hat{\mathbf{d}}, \mathbf{p}_1)$  can also be calculated easily from the leading-order resistance matrix  $S_{ij}^{(0)}(\mathbf{p}_1)$  and two minor follow-up calculations.

### 6.2.7 Force moments for second-order correction

The tensor  $P_{ij}$  defined in Eq. (6.39) is constructed in a similar way to the last three rows of the leading-order resistance matrix from Eq. (6.25). If we introduce the quantity

$$M_{lkj}(\mathbf{p}_2) = \int_{-1}^{+1} (\mathbf{r}_2(s))_l (\boldsymbol{\Sigma}_2(s))_{km} (\delta_{mj} + \varepsilon_{j-3, nm} (\mathbf{r}_2(s))_n) ds, \quad (6.42)$$

which represents force moments along the centreline of a filament with orientation  $\mathbf{p}_2$ , then what we want to compute is

$$P_{ij}(\hat{\mathbf{d}}, \mathbf{p}_2) = K_{ikl}(\hat{\mathbf{d}}) M_{lkj}(\mathbf{p}_2), \quad (6.43)$$

but we already have an expression for the last three rows ( $4 \leq i \leq 6$ ) of the resistance matrix

$$S_{ij}^{(0)}(\mathbf{p}_2) = \varepsilon_{i-3, lk} M_{lkj}(\mathbf{p}_2), \quad (6.44)$$

in the laboratory frame, Eq. (6.27).

So far we have assumed that the laboratory and interaction frame are identical, and we have only talked about changing basis from the body frame to the laboratory frame, Eq. (6.27). This was convenient because  $S_{ij}^{(0)}(\mathbf{p}_2)$  has a simple representation in the body frame of the second filament, since the orientation of the filament is  $\mathbf{p}_2 = \mathbf{0}$  relative to this frame. But the natural frame in which to describe the tensor  $K_{ikl}(\hat{\mathbf{d}})$  is the interaction frame where  $\hat{\mathbf{d}} = \mathbf{e}_x^{(1 \rightarrow 2)}$ , as shown in Fig. 6.1 (b). In this frame, the tensor  $K_{ijp}(\hat{\mathbf{d}})$  defined in Eq. (6.23) has components

$$K_{1kl}(\mathbf{e}_x^{(1 \rightarrow 2)}) = \frac{1}{8\pi} \begin{pmatrix} -2 & 0 & 0 \\ 0 & 1 & 0 \\ 0 & 0 & 1 \end{pmatrix}, \quad K_{2kl}(\mathbf{e}_x^{(1 \rightarrow 2)}) = \frac{1}{8\pi} \begin{pmatrix} 0 & 1 & 0 \\ -1 & 0 & 0 \\ 0 & 0 & 0 \end{pmatrix}, \quad (6.45)$$

$$K_{3kl}(\mathbf{e}_x^{(1 \rightarrow 2)}) = \frac{1}{8\pi} \begin{pmatrix} 0 & 0 & 1 \\ 0 & 0 & 0 \\ -1 & 0 & 0 \end{pmatrix}. \quad (6.46)$$

Hence, the tensor  $P_{ij}(\hat{\mathbf{d}}, \mathbf{p}_2)$  can be written in the interaction frame as

$$P_{ij}(\mathbf{e}_x^{(1 \rightarrow 2)}, \mathbf{p}'_2) = \frac{1}{8\pi} \delta_{i1} (-2M_{11j}(\mathbf{p}'_2) + M_{22j}(\mathbf{p}'_2) + M_{33j}(\mathbf{p}'_2)) \\ + \frac{1}{8\pi} \delta_{i2} (-M_{12j}(\mathbf{p}'_2) + M_{21j}(\mathbf{p}'_2)) + \frac{1}{8\pi} \delta_{i3} (-M_{13j}(\mathbf{p}'_2) + M_{31j}(\mathbf{p}'_2)), \quad (6.47)$$

whereas the last three rows ( $4 \leq i \leq 6$ ) of the resistance matrix are

$$S_{ij}^{(0)}(\mathbf{p}'_2) = \delta_{i4}(M_{23j}(\mathbf{p}'_2) - M_{32j}(\mathbf{p}'_2)) \\ + \delta_{i5}(-M_{13j}(\mathbf{p}'_2) + M_{31j}(\mathbf{p}'_2)) + \delta_{i6}(M_{12j}(\mathbf{p}'_2) - M_{21j}(\mathbf{p}'_2)). \quad (6.48)$$

Note that we have used the notation  $\mathbf{p}'_2$  to indicate the orientation of the filament relative to the interaction frame, so the tensors  $\mathbf{M}(\mathbf{p}'_2)$  and  $\mathbf{S}^{(0)}(\mathbf{p}'_2)$  are also to be expressed in these coordinates. By comparing the two expressions in Eqs. (6.47) and (6.48), we deduce that

$$P_{2j}(\mathbf{e}_x^{(1 \rightarrow 2)}, \mathbf{p}'_2) = -\frac{S_{6j}^{(0)}(\mathbf{p}'_2)}{8\pi}, \quad P_{3j}(\mathbf{e}_x^{(1 \rightarrow 2)}, \mathbf{p}'_2) = \frac{S_{5j}^{(0)}(\mathbf{p}'_2)}{8\pi}, \quad (6.49)$$

so we get the last two rows of  $P_{ij}$  for free.

To complete the top row of  $P_{ij}$  we simply need to calculate the quantity

$$P_{1j}(\mathbf{e}_x^{(1 \rightarrow 2)}, \mathbf{p}'_2) = \frac{1}{8\pi}(-2M_{11j}(\mathbf{p}'_2) + M_{22j}(\mathbf{p}'_2) + M_{33j}(\mathbf{p}'_2)), \quad (6.50)$$

which is more easily calculated in the body frame of the filament and then transferred to the interaction frame by a change of basis.

Everything we have done so far is valid for filaments of arbitrary shape. Below, we go into more detail about the evaluation of the new row  $P_{1j}$  for helical filaments, which will be used later for the validation and application of our theory. In the body frame of a helical filament, where  $\mathbf{p}'_2 \rightarrow \mathbf{0}$ , we denote the right-hand side of Eq. (6.50) by

$$(\mathbf{m}_0)_j = -2M_{11j}(\mathbf{0}) + M_{22j}(\mathbf{0}) + M_{33j}(\mathbf{0}). \quad (6.51)$$

The helical centreline introduced in Eq. (6.3) is symmetric under a rotation by angle  $\pi$  around the unit vector  $\mathbf{e}_1$ . Due to this symmetry, the vector  $\mathbf{m}_0$  has vanishing components along the  $\mathbf{e}_2$  and  $\mathbf{e}_3$  directions, regardless of the method (RFT or SBT) by which we choose to evaluate it, meaning that

$$(\mathbf{m}_0)_i = (\mathcal{M}_1 \mathbf{e}_1)_i, \quad (\mathbf{m}_0)_{i+3} = (\mathcal{M}_4 \mathbf{e}_1)_i, \quad (6.52)$$

for index  $i = 1, 2, 3$ . Hence, when we move this result to the interaction frame of two helices, we obtain the final result for the matrix  $\mathbf{P}(\mathbf{e}_x^{(1 \rightarrow 2)}, \mathbf{p}'_2)$

$$\mathbf{P}(\dots) = \frac{1}{8\pi} \begin{pmatrix} \mathcal{M}_1 \alpha(\mathbf{p}'_2) & \mathcal{M}_1 \beta(\mathbf{p}'_2) & \mathcal{M}_1 \gamma(\mathbf{p}'_2) & \mathcal{M}_4 \alpha(\mathbf{p}'_2) & \mathcal{M}_4 \beta(\mathbf{p}'_2) & \mathcal{M}_4 \gamma(\mathbf{p}'_2) \\ -S_{61}^{(0)}(\mathbf{p}'_2) & -S_{62}^{(0)}(\mathbf{p}'_2) & -S_{63}^{(0)}(\mathbf{p}'_2) & -S_{64}^{(0)}(\mathbf{p}'_2) & -S_{65}^{(0)}(\mathbf{p}'_2) & -S_{66}^{(0)}(\mathbf{p}'_2) \\ S_{51}^{(0)}(\mathbf{p}'_2) & S_{52}^{(0)}(\mathbf{p}'_2) & S_{53}^{(0)}(\mathbf{p}'_2) & S_{54}^{(0)}(\mathbf{p}'_2) & S_{55}^{(0)}(\mathbf{p}'_2) & S_{56}^{(0)}(\mathbf{p}'_2) \end{pmatrix}, \quad (6.53)$$

where  $\alpha(\mathbf{p}'_2) = \mathbf{e}_1^{(2)} \cdot \mathbf{e}_x^{(1 \rightarrow 2)}$ ,  $\beta(\mathbf{p}'_2) = \mathbf{e}_1^{(2)} \cdot \mathbf{e}_y^{(1 \rightarrow 2)}$  and  $\gamma(\mathbf{p}'_2) = \mathbf{e}_1^{(2)} \cdot \mathbf{e}_z^{(1 \rightarrow 2)}$  are the components of  $\mathbf{e}_1^{(2)}$  relative to the interaction frame of filaments 1 and 2. If the interaction frame does not coincide with the laboratory frame (e.g. if there are more than two filaments), this result would have to be moved to the laboratory frame by a change of basis on each three-by-three block.

### 6.2.8 Evaluating coefficients in the series expansion

The first and second-order coefficients in the series expansion only require the leading-order resistance matrix,  $\mathbf{S}^{(0)}$ , and the force moment,  $\mathbf{m}_0$ , which themselves only depend on the shape of the filament,  $\mathbf{r}(s)$ , and the drag tensor,  $\boldsymbol{\Sigma}(s)$ . We now explain how to evaluate these coefficients using both resistive-force theory (RFT) and slender-body theory (SBT). The former has the advantage of being analytically tractable at the cost of logarithmically-decaying errors, while the latter is algebraically correct but requires numerical computations.

In RFT [69, 79, 132], the drag tensor depends only on the local tangent to the filament,

$$\boldsymbol{\Sigma}_{\text{RFT}}(s) = c_{\perp} [\mathbf{I} - \hat{\mathbf{t}}(s)\hat{\mathbf{t}}(s)] + c_{\parallel} \hat{\mathbf{t}}(s)\hat{\mathbf{t}}(s), \quad (6.54)$$

and quantifies the anisotropic drag on the filament through the perpendicular,  $c_{\perp}$ , and parallel,  $c_{\parallel}$ , drag coefficients

$$c_{\perp} = \frac{4\pi\mu}{\ln(L/\varepsilon) + 1/2}, \quad c_{\parallel} = \frac{2\pi\mu}{\ln(L/\varepsilon) - 1/2}. \quad (6.55)$$

Note that, for clarity, we have included the dimensionless viscosity  $\mu = 1$  in the above definition of the drag coefficients. For the special case of a helical filament, we use RFT to derive analytical expressions for  $\mathbf{S}_0$  in Appendix 6.A and for  $\mathbf{m}_0$  in Appendix 6.B.

In SBT [32, 105, 131], on the other hand, the relationship between force density and velocity is non-local, so we cannot express the drag tensor as a local object. The value of  $\boldsymbol{\Sigma}_{\text{SBT}}(s)$  at each point  $s$  along the centreline depends on the specifics of the motion relative to the shape of the filament. However, we do not need to know the general form of  $\boldsymbol{\Sigma}_{\text{SBT}}(s)$

in order to evaluate the coefficients in our asymptotic series expansion using SBT. An inspection of Eqs. (6.25) and (6.39) reveals that the drag tensor always appears contracted with the six modes of rigid-body motion that are available to our rigid filaments, in the form  $\Sigma_{ik}(s)(\delta_{kj} + \varepsilon_{j-3,ik}r_l(s))$ . Therefore, we only need to know the SBT drag tensor as it pertains to rigid-body motion,

$$\boldsymbol{\Sigma}_{\text{SBT}}(s) \cdot (\mathbf{U} + \boldsymbol{\Omega} \times \mathbf{r}(s)) \equiv \mathbf{f}_{\text{SBT}}(s; \mathbf{U}, \boldsymbol{\Omega}), \quad (6.56)$$

where  $\mathbf{f}_{\text{SBT}}(s; \mathbf{U}, \boldsymbol{\Omega})$  is the SBT force density along a filament with kinematics  $(\mathbf{U}, \boldsymbol{\Omega})$ . By considering each mode of rigid-body motion individually, we can write

$$\Sigma_{ik}(s)(\delta_{kj} + \varepsilon_{j-3,ik}r_l(s)) \equiv (\mathbf{f}_{\text{SBT}}^{(j)}(s))_i, \quad (6.57)$$

where  $\mathbf{f}_{\text{SBT}}^{(j)}(s)$  is now the force density computed from SBT for the  $j$ th mode of rigid body motion ( $j = 1, 2, 3$  for translations,  $j = 4, 5, 6$  for rotations).

From Eqs. (6.25) and (6.57), we get the leading-order resistance matrix,  $\mathbf{S}^{(0)}$ , from SBT

$$(\mathbf{S}_{\text{SBT}}^{(0)})_{ij} = \int_{-1}^{+1} (\delta_{ik} + \varepsilon_{i-3,ik}(\mathbf{r}_1(s)))_l (\mathbf{f}_{\text{SBT}}^{(j)}(s))_k ds. \quad (6.58)$$

Similarly, from Eqs. (6.42), (6.51) and (6.57), we find the SBT equivalent of  $\mathbf{m}_0$  as

$$(\mathbf{m}_0^{\text{SBT}})_j = \int_{-1}^{+1} \mathbf{r}(s) \cdot (\mathbf{I} - 3\mathbf{e}_x^{(1 \rightarrow 2)} \mathbf{e}_x^{(1 \rightarrow 2)}) \cdot \mathbf{f}_{\text{SBT}}^{(j)}(s) ds. \quad (6.59)$$

Evaluating the force density  $\mathbf{f}_{\text{SBT}}^{(j)}(s)$  does require a numerical computation but for a rigid filament this only needs to be done once, in the body frame of the filament, and then modified with a change of basis if the filament changes orientation over time. The SBT computation consists of solving Eq. (6.60) numerically, exactly as described in §6.3.1, but without the interaction term  $\mathcal{J}[\mathbf{f}_2(s'), \mathbf{d}]$ .

In the following sections, when we refer to the asymptotic theory with RFT or SBT coefficients, we mean that we have used the series expansion for the extended resistance matrix from Eqs. (6.15) and (6.16), with coefficients up to second order given by Eqs. (6.17), (6.25), (6.30), (6.32), (6.37) and (6.41), but these coefficients have been evaluated either analytically with RFT or computationally with SBT. The RFT calculations for the matrix  $\mathbf{S}^{(0)}$  and the vector  $\mathbf{m}_0$  are given in Appendices 6.A and 6.B, respectively, while the computational method for SBT is described in §6.3.1 (except that the interaction term  $\mathcal{J}$  is not included in the SBT computation for a single filament).

### 6.3 Validation of asymptotic expansion

We now verify the asymptotic theory with RFT/SBT coefficients against numerical simulations based on SBT. In this section, we focus on filaments with a helical centreline, which are very common in microscopic scale flows (e.g. the helical flagellar filaments of bacteria, helical microbots actuated by external magnetic fields, elongated microorganisms with a spiral body shape).

#### 6.3.1 Computational method for hydrodynamic interactions

In order to validate our asymptotic model, we implement Johnson's slender-body theory [105, 119] with additional interactions between the filaments [205]. In our computational method, we replace Eq. (6.8) with the following relationship between the force density and velocity along the filament centreline,

$$8\pi\mu\mathbf{u}(\mathbf{r}_1(s)) = \mathcal{L}[\mathbf{f}_1(s)] + \mathcal{K}[\mathbf{f}_1(s')] + \mathcal{J}[\mathbf{f}_2(s'), \mathbf{d}], \quad (6.60)$$

where the first operator represents local effects

$$\mathcal{L}[\mathbf{f}_1(s)] = \left[ 2 \left( \ln \left( \frac{2}{\varepsilon} \right) + \frac{1}{2} \right) \mathbf{I} + 2 \left( \ln \left( \frac{2}{\varepsilon} \right) - \frac{3}{2} \right) \hat{\mathbf{t}}_1(s) \hat{\mathbf{t}}_1(s) \right] \cdot \mathbf{f}_1(s), \quad (6.61)$$

and the second operator represents non-local effects

$$\begin{aligned} \mathcal{K}[\mathbf{f}_1(s')] = \int_{-1}^{+1} \left[ \frac{\mathbf{I} + \hat{\mathbf{R}}_0(s, s') \hat{\mathbf{R}}_0(s, s')}{|\mathbf{R}_0(s, s')|} - \frac{\mathbf{I} + \hat{\mathbf{t}}_1(s) \hat{\mathbf{t}}_1(s)}{|s' - s|} \right] \cdot \mathbf{f}_1(s') ds' \\ + (\mathbf{I} + \hat{\mathbf{t}}_1(s) \hat{\mathbf{t}}_1(s)) \cdot \int_{-1}^{+1} \frac{\mathbf{f}_1(s') - \mathbf{f}_1(s)}{|s' - s|} ds', \end{aligned} \quad (6.62)$$

where  $\mathbf{R}_0(s, s') = \mathbf{r}_1(s) - \mathbf{r}_1(s')$ , and we have split the terms in such a way that both integrals have a removable singularity at  $s' = s$  (compare with Eq. (2.26)). Finally, the third operator represents interactions between the two filaments as previously modelled by Tornberg and Shelley [205],

$$\mathcal{J}[\mathbf{f}_2(s'), \mathbf{d}] = \int_{-1}^{+1} \left[ \frac{\mathbf{I} + \hat{\mathbf{R}}_d(s, s') \hat{\mathbf{R}}_d(s, s')}{|\mathbf{R}_d(s, s')|} + \frac{\varepsilon^2 \mathbf{I} - 3 \hat{\mathbf{R}}_d(s, s') \hat{\mathbf{R}}_d(s, s')}{2 |\mathbf{R}_d(s, s')|^3} \right] \cdot \mathbf{f}_2(s') ds', \quad (6.63)$$

where  $\mathbf{R}_d(s, s') = \mathbf{d} + \mathbf{r}_2(s') - \mathbf{r}_1(s)$ . In our computational method, which was implemented for purposes beyond the present study, we choose to include the source dipole term that was left out of our asymptotic theory, Eq. (6.11), because it would have contributed to

the asymptotic series expansion only at order  $\mathcal{O}(d^{-3})$ . Note that we have used the same prefactor of  $1/2$  for the dipole term as in [205], while a more recent study based on the Rotne-Prager-Yamakawa kernel and matched asymptotics uses a larger prefactor of  $e^3/24$  [147].

We solve Eqs. (6.60)-(6.63) numerically using a Galerkin method based on Legendre polynomials as in Refs. [119, 197]. Other studies have chosen to solve these integral equations by regularizing the integral operator  $\mathcal{K}$  and approximating its arguments with piecewise polynomials [205], or more recently using a spectral method based on Chebyshev polynomials [147]. In the present study, the choice of Legendre polynomials as a set of basis functions is motivated by their being eigenfunctions of the second integral in the non-local operator  $\mathcal{K}$ , meaning that

$$\int_{-1}^{+1} \frac{P_n(s') - P_n(s)}{|s' - s|} ds' = E_n P_n(s), \quad (6.64)$$

with eigenvalues  $E_0 = 0$  and

$$E_n = -2 \sum_{j=1}^n \frac{1}{j}, \quad (6.65)$$

for  $n > 0$  [67].

We discretise the force density and velocity along the filaments as

$$\mathbf{u}(\mathbf{r}_k(s)) = \sum_{n=0}^{\infty} \mathbf{u}_k^{(n)} P_n(s), \quad \mathbf{f}_k(s) = \sum_{n=0}^{\infty} \mathbf{f}_k^{(n)} P_n(s), \quad (6.66)$$

where the velocity coefficients  $\mathbf{u}_k^{(n)}$  are known from the prescribed kinematics, and the force coefficients  $\mathbf{f}_k^{(n)}$  must be solved for. After projecting Eq. (6.60) onto the space of Legendre polynomials and making use of the orthogonality condition

$$\int_{-1}^{+1} P_n(s) P_m(s) ds = \frac{2\delta_{mn}}{2n+1}, \quad (6.67)$$

we recover the following system of equations relating the velocity and the force coefficients

$$8\pi\mu\mathbf{u}_1^{(n)} = \left[ 2 \left( \ln \left( \frac{2}{\varepsilon} \right) + \frac{1}{2} \right) + E_n \right] \mathbf{f}_1^{(n)} + \frac{2n+1}{2} \sum_{m=0}^{\infty} \left[ \left[ 2 \left( \ln \left( \frac{2}{\varepsilon} \right) - \frac{3}{2} \right) + E_m \right] \mathbf{M}_{\parallel}^{(n,m)} \mathbf{f}_1^{(m)} + \mathbf{M}_0^{(n,m)} \mathbf{f}_1^{(m)} + \mathbf{M}_d^{(n,m)} \mathbf{f}_2^{(m)} \right], \quad (6.68)$$

where the matrices  $\mathbf{M}_{\parallel}^{(n,m)}$ ,  $\mathbf{M}_0^{(n,m)}$  and  $\mathbf{M}_d^{(n,m)}$  are given by

$$\mathbf{M}_{\parallel}^{(n,m)} = \int_{-1}^{+1} \hat{\mathbf{t}}_1(s) \hat{\mathbf{t}}_1(s) P_n(s) P_m(s) ds, \quad (6.69)$$

$$\mathbf{M}_0^{(n,m)} = \int_{-1}^{+1} \int_{-1}^{+1} \left[ \frac{\mathbf{I} + \hat{\mathbf{R}}_0(s, s') \hat{\mathbf{R}}_0(s, s')}{|\mathbf{R}_0(s, s')|} - \frac{\mathbf{I} + \hat{\mathbf{t}}_1(s) \hat{\mathbf{t}}_1(s)}{|s' - s|} \right] P_n(s) P_m(s') ds' ds, \quad (6.70)$$

$$\mathbf{M}_d^{(n,m)} = \int_{-1}^{+1} \int_{-1}^{+1} \left[ \frac{\mathbf{I} + \hat{\mathbf{R}}_d(s, s') \hat{\mathbf{R}}_d(s, s')}{|\mathbf{R}_d(s, s')|} + \frac{\varepsilon^2 \mathbf{I} - 3 \hat{\mathbf{R}}_d \hat{\mathbf{R}}_d}{2 |\mathbf{R}_d(s, s')|^3} \right] P_n(s) P_m(s') ds' ds \quad (6.71)$$

The second of these matrices involves a removable singularity at  $s' = s$ , but the quadrature integration methods readily available in MATLAB can evaluate this integral accurately so long as the singular points lie on the boundaries of the integration domain. Therefore, when computing the matrices  $\mathbf{M}_0^{(n,m)}$  in MATLAB we split the double integral into two parts -  $s \in [-1, +1]$ ,  $s' \in [-1, s]$  and  $s \in [-1, +1]$ ,  $s' \in [s, +1]$ .

The infinite system of linear equations from Eq. (6.68) is truncated to  $m \leq N_{\text{Legendre}}$  modes and inverted numerically, in order to find the force density coefficients  $\mathbf{f}_1^{(k)}$  in terms of the velocity coefficients  $\mathbf{u}_1^{(k)}$ , which themselves are linearly dependent on the filament kinematics  $(\mathbf{U}_k, \mathbf{\Omega}_k)$ . The force density is then integrated along the filaments to find the extended resistance matrix that relates filament kinematics and dynamics. We implement this algorithm in MATLAB and validate it using the tests described in Appendix 6.D.

For each set of parameters  $(N, \psi, \varepsilon)$  describing the geometry of the helical filament, we vary the number of Legendre modes in our truncation until the numerical solution for an isolated helix settles to within 1% error. We then make the reasonable assumption that the number of Legendre modes determined from this single-helix self-convergence test is sufficient to obtain the same level of accuracy in our double-helix simulations as well. In general, we find that the required number of Legendre modes increases with the number of helical turns of the filament, because we must be able to capture variations in the force density and filament velocity which have the same wavenumber as the filament centreline. For most simulations presented in this chapter it was sufficient to use  $N_{\text{Legendre}} = 15$ , because the helices have a small number of helical turns.

### 6.3.2 Relative errors

In the absence of an exact solution, we use the numerical solution from SBT as a reference value against which to validate our asymptotic model. In the previous section, we derived a

series expansion for the extended resistance,  $\mathbf{R}$ , in the form

$$\mathbf{R} = \mathbf{R}^{(0)} + d^{-1}\mathbf{R}^{(1)} + d^{-2}\mathbf{R}^{(2)} + \mathcal{O}(d^{-3}), \quad (6.72)$$

up to and including second-order terms. We wish to compare this expansion of the resistance matrix with the numerical solution,  $\tilde{\mathbf{R}}$ , of the fully-coupled integral equations described in §6.3.1. However, we cannot compare the matrices  $\mathbf{R}$  and  $\tilde{\mathbf{R}}$  component-wise, because this would depend on the basis in which we represent the matrices. One can always choose a vector basis in which some component of the “true” solution  $\tilde{\mathbf{R}}$  is zero, relative to which our approximate solution  $\mathbf{R}$  would have an infinite relative error. Therefore, we need to think of the extended resistance matrices as linear operators between the space of filament kinematics and the space of filament dynamics, and define an error for the operator as a whole in a way that is basis-independent. A standard way to do this is to use an operator norm.

Suppose we have some given kinematics  $\mathbf{x}$  (two linear and two angular velocities, so a vector with twelve components) and we want to compute the dynamics  $\mathbf{y}$ . Then the error in  $\mathbf{y}$  is  $\Delta\mathbf{y} = \mathbf{R}\mathbf{x} - \tilde{\mathbf{R}}\mathbf{x}$ . We define the “relative error” in the dynamics to be

$$E_{\text{dyn}} \equiv \sup_{\mathbf{x}} \left\{ \frac{\|\tilde{\mathbf{R}}\mathbf{x} - \mathbf{R}\mathbf{x}\|_p}{\|\tilde{\mathbf{R}}\mathbf{x}\|_p} \right\} = \sup_{\mathbf{y}} \left\{ \frac{\|(\mathbf{I} - \mathbf{R}\tilde{\mathbf{R}}^{-1})\mathbf{y}\|_p}{\|\mathbf{y}\|_p} \right\}, \quad (6.73)$$

in other words the operator norm of  $\mathbf{I} - \mathbf{R}\tilde{\mathbf{R}}^{-1}$ . Note that taking the supremum over the entire space of filament kinematics is important, so that the value we compute for the relative error is not dependent on an arbitrary choice of filament kinematics.

Similarly, we can define the relative error in the kinematics as

$$E_{\text{kin}} \equiv \sup_{\mathbf{y}} \left\{ \frac{\|\tilde{\mathbf{R}}^{-1}\mathbf{y} - \mathbf{R}^{-1}\mathbf{y}\|_p}{\|\tilde{\mathbf{R}}^{-1}\mathbf{y}\|_p} \right\} = \sup_{\mathbf{x}} \left\{ \frac{\|(\mathbf{I} - \mathbf{R}^{-1}\tilde{\mathbf{R}})\mathbf{x}\|_p}{\|\mathbf{x}\|_p} \right\}, \quad (6.74)$$

so the operator norm of  $\mathbf{I} - \mathbf{R}^{-1}\tilde{\mathbf{R}}$ . Here again, taking the supremum is important, so that the relative error we compute does not depend on an arbitrary choice of filament dynamics.

In Fig. 6.2 (a) and (b) we compare the relative errors, defined with a  $p = 2$  norm, for different orders in our asymptotic theory with SBT coefficients. If our asymptotic series expansion up to  $\mathcal{O}(d^{-m})$  terms was calculated correctly, then we would expect the relative error to decay like  $d^{-(m+1)}$ , the order of the first neglected terms. This is confirmed by the slopes of our log-log plots, which validate our asymptotic series expansion up to  $\mathcal{O}(d^{-2})$ . Note that the comparison is only meaningful between the computations and the asymptotic theory with SBT coefficients. This is an unavoidable consequence of our choice to implement the computational method based on SBT. The asymptotic theory with RFT coefficients differs

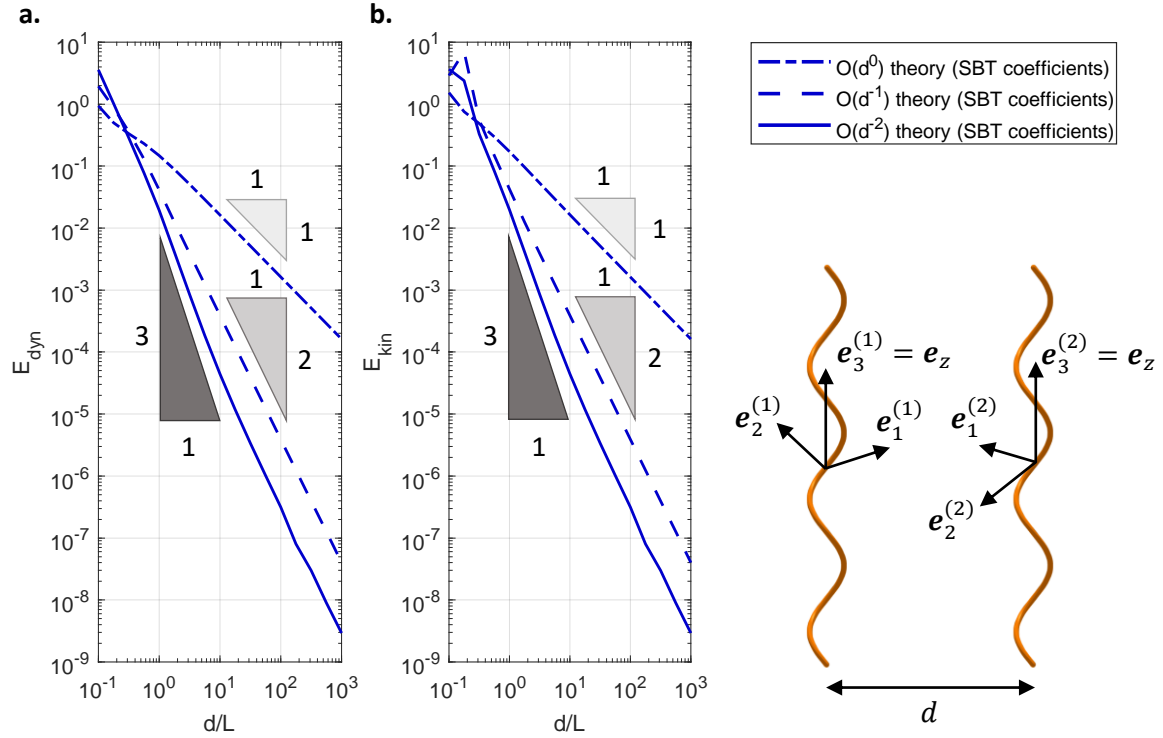


Fig. 6.2 Relative error in (a) helix dynamics and (b) helix kinematics, as defined in Eqs. (6.73) and (6.74) respectively, with  $p = 2$ . As we increase the helix separation,  $d$ , the asymptotic theory with SBT coefficients converges to the numerical solution, and the error decays as expected with each higher order included in the theory. Parameter specification: helices have configurations  $(\theta_1, \chi_1, \phi_1) = (0, 0, \pi/6)$  and  $(\theta_2, \chi_2, \phi_2) = (0, 0, 2\pi/3)$ , and  $N = 2.75$  helical turns. Helix angle,  $\psi = 0.5$  rad, and filament slenderness,  $\varepsilon = 10^{-2}$ , are representative of bacterial flagella.

at leading order from the numerical solution based on SBT, and so we would not be able to observe convergence unless we implemented a different computational method based on RFT. The results presented in Fig. 6.2 (a) and (b) serve to validate the asymptotic series expansion in itself, regardless of the method (RFT or SBT) by which we choose to calculate the leading-order resistance matrix,  $\mathbf{S}^{(0)}$ , and the force moment,  $\mathbf{m}_0$ .

Furthermore, by examining the size of the relative error, we deduce that the asymptotic theory can be useful for any  $d > L$ , which is the regime of validity for our binomial expansion of the Oseen tensor. When the filaments are parallel and orthogonal to the line that connects their centres, we observe that our asymptotic theory with SBT coefficients can achieve 99% accuracy for  $d/L > 1.4$ . This accuracy is achieved by the asymptotic solution up to and including  $\mathcal{O}(d^{-2})$  terms. Higher accuracy could be obtained either by including more terms in the asymptotic series expansion, or by increasing the distance between the filaments.

Based on further results presented in this study, where we also vary the phase difference between filaments, we believe this accuracy estimate to be representative of any parallel configuration of two filaments with this particular helical geometry. A broader numerical investigation would be necessary to determine the accuracy of our method for rigid filaments of arbitrary geometry and non-parallel configurations.

### 6.3.3 Time evolution of forces and torques

The main purpose of the asymptotic theory presented in this chapter is to provide a systematic method to calculate analytically the specific HIs between two filaments. When carrying out calculations by hand, we are interested in finding relative patterns more than in calculating accurate absolute values, which is the purpose of numerical schemes. With this perspective in mind, we propose to validate the asymptotic theory with RFT coefficients by looking at the time variation of hydrodynamically-induced forces and torques. We consider the case of two slender helices rotating in parallel with the same angular velocity.

Back in Fig. 6.2, we examined the relative error for a fixed orientation of the helices, and we varied the distance between the filaments to see how the error decays - a quantitative validation of our asymptotic model. In Figs. 6.3 and 6.4, however, we fix the distance between the helical filaments and we let time flow, and the orientation of the filaments along with it, to look for patterns over time - a qualitative validation of our asymptotic model. Because the helices are vertical, their body-fixed axis  $\mathbf{e}_3$  is parallel to the laboratory frame  $\mathbf{e}_z$ . Hence, the phase angle  $\phi$  around  $\mathbf{e}_z$  and the spin angle  $\chi$  around  $\mathbf{e}_3$ , as defined in §2.1.1, are interchangeable. Without loss of generality, we describe the configuration of the filaments from Figs. 6.3 and 6.4 as  $(\theta_1, \chi_1, \phi_1) = (0, 0, \Omega t)$  and  $(\theta_2, \chi_2, \phi_2) = (0, 0, \Omega t + \Delta\phi)$ .

Our asymptotic theory with both RFT and SBT coefficients captures the qualitative features of the interaction even for smaller helix separations, Fig. 6.3, with the agreement becoming quantitative at larger separations, Fig. 6.4. This indicates that our asymptotic series expansion can be used to derive meaningful analytical expressions for the HIs between filaments separated by a distance greater than their contour length, as later demonstrated in §6.4. We also provide a direct comparison between the asymptotic theory with SBT coefficients at  $\mathcal{O}(d^{-1})$  and  $\mathcal{O}(d^{-2})$ , in Figs. 6.5 and 6.6. These plots provide clearer visual evidence that higher-order corrections improve the fidelity of the asymptotic solution, as opposed to Fig. 6.2 where the evidence spanned a wider range of kinematic conditions, but was presented in a more condensed format.

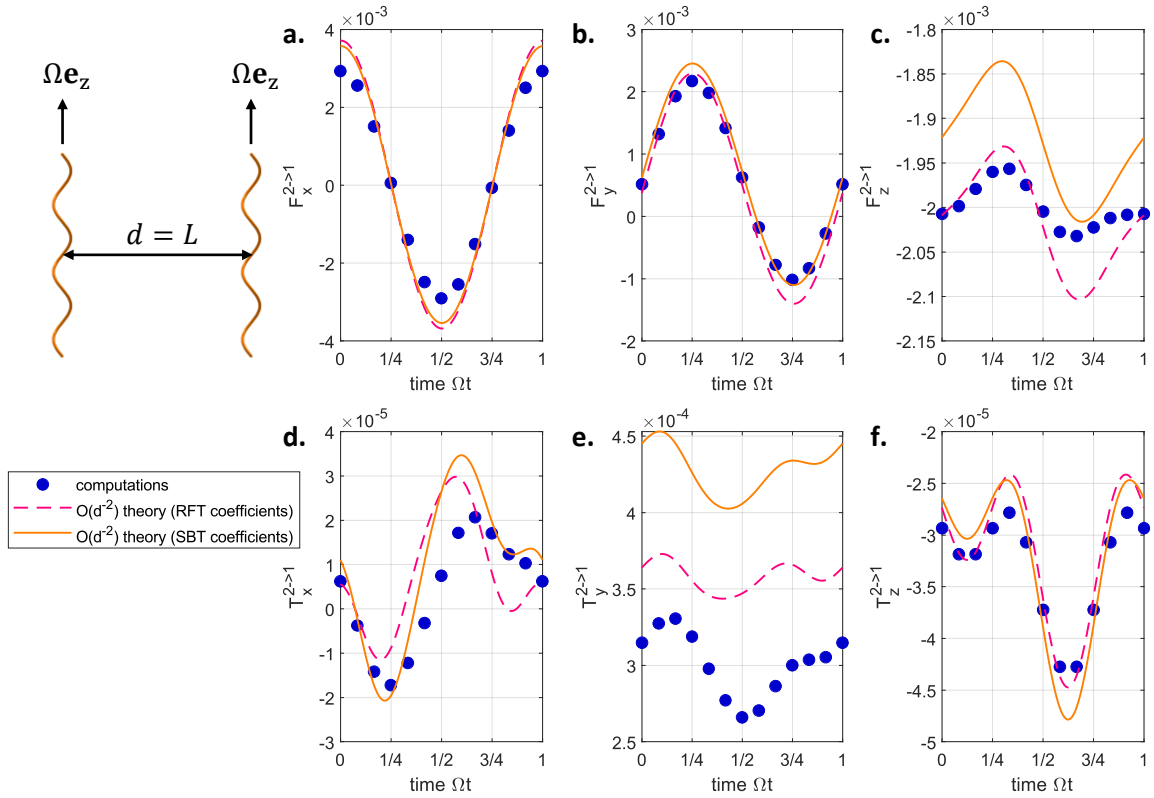


Fig. 6.3 Comparison between computations and the asymptotic theory with RFT/SBT coefficients, by means of the time evolution of forces and torques induced by the second (rightmost) filament on the first (leftmost). The helices are vertical ( $\theta = 0$ ) and rotating with constant angular velocity  $\Omega \mathbf{e}_z$ . We fix the phase difference  $\Delta\phi = \pi/2$  and the horizontal distance  $d = L$  between the helices. The pitch angle,  $\psi = 0.5043$  rad, and filament slenderness,  $\varepsilon = 0.0038$ , were chosen as representative of bacterial flagellar filaments. The helices have  $N = 2.5$  helical turns.

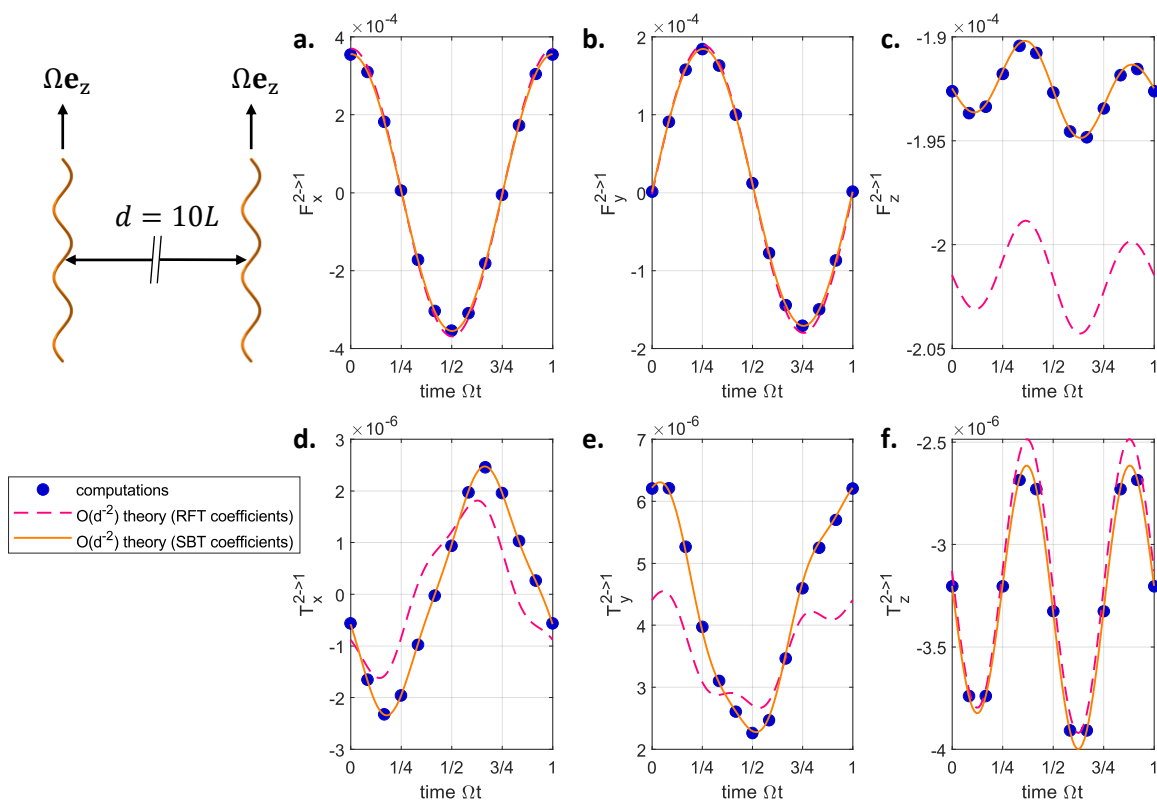


Fig. 6.4 Comparison between computations and the asymptotic theory with RFT/SBT coefficients – continued. The horizontal distance between the helices is now  $d = 10L$ .

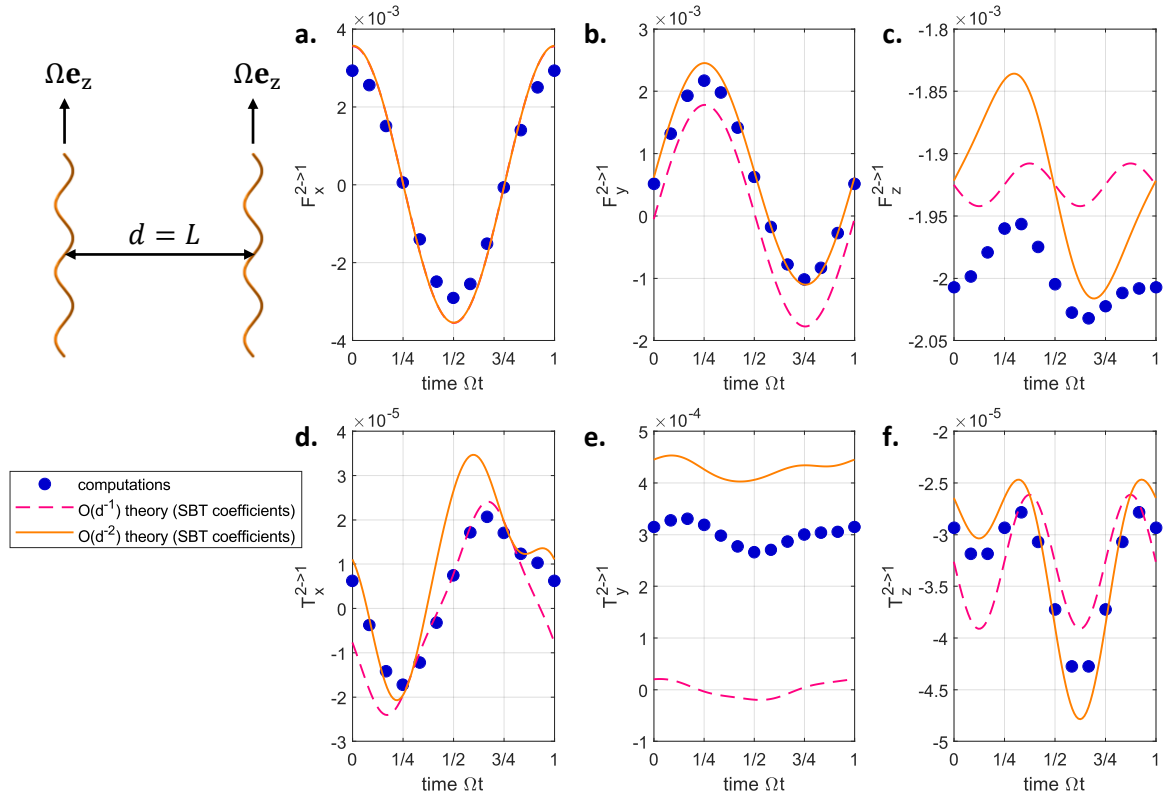


Fig. 6.5 Comparison between computations and the asymptotic theory with SBT coefficients to  $\mathcal{O}(d^{-1})$  and  $\mathcal{O}(d^{-2})$ , by means of the time evolution of forces and torques induced by the second (rightmost) filament on the first (leftmost). The helices are vertical ( $\theta = 0$ ) and rotating with constant angular velocity  $\Omega \mathbf{e}_z$ . We fix the phase difference  $\Delta\phi = \pi/2$  and the horizontal distance  $d = L$  between the helices. The pitch angle,  $\psi = 0.5043$  rad, and filament slenderness,  $\varepsilon = 0.0038$ , were chosen as representative of bacterial flagellar filaments. The helices have  $N = 2.5$  helical turns.

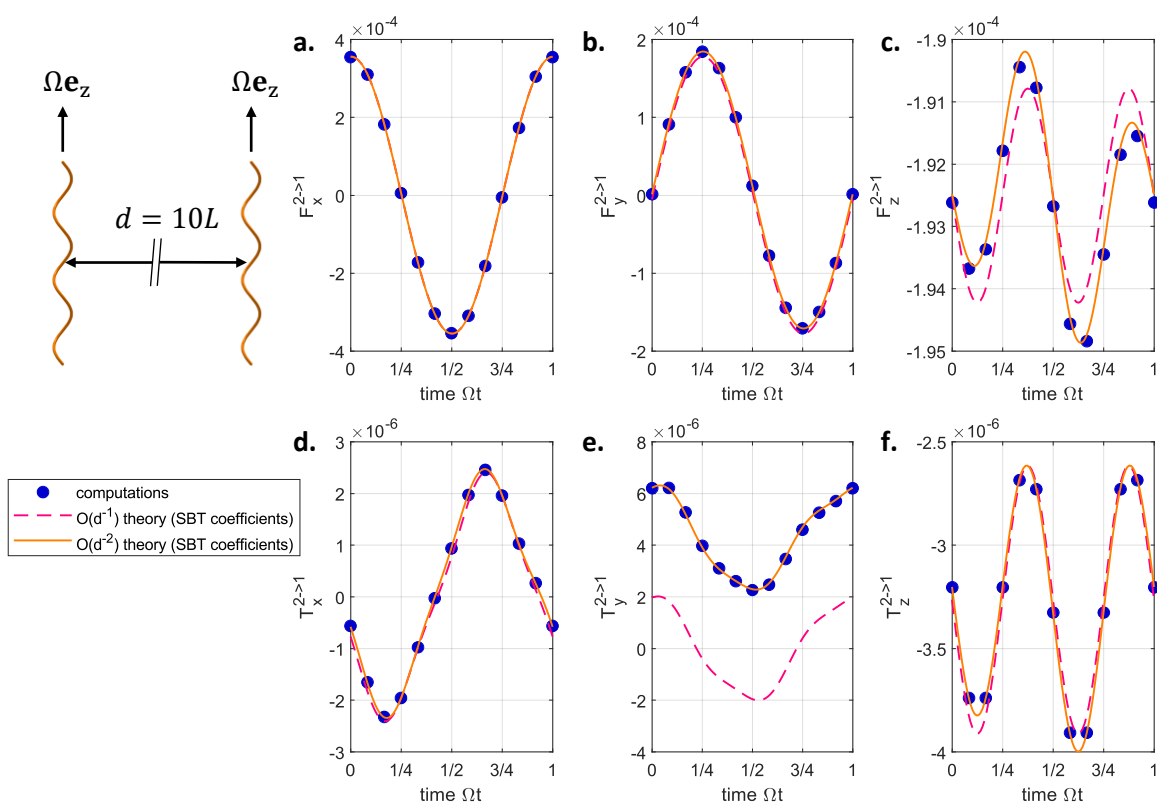


Fig. 6.6 Comparison between computations and the asymptotic theory with SBT coefficients to  $\mathcal{O}(d^{-1})$  and  $\mathcal{O}(d^{-2})$  – continued. The horizontal distance between the helices is now  $d = 10L$ .

## 6.4 Application to helical pumps

To demonstrate the usefulness of our asymptotic theory, we now apply and extend our analytical calculations to the interaction of rotating helical pumps. This particular application of our theory is motivated by previous theoretical studies [18, 43] and experiments [37, 38, 110, 145] with helical micropumps. Experimentally, these systems often take the form of bacterial carpets or forests, where the bacteria are stuck to a substrate while their helical flagellar filaments are free to rotate and pump fluid around.

The specific problem of mixing and pumping by a pair of rotating helices has previously been investigated by Buchmann et al. [18] using the method of regularised Stokeslets. Their study is focused on quantifying the thrust, power, and mixing efficiency of a two-pump system both near a wall and in free space. Here, we consider helical pumps operating in free space only, but we support our SBT numerical computations with analytical results and an illustration of the physical mechanism by which HIs reduce the pumping force exerted by each helix. We also ask if there is any net attraction or repulsion between the helical pumps, and we use our physical understanding of pairwise HIs to make projections about the dynamics of a circular array of helical pumps.

### 6.4.1 Problem specification

We consider two parallel identical helices, rotating with constant angular velocity  $\tilde{\Omega}$ , as illustrated in Fig. 6.7. We may choose the laboratory frame so that the filaments are parallel to the  $z$ -axis and, therefore, the tilt angle  $\theta$  is identically zero. When  $\theta = 0$ , the angles  $\phi$  and  $\chi$  can be used interchangeably to refer to the rotation of the filament about its own axis, because the body-fixed axis  $\mathbf{e}_3$  is parallel to  $\mathbf{e}_z$ . Without loss of generality, we describe the configuration of the filaments using the angle  $\chi = 0$  and a varying phase  $\phi$ . Because they are driven at constant angular velocity, the helices maintain a fixed phase difference  $\phi_2 - \phi_1 = \Delta\phi$ . If we rescale time by  $\tilde{\Omega}^{-1}$ , such that  $\Omega = 1$  in dimensionless terms, then

$$\phi_1 = t, \quad \phi_2 = t + \Delta\phi. \quad (6.75)$$

Since the helices are held in place, they exert a net force on the fluid, which is pumped in the positive  $z$  direction for left-handed helices rotating clockwise.

To characterise the net long-term effect of the helical pumps, we need to consider the time-averaged forces and torques exerted by the rotating filaments on the fluid, so we define the mean

$$\langle Y \rangle = \frac{1}{2\pi} \int_0^{2\pi} Y(t) dt, \quad (6.76)$$

for any time-varying quantity  $Y$  that we are interested in. We may also want to look at the oscillations of this quantity around its mean value, so we define the variance over time as

$$\text{var}(Y) = \frac{1}{2\pi} \int_0^{2\pi} (Y(t) - \langle Y \rangle)^2 dt. \quad (6.77)$$

Because our focus is on the HIs between helical pumps, we need to compare the effect of a helical pump when it is part of an ensemble, to what it otherwise would be if the helical pump was operating on its own. If  $Y(t; d)$  is a force or torque exerted by a helical pump when there is second helical pump operating at distance  $d$  away, then we define

$$Y_\infty(t) = \lim_{d \rightarrow \infty} Y(t; d), \quad (6.78)$$

which is the force or torque that the same helical pump would exert in isolation. For our asymptotic theory, this corresponds to the leading-order terms in §6.2.4. For our computational method, this corresponds to the numerical solution of Eq. (6.60) without the interaction term  $\mathcal{J}[\mathbf{f}_2(s'), \mathbf{d}]$ .

In the next sections, we will look at differences of the form  $\langle Y \rangle - \langle Y_\infty \rangle$  to understand if HIs increase or decrease the net effect of the helical pumps on the fluid, and differences of the form  $\text{var}(Y) - \text{var}(Y_\infty)$  to investigate whether HIs make the pumping fluctuate more or less over time.

## 6.4.2 Computational results

In our simulations, we sample the forces and torques exerted by two helical pumps at twelve regular intervals over one period of rotation, i.e.  $0 \leq \Omega t \leq 2\pi$ . The time-averaged forces and torques obtained in this way are shown in Fig. 6.7, while their variances over time are shown in Fig. 6.8, both for a given phase difference  $\Delta\phi = \pi/4$  and varying inter-filament distance. The geometry of the helices was chosen to be representative of bacterial flagella: helix angle,  $\psi = 0.5043$  rad, filament slenderness,  $\varepsilon = 0.0038$ , and  $N = 2.5$  helical turns.

We will now seek to interpret the trends observed in these computations using our asymptotic theory. Specifically, we want to understand why the interaction between the filaments alters the time average of  $F_z$  and  $T_z$  by  $\mathcal{O}(d^{-1})$ , but their fluctuation over time by  $\mathcal{O}(d^{-2})$ . Meanwhile, for the forces and torques in the  $x$  and  $y$  direction, we want to understand why the time average changes by  $\mathcal{O}(d^{-2})$  due to inter-filament interaction, but their fluctuation over time changes by  $\mathcal{O}(d^{-1})$ .

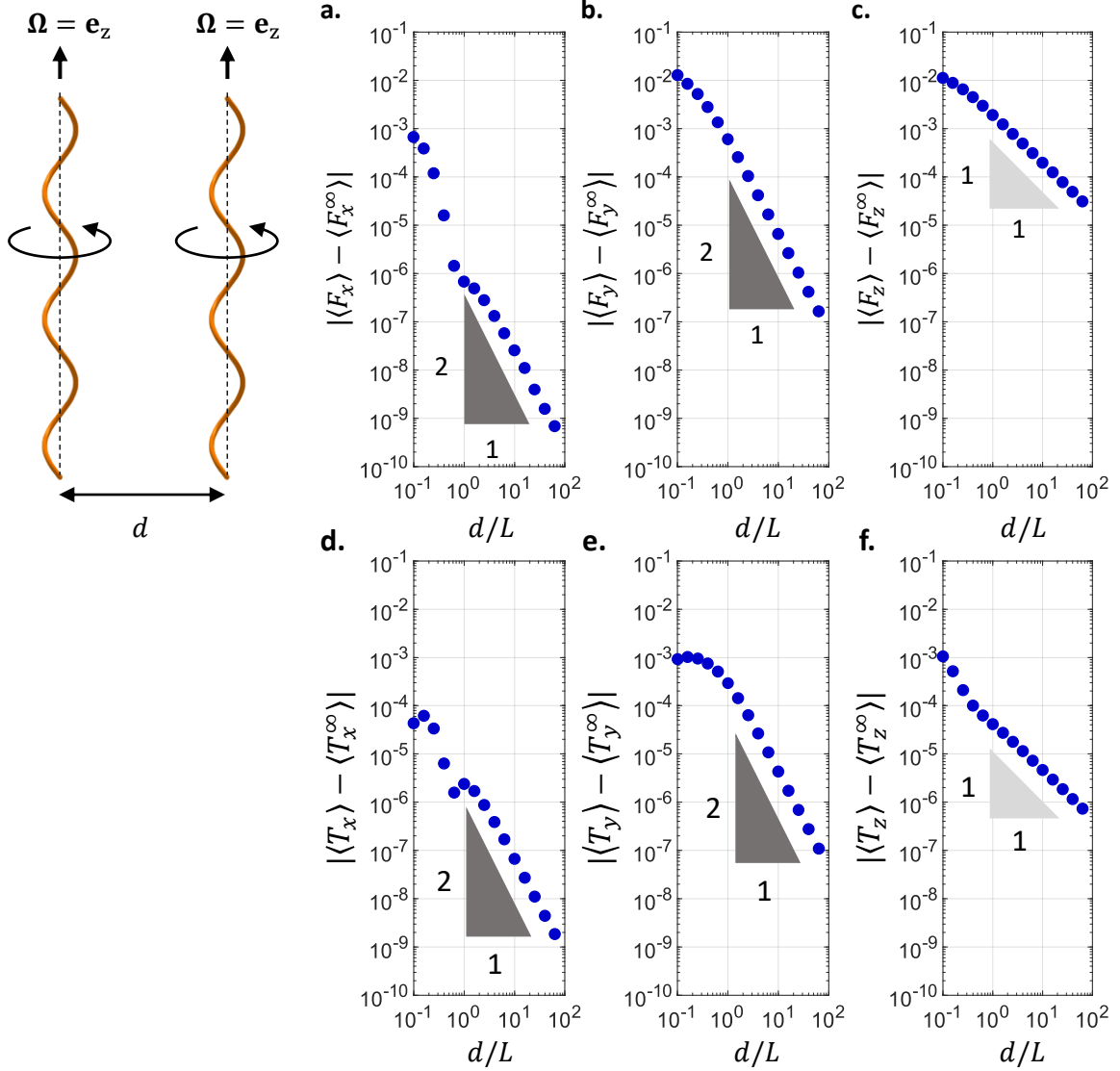


Fig. 6.7 Average forces and torques exerted by the leftmost helix due to the presence of a second parallel helix rotating at a distance  $d$  to the right, with fixed phase difference  $\Delta\phi = \pi/4$ . The data points come from SBT simulations including HIs. The power law triangles indicate that the average forces and torques along the axis of the helix (c,f) are an  $\mathcal{O}(d^{-1})$  effect, while the other forces and torques (a,b,d,e) are an  $\mathcal{O}(d^{-2})$  effect. Simulation parameters:  $\psi = 0.5043$  rad,  $\varepsilon = 0.0038$ ,  $N = 2.5$  helical turns.

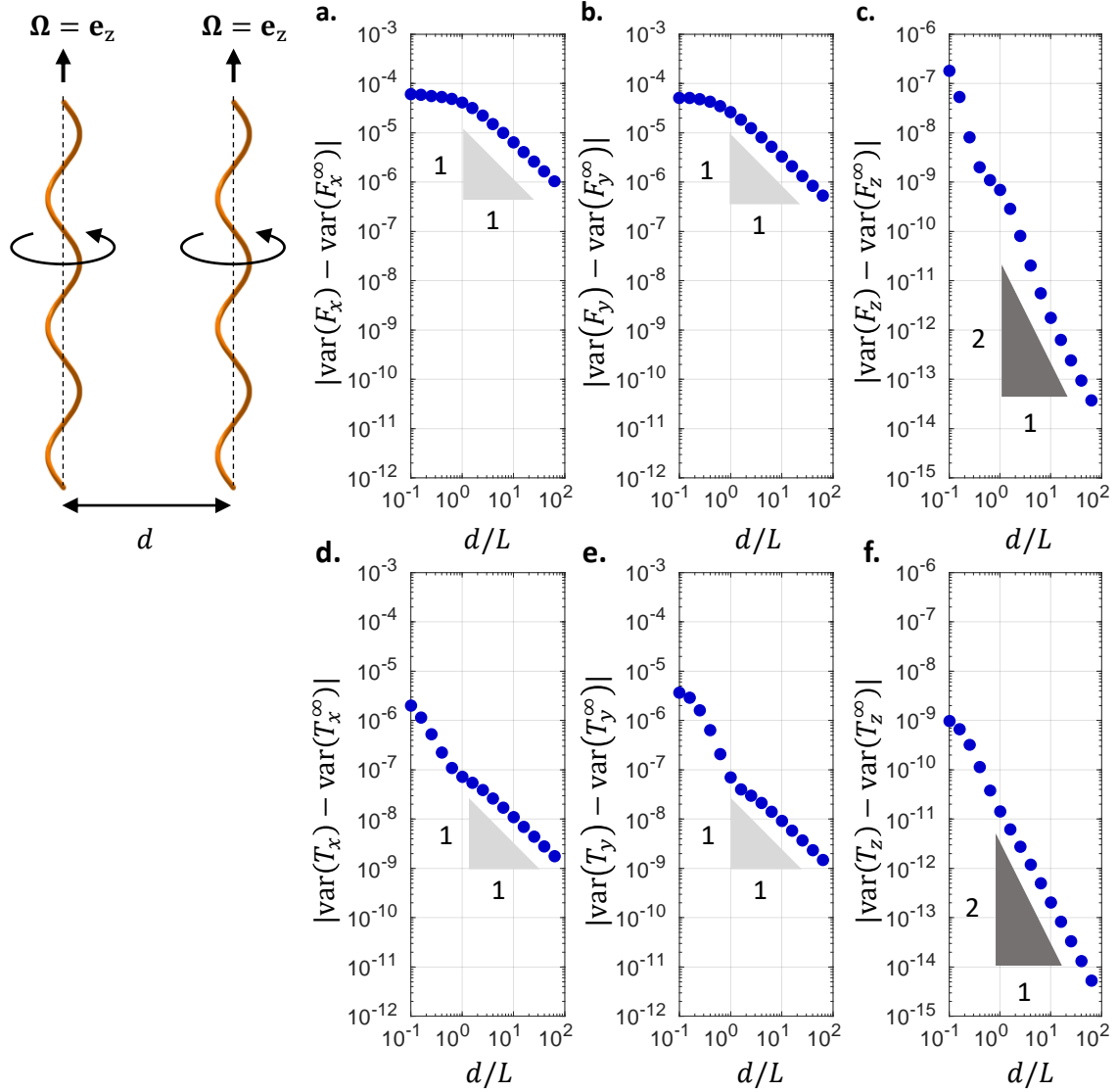


Fig. 6.8 Variance over time in the forces and torques exerted by the leftmost helix due to the presence of a second parallel helix rotating at a distance  $d$  to the right, with fixed phase difference  $\Delta\phi = \pi/4$ . The data points come from SBT simulations including HIs. The power law triangles indicate that the variances in force and torque along the axis of the helix (c,f) are an  $\mathcal{O}(d^{-2})$  effect, while the other forces and torques (a,b,d,e) are an  $\mathcal{O}(d^{-1})$  effect. Simulation parameters:  $\psi = 0.5043$  rad,  $\varepsilon = 0.0038$ ,  $N = 2.5$  helical turns.

### 6.4.3 Asymptotic theory

We start by computing the intrinsic resistance matrix  $\mathbf{S}^{(0)}(0, 0, \phi)$  for a vertical helix with arbitrary phase  $\phi$ , which we will denote from now on simply as  $\mathbf{S}^{(0)}(\phi)$ . We need to apply the change of basis from Eqs. (6.27) with the orthogonal matrix

$$\mathbf{Q}(0, 0, \phi) = \begin{pmatrix} \cos \phi & -\sin \phi & 0 \\ \sin \phi & \cos \phi & 0 \\ 0 & 0 & 1 \end{pmatrix}. \quad (6.79)$$

Because the filament is symmetric under a rotation by angle  $\pi$  around the first vector ( $\mathbf{e}_1$ ) in the body frame basis, the resistance matrix expressed in the body frame has the structure

$$\mathbf{S}_0 = \begin{pmatrix} A_{11} & 0 & 0 & B_{11} & 0 & 0 \\ 0 & A_{22} & A_{23} & 0 & B_{22} & B_{23} \\ 0 & A_{32} & A_{33} & 0 & B_{32} & B_{33} \\ B_{11} & 0 & 0 & D_{11} & 0 & 0 \\ 0 & B_{22} & B_{32} & 0 & D_{22} & D_{23} \\ 0 & B_{23} & B_{33} & 0 & D_{32} & D_{33} \end{pmatrix}, \quad (6.80)$$

noting that  $A_{23} = A_{32}$  and  $D_{23} = D_{32}$  because the resistance matrix is symmetric. Hence, after a rotation by angle  $\phi$ , the matrix can be written as

$$\mathbf{S}^{(0)}(\phi) = \begin{pmatrix} \mathbf{A}(\phi) & \mathbf{B}(\phi) \\ \mathbf{B}(\phi)^T & \mathbf{D}(\phi) \end{pmatrix}, \quad (6.81)$$

where the matrices  $\mathbf{A}(\phi)$ ,  $\mathbf{B}(\phi)$  and  $\mathbf{D}(\phi)$  have the same structure with respect to  $\phi$ , that is

$$\mathbf{A}(\phi) = \begin{pmatrix} A_0 + \Delta A \cos(2\phi) & \Delta A \sin(2\phi) & -A_{23} \sin(\phi) \\ \Delta A \sin(2\phi) & A_0 - \Delta A \cos(2\phi) & A_{23} \cos(\phi) \\ -A_{32} \sin(\phi) & A_{32} \cos(\phi) & A_{33} \end{pmatrix}, \quad (6.82)$$

where we define  $A_0 = (A_{11} + A_{22})/2$  and  $\Delta A = (A_{11} - A_{22})/2$ , and similarly for  $\mathbf{B}(\phi)$  and  $\mathbf{D}(\phi)$  but with  $A_{ij} \mapsto B_{ij}$  and  $A_{ij} \mapsto D_{ij}$  respectively.

Without loss of generality, we may choose our laboratory frame to coincide with the interaction frame of the two filaments, so the directed distance between the two helices is  $\mathbf{d} = d\mathbf{e}_x$ . From Eqs. (6.22) and (6.32), we can write

$$C_{ij}^{(1)}(\phi_1, \phi_2) = -\frac{1}{8\pi} \left( 2S_{i1}^{(0)}(\phi_1)S_{1j}^{(0)}(\phi_2) + S_{i2}^{(0)}(\phi_1)S_{2j}^{(0)}(\phi_2) + S_{i3}^{(0)}(\phi_1)S_{3j}^{(0)}(\phi_2) \right), \quad (6.83)$$

and then replace the expressions for the elements of  $\mathbf{S}(\phi)$  from Eqs. (6.81)-(6.82).

Furthermore, from Eq. (6.53) we derive the matrix

$$\mathbf{P}(\phi) = \begin{pmatrix} \mathbf{P}_B(\phi) & \mathbf{P}_D(\phi) \end{pmatrix}, \quad (6.84)$$

where the matrices  $\mathbf{P}_B(\phi)$  and  $\mathbf{P}_D(\phi)$  have the same structure with respect to the phase  $\phi$ . Because  $\mathbf{e}_1 = \cos \phi \mathbf{e}_x + \sin \phi \mathbf{e}_y$ , we have

$$\mathbf{P}_B(\phi) = \frac{1}{8\pi} \begin{pmatrix} \mathcal{M}_1 \cos \phi & \mathcal{M}_1 \sin \phi & 0 \\ B_{23} \sin(\phi) & -B_{23} \cos(\phi) & -B_{33} \\ \Delta B \sin(2\phi) & B_0 - \Delta B \cos(2\phi) & B_{32} \cos(\phi) \end{pmatrix}, \quad (6.85)$$

and similarly for  $\mathbf{P}_D(\phi)$  but with  $B_{ij} \mapsto D_{ij}$  and  $\mathcal{M}_1 \mapsto \mathcal{M}_4$ . The constants  $\mathcal{M}_1$  and  $\mathcal{M}_4$  are defined in Eq. (6.52) and calculated via RFT in Appendix 6.B.

We are now ready to evaluate the mean forces and torques, and their fluctuations over time, for the specific case of constant rotation about the helical axis  $\mathbf{e}_3 = \mathbf{e}_z$ . The two helical pumps rotate with constant angular velocities  $\boldsymbol{\Omega}_1 = \mathbf{e}_z$  and  $\boldsymbol{\Omega}_2 = \mathbf{e}_z$ , since  $\Omega = 1$  in our chosen units of time. Therefore, the forces and torques exerted by the first filament are

$$\begin{pmatrix} \mathbf{F}_1 \\ \mathbf{T}_1 \end{pmatrix}_i = S_{i6}^{(0)}(t) + \frac{C_{i6}^{(1)}(t, t + \Delta\phi)}{d} + \frac{S_{i6}^{(2)}(t, t + \Delta\phi) + C_{i6}^{(2)}(t, t + \Delta\phi)}{d^2} + \mathcal{O}(d^{-3}), \quad (6.86)$$

where we have substituted the phases  $\phi_1 = t$ ,  $\phi_2 = t + \Delta\phi$ .

#### 6.4.4 Forces and torques parallel to axis of rotation

We begin by looking at the force exerted by the leftmost filament along its helical axis,  $\mathbf{e}_3 = \mathbf{e}_z$ . From Eqs. (6.81),(6.82) and (6.86), we see that

$$F_z(t) = B_{33} + d^{-1}C_{36}^{(1)}(t, t + \Delta\phi) + \mathcal{O}(d^{-2}), \quad (6.87)$$

which is constant at leading order with  $\langle F_z^\infty \rangle = B_{33}$ . The first-order correction, given by Eqs. (6.81),(6.82) and (6.83), will be

$$C_{36}^{(1)} = -\frac{1}{8\pi} [A_{33}B_{33} + A_{23}B_{23} (2 \sin(t) \sin(t + \Delta\phi) + \cos(t) \cos(t + \Delta\phi))], \quad (6.88)$$

which has a non-zero time-average. Hence, the mean thrust provided by the helical pump is

$$\langle F_z \rangle - \langle F_z^\infty \rangle = -\frac{1}{8\pi d} \left( A_{33}B_{33} + \frac{3}{2}A_{23}B_{23} \cos(\Delta\phi) \right) + \mathcal{O}(d^{-2}), \quad (6.89)$$

so indeed the interaction between the filaments changes the mean thrust by  $\mathcal{O}(d^{-1})$ , as seen in the computations. Note that the result in Eq. (6.89) is independent of the method (RFT or SBT) by which we choose to evaluate the coefficients  $A_{33}, B_{33}, A_{23}$  and  $B_{23}$ . In Fig. 6.9 (e), we examine how the  $\mathcal{O}(d^{-1})$  change in thrust depends on the phase difference between the filaments. The asymptotic theory with SBT coefficients provides perfect quantitative agreement in the limit of large  $d$ , while the asymptotic theory with RFT coefficients has an approximate error of 5% but captures all qualitative features.

Because  $F_z$  is constant at leading order, i.e.  $\text{var}(F_z^\infty) = 0$ , its variance over time will be given by

$$\text{var}(F_z) - \text{var}(F_z^\infty) = \frac{1}{d^2} \left( \langle C_{36}^{(1)}(t, t + \Delta\phi)^2 \rangle - \langle C_{36}^{(1)}(t, t + \Delta\phi) \rangle^2 \right) + \mathcal{O}(d^{-3}), \quad (6.90)$$

which is indeed an  $\mathcal{O}(d^{-2})$  effect as seen in computations. This is shown in Fig. 6.10 (e), where we look at how this  $\mathcal{O}(d^{-2})$  effect depends on the phase difference between the filaments. Once again, the asymptotic theory with SBT coefficients provides quantitative agreement, while the theory with RFT coefficients captures the correct shape and order of magnitude.

Moving on to the torque exerted by the leftmost filament along its helical axis, we can derive in a similar way expressions for the time-average

$$\langle T_z \rangle - \langle T_z^\infty \rangle = -\frac{1}{8\pi d} \left( B_{33}^2 + \frac{3}{2}B_{23}^2 \cos(\Delta\phi) \right) + \mathcal{O}(d^{-2}), \quad (6.91)$$

and the fluctuation over time

$$\text{var}(T_z) - \text{var}(T_z^\infty) = \frac{1}{d^2} \left( \langle C_{66}^{(1)}(t, t + \Delta\phi)^2 \rangle - \langle C_{66}^{(1)}(t, t + \Delta\phi) \rangle^2 \right) + \mathcal{O}(d^{-3}), \quad (6.92)$$

which we compare against computations in Figs. 6.9 (f) and 6.10 (f), respectively.

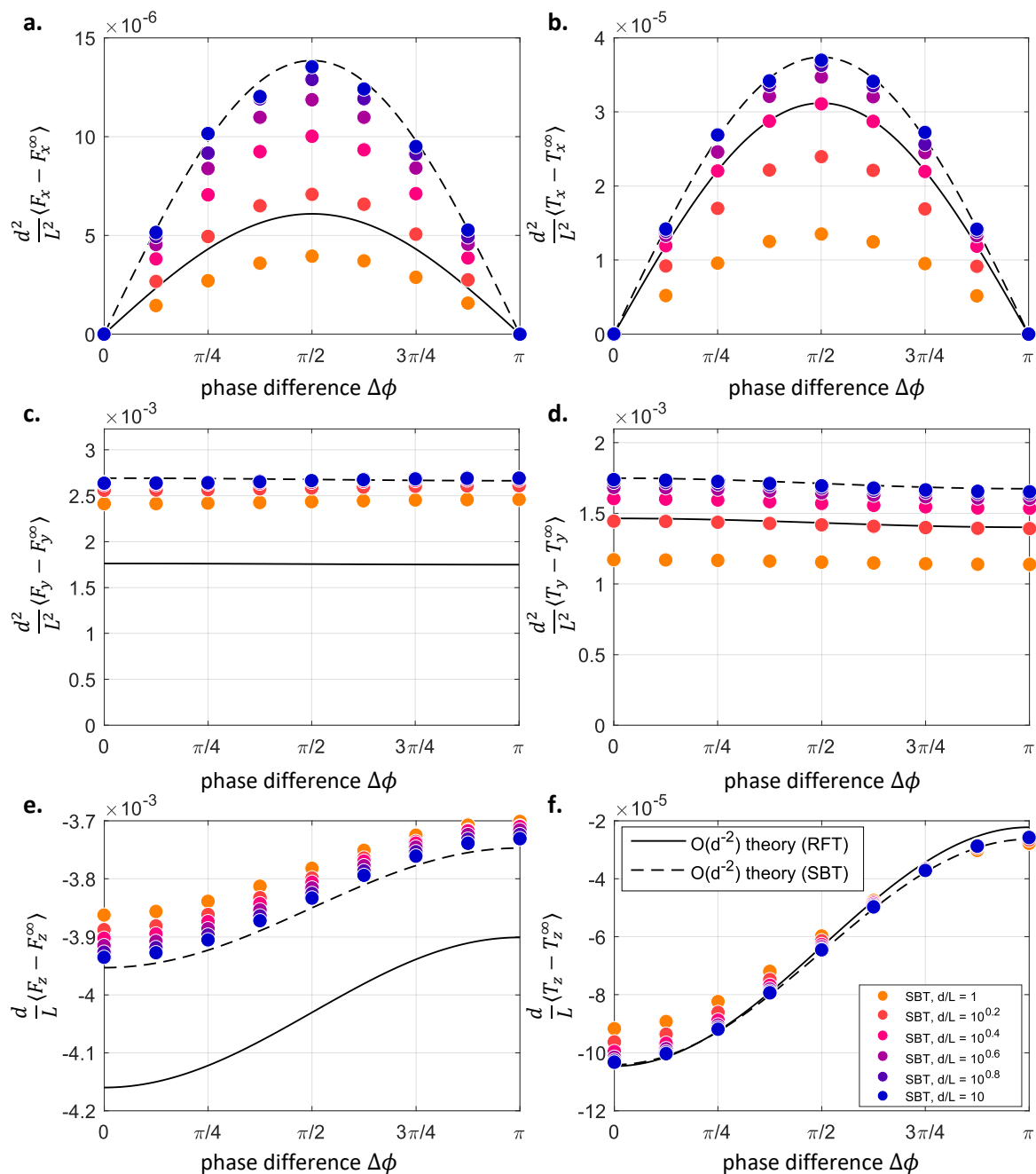


Fig. 6.9 Average forces (a,c,e) and torques (b,d,f) due to HIs between the helices, as a function of the phase difference between filaments. The helix angle,  $\psi = 0.5043$  rad, and filament slenderness,  $\varepsilon = 0.0038$ , were chosen as representative of bacterial flagella. The helices have  $N = 2.5$  helical turns. The legend in (f) applies to all panels.

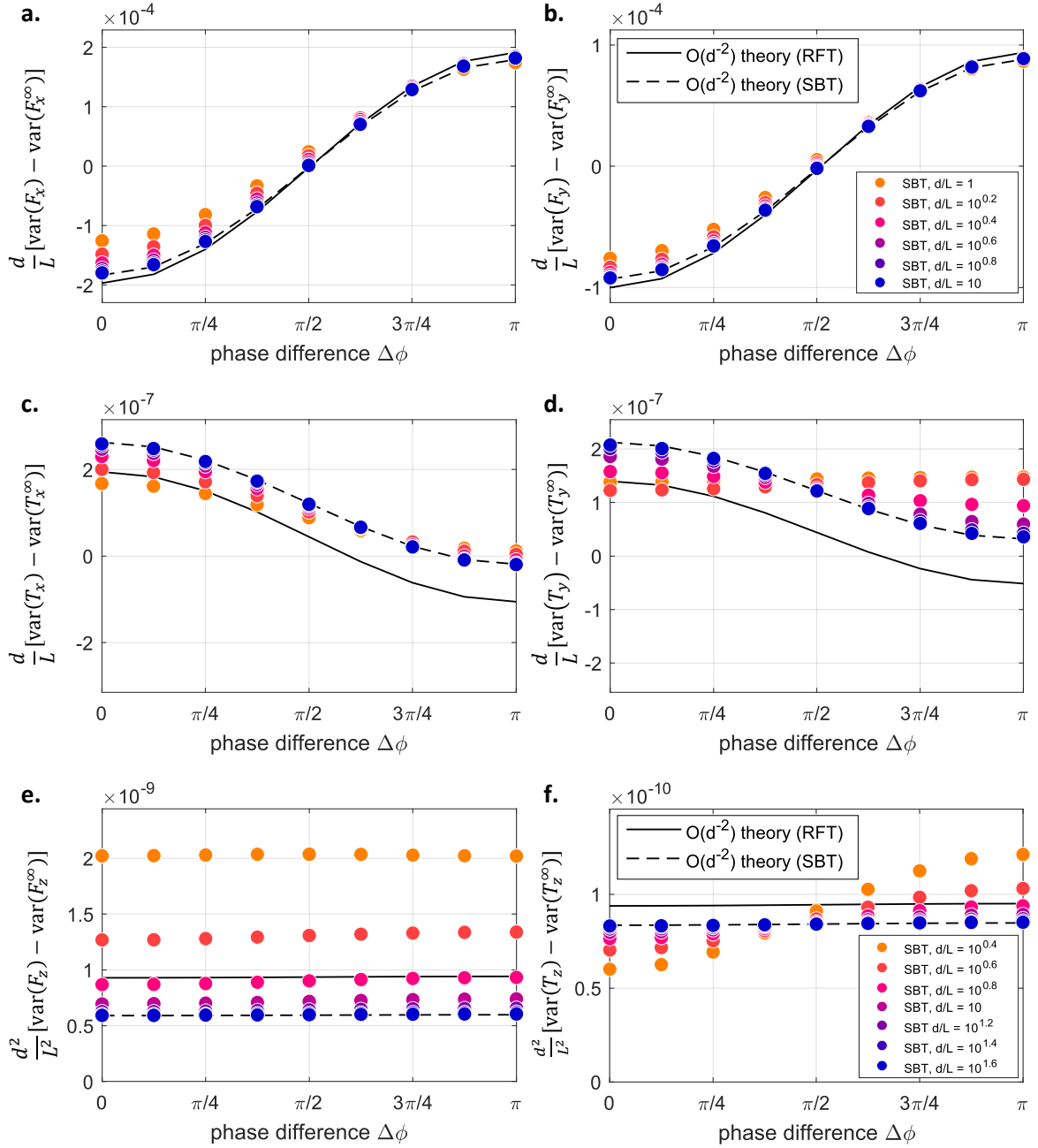


Fig. 6.10 Variance in forces (a,b,e) and torques (c,d,f) due to HIs between the helices, as a function of the phase difference between filaments. The helix angle,  $\psi = 0.5043$  rad, and filament slenderness,  $\varepsilon = 0.0038$ , were chosen as representative of bacterial flagella. The helices have  $N = 2.5$  helical turns. The legend in (b) applies to (a-d), while the legend in (f) applies to (e-f).

### 6.4.5 Forces and torques perpendicular to axis of rotation

Next, we evaluate the forces and torques perpendicular to the filament axis, starting with  $F_x$ . From Eqs. (6.81),(6.82) and (6.86), we see that

$$F_x(t) = -B_{23} \sin(t) + d^{-1} C_{16}^{(1)}(t, t + \Delta\phi) + d^{-2} (S_{16}^{(2)}(t, t + \Delta\phi) + C_{16}^{(2)}(t, t + \Delta\phi)) + \mathcal{O}(d^{-3}), \quad (6.93)$$

which averages out to zero at leading order, i.e.  $\langle F_x^\infty \rangle = 0$ . The first-order correction,

$$C_{16}^{(1)} = -\frac{1}{8\pi} [-A_{23} B_{33} \sin(t) - 2A_0 B_{23} \sin(t + \Delta\phi) - \Delta A B_{23} (2 \cos(2t) \sin(t + \Delta\phi) - \sin(2t) \cos(t + \Delta\phi))], \quad (6.94)$$

also averages out to zero, so the mean of  $F_x$  is an  $\mathcal{O}(d^{-2})$  effect as seen in Fig. 6.7 (a). Using Eqs. (6.37),(6.81) and (6.82), we obtain that

$$\langle S_{16}^{(2)}(t, t + \Delta\phi) \rangle = 0. \quad (6.95)$$

Then, by using Eqs. (6.41),(6.81),(6.82),(6.84) and (6.85), we get that

$$\langle C_{16}^{(2)}(t, t + \Delta\phi) \rangle = -\frac{1}{16\pi} (A_{23} D_{23} + B_{23}^2 + B_{23} \mathcal{M}_1) \sin(\Delta\phi), \quad (6.96)$$

and hence

$$\langle F_x \rangle - \langle F_x^\infty \rangle = -\frac{1}{16\pi d^2} (A_{23} D_{23} + B_{23}^2 + B_{23} \mathcal{M}_1) \sin(\Delta\phi). \quad (6.97)$$

Because the time-average of  $F_x$  is only  $\mathcal{O}(d^{-2})$ , we deduce that the variance over time is

$$\text{var}(F_x) = \langle (-B_{23} \sin(t) + d^{-1} C_{16}^{(1)}(t, t + \Delta\phi) + \mathcal{O}(d^{-2}))^2 \rangle. \quad (6.98)$$

Because  $F_x$  oscillates at leading order with variance  $\text{var}(F_x^\infty) = A_{23}^2/22$ , we deduce that the variance due to HIs is given by

$$\text{var}(F_x) - \text{var}(F_x^\infty) = -\frac{2B_{23}}{d} \langle \sin(t) C_{16}^{(1)}(t, t + \Delta\phi) \rangle + \mathcal{O}(d^{-2}), \quad (6.99)$$

so indeed an  $\mathcal{O}(d^{-1})$  effect as seen in Fig. 6.8 (a). Using Eq. (6.94), we arrive at the final result

$$\text{var}(F_x) - \text{var}(F_x^\infty) = -\frac{B_{23}}{8\pi d} \left( A_{23}B_{33} + 2A_0B_{23} \cos(\Delta\phi) + \frac{1}{2}\Delta AB_{23} \cos(\Delta\phi) \right) + \mathcal{O}(d^{-2}). \quad (6.100)$$

The analytical expressions from Eqs. (6.97) and (6.100) are compared against computational results in Fig. 6.9 (a) and 6.10 (a), respectively. As above, we have quantitative agreement between computations and the asymptotic theory with SBT coefficients in the limit  $d \rightarrow \infty$ , and qualitative agreement with the asymptotic theory with RFT coefficients.

Just as we have done for  $F_x$ , we may compute the time-average of the other transverse forces and torques to  $\mathcal{O}(d^{-2})$ ,

$$\langle F_y \rangle - \langle F_y^\infty \rangle = \frac{1}{16\pi d^2} \left( 2(A_0D_{33} + B_0B_{33}) - (A_{23}D_{23} + B_{23}^2 + B_{23}\mathcal{M}_1) \cos \Delta\phi \right), \quad (6.101)$$

$$\langle T_x \rangle - \langle T_x^\infty \rangle = -\frac{1}{16\pi d^2} (B_{23}D_{23} + B_{23}D_{23} + B_{23}\mathcal{M}_4) \sin \Delta\phi, \quad (6.102)$$

$$\langle T_y \rangle - \langle T_y^\infty \rangle = \frac{1}{16\pi d^2} \left( 2(B_0D_{33} + D_0B_{33}) - (B_{23}D_{23} + B_{23}D_{23} + B_{23}\mathcal{M}_4) \cos \Delta\phi \right). \quad (6.103)$$

Similarly, we can derive the fluctuations over time to  $\mathcal{O}(d^{-1})$ ,

$$\text{var}(F_y) - \text{var}(F_y^\infty) = -\frac{B_{23}}{8\pi d} \left( A_{23}B_{33} + \left( A_0 - \frac{3}{2}\Delta A \right) B_{23} \cos(\Delta\phi) \right), \quad (6.104)$$

$$\text{var}(T_x) - \text{var}(T_x^\infty) = -\frac{D_{23}}{8\pi d} \left( B_{32}B_{33} + \left( 2B_0 + \frac{1}{2}\Delta B \right) B_{23} \cos(\Delta\phi) \right), \quad (6.105)$$

$$\text{var}(T_y) - \text{var}(T_y^\infty) = -\frac{D_{23}}{8\pi d} \left( B_{32}B_{33} + \left( B_0 - \frac{3}{2}\Delta B \right) B_{23} \cos(\Delta\phi) \right). \quad (6.106)$$

The analytical expressions from Eqs. (6.101)-(6.106) are compared against computational results in Fig. 6.9 (b)-(d) and 6.10 (b)-(d).

The reason why we have calculated the variances in forces and torques over time is to understand whether HIs dampen or enhance fluctuations in the dynamics of the helical pumps. The results in Fig. 6.10 suggest that HIs tend to increase the variances over time for most forces and torques. The only exceptions we observe, for this set of parameters, are the forces  $F_x$  and  $F_y$  when  $|\Delta\phi| < \pi/2$  and the torque  $T_x$  in a small interval around  $\Delta\phi = \pi$ .

### 6.4.6 Deducing the dynamics of the second filament

We remind the reader that the forces and torques plotted in Fig. 6.9 are those exerted by the leftmost filament *on* the fluid - see Fig. 6.12 (a). Relative to this, the rightmost filament is in the positive  $x$  direction, and accordingly we have taken  $\hat{\mathbf{d}} = \mathbf{e}_x$  in our calculation of second-order corrections from Eqs. (6.97), (6.101)-(6.103). To obtain the forces and torques exerted by the rightmost filament, we can rotate our coordinate system by an angle  $\pi$  about the  $z$ -axis. First of all, this swaps the filaments around and, hence, reverses the sign of the phase difference. It also changes the signs of all  $x$  and  $y$  components, but not the  $z$  components. Hence, the average dynamics of the second filament satisfy the relations  $-\Gamma_{x,y}^{(2)}(\Delta\phi) = \Gamma_{x,y}^{(1)}(-\Delta\phi)$  and  $\Gamma_z^{(2)}(\Delta\phi) = \Gamma_z^{(1)}(-\Delta\phi)$ , where  $\Gamma^{(k)}$  is a placeholder for the time-averaged force or torque exerted by the  $k$ th filament on the fluid.

Because  $\langle F_x \rangle$  and  $\langle T_x \rangle$  depend on the sine of the phase difference (see Eqs. (6.97) and (6.102)), the rightmost helix exerts the same average force  $\langle F_x \rangle$  and torque  $\langle T_x \rangle$  as the leftmost helix. Meanwhile, for  $\langle F_y \rangle$  and  $\langle T_y \rangle$ , which depend on the cosine of the phase difference (see Eqs. (6.101) and (6.103)), the rightmost helix exerts an equal and opposite average force and torque to the leftmost helix. Finally, the average  $\langle F_z \rangle$  and  $\langle T_z \rangle$  are the same for the two helices, because the two quantities depend on the cosine of the phase difference (see Eqs. (6.89) and (6.91)), and the sign of  $z$  components has not changed due to the rotation.

### 6.4.7 Interpretation of results

We now provide some physical interpretation for the earlier computational results, focusing on the effect that HIs have on the pumping force exerted by each helix, and whether HIs lead to any attraction or repulsion between the helical pumps.

#### Deficit in pumping force

Since the main purpose of the helical pumps is to push fluid along their axes, we start by explaining how HIs affect the vertical pumping force,  $\langle F_z \rangle$ . The leading-order dynamics of a rotating helical pump are illustrated in Fig. 6.11 (a) using a local description of the problem (i.e. no end effects). The local velocity of the centreline relative to the fluid is shown at various points along the filament. At one of these points we decompose the velocity into the directions tangent and perpendicular to the filament. Because the perpendicular drag coefficient on a slender rod is higher, by roughly a factor of two, than the parallel drag coefficient, this gives rise to a leading-order viscous drag on the filament,  $-\mathbf{f}_1^{(0)}(s)$ , that has a negative vertical component. Below the three-dimensional picture of the filament, we draw the projection of the filament centreline onto the horizontal plane. At each point on

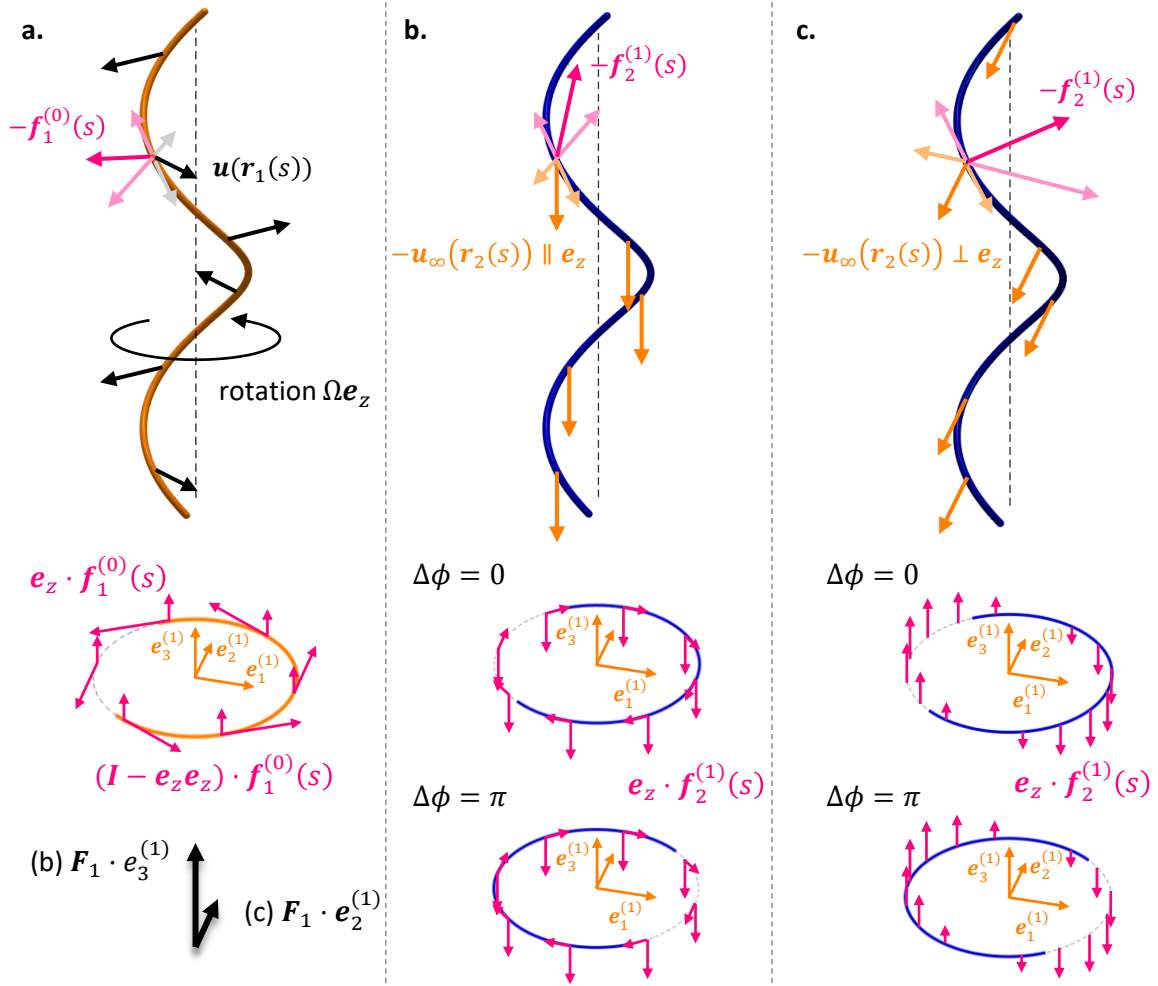


Fig. 6.11 (Not to scale) Physical mechanism for the reduction in pumping force due to HIs. Top panels illustrate the local velocity of the filament relative to the surrounding fluid. Lower panels show the periodic force density along the filament, rendered at points along a horizontal projection of the centreline. The total force and torque exerted by the helical pump are obtained by integrating the force density around the circle as many times as needed. (a) Due to the anisotropic drag on the slender filament, a rotating helix exerts a net force along its axis of rotation,  $\mathbf{e}_3^{(1)}$ . If the helix does not have an integer number of turns, there is also a net component of the force along the  $\mathbf{e}_2^{(1)}$  direction, due to a “surplus” of filament on one side (indicated by a thick orange arc on the circular projection of the centreline). (b) Changes to the force density along the second filament due to the  $\mathbf{e}_3^{(1)}$  component of the force exerted by the first filament on the fluid. (c) Likewise for the  $\mathbf{e}_2^{(1)}$  component of the force.

this circular projection, we show the corresponding force density exerted by the filament on the fluid,  $\mathbf{f}_1^{(0)}(s)$ , decomposed into vertical and horizontal components. Notice that the force density simply rotates about the axis  $\mathbf{e}_3^{(1)} = \mathbf{e}_z$  as we rotate around the circle, due to the rotational symmetry of the system. The total force and torque exerted by the helical pump are obtained by integrating the force density along the entirety the filament, or equivalently by integrating around the circular projection as many times as needed. For left-handed helices rotating counter-clockwise, the vertical components of the force density are positive, so the helical pump exerts a net positive force in the  $\mathbf{e}_3^{(1)}$  direction. The fluid is pumped vertically upwards. By integrating the horizontal components of the force density, we also obtain a net counter-clockwise torque that must be applied to the helical pump to keep it rotating. Furthermore, if the helical filament does not have an integer number of turns, there will be a surplus of filament on one side, indicated by a thick orange line on the circular projection. This means that the helical pump also exerts a net horizontal force on the fluid along the  $\mathbf{e}_2^{(1)}$  direction.

In Fig. 6.11 (b) and (c) we explain how the  $\mathbf{e}_3^{(1)}$  and the  $\mathbf{e}_2^{(1)}$  components of the leading-order force exerted by the first helical pump, respectively, affect the pumping force exerted by the second helical pump. Firstly, the  $\mathbf{e}_3^{(1)}$  component of the pumping force exerted by one helical pump on the fluid leads to an upward vertical flow at the position of the other helical pump. This flow is uniform to leading-order in the distance between the filaments. Therefore, the second filament appears to be moving in the negative vertical direction relative to the fluid, with velocity  $-\mathbf{u}_\infty(\mathbf{r}_2(s))$ , as indicated at various points along the filament in Fig. 6.11 (b). Following the same procedure as above, we can determine the local force density along the second filament and depict it along the horizontal projection of the centreline. The first-order change in the force density,  $\mathbf{f}_2^{(1)}(s)$ , has negative vertical components, because the second filament appears to be moving downward with respect to the background flow. When integrated along the filament, this leads to a deficit in pumping force due to the HIs between the helical pumps. This is confirmed by the negative sign in Fig. 6.9 (e). Note that this effect is independent of the phase difference between the filaments, because the force density has a constant vertical component along the entire filament, due to rotational symmetry. By integrating the horizontal components of the force density, we also deduce that HIs lead to a deficit in the torque exerted by the helical pumps, as seen in Fig. 6.9 (f) as well. Hence, less power is needed to actuate two helical pumps with the same angular velocity, if they are rotating in parallel.

Secondly, the  $\mathbf{e}_2^{(1)}$  component of the leading-order force exerted by the first helical pump generates a horizontal flow at the position of the second helical pump, which is again depicted at various points along the filament in Fig. 6.11 (c). Because the flow is horizontal, we no

longer have rotational symmetry so the force density is variable along the filament. Note that we only depict the vertical components of the force in the lower panels of Fig. 6.11 (c), to avoid overcrowding the diagram. Unlike Figs. 6.11 (a) and (b), where the force density simply rotates around the vertical axis as we go around the centreline, in Fig. 6.11 (c) we observe that the vertical component of the force density depends on the alignment of the tangent vector and the direction of the flow. Where the velocity of the filament relative to the background flow,  $-\mathbf{u}_\infty(\mathbf{r}_2(s))$ , has a positive (or negative) component in the direction of the local tangent, the force density has a positive (or negative) vertical component. Hence, this particular contribution of HIs to the pumping force will depend on the phase difference between the two helical pumps. If the two are in-phase,  $\Delta\phi = 0$  and  $\mathbf{e}_2^{(2)} = \mathbf{e}_2^{(1)}$ , there is a surplus of negative vertical force as we integrate along the centreline. If the pumps are anti-phase,  $\Delta\phi = \pi$  and  $\mathbf{e}_2^{(2)} = -\mathbf{e}_2^{(1)}$ , there is a surplus of positive vertical force instead. This dependence on the phase difference is confirmed by Fig. 6.9 (e), where the deficit in pumping force is greater when the filaments are in-phase than anti-phase.

It is important to emphasise that the dominant effect here comes from the flow discussed in Fig. 6.11 (b), which is a result of integrating a constant force along the entire length of the filament. The effect described in Fig. 6.11 (c) is a correction that comes from integrating forces along just a fraction of the filament, if the helix deviates from an integer number of turns. Regardless of the phase difference between the helical pumps, each of them will pump fluid with less force when they are interacting, because each filament tries to push fluid that has already been entrained by the other pump. The deficit is greatest when the filaments are in-phase, because they entrain the fluid in the same direction both vertically and horizontally, whereas filaments that are anti-phase will work against each other in the horizontal plane (Fig. 6.11 (c)).

### Attraction vs. repulsion

We have so far considered the average forces and torques exerted by the filaments on the fluid while they are held in place, except for rotating about the vertical axis. It is also important to consider what would happen to the helices if they were not held in place, but free to move in response to the forces and torques exerted on them by the fluid. Note that the time averages we previously computed assumed that the helices remain vertical. However, we may still use these results to get a sense for what happens in the early stages, when the axes of the helices are still close to vertical.

In Fig. 6.12 (b) and (c) we show the horizontal components of the average force exerted by the fluid on two left-handed filaments rotating counter-clockwise. The relative directions of the forces and torques on the two helices were established in §IV F. The first observation

is that, at second order, there is no net attraction or repulsion between the helices. Previous theoretical work had ruled out the possibility of attraction or repulsion between two helices rotating with zero phase difference, based on symmetry arguments [111]. Our findings add to that observation by excluding any net attraction or repulsion between helices rotating with any phase difference, so long as they are parallel. Instead, we discover a net migration to one side, because the two filaments experience the same force along the  $x$  direction – Fig. 6.12 (b). The direction of migration depends on the sine of the phase difference, so it is not a consistent behaviour. On the other hand, the helices will be swirled around by the fluid in the counter-clockwise direction, because they experience equal and opposite forces along the  $y$  direction – Fig. 6.12 (c). The direction of the swirl is consistent with the individual rotation of the helices, and this effect is persistent across all phase differences, as demonstrated by Fig. 6.9 (c).

Note from Fig. 6.9 (a)-(d) that the sign of  $\langle T_x \rangle$  is the same as  $\langle F_x \rangle$ , likewise for  $\langle T_y \rangle$  and  $\langle F_y \rangle$ . Hence, the arrows in Fig. 6.12 (b) and (c) could equally well represent the horizontal components of the torques exerted by the fluid on the filaments. The key observation here is that, due to equal and opposite average torques along  $y$ , the helices would initially experience a splaying out effect where the fluid pushes the tips of the helical pumps apart (the tips being the ends pointing in the same direction as the angular velocity) and brings their bases together.

### 6.4.8 Outlook: circular array of helical pumps

Once we understand the basic principles of pairwise HIs between helical pumps, it is natural to consider ensembles with more than two helical pumps. The simplest example is a ring of regularly spaced helical pumps, illustrated from the top in Fig. 6.12 (d). For simplicity, let us consider a ring of sufficiently large radius that the dominant HIs come from the nearest neighbours only. We expect the dominant contribution to the horizontal force to come from  $\langle F_y \rangle$ , which is two orders of magnitude larger than  $\langle F_x \rangle$  – cf. Fig 6.9 (a) and (c). The effects of  $\langle F_y \rangle$  are also consistent, compared to  $\langle F_x \rangle$  which depends strongly on the phase difference. In conclusion, we need to focus on the force components perpendicular to the distance between nearest neighbours, depicted in Fig. 6.12 (c).

By adding the contributions from the left nearest neighbour (L) and the right nearest neighbour (R), we find that the net effect is a force along the circumference of the ring. Therefore, the ring of helical pumps experiences a tendency towards counter-clockwise swirling about the centre. If instead of forces we consider the torques  $\langle T_y \rangle$ , which are likewise dominant over  $\langle T_x \rangle$ , we find once again that there is a net torque along the circumference of the circle. This means that the tips of the helical pumps have a tendency to spread out

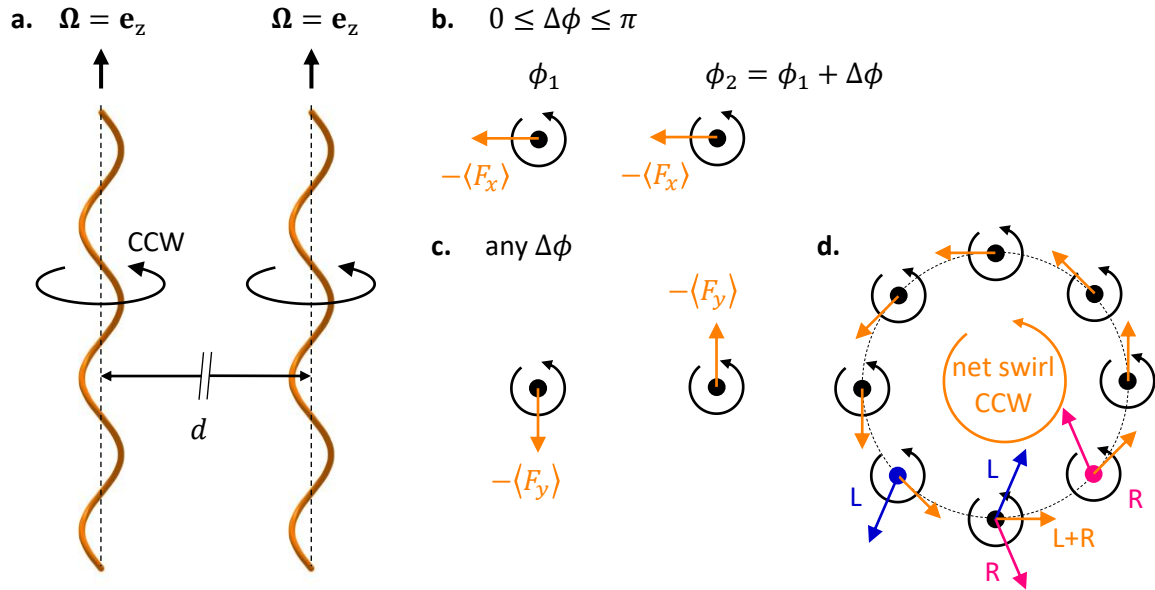


Fig. 6.12 Basic principles of HIs between helical pumps. (a) Minimal setup with two helical pumps rotating with constant angular velocity around their axes. (b) There is no net attraction or repulsion between the two rotating helices (cf. symmetry arguments for zero phase difference in Ref. [111]), but rather a sideways migration whose sign depends on the phase difference. (c) There is a persistent (i.e. independent of phase difference) swirling effect in the same direction as the rotation of the helices. (d) A ring of helical pumps would initially experience counter-clockwise swirling (due to the forces  $-\langle F_y \rangle$  exerted by the fluid) and outward splaying of the tips (due to the torques  $-\langle T_y \rangle$  exerted by the fluid).

and away from the centre of the ring. Note that the sign of these two hydrodynamic effects (swirling and splaying) would stay the same if we include more than nearest neighbour interactions, due to the symmetry of the system.

## 6.5 Discussion

In this final section, we summarise the analytical and computational results presented in this chapter, we discuss the advantages and limitations of our theory for HIs between slender filaments, and we suggest potential applications for the theory.

### 6.5.1 Summary of results

In this chapter, we have considered the problem of HIs between slender filaments in viscous fluids. We have approached the topic theoretically, focusing on the case of two interacting rigid filaments whose dynamics can be described by an extended resistance matrix, Eq. (6.5).

We have solved for the extended resistance matrix and the force distribution along two arbitrarily-shaped filaments as series expansions in inverse powers of the distance between the filaments, up to second-order corrections. Our asymptotic results from §6.2 are valid in the limit of small aspect ratio,  $\varepsilon \ll 1$ , and in the regime,  $d > L$ , where the inter-filament separation is greater than the contour length of the filament. Although HIs decrease in magnitude with increasing distance between the filaments, they continue to play a leading-order role important to physical mechanisms such as synchronisation and self-organisation. This provides a strong motivation for developing an analytical theory of HIs to advance our fundamental understanding of such phenomena. While other studies have dealt with the limit  $d \ll L$ , here we have chosen to focus on the regime  $d > L$ , which can provide just as many valuable physical insights.

We have evaluated the coefficients in the asymptotic series expansion using both resistive-force theory (RFT) and slender-body theory (SBT), and validated our asymptotic theory against numerical simulations in §6.3. In the final part, §6.4, motivated by bacterial microfluidic pumps [38, 43, 110, 145], we have demonstrated the usefulness of our asymptotic theory by applying it to the interaction of two rotating helical pumps. Here, we have identified the dependence of forces and torques on the distance and phase difference between the helices, which is illustrated in Figs. 6.9 and 6.10 and made explicit in Eqs. (6.89)-(6.92), (6.97), (6.100)-(6.106). The analytical expressions are also implicitly dependent on the helix geometry through the components  $A_{ij}, B_{ij}, D_{ij}$  of the single-helix resistance matrix, which are given in Appendix 6.A, and the force moments  $\mathcal{M}_i$  from Appendix 6.B.

Our theory provides us with new physical understanding of the HIs between helical pumps. We find that the pumping force exerted by each rotating helix is reduced due to HIs, and the reduction is greatest when the helical pumps are rotating in phase with each other. Similarly, the torque required to rotate the two helical pumps is lowest when they are in-phase and greatest when they are antiphase, as the helices are working against each other in the latter case. Because we include second-order corrections in our calculation of the average forces and torques acting on the helical pumps, we are able to determine that there is no net attraction or repulsion between the filaments, but rather a sideways migration whose sign depends on the phase difference. However, we identify two persistent hydrodynamic effects which are independent of the phase difference: a swirl in the direction of rotation of the helices and a splaying out at the tips of the helical pumps (i.e. the ends pointing in the same direction as the angular velocity). We believe that these effects are consistent with the behaviour observed by Kim and co-authors in the initial stage (i.e. when the filaments are still nearly parallel) of their macroscopic-scale experiments of flagellar bundling [113], despite the fact that our theory is intended for  $d > L$  while the experiments were carried out in the

$d < L$  regime. This suggests that there may be fundamental similarities in the HIs between helical filaments across different regimes of separation. Without further investigation, it is not possible to quantify in which ways the HIs between bacterial flagella within a bundle ( $d < L$ ) are qualitatively different from the HIs between flagellar filaments that are further apart ( $d > L$ ). Our theory provides a starting point to investigate these questions further, analytically.

### 6.5.2 Advantages and limitations

The primary purpose of our asymptotic theory is to provide a method to calculate, analytically, the specific HIs between two rigid filaments, as opposed to previous theoretical studies which focus on the bulk properties of suspensions of fibers [137, 190]. The asymptotic theory with RFT coefficients is suitable for this purpose, since all the coefficients have closed-form solutions provided in Appendices 6.A and 6.B. The asymptotic theory with SBT coefficients can provide a quantitative improvement on some of these results, since SBT calculates the force density along the filament with algebraic accuracy, but the ultimate goal of the asymptotic theory is to capture the qualitative features of HIs such as the dependence on filament geometry and relative configuration.

A secondary use of the asymptotic theory could be to speed up the simulation of long time-evolution problems governed by HIs or, in special cases, to provide a way to integrate the equations of motion by hand. The reduction in computation time would come from removing the need to recompute the interaction term  $\mathcal{I}$  (see §6.3.1) at each time step, as the relative orientation of the two filaments changes. Our asymptotic series expansion provides expression for the HIs between filaments in terms of the resistance matrix of a single filament, which can be precomputed (either by evaluating the analytical expressions from RFT, or by numerically solving the integral equations of SBT for a single filament) and updated at each time step using a rigid-body rotation to reflect changes in filament orientation. This relies on the filaments being rigid so that the shape of their centreline does not change over time. However, we reiterate that the main purpose of our asymptotic theory is to provide a way to evaluate the HIs between filaments analytically, and not to challenge well-established computational methods. For the simulation of flexible fibers, there exist specialised computational methods that can handle large numbers of filaments with HIs efficiently [147, 205].

One advantage of the current asymptotic theory is the compactness of the final results in Eqs. (6.32), (6.37), and (6.41), which means they can be used to develop analytical models for certain hydrodynamic phenomena that have predominantly been studied computationally until now. We demonstrate this in the next chapter, where we consider the issue of hydrodynamic

synchronisation between rotating bacterial flagella. Another advantage is that the results of Eqs. (6.32), (6.37), and (6.41) are valid for arbitrary filament shapes, in contrast to other theories of HIs which require a small-amplitude assumption for the shape of the filament.

However, no theory is without its limitations. One important restriction is that, within the current setup, our asymptotic theory can only handle filaments in an infinite fluid domain. Further work would be needed to account for external surface such as the cell body of the organism to which the filaments might be attached. Just as important is the fact that our asymptotic theory, in its current state, can only fully describe the interaction of rigid filaments. A possible extension is to refine the series expansions for the force distributions from Eqs. (6.28) and (6.35), which are valid for any type of filament, in order to obtain a comprehensive theory for HIs between flexible filaments as well. We also note that we have neglected HIs due to moment distributions along the centrelines of the filaments. This is because such contributions would scale like  $\varepsilon^2/d^2$  and would always be smaller than the second-order corrections from the force distributions, which scale like  $\log(\varepsilon)/d^2$  and are the final terms included in our asymptotic theory.

We have also considered the interactions between multiple slender filaments but only in a qualitative way, when discussing the physics of HIs in a circular array of helical pumps. Our asymptotic theory can be easily extended to include HIs between more than two filaments, because it is based on the method of reflections. With this approach,  $j$ th-order corrections to the extended resistance matrix come from hydrodynamic effects that have reflected  $j$  times between the filament that induces the flow and the filament that feels its effect. The only complication comes from the fact that, in a collection of  $N > 2$  filaments, there is no single expansion parameter. Instead, there are  $\frac{1}{2}N(N-1)$  pairwise distances between the filaments. Hence, the order in which corrections appear in the series expansion must be considered carefully, unless the filaments are so far apart that it is sufficient to consider first-order corrections due to pairwise interactions.

### 6.5.3 Potential applications

There are many possible applications for the theoretical results presented in this chapter, beyond the case of helical pumps discussed in §6.4. Our asymptotic theory can be used to investigate the collective swimming of elongated microorganisms like the *Spirochaetes* and *Spiroplasma*, as well as some artificial micro-swimmers (e.g. helical micromachines actuated by an external magnetic field). Amongst all moving appendages in the microscopic world, the closest to being rigid are the bacterial flagellum and nodal cilia, which makes them more suitable for applications of our asymptotic theory. Although the distance between flagellar filaments within a bundle is less than their contour length, there are other situations

in which bacterial flagella interact on a larger length scale, making these problems directly relevant to our asymptotic theory. Examples include the HIs between filaments at either pole of an amphitrichous bacterium or filaments belonging to different cells in a sparse bacterial carpet or swarm. Following an extension of our theory to the case of flexible filaments, as discussed before, one could also examine the HIs between eukaryotic cilia and flagella, or between fluctuating polymeric filaments in the cytoplasm, such as actin filaments and microtubules. Another, more technical, avenue for future research will be to bridge the gap between near-field ( $d \ll L$ ) theories of HIs [142] and the present theory ( $d > L$ ).

This chapter is based on a research article that will appear in *Physical Review Fluids* [207]. The dissertation author is the primary investigator and author of this article. Modifications were made to the text and figures for consistency with the rest of the dissertation, and to avoid overlap with other chapters.

## Appendix 6.A Calculating the leading-order resistance matrix from RFT

We calculate the leading-order resistance matrix from Eq. (6.27) using the resistive-force theory (RFT) representation of the force density from Eq. (6.54). In the body frame of the filament, i.e. relative to basis vectors  $\{\mathbf{e}_1, \mathbf{e}_2, \mathbf{e}_3\}$ , the local resistance tensor  $\boldsymbol{\Sigma}(s)$  (defined in Eq. (6.54)) can be written as

$$\boldsymbol{\Sigma}_{11} = c_{\perp} + (c_{\parallel} - c_{\perp}) \sin^2 \psi \sin^2(\pi N s), \quad (6.107)$$

$$\boldsymbol{\Sigma}_{22} = c_{\perp} + (c_{\parallel} - c_{\perp}) \sin^2 \psi \cos^2(\pi N s), \quad (6.108)$$

$$\boldsymbol{\Sigma}_{33} = c_{\perp} + (c_{\parallel} - c_{\perp}) \cos^2 \psi, \quad (6.109)$$

$$\boldsymbol{\Sigma}_{12} = -\sigma(c_{\parallel} - c_{\perp}) \sin^2 \psi \sin(\pi N s) \cos(\pi N s) = \boldsymbol{\Sigma}_{21}, \quad (6.110)$$

$$\boldsymbol{\Sigma}_{13} = -(c_{\parallel} - c_{\perp}) \sin \psi \cos \psi \sin(\pi N s) = \boldsymbol{\Sigma}_{31}, \quad (6.111)$$

$$\boldsymbol{\Sigma}_{23} = \sigma(c_{\parallel} - c_{\perp}) \sin \psi \cos \psi \cos(\pi N s) = \boldsymbol{\Sigma}_{32}, \quad (6.112)$$

where we have used the components of the tangent vector from Eq. (6.4).

From Eqs. (6.25) and (6.26) we write down an equivalent definition of matrix  $\mathbf{A}$  as

$$A_{ij} = \int_{-1}^{+1} \Sigma_{ij}(s) ds. \quad (6.113)$$

Using the integrals in Appendix 6.C, we determine the components of matrix  $\mathbf{A}$ , which describes the force exerted by a translating filament,

$$A_{11} = \int_{-1}^{+1} \Sigma_{11} ds = 2c_{\perp} + (c_{\parallel} - c_{\perp}) \sin^2 \psi \left( 1 - \frac{\sin(2\pi N)}{2\pi N} \right), \quad (6.114)$$

$$A_{22} = \int_{-1}^{+1} \Sigma_{22} ds = 2c_{\perp} + (c_{\parallel} - c_{\perp}) \sin^2 \psi \left( 1 + \frac{\sin(2\pi N)}{2\pi N} \right), \quad (6.115)$$

$$A_{33} = \int_{-1}^{+1} \Sigma_{33} ds = 2(\cos^2 \psi c_{\parallel} + \sin^2 \psi c_{\perp}), \quad (6.116)$$

$$A_{12} = \int_{-1}^{+1} \Sigma_{12} ds = 0 = A_{21}, \quad (6.117)$$

$$A_{13} = \int_{-1}^{+1} \Sigma_{13} ds = 0 = A_{31}, \quad (6.118)$$

$$A_{23} = \int_{-1}^{+1} \Sigma_{23} ds = \sigma(c_{\parallel} - c_{\perp}) \sin \psi \cos \psi \frac{2 \sin(\pi N)}{\pi N} = A_{32}. \quad (6.119)$$

Similarly, from Eqs. (6.25) and (6.26) we write down an equivalent definition of matrix  $\mathbf{B}$  as

$$B_{ij} = \int_{-1}^{+1} \varepsilon_{jkl} r_k(s) \Sigma_{il}(s) ds. \quad (6.120)$$

Using the integrals from Appendix 6.C, we determine the components of matrix  $\mathbf{B}$ , which describes the force exerted by a rotating filament (or, alternatively, the torque exerted by a translating filament)

$$\begin{aligned} B_{11} &= \int_{-1}^{+1} r_2 \Sigma_{13} - r_3 \Sigma_{12} ds = -\sigma R(c_{\parallel} - c_{\perp}) \sin \psi \cos \psi \int_{-1}^{+1} \sin^2(\pi N s) ds \\ &\quad + \sigma(c_{\parallel} - c_{\perp}) \sin^2 \psi \cos \psi \int_{-1}^{+1} s \sin(\pi N s) \cos(\pi N s) ds \\ &= \sigma(c_{\parallel} - c_{\perp}) \sin^2 \psi \cos \psi \left( -\frac{1}{\pi N} - \frac{\cos(2\pi N)}{2\pi N} + \frac{3 \sin(2\pi N)}{(2\pi N)^2} \right), \end{aligned} \quad (6.121)$$

$$\begin{aligned} B_{12} &= \int_{-1}^{+1} r_3 \Sigma_{11} - r_1 \Sigma_{13} ds = (c_{\parallel} - c_{\perp}) \sin^2 \psi \cos \psi \int_{-1}^{+1} s \sin^2(\pi N s) ds \\ &\quad + R(c_{\parallel} - c_{\perp}) \sin \psi \cos \psi \int_{-1}^{+1} \sin(\pi N s) \cos(\pi N s) ds = 0, \end{aligned} \quad (6.122)$$

$$B_{13} = \int_{-1}^{+1} r_1 \Sigma_{12} - r_2 \Sigma_{11} ds = -\sigma R(c_{\parallel} - c_{\perp}) \sin^2 \psi \int_{-1}^{+1} \sin(\pi N s) ds = 0, \quad (6.123)$$

$$\begin{aligned}
B_{21} &= \int_{-1}^{+1} r_2 \Sigma_{23} - r_3 \Sigma_{22} ds = R(c_{\parallel} - c_{\perp}) \sin \psi \cos \psi \int_{-1}^{+1} \sin(\pi N s) \cos(\pi N s) ds \\
&\quad - (c_{\parallel} - c_{\perp}) \sin^2 \psi \cos \psi \int_{-1}^{+1} s \cos^2(\pi N s) ds = 0, \quad (6.124)
\end{aligned}$$

$$\begin{aligned}
B_{22} &= \int_{-1}^{+1} r_3 \Sigma_{21} - r_1 \Sigma_{23} ds = -\sigma(c_{\parallel} - c_{\perp}) \sin^2 \psi \cos \psi \int_{-1}^{+1} s \sin(\pi N s) \cos(\pi N s) ds \\
&\quad - \sigma R(c_{\parallel} - c_{\perp}) \sin \psi \cos \psi \int_{-1}^{+1} \cos^2(\pi N s) ds \\
&= -\sigma(c_{\parallel} - c_{\perp}) \sin^2 \psi \cos \psi \left( \frac{1}{\pi N} - \frac{\cos(2\pi N)}{2\pi N} + \frac{3 \sin(2\pi N)}{(2\pi N)^2} \right), \quad (6.125)
\end{aligned}$$

$$\begin{aligned}
B_{23} &= \int_{-1}^{+1} r_1 \Sigma_{22} - r_2 \Sigma_{21} ds \\
&= R c_{\perp} \int_{-1}^{+1} \cos(\pi N s) ds + R(c_{\parallel} - c_{\perp}) \sin^2 \psi \int_{-1}^{+1} \cos(\pi N s) ds \\
&= \frac{2 \sin(\pi N) \sin(\psi)}{(\pi N)^2} (\cos^2 \psi c_{\perp} + \sin^2 \psi c_{\parallel}), \quad (6.126)
\end{aligned}$$

$$\begin{aligned}
B_{31} &= \int_{-1}^{+1} r_2 \Sigma_{33} - r_3 \Sigma_{32} ds = \sigma R (\cos^2 \psi c_{\parallel} \\
&\quad + \sin^2 \psi c_{\perp}) \int_{-1}^{+1} \sin(\pi N s) ds - \sigma(c_{\parallel} - c_{\perp}) \sin \psi \cos^2 \psi \int_{-1}^{+1} s \cos(\pi N s) ds = 0, \quad (6.127)
\end{aligned}$$

$$\begin{aligned}
B_{32} &= \int_{-1}^{+1} r_3 \Sigma_{31} - r_1 \Sigma_{33} ds \\
&= -(c_{\parallel} - c_{\perp}) \sin \psi \cos^2 \psi \int_{-1}^{+1} s \sin(\pi N s) ds - R (\cos^2 \psi c_{\parallel} + \sin^2 \psi c_{\perp}) \int_{-1}^{+1} \cos(\pi N s) ds \\
&= \frac{2 \sin(\pi N) \sin(\psi)}{(\pi N)^2} (\cos(2\psi) c_{\perp} - (1 + \cos(2\psi)) c_{\parallel}) + \frac{\sin(2\psi) \cos \psi \cos(\pi N)}{\pi N} (c_{\parallel} - c_{\perp}), \quad (6.128)
\end{aligned}$$

$$\begin{aligned}
B_{33} &= \int_{-1}^{+1} r_1 \Sigma_{32} - r_2 \Sigma_{31} ds \\
&= \sigma R (c_{\parallel} - c_{\perp}) \sin \psi \cos \psi \int_{-1}^{+1} \cos^2(\pi N s) ds + \sigma R (c_{\parallel} - c_{\perp}) \sin \psi \cos \psi \int_{-1}^{+1} \sin^2(\pi N s) ds \\
&= \sigma \frac{\sin(\psi) \sin(2\psi)}{\pi N} (c_{\parallel} - c_{\perp}). \quad (6.129)
\end{aligned}$$

Note that we have used the identity  $R = \sin \psi / (\pi N)$  to simplify the answers.

Finally, from Eqs. (6.25) and (6.26) we write down an equivalent definition of matrix  $\mathbf{D}$  as

$$D_{ij} = \int_{-1}^{+1} \varepsilon_{ikl} \varepsilon_{jmn} r_k(s) \Sigma_{ln}(s) r_m(s) ds. \quad (6.130)$$

Using the integrals from Appendix 6.C, we determine the components of matrix  $\mathbf{D}$ , which describes the torque exerted by a rotating filament:

$$\begin{aligned}
D_{11} &= \int_{-1}^{+1} (r_2^2 \Sigma_{33} + r_3^2 \Sigma_{22} - 2r_2 r_3 \Sigma_{23}) ds \\
&= (\cos^2 \psi c_{\parallel} + \sin^2 \psi c_{\perp}) R^2 \int_{-1}^{+1} \sin^2(\pi N s) ds \\
&\quad + c_{\perp} \cos^2 \psi \int_{-1}^{+1} s^2 ds + (c_{\parallel} - c_{\perp}) \sin^2 \psi \cos^2 \psi \int_{-1}^{+1} s^2 \cos^2(\pi N s) ds \\
&\quad - 2(c_{\parallel} - c_{\perp}) R \sin \psi \cos^2 \psi \int_{-1}^{+1} s \sin(\pi N s) \cos(\pi N s) ds \\
&= \frac{\sin^2 \psi}{(\pi N)^2} (\sin^2 \psi c_{\perp} + \cos^2 \psi c_{\parallel}) + \frac{2}{3} \cos^2 \psi \left[ \left( 1 - \frac{1}{2} \sin^2 \psi \right) c_{\perp} + \frac{1}{2} \sin^2 \psi c_{\parallel} \right] \\
&\quad - \sin^2 \psi \left[ c_{\perp} \frac{4 \sin(2\pi N)}{(2\pi N)^3} + (c_{\parallel} - c_{\perp}) \cos^2 \psi \left( -\frac{\sin(2\pi N)}{2\pi N} - \frac{6 \cos(2\pi N)}{(2\pi N)^2} + \frac{10 \sin(2\pi N)}{(2\pi N)^3} \right) \right], \quad (6.131)
\end{aligned}$$

$$\begin{aligned}
D_{22} &= \int_{-1}^{+1} (r_1^2 \Sigma_{33} + r_3^2 \Sigma_{11} - 2r_1 r_3 \Sigma_{13}) ds \\
&= (\cos^2 \psi c_{\parallel} + \sin^2 \psi c_{\perp}) R^2 \int_{-1}^{+1} \cos^2(\pi N s) ds \\
&\quad + c_{\perp} \cos^2 \psi \int_{-1}^{+1} s^2 ds + (c_{\parallel} - c_{\perp}) \sin^2 \psi \cos^2 \psi \int_{-1}^{+1} s^2 \sin^2(\pi N s) ds \\
&\quad + 2(c_{\parallel} - c_{\perp}) R \sin \psi \cos^2 \psi \int_{-1}^{+1} s \sin(\pi N s) \cos(\pi N s) ds \\
&= \frac{\sin^2 \psi}{(\pi N)^2} (\sin^2 \psi c_{\perp} + \cos^2 \psi c_{\parallel}) + \frac{2}{3} \cos^2 \psi \left[ \left(1 - \frac{1}{2} \sin^2 \psi\right) c_{\perp} + \frac{1}{2} \sin^2 \psi c_{\parallel} \right] \\
&+ \sin^2 \psi \left[ c_{\perp} \frac{4 \sin(2\pi N)}{(2\pi N)^3} + (c_{\parallel} - c_{\perp}) \cos^2 \psi \left( -\frac{\sin(2\pi N)}{2\pi N} - \frac{6 \cos(2\pi N)}{(2\pi N)^2} + \frac{10 \sin(2\pi N)}{(2\pi N)^3} \right) \right], \tag{6.132}
\end{aligned}$$

$$\begin{aligned}
D_{33} &= \int_{-1}^{+1} (r_1^2 \Sigma_{22} + r_2^2 \Sigma_{11} - 2r_1 r_2 \Sigma_{12}) ds \\
&= R^2 c_{\perp} \int_{-1}^{+1} (\sin^2(\pi N s) + \cos^2(\pi N s)) ds \\
&\quad + R^2 (c_{\parallel} - c_{\perp}) \sin^2 \psi \int_{-1}^{+1} (\cos^4(\pi N s) + \sin^4(\pi N s) + 2 \sin^2(\pi N s) \cos^2(\pi N s)) ds \\
&= \frac{2 \sin^2 \psi}{(\pi N)^2} (\cos^2 \psi c_{\perp} + \sin^2 \psi c_{\parallel}), \tag{6.133}
\end{aligned}$$

$$\begin{aligned}
D_{12} = D_{21} &= \int_{-1}^{+1} (r_2 r_3 \Sigma_{13} + r_1 r_3 \Sigma_{23} - r_1 r_2 \Sigma_{33} - r_3^2 \Sigma_{12}) ds \\
&= -\sigma (c_{\parallel} - c_{\perp}) R \sin \psi \cos^2 \psi \int_{-1}^{+1} s \sin^2(\pi N s) ds \\
&\quad + \sigma (c_{\parallel} - c_{\perp}) R \sin \psi \cos^2 \psi \int_{-1}^{+1} s \cos^2(\pi N s) ds \\
&\quad - \sigma (\cos^2 \psi c_{\perp} + \sin^2 \psi c_{\parallel}) R^2 \int_{-1}^{+1} \sin(\pi N s) \cos(\pi N s) ds \\
&\quad + \sigma (c_{\parallel} - c_{\perp}) \sin^2 \psi \cos^2 \psi \int_{-1}^{+1} s^2 \sin(\pi N s) \cos(\pi N s) ds = 0, \tag{6.134}
\end{aligned}$$

$$\begin{aligned}
D_{13} = D_{31} &= \int_{-1}^{+1} (r_2 r_3 \Sigma_{12} + r_1 r_2 \Sigma_{23} - r_1 r_3 \Sigma_{22} - r_2^2 \Sigma_{13}) ds \\
&= -(c_{\parallel} - c_{\perp}) R \sin^2 \psi \cos \psi \int_{-1}^{+1} s \sin^2(\pi N s) \cos(\pi N s) ds \\
&\quad + (c_{\parallel} - c_{\perp}) R^2 \sin \psi \cos \psi \int_{-1}^{+1} \sin(\pi N s) \cos^2(\pi N s) ds \\
&\quad - c_{\perp} R \cos \psi \int_{-1}^{+1} s \cos(\pi N s) ds - (c_{\parallel} - c_{\perp}) R \sin^2 \psi \cos \psi \int_{-1}^{+1} s \cos^3(\pi N s) ds \\
&\quad + (c_{\parallel} - c_{\perp}) R^2 \sin \psi \cos \psi \int_{-1}^{+1} \sin^3(\pi N s) ds = 0, \quad (6.135)
\end{aligned}$$

$$\begin{aligned}
D_{23} = D_{32} &= \int_{-1}^{+1} (r_1 r_3 \Sigma_{12} + r_1 r_2 \Sigma_{13} - r_2 r_3 \Sigma_{11} - r_1^2 \Sigma_{23}) ds \\
&= -\sigma (c_{\parallel} - c_{\perp}) R \sin^2 \psi \cos \psi \int_{-1}^{+1} s \sin(\pi N s) \cos^2(\pi N s) ds \\
&\quad - \sigma (c_{\parallel} - c_{\perp}) R^2 \sin \psi \cos \psi \int_{-1}^{+1} \sin^2(\pi N s) \cos(\pi N s) ds \\
&\quad - \sigma c_{\perp} R \cos \psi \int_{-1}^{+1} s \sin(\pi N s) ds - \sigma (c_{\parallel} - c_{\perp}) R \sin^2 \psi \cos \psi \int_{-1}^{+1} s \sin^3(\pi N s) ds \\
&\quad - \sigma (c_{\parallel} - c_{\perp}) R^2 \sin \psi \cos \psi \int_{-1}^{+1} \cos^3(\pi N s) ds \\
&= -\frac{\sigma \sin(2\psi)}{(\pi N)^2} \left[ (\cos(2\psi) c_{\perp} + (1 - \cos(2\psi)) c_{\parallel}) \frac{\sin(\pi N)}{\pi N} \right. \\
&\quad \left. - (\cos^2 \psi c_{\perp} + \sin^2 \psi c_{\parallel}) \cos(\pi N) \right]. \quad (6.136)
\end{aligned}$$

## Appendix 6.B Calculating force moments from RFT

In this section we use RFT to calculate analytical expressions for the vector of force moments  $\mathbf{m}_0$  defined in Eqs. (6.42) and (6.51). In the body frame of a filament with centreline  $\mathbf{r}(s)$  and local resistance tensor  $\Sigma(s)$ , we have

$$(\mathbf{m}_0)_{1 \leq j \leq 3} = (-2\delta_{k1} \delta_{l1} + \delta_{k2} \delta_{l2} + \delta_{k3} \delta_{l3}) \int_{-1}^{+1} r_l(s) \Sigma_{kj}(s) ds, \quad (6.137)$$

$$(\mathbf{m}_0)_{4 \leq j \leq 6} = (-2\delta_{k1} \delta_{l1} + \delta_{k2} \delta_{l2} + \delta_{k3} \delta_{l3}) \int_{-1}^{+1} r_l(s) \Sigma_{km}(s) \mathcal{E}_{j-3, nm} r_n(s) ds. \quad (6.138)$$

The first component is

$$(\mathbf{m}_0)_1 = \int_{-1}^{+1} -2r_1 \Sigma_{11} + r_2 \Sigma_{21} + r_3 \Sigma_{31} ds. \quad (6.139)$$

Substituting the components of  $\mathbf{r}(s)$  from Eq. (6.3) and the values of  $\Sigma(s)$  from Eqs. (6.107)-(6.112), we find that

$$\begin{aligned} (\mathbf{m}_0)_1 = & -2Rc_{\perp} \int_{-1}^{+1} \cos(\pi Ns) ds - 3R(c_{\parallel} - c_{\perp}) \sin^2 \psi \int_{-1}^{+1} \cos(\pi Ns) \sin^2(\pi Ns) ds \\ & - (c_{\parallel} - c_{\perp}) \sin \psi \cos^2 \psi \int_{-1}^{+1} s \sin(\pi Ns) ds. \end{aligned} \quad (6.140)$$

Using the integrals in Appendix 6.C, Eqs. (6.152),(6.155) and (6.157), we determine that

$$\begin{aligned} (\mathbf{m}_0)_1 = & -2Rc_{\perp} \frac{2 \sin(\pi N)}{\pi N} - 3R(c_{\parallel} - c_{\perp}) \sin^2 \psi \frac{2 \sin^3(\pi N)}{3\pi N} \\ & - (c_{\parallel} - c_{\perp}) \sin \psi \cos^2 \psi \left( -\frac{2 \cos(\pi N)}{\pi N} + \frac{2 \sin(\pi N)}{(\pi N)^2} \right). \end{aligned} \quad (6.141)$$

Finally, with the substitution  $R = \sin \psi / \pi N$  and notation  $(\mathbf{m}_0)_1 = \mathcal{M}_1$ , we get

$$\begin{aligned} \mathcal{M}_1 = & 2c_{\perp} \sin \psi \left[ \cos^2 \psi \left( -\frac{\cos(\pi N)}{\pi N} + \frac{\sin(\pi N)}{(\pi N)^2} \right) + \sin^2 \psi \frac{\sin^3(\pi N)}{(\pi N)^2} - \frac{2 \sin(\pi N)}{(\pi N)^2} \right] \\ & - 2c_{\parallel} \sin \psi \left[ \cos^2 \psi \left( -\frac{\cos(\pi N)}{\pi N} + \frac{\sin(\pi N)}{(\pi N)^2} \right) + \sin^2 \psi \frac{\sin^3(\pi N)}{(\pi N)^2} \right]. \end{aligned} \quad (6.142)$$

The next two components are zero

$$(\mathbf{m}_0)_2 = \int_{-1}^{+1} -2r_1 \Sigma_{12} + r_2 \Sigma_{22} + r_3 \Sigma_{32} ds = 0, \quad (6.143)$$

$$(\mathbf{m}_0)_3 = \int_{-1}^{+1} -2r_1 \Sigma_{13} + r_2 \Sigma_{23} + r_3 \Sigma_{33} ds = 0, \quad (6.144)$$

because each term in the integrals is an odd function of  $s$ .

The fourth component is

$$(\mathbf{m}_0)_4 = \int_{-1}^{+1} -2r_1 (\Sigma_{13} r_2 - \Sigma_{12} r_3) + r_2 (\Sigma_{23} r_2 - \Sigma_{22} r_3) + r_3 (\Sigma_{33} r_2 - \Sigma_{32} r_3) ds = 0. \quad (6.145)$$

We group terms according to their  $s$  dependence as

$$(\mathbf{m}_0)_4 = \int_{-1}^{+1} (-2r_1r_2\Sigma_{13} + r_2^2\Sigma_{23})ds + \int_{-1}^{+1} (2r_1r_3\Sigma_{12} + r_2r_3(\Sigma_{33} - \Sigma_{22}))ds - \int_{-1}^{+1} r_3^2\Sigma_{23}ds. \quad (6.146)$$

After substituting the components of  $\mathbf{r}(s)$  from Eq. (6.3) and the values of  $\Sigma(s)$  from Eqs. (6.107)-(6.112), this becomes

$$(\mathbf{m}_0)_4 = \sigma(c_{\parallel} - c_{\perp}) \left[ 3R^2 \sin \psi \cos \psi \int_{-1}^{+1} \cos(\pi N s) \sin^2(\pi N s) ds + R \cos^3 \psi \int_{-1}^{+1} s \sin(\pi N s) ds - 3R \sin^2 \psi \cos \psi \int_{-1}^{+1} s \sin(\pi N s) \cos^2(\pi N s) ds - \sin \psi \cos^3 \psi \int_{-1}^{+1} s^2 \cos(\pi N s) ds \right]. \quad (6.147)$$

Using the integrals in Appendix 6.C, Eqs. (6.155),(6.157),(6.159) and (6.160), we determine that

$$(\mathbf{m}_0)_4 = \sigma(c_{\parallel} - c_{\perp}) \left[ 3R^2 \sin \psi \cos \psi \frac{2 \sin^3(\pi N)}{3\pi N} + R \cos^3 \psi \left( -\frac{2 \cos(\pi N)}{\pi N} + \frac{2 \sin(\pi N)}{(\pi N)^2} \right) - 3R \sin^2 \psi \cos \psi \left( -\frac{2 \cos^3(\pi N)}{3\pi N} + \frac{2 \sin(\pi N)}{3(\pi N)^2} - \frac{2 \sin^3(\pi N)}{9(\pi N)^2} \right) - \sin \psi \cos^3 \psi \left( \frac{2 \sin(\pi N)}{\pi N} + \frac{4 \cos(\pi N)}{(\pi N)^2} - \frac{4 \sin(\pi N)}{(\pi N)^3} \right) \right]. \quad (6.148)$$

Finally, with the substitution  $R = \sin \psi / \pi N$  and notation  $(\mathbf{m}_0)_4 = \mathcal{M}_4$ , we get

$$\mathcal{M}_4 = \sigma(c_{\parallel} - c_{\perp}) \sin(2\psi) \left[ \cos^2 \psi \left( -\frac{\sin(\pi N)}{\pi N} - \frac{3 \cos(\pi N)}{(\pi N)^2} + \frac{3 \sin(\pi N)}{(\pi N)^3} \right) + \sin^2 \psi \left( \frac{\cos^3(\pi N)}{(\pi N)^2} + \frac{4 \sin^3(\pi N)}{3(\pi N)^3} - \frac{\sin(\pi N)}{(\pi N)^3} \right) \right]. \quad (6.149)$$

The next two components are also zero

$$(\mathbf{m}_0)_5 = \int_{-1}^{+1} -2r_1(\Sigma_{11}r_3 - \Sigma_{13}r_1) + r_2(\Sigma_{21}r_3 - \Sigma_{23}r_1) + r_3(\Sigma_{31}r_3 - \Sigma_{33}r_1)ds = 0, \quad (6.150)$$

$$(\mathbf{m}_0)_6 = \int_{-1}^{+1} -2r_1(\Sigma_{12}r_1 - \Sigma_{11}r_2) + r_2(\Sigma_{22}r_1 - \Sigma_{21}r_2) + r_3(\Sigma_{32}r_1 - \Sigma_{31}r_2) ds = 0, \quad (6.151)$$

because each term in the integrals is an odd function of  $s$ .

## Appendix 6.C Useful integrals

We provide some useful integrals for the RFT calculations in Appendices 6.A and 6.B.

$$\int_{-1}^{+1} \cos(\pi N s) ds = \frac{2 \sin(\pi N)}{\pi N}, \quad (6.152)$$

$$\int_{-1}^{+1} \sin^2(\pi N s) ds = 1 - \frac{\sin(2\pi N)}{2\pi N}, \quad (6.153)$$

$$\int_{-1}^{+1} \cos^2(\pi N s) ds = 1 + \frac{\sin(2\pi N)}{2\pi N}, \quad (6.154)$$

$$\int_{-1}^{+1} \sin^2(\pi N s) \cos(\pi N s) ds = \frac{2 \sin^3(\pi N)}{3\pi N}, \quad (6.155)$$

$$\int_{-1}^{+1} \cos^3(\pi N s) ds = \frac{2 \sin(\pi N)}{\pi N} - \frac{2 \sin^3(\pi N)}{3\pi N}, \quad (6.156)$$

$$\int_{-1}^{+1} s \sin(\pi N s) ds = -\frac{2 \cos(\pi N)}{\pi N} + \frac{2 \sin(\pi N)}{(\pi N)^2}, \quad (6.157)$$

$$\int_{-1}^{+1} s \sin(\pi N s) \cos(\pi N s) ds = -\frac{\cos(2\pi N)}{2\pi N} + \frac{\sin(2\pi N)}{(2\pi N)^2}, \quad (6.158)$$

$$\int_{-1}^{+1} s \sin(\pi N s) \cos^2(\pi N s) ds = -\frac{2 \cos^3(\pi N)}{3\pi N} + \frac{2 \sin(\pi N)}{3(\pi N)^2} - \frac{2 \sin^3(\pi N)}{9(\pi N)^2}, \quad (6.159)$$

$$\int_{-1}^{+1} s^2 \cos(\pi N s) ds = \frac{2 \sin(\pi N)}{\pi N} + \frac{4 \cos(\pi N)}{(\pi N)^2} - \frac{4 \sin(\pi N)}{(\pi N)^3}, \quad (6.160)$$

$$\int_{-1}^{+1} s^2 \sin^2(\pi N s) ds = \frac{1}{3} - \left[ \frac{\sin(2\pi N)}{2\pi N} + \frac{2 \cos(2\pi N)}{(2\pi N)^2} - \frac{2 \sin(2\pi N)}{(2\pi N)^3} \right], \quad (6.161)$$

$$\int_{-1}^{+1} s^2 \cos^2(\pi N s) ds = \frac{1}{3} + \left[ \frac{\sin(2\pi N)}{2\pi N} + \frac{2 \cos(2\pi N)}{(2\pi N)^2} - \frac{2 \sin(2\pi N)}{(2\pi N)^3} \right]. \quad (6.162)$$

In addition to these, we point out that

$$\int_{-1}^{+1} s^j \sin^k(\pi N s) \cos^l(\pi N s) ds = 0, \quad (6.163)$$

for any non-negative integer powers  $j, k, l$  so long as  $j + k \equiv 1 \pmod{2}$ , because the integrand is an odd function of  $s$ .

## Appendix 6.D Validation of computational method

In order to validate our implementation of slender-body theory (SBT), we carry out four different tests. For the implementation of single-filament dynamics (i.e. standard SBT), we verify our computations against classical results for prolate spheroids (Fig. 6.13), semi-circular arcs (Fig. 6.14) and helices (Fig. 6.15). In all three cases, our implementation of SBT is in excellent agreement with results published in the literature. To test cross-filament interactions, we compare the hydrodynamic resistance of two helical filaments placed head-to-head and that of a single helical filament with twice the length (Fig. 6.16). The relative error between the two setups decays with decreasing distance between the two half-filaments, thus validating our implementation of cross-filament HIs as well.

To determine the appropriate level of truncation in our Galerkin method implementation of SBT, we perform self-convergence tests for a single helical filament. In Fig. 6.17, we vary the number of Legendre polynomial modes from 10 to 20, and we compare the resistance matrix at a given number of modes,  $N_{\text{Legendre}}$ , with the most refined numerical solution available, i.e.  $N_{\text{Legendre}} = 20$ . The results of the self-convergence test for a helix with four helical turns suggest that a truncation level of  $N_{\text{Legendre}} = 15$  is sufficient to obtain 99% accuracy. Unless otherwise stated, this is the level of truncation used for the simulations presented in this chapter.

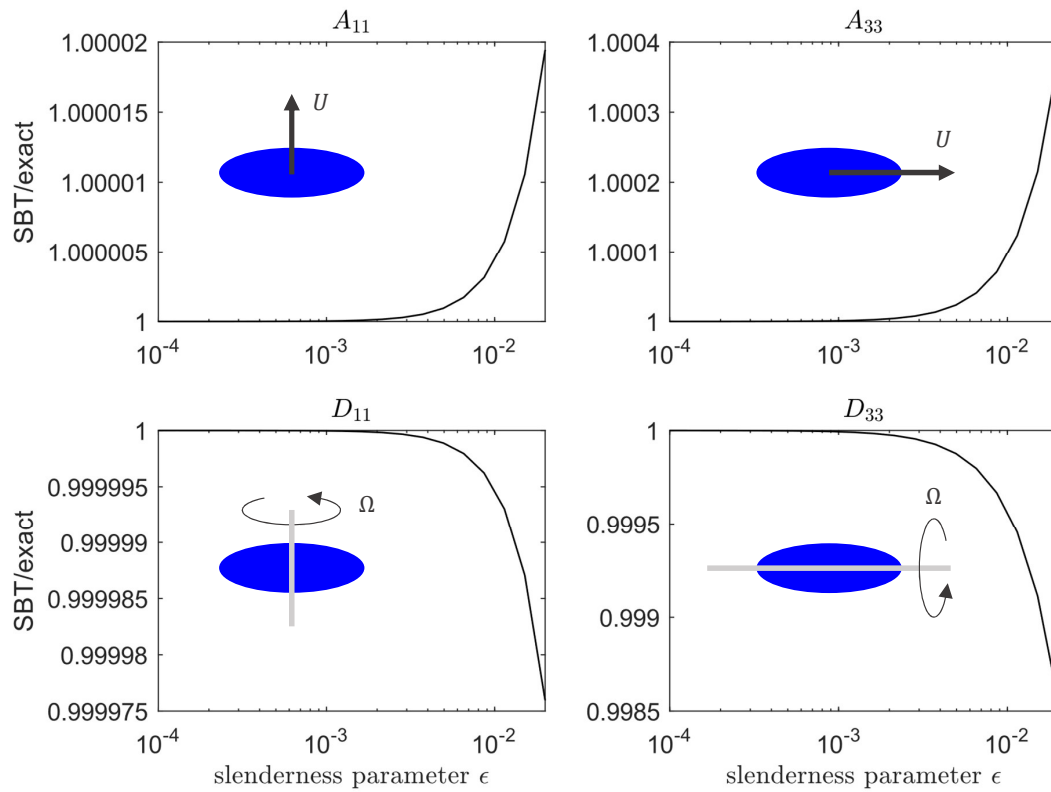


Fig. 6.13 Tests for a prolate spheroid. Verifying our implementation of SBT against the exact solution for spheroids [26]. In our implementation of SBT, we truncate the numerical solution to five Legendre polynomial modes,  $N_{\text{Legendre}} = 5$ .

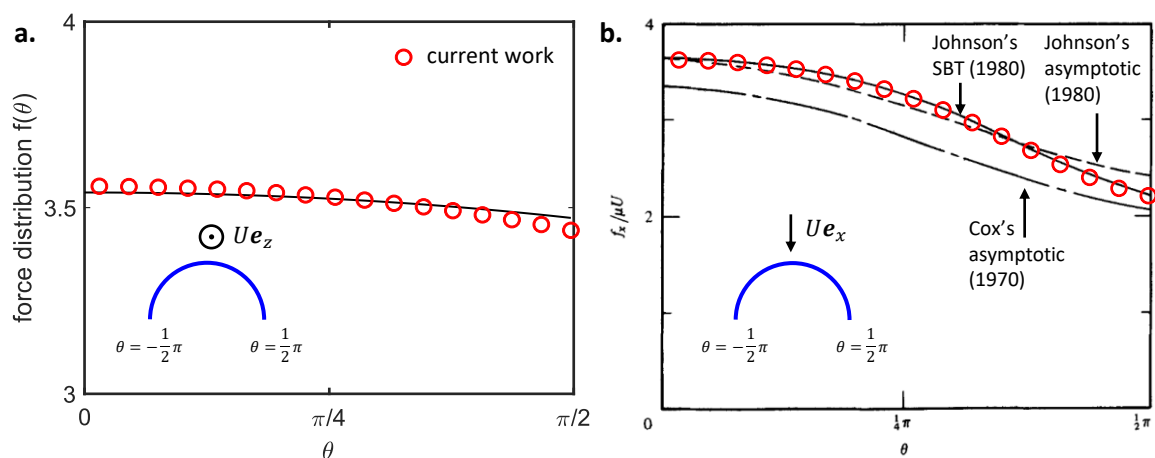


Fig. 6.14 Tests for a semi-circular filament. (a) Verifying our implementation of SBT (red circles) against Johnson's asymptotic solution (solid line) from Eq. (36) in Ref. [105]. The quantity being plotted is the vertical component of the force density exerted by a horizontal semi-circular filament, with slenderness  $\varepsilon = 0.1$ , translating vertically as shown in the inset. (b) Verifying our implementation of SBT (red circles) against Johnson's SBT computations (solid line) and two asymptotic solutions (dashed lines) by Cox [32] and Johnson [105]. The quantity being plotted is the drag force per unit length on a semi-circular filament, with slenderness  $\varepsilon = 0.1$ , translating along its axis of symmetry as shown in the inset. For both (a) and (b), we use a truncation of  $N_{\text{Legendre}} = 10$  in our implementation of SBT. In (b), our results are overlaid onto Fig. 4 from Ref. [105].

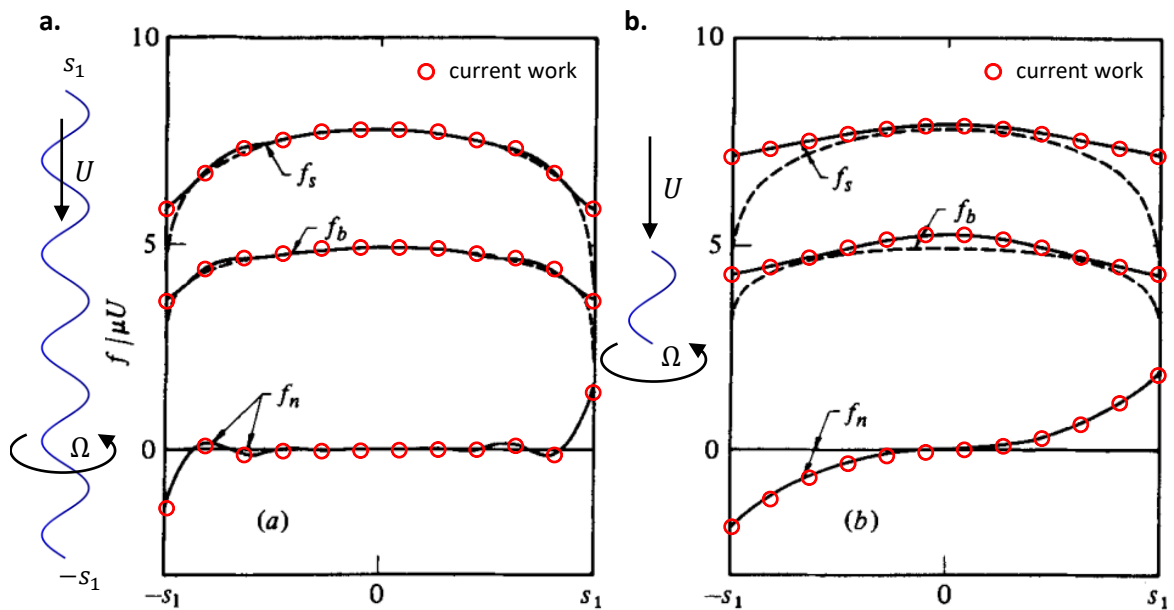


Fig. 6.15 Tests for a helical filament. Verifying our implementation of SBT (red circles) against Lighthill's exact solution for infinite helices (dashed line) [131] and Johnson's SBT (solid line) [105]. The three data series represent the tangential ( $f_s$ ), normal ( $f_n$ ) and binormal ( $f_b$ ) components of the force density along a helix (with a prolate spheroidal cross-section) that is translating and rotating about its axis of symmetry such that the net force along the axis is zero. Helix parameters: (a) five helical turns,  $\varepsilon = 0.0021$ ,  $\psi = 1.0039$  rad; (b) one helical turn,  $\varepsilon = 0.0107$ ,  $\psi = 1.0039$  rad. In our implementation of SBT, we truncate the solution to  $N_{\text{Legendre}} = 25$  Legendre polynomial modes. Our results are overlaid onto Fig. 6 from Ref. [105].

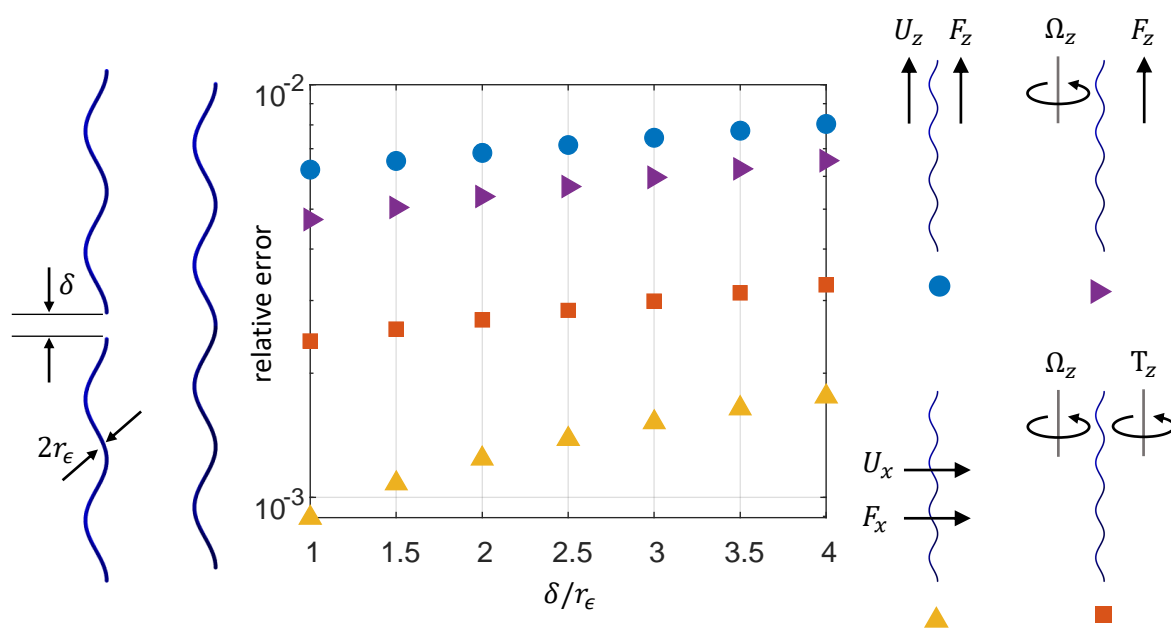


Fig. 6.16 Tests for cross-filament HIs. We compare the hydrodynamic resistance of two interacting helical filaments, having two helical turns each and placed head-to-head (H2H), with that of one helical filament that has four helical turns (ONE). In the limit  $\delta \rightarrow 0$ , the two problems are identical. We plot (on a log-linear scale) the relative errors in the coefficients of the resistance matrix  $A_{33} = F_z/U_z$  (blue circles),  $B_{33} = F_z/\Omega_z$  (purple rightward triangles),  $A_{11} = F_x/U_x$  (yellow upward triangles) and  $D_{33} = T_z/\Omega_z$  (orange squares). The relative error is defined as  $|1 - \text{H2H}/\text{ONE}|$  and decays with decreasing separation  $\delta$ , thus validating our implementation of cross-filament HIs. Helix parameters:  $\psi = 0.5043$  rad,  $\epsilon = 0.0024$  (for  $N = 4$  helical turns) and  $\epsilon = 0.0048$  (for  $N = 2$  helical turns).

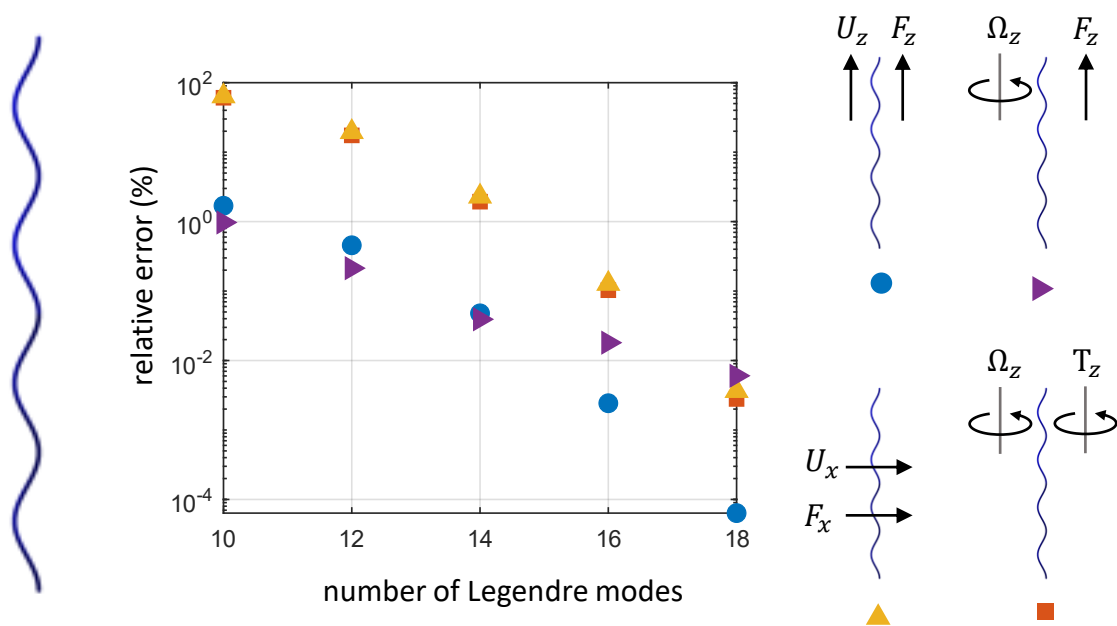


Fig. 6.17 Self-convergence test for a single helical filament. The percentage errors in  $A_{33} = F_z/U_z$  (blue circles),  $B_{33} = F_z/\Omega_z$  (purple rightward triangles),  $A_{11} = F_x/U_x$  (yellow upward triangles) and  $D_{33} = T_z/\Omega_z$  (orange squares) are calculated at each number of Legendre modes relative to the most accurate numerical solution available, in this case  $N_{\text{Legendre}} = 20$ . Helix parameters:  $\psi = 0.5043$  rad,  $\varepsilon = 0.0038$ ,  $N = 4$  helical turns.



# Chapter 7

## Hydrodynamic synchronisation of rotating bacterial flagella

In this chapter, we combine the theory for hydrodynamic interactions from Chapter 6 with a multiple scales analysis in order to rigorously coarse-grain the equations of motion of two rotating bacterial flagella into an evolution equation for their phase difference. We find that hydrodynamic interactions generically lead to in-phase synchronisation, at a rate dependent on the helical geometry of the filaments and the strength of elastic compliance. We verify our theoretical predictions using numerical simulations, and we provide an illustrated explanation of the physical mechanism that leads to synchronisation. Finally, we discuss the biophysical implications of our results for bacterial flagella by considering (i) how the elasticity of the hook and flagellar filament relate to the optimum elastic compliance for synchronisation, and (ii) a comparative analysis of the four most common bacterial polymorphic shapes.

### 7.1 Introduction

Synchronisation pervades the living world, often in the form of coordination between members of the same species, such as crickets chirping in unison [219] and fireflies flashing together in large numbers [194]. Both are examples of pulse-coupled biological oscillators and have been studied theoretically [151]. When it comes to human behaviour, hyperscanning methods such as fMRI are starting to shed light on the inter-brain synchronisation of motor and cognitive processes due to social interactions [33], while the advent of social media is giving us the opportunity to observe global patterns of synchronisation in human communications [154]. Synchronisation is also very important for the regulation of physiological processes within the same organism. Examples include the pacemaker cells in the heart

[99, 150], the insulin secreting cells in the pancreas [192] and the neuro-muscular oscillators that generate contractions in the small intestine [165].

One area of research where synchronisation plays a particularly important role is locomotion. Whenever an organism uses multiple periodically-actuated limbs or flagella to generate motion, there is a necessity for some form of coordination between them, as we have from the geometrical constraints on bundling discussed in Chapter 5. The emergence of animal gaits such as the trot or the gallop can be explained, on a conceptual level, using the symmetries of a fixed number of limbs modelled as coupled nonlinear oscillators [30]. Microscopic equivalents of these quadrupedal gaits have also been observed in quadriflagellate algae from the genus *Pyramimonas* [220]. In the same microscopic world, biflagellate algae such as *Chlamydomonas reinhardtii* swim forward using a synchronous breast-stroke beating of their flagella [66, 167], while the cilia covering the body of *Paramecium* self-organise their beating into metachronal waves [136]. In micro-organisms such as these, the synchronisation of swimming appendages is achieved passively, without the control of a central nervous system that is plausibly involved in the generation of locomotory patterns in vertebrates [29].

### 7.1.1 Synchronisation of eukaryotic flagella

Depending on the organism, the passive synchronisation of eukaryotic flagella and cilia is promoted by factors including direct hydrodynamic interactions between the filaments [17], an elastic coupling through the basal bodies [75, 173, 220], steric interactions [24], and the coupling of the filaments to the motion of the cell body [7, 62]. Theoretically, the formation of metachronal waves (MCWs) in arrays of cilia is best approached using mean field models [73], due to the sheer size and density of ciliary carpets. MCWs have also been successfully simulated numerically [52] and recreated in the laboratory [70]. Simplified models of ciliary synchronisation have also been proposed, in which the tip of the cilium is modelled by a sphere undergoing periodic motion above a rigid surface, which represents the cell body [16, 159, 203, 211, 212, 216]. More abstract models of hydrodynamic synchronisation simply consider the interactions between driven colloidal oscillators in an infinite fluid, also called rowers [78, 226], a setup that has also been reconstructed in experiments [120]. If the modelling is focused on the synchronisation of two beating cilia, instead of an entire ciliary carpet, it becomes possible to study mechanistic models that take into account the full elastohydrodynamic evolution of the shape of the filament [22, 65, 74, 75, 141] and, in some studies, also the details of internal actuation from the dynein motors [22, 72]. Other studies have solved a two-dimensional version of this problem, using Taylor's waving sheet as a model for a beating flagellum [50, 51, 130, 163].

### 7.1.2 Synchronisation of bacterial flagella

Compared to eukaryotic flagella, the synchronisation of rotating bacterial flagella is relatively less well understood from an analytical and physical standpoint. What we do know from computational studies is that, in addition to hydrodynamic interactions, it is also necessary to have some degree of elastic compliance, since hydrodynamically-coupled helices rotating rigidly about a fixed axis do not synchronise [111, 175]. Computational studies have also revealed that the balance between bundling and synchronisation times depends strongly on the initial separation between the rotating helical filaments [176], and that the filaments can slip out of synchrony if they are driven by unequal torques [177]. The critical torque difference for slippage was also found to depend on the distance between the filaments, which directly affects the strength of hydrodynamic coupling between the oscillators. Experimental studies on the topic of synchronisation between rotating objects include systems of light-driven microrotors [44] and of macroscopic-scale rotating paddles [171]. One case that has been studied analytically is a minimal model of synchronisation between two rotating paddles that are coupled hydrodynamically to each other, and elastically to the motors that drive them [171].

Synchronisation is especially important for multiflagellated bacteria like *Escherichia coli*, whose flagellar filaments gather in a bundle at the back of the cell body as the bacterium swims forward. In order for the bundle to operate smoothly, without collisions between the filaments, the phase difference between the filaments must be smaller than a critical value dependent on their helical geometry and separation. The geometric constraint for parallel filaments was first discussed by Macnab [138], while the constraints for a converging bundle of filaments were derived in Chapter 5. The level of synchronisation between filaments is expected to influence the propulsive efficiency of the bundle, while intermittent loss of synchronisation may contribute to the initiation of tumbling events [40, 177]. With increased synchronisation, a cell of the same size could accommodate a higher number of flagellar filaments, leading to a potential increase in swimming speed [158].

### 7.1.3 Current approach

Because the bacterial flagellum is fundamentally different in its actuation, shape and rigidity, we expect that the analytical models proposed for ciliary synchronisation, in which the tip of a beating flagellum is modelled as a rotating bead [159, 211], may not be able to capture the essential features of synchronisation between bacterial flagella. In this chapter, we propose a reduced model of the bacterial flagellum which preserves the salient features of the organelle: a rotary motor [196] which applies a constant torque about the axis of the flagellar filament,

a flexible hook [188] which exerts an elastic restoring force, and a rigid flagellar filament with helical geometry [81]. Since bacterial flagellar filaments have a helical amplitude much smaller than their length, their resistance to rotation about their own axis is much smaller than their resistance to translations. We find that, in the absence of hydrodynamic interactions, this distinctive feature of bacterial flagella leads to intrinsic kinematics of the filaments that cannot be captured by a spherical bead, and these leading-order kinematics influence the dynamics of synchronisation in an essential way.

## 7.2 Mathematical modelling

In this section we introduce our minimal setup for the hydrodynamic synchronisation of two rotating helical filaments, we write down the systems of equations relating the dynamics and the kinematics of the filaments, and we solve the equations of motion in the far-field (i.e. the distance between the filaments being greater than their contour length) by exploiting the separation of time scales between the rotation of the filaments and their synchronisation.

### 7.2.1 Minimal setup for synchronisation

In contrast to earlier studies on synchronisation, our analytical model takes into account the full helical geometry of the flagellar filament. This geometry is depicted in Fig. 7.1 (a), where all lengths have been rescaled such that the dimensionless contour length of the filament is  $L = 2$ , with the arc length,  $s$ , covering the interval  $(-1, +1)$  from one end of the filament to the other. The diagram also indicates the dimensionless helical radius,  $R$ , and helical pitch,  $p$ , which are related to the pitch angle,  $\psi$ , and the number of helical turns,  $N$ , through the expressions

$$R = \frac{\sin \psi}{\pi N}, \quad p = \frac{\cos \psi}{N}. \quad (7.1)$$

The final geometric parameter is the dimensionless cross-sectional radius of the filament,  $\varepsilon$ . For a bacterial flagellar filament with diameter 24 nm [222] and typical length 6  $\mu\text{m}$ , the aspect ratio  $\varepsilon = 0.004$  is very small indeed.

Our minimal model of synchronisation, illustrated in Fig. 7.1 (b), consists of two identical and elastically-tethered helices rotating about their own axes. The tethering points are separated by a distance  $d > L$  along the  $x$  axis, and the filaments are coupled hydrodynamically through the fluid. In order for the kinematics to be analytically tractable, we restrict the motion of the helices to only two degrees of freedom for each filament: a phase  $\phi_j$  describing the rotation about the vertical axis, and a displacement  $x_j$  describing sideways translations. The system evolves due to a constant driving torque,  $\tilde{T}_0 \mathbf{e}_z$ , and an elastic restoring force,

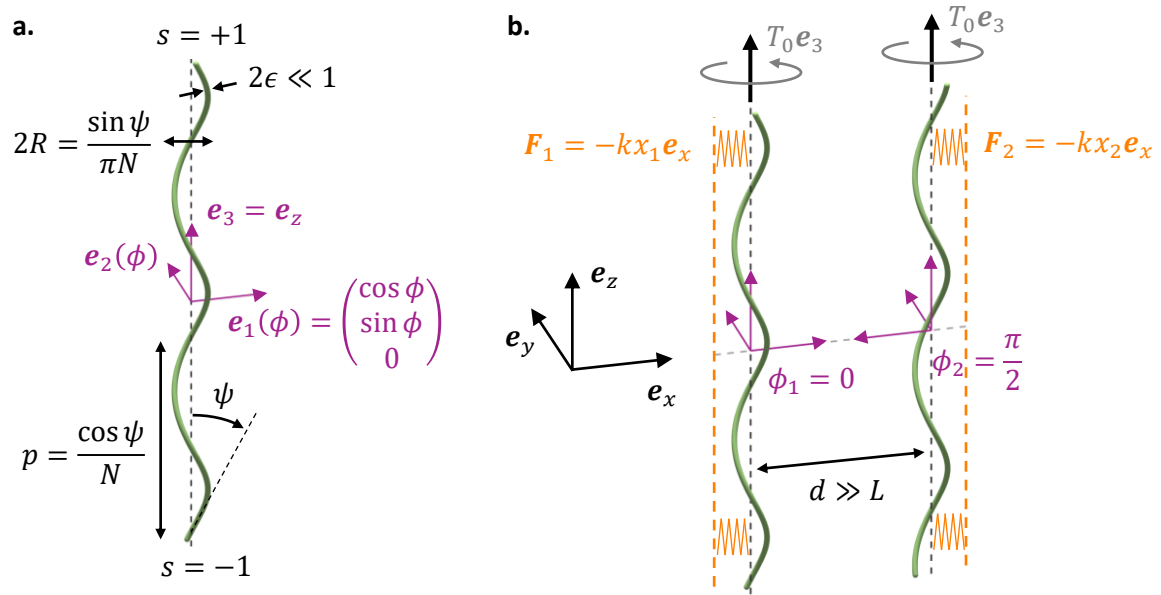


Fig. 7.1 Geometric and dynamical setup. (a) Dimensionless parameters describing the helical geometry of the flagellar filament, rescaled such that the contour length of the filament is  $L = 2$ . The body-fixed frame  $\{\mathbf{e}_1, \mathbf{e}_2, \mathbf{e}_3\}$  is shown in purple. The phase  $\phi$  describes the rotation of the helix around its own axis,  $\mathbf{e}_3$ , which remains vertical for all time. (b) Minimal setup for synchronisation includes a constant driving torque,  $T_0$ , about the axis of the filament, and an elastic restoring force with strength  $K$ , which pulls the axis of the filament back to a reference position. The reference positions of the two helical axes are separated by a distance  $d > L$  along the  $x$  direction, and the helical axes are allowed to oscillate in the  $x$  direction only. In our simulations, we initialise the filaments with phases  $\phi_1 = 0, \phi_2 = \pi/2$ .

$-\tilde{k}\tilde{x}_j\mathbf{e}_x$ , applied to each filament. Unless otherwise stated, we will use tildes to denote the dimensional counterpart of every dimensionless quantity throughout the chapter.

We make the problem fully dimensionless by measuring forces in units of  $2\tilde{T}_0/\tilde{L}$  and time in units of  $\tilde{\mu}\tilde{L}^3/8\tilde{T}_0$ . This is equivalent to taking  $T_0 = 1$  and  $\mu = 1$  in dimensionless terms, in addition to the contour length of the filament,  $L = 2$ , that we introduced earlier. This non-dimensionalisation step introduces a key dimensionless parameter

$$k = \frac{\tilde{k}\tilde{L}^2}{4\tilde{T}_0}, \quad (7.2)$$

which encapsulates the dynamical mechanism acting on the filament (rotary motor and flexible hook).

## 7.2.2 Hydrodynamic interactions

The Reynolds number for a flagellar filament of length  $\tilde{L} = 6 \mu\text{m}$ , rotating on a time scale  $\tilde{t}_{\text{rot}} = 10^{-2} \text{ s}$  in a fluid with dynamic viscosity  $\tilde{\mu} = 1 \text{ mPa}\cdot\text{s}$  and density  $\tilde{\rho} = 10^3 \text{ kg}\cdot\text{m}^{-3}$  (water at  $20^\circ \text{ C}$ ) is very small,  $\text{Re} = \tilde{\rho}\tilde{L}^2/\tilde{\mu}\tilde{t}_{\text{rot}} = 3.6 \times 10^{-3}$ . This means that we find ourselves in the Stokes flow regime where inertia is negligible, and the forces exerted by the filaments on the fluid are linearly proportional to their velocities. For the case of two rigid filaments, this linear relationship can be expressed as a matrix equation involving an extended resistance matrix,

$$\begin{pmatrix} \mathbf{F}_1 \\ \mathbf{T}_1 \\ \mathbf{F}_2 \\ \mathbf{T}_2 \end{pmatrix} = \begin{pmatrix} \mathbf{S}(\mathbf{x}_1, \mathbf{x}_2, \mathbf{p}_1, \mathbf{p}_2) & \mathbf{C}(\mathbf{x}_1, \mathbf{x}_2, \mathbf{p}_1, \mathbf{p}_2) \\ \mathbf{C}(\mathbf{x}_2, \mathbf{x}_1, \mathbf{p}_2, \mathbf{p}_1) & \mathbf{S}(\mathbf{x}_2, \mathbf{x}_1, \mathbf{p}_2, \mathbf{p}_1) \end{pmatrix} \begin{pmatrix} \mathbf{U}_1 \\ \boldsymbol{\Omega}_1 \\ \mathbf{U}_2 \\ \boldsymbol{\Omega}_2 \end{pmatrix}, \quad (7.3)$$

where  $\mathbf{F}_j$  and  $\mathbf{T}_j$  are the hydrodynamic forces and torques exerted *by* the filaments *on* the fluid. The matrix  $\mathbf{S}$  stands for self-induced dynamics and tells us how each filament responds to its own motion, while the matrix  $\mathbf{C}$  represents cross-interactions between the filaments and tells us how the forces and torques exerted by one filament depend on the linear and angular velocities of the second filament. We have made it explicit that the resistance matrices depend on the positions,  $\mathbf{x}_j$ , and orientations,  $\mathbf{p}_j$ , of the two filaments. The orientations of the filaments will be defined by the phase angles,  $\phi_j$ , as described in §2.1.1.

In our earlier work from Chapter 6, we have calculated analytical expressions for the extended resistance matrix of two rigid slender filaments in the form of a series expansion in

inverse powers of the distance between the filaments,

$$\mathbf{S}(\mathbf{x}_1, \mathbf{x}_2, \mathbf{p}_1, \mathbf{p}_2) = \mathbf{S}^{(0)}(\mathbf{p}_1) + d^{-2}\mathbf{S}^{(2)}(\hat{\mathbf{d}}, \mathbf{p}_1, \mathbf{p}_2) + \mathcal{O}(d^{-3}), \quad (7.4)$$

$$\mathbf{C}(\mathbf{x}_1, \mathbf{x}_2, \mathbf{p}_1, \mathbf{p}_2) = d^{-1}\mathbf{C}^{(1)}(\hat{\mathbf{d}}, \mathbf{p}_1, \mathbf{p}_2) + d^{-2}\mathbf{C}^{(2)}(\hat{\mathbf{d}}, \mathbf{p}_1, \mathbf{p}_2) + \mathcal{O}(d^{-3}), \quad (7.5)$$

where  $\hat{\mathbf{d}}$  is the unit vector in the direction  $\mathbf{d} = \mathbf{x}_2 - \mathbf{x}_1$  from the centre of the first filament to the centre of the second filament. If the filaments are tethered sufficiently far apart, the distance between their centres is, to leading order, the same as the distance between their tethering points, so  $\hat{\mathbf{d}} = \mathbf{e}_x$ . This expansion is valid in the regime  $d > L$ .

For the present work on synchronisation, it is sufficient to consider the hydrodynamic interactions up to and including  $\mathcal{O}(d^{-1})$ , which is where the relevant dynamics happen. In our setup, the orientation of the filaments is uniquely determined by the phase angles  $\phi_j$  about the vertical axis, so we write down the simplified linear system

$$\begin{pmatrix} \mathbf{F}_1 \\ \mathbf{T}_1 \\ \mathbf{F}_2 \\ \mathbf{T}_2 \end{pmatrix} = \begin{pmatrix} \mathbf{S}^{(0)}(\phi_1) & d^{-1}\mathbf{C}^{(1)}(\mathbf{e}_x, \phi_1, \phi_2) \\ d^{-1}\mathbf{C}^{(1)}(-\mathbf{e}_x, \phi_2, \phi_1) & \mathbf{S}^{(0)}(\phi_2) \end{pmatrix} \begin{pmatrix} \mathbf{U}_1 \\ \boldsymbol{\Omega}_1 \\ \mathbf{U}_2 \\ \boldsymbol{\Omega}_2 \end{pmatrix}. \quad (7.6)$$

The reason why we are able to make analytical progress is that both  $\mathbf{S}^{(0)}(\phi_1)$  and  $\mathbf{C}^{(1)}(\mathbf{e}_x, \phi_2, \phi_1)$  can be written in terms of a single building block. This fundamental building block is the single-filament resistance matrix calculated in the body-fixed frame of the filament,

$$\mathbf{S}_0 = \begin{pmatrix} \mathbf{A} & \mathbf{B} \\ \mathbf{B}^T & \mathbf{D} \end{pmatrix}. \quad (7.7)$$

Because the filaments are slender ( $\varepsilon \ll 1$ ), the coefficients of this resistance matrix can be calculated using the well-established methods of resistive-force theory (RFT) [69, 79, 132] or slender-body theory (SBT) [32, 105, 131]. In Appendix §7.A, we provide a summary of analytical expressions for those components of  $\mathbf{S}_0$  needed in this chapter.

Note that  $\mathbf{S}_0$  is equivalent to  $\mathbf{S}^{(0)}(\phi)$  at phase angle  $\phi = 0$ , when the body-fixed frame  $\{\mathbf{e}_1, \mathbf{e}_2, \mathbf{e}_3\}$  coincides with the laboratory frame  $\{\mathbf{e}_x, \mathbf{e}_y, \mathbf{e}_z\}$  – see Fig. 7.1 (a). For any other orientation of the filament,  $\mathbf{S}^{(0)}(\phi)$  can be obtained from  $\mathbf{S}_0$  by applying a block-by-block rotation,

$$\mathbf{S}^{(0)}(\phi) = \begin{pmatrix} \mathbf{QAQ}^T & \mathbf{QBQ}^T \\ \mathbf{QB}^T\mathbf{Q}^T & \mathbf{QDQ}^T \end{pmatrix} \quad \mathbf{Q}(\phi) = \begin{pmatrix} \cos \phi & -\sin \phi & 0 \\ \sin \phi & \cos \phi & 0 \\ 0 & 0 & 1 \end{pmatrix}. \quad (7.8)$$

Finally, the hydrodynamic interactions between the two filaments are captured by the leading-order term in the cross-interaction matrix,

$$d^{-1}C_{ij}^{(1)}(\mathbf{e}_x, \phi_1, \phi_2) = -S_{im}^{(0)}(\phi_1) \frac{(\mathbf{I} + \mathbf{e}_x \mathbf{e}_x)_{mn}}{8\pi\mu d} S_{nj}^{(0)}(\phi_2), \quad (7.9)$$

where the free indices  $i$  and  $j$  run from 1 to 6, but the repeated indices  $m$  and  $n$  are summed over from 1 to 3. The mathematical derivation and physical interpretation of this result is given in Chapter 6.

The sum over the repeated indices can be expanded out into the result

$$d^{-1}C_{ij}^{(1)}(\phi_1, \phi_2) = -\frac{2S_{i1}^{(0)}(\phi_1)S_{1j}^{(0)}(\phi_2) + S_{i2}^{(0)}(\phi_1)S_{2j}^{(0)}(\phi_2) + S_{i3}^{(0)}(\phi_1)S_{3j}^{(0)}(\phi_2)}{8\pi\mu d}, \quad (7.10)$$

where  $S_{ij}^{(0)}(\phi)$  can be determined from Eq. (7.8) and the relevant components of the matrices **A**, **B** and **D** provided in Appendix 7.A.

### 7.2.3 Governing equations

By projecting the full set of equations, Eq. (7.6), onto the four degrees of freedom in our system (two phases and two lateral displacements) and substituting the dimensionless values of the driving torque,  $\mathbf{T}_j = T_0 \mathbf{e}_z$ , and elastic restoring force,  $\mathbf{F}_j = -kx_j \mathbf{e}_x$ , applied to each filament, we arrive at the following governing equations

$$\begin{pmatrix} -kx_1 \\ T_0 \\ -kx_2 \\ T_0 \end{pmatrix} = \begin{pmatrix} \tilde{\mathbf{S}}(\phi_1) & \tilde{\mathbf{C}}(\phi_1, \phi_2) \\ \tilde{\mathbf{C}}(\phi_2, \phi_1) & \tilde{\mathbf{S}}(\phi_2) \end{pmatrix} \begin{pmatrix} \dot{x}_1 \\ \dot{\phi}_1 \\ \dot{x}_2 \\ \dot{\phi}_2 \end{pmatrix}, \quad (7.11)$$

where we have introduced the notation

$$\tilde{\mathbf{S}}(\phi) = \begin{pmatrix} S_{11}^{(0)}(\phi) & S_{16}^{(0)}(\phi) \\ S_{61}^{(0)}(\phi) & S_{66}^{(0)}(\phi) \end{pmatrix}, \quad \tilde{\mathbf{C}}(\phi_1, \phi_2) = d^{-1} \begin{pmatrix} C_{11}^{(1)}(\phi_1, \phi_2) & C_{16}^{(1)}(\phi_1, \phi_2) \\ C_{61}^{(1)}(\phi_1, \phi_2) & C_{66}^{(1)}(\phi_1, \phi_2) \end{pmatrix}. \quad (7.12)$$

Note that this is the only place in the chapter where we use tildes to denote something other than dimensional counterparts of dimensionless quantities.

The left-hand side of Eq. (7.11) represents the forces and torques applied to the filaments by an external mechanism (in our case, an idealised version of the bacterial flagellar motor

and the hook). The right-hand side of Eq. (7.11) represents the forces and torques applied by the filament to the fluid, which are the opposite of the hydrodynamic forces and torques exerted by the fluid on the filaments. Hence, by bringing all the terms to the left-hand side, we see that Eq. (7.11) rests on the assumption that the filaments are force-free, so that the forces applied to them by the external mechanism are exactly balanced out by the viscous drag on the filaments.

### 7.2.4 Intrinsic kinematics of a single helical filament

We start by solving for the intrinsic motion of a single rotating helix in the absence of hydrodynamic interactions. In the limit  $d \rightarrow \infty$ , Eq. (7.11) gives

$$\begin{pmatrix} -kx_j \\ T_0 \end{pmatrix} = \tilde{\mathbf{S}}(\phi_j) \begin{pmatrix} \dot{x}_j \\ \dot{\phi}_j \end{pmatrix}. \quad (7.13)$$

Using Eqs. (7.8) and (7.12), we write down the reduced resistance matrix

$$\tilde{\mathbf{S}}(\phi) = \begin{pmatrix} A_0 + \Delta A \cos(2\phi) & -B_{23} \sin(\phi) \\ -B_{23} \sin(\phi) & D_{33} \end{pmatrix}, \quad (7.14)$$

where we have introduced the notation  $A_0 = (A_{11} + A_{22})/2$  and  $\Delta A = (A_{11} - A_{22})/2$ . To invert this matrix and obtain the time evolution of  $x_j$  and  $\phi_j$ , we exploit a separation of scales between the coefficients  $A_0, \Delta A, B_{23}$  and  $D_{33}$ . From the analytical expressions in Appendix 7.A, we write down how these coefficients scale with the number of helical turns of the helix,  $N$ , at a fixed pitch angle,  $\psi$ ,

$$A_0 \sim \mathcal{O}(1), \quad (7.15)$$

$$\Delta A \sim \mathcal{O}((\pi N)^{-1}), \quad (7.16)$$

$$B_{23}, D_{33} \sim \mathcal{O}((\pi N)^{-2}). \quad (7.17)$$

For bacterial flagella, a filament of length  $8\mu\text{m}$  in the normal polymorphic form corresponds to  $(\pi N)^{-1} \approx 0.1$  (or more, for the other polymorphic forms), so we may reasonably compute the inverse matrix  $\tilde{\mathbf{S}}^{-1}(\phi)$  as a series expansion in powers of  $(\pi N)^{-1}$ ,

$$\tilde{\mathbf{S}}^{-1}(\phi) = \hat{\mathbf{S}}_2(\phi) + \hat{\mathbf{S}}_0(\phi) + \mathcal{O}((\pi N)^{-1}). \quad (7.18)$$

From Eqs. (7.14)-(7.17), we find the first two coefficients

$$\hat{\mathbf{S}}_2(\phi) = \begin{pmatrix} 0 & 0 \\ 0 & D_{33}^{-1} \end{pmatrix} \sim (\pi N)^2, \quad (7.19)$$

$$\hat{\mathbf{S}}_0(\phi) = \begin{pmatrix} A_0^{-1} & A_0^{-1} B_{23} D_{33}^{-1} \sin(\phi) \\ A_0^{-1} B_{23} D_{33}^{-1} \sin(\phi) & A_0^{-1} (B_{23} D_{33}^{-1} \sin(\phi))^2 \end{pmatrix} \sim (\pi N)^0. \quad (7.20)$$

At leading order,  $\mathcal{O}((\pi N)^2)$ , the motion of the helix is given by

$$\begin{pmatrix} \dot{x}_j \\ \dot{\phi}_j \end{pmatrix} = \begin{pmatrix} 0 & 0 \\ 0 & D_{33}^{-1} \end{pmatrix} \begin{pmatrix} -kx_j \\ T_0 \end{pmatrix}, \quad (7.21)$$

so the lateral velocity,  $\dot{x}_j$ , is zero at this order, but the phase angle evolves as

$$\phi_j(t) = \phi_j(0) + \Omega_0 t, \quad \Omega_0 = \frac{T_0}{D_{33}}. \quad (7.22)$$

For the lateral displacement, the leading-order effect comes from the  $\mathcal{O}((\pi N)^0)$  terms,

$$\dot{x}_j = -\frac{k}{A_0} x_j + \frac{B_{23} T_0}{A_0 D_{33}} \sin(\phi_j). \quad (7.23)$$

After multiplying by an integrating factor, we find the solution

$$x_j(t) = \frac{B_{23} T_0}{A_0 D_{33}} e^{-kt/A_0} \int^t e^{ks/A_0} \sin(\phi_j) ds. \quad (7.24)$$

The integration can be carried out by parts using the fact that  $\dot{\phi}_j = T_0 D_{33}^{-1}$  at leading order, and we find

$$x_j(t) = X_j e^{-kt/A_0} + \frac{B_{23} T_0}{A_0 D_{33}} \times \frac{k A_0^{-1} \sin(\phi_j) - T_0 D_{33}^{-1} \cos(\phi_j)}{k^2 A_0^{-2} + T_0^2 D_{33}^{-2}}. \quad (7.25)$$

Once the initial transients have decayed, and the helix has settled into its preferred oscillatory motion, the solution is

$$x_j(t) \approx \frac{B_{23}}{A_0} \times \frac{K \sin(\phi_j) - \cos(\phi_j)}{K^2 + 1}, \quad K = \frac{k D_{33}}{A_0 T_0}. \quad (7.26)$$

For reasons that will become clearer when we discuss the physical mechanism for synchronisation, but also to make the algebra more compact, we rewrite this expression as

$$x_j(t) \approx \rho(K) \cos(\phi_j - \nu(K)), \quad (7.27)$$

where the amplitude,  $\rho$ , and the phase lag,  $\nu$ , depend on the strength of the elastic tethering,

$$\rho(K) = \frac{B_{23}}{A_0 \sqrt{K^2 + 1}}, \quad \nu(K) = \tan^{-1}(-K) \in \left(\frac{\pi}{2}, \pi\right). \quad (7.28)$$

Note that the amplitude of the oscillations tends to zero as  $K \rightarrow \infty$ , which is to be expected in the limit of infinitely strong elastic tethering strength. Furthermore, the lateral displacement lags behind  $\cos(\phi_j)$ , which can be interpreted as the  $x$  component of the body-frame vector  $\mathbf{e}_1(\phi_j)$  - see Fig. 7.1.

In summary, the intrinsic kinematics of an elastically-tethered rotating filament is to rotate about the vertical axis with angular velocity  $\Omega_0 = \frac{T_0}{D_{33}}$  (constant at leading order), while the axis of the filament oscillates left and right, lagging behind the rotation of the helix by an angle between  $\pi/2$  and  $\pi$ . Notably, there is a one-way coupling between the lateral displacement and the phase angle of the filament, at leading order.

### 7.2.5 Multiple scales analysis

Now that we understand the intrinsic kinematics of each filament rotating in isolation, we consider how the two filaments behave when they rotate next to each other. To this end, we must invert the extended resistance matrix from Eq. (7.11), including the interaction terms. Note that the elements of  $\tilde{\mathbf{S}}$  are of  $\mathcal{O}(d^0)$  while the elements of  $\tilde{\mathbf{C}}$  are of  $\mathcal{O}(d^{-1})$ . In the far-field limit,  $d \gg 1$ , we calculate the inverse of the extended resistance matrix as an asymptotic series expansion in  $d$ , writing

$$\begin{aligned} \begin{pmatrix} \tilde{\mathbf{S}}(\phi_1) & \tilde{\mathbf{C}}(\phi_1, \phi_2) \\ \tilde{\mathbf{C}}^T(\phi_1, \phi_2) & \tilde{\mathbf{S}}(\phi_2) \end{pmatrix}^{-1} &= \begin{pmatrix} \tilde{\mathbf{S}}^{-1}(\phi_1) & 0 \\ 0 & \tilde{\mathbf{S}}^{-1}(\phi_2) \end{pmatrix} \\ &+ \begin{pmatrix} 0 & -\tilde{\mathbf{S}}^{-1}(\phi_1)\tilde{\mathbf{C}}(\phi_1, \phi_2)\tilde{\mathbf{S}}^{-1}(\phi_2) \\ -\tilde{\mathbf{S}}^{-1}(\phi_2)\tilde{\mathbf{C}}(\phi_2, \phi_1)\tilde{\mathbf{S}}^{-1}(\phi_1) & 0 \end{pmatrix} + \mathcal{O}(d^{-2}). \end{aligned} \quad (7.29)$$

Therefore, the dynamical system describing the evolving kinematics of the first helix is

$$\begin{pmatrix} \dot{x}_1 \\ \dot{\phi}_1 \end{pmatrix} = \tilde{\mathbf{S}}^{-1}(\phi_1) \begin{pmatrix} -kx_1 \\ T_0 \end{pmatrix} - \tilde{\mathbf{S}}^{-1}(\phi_1)\tilde{\mathbf{C}}(\phi_1, \phi_2)\tilde{\mathbf{S}}^{-1}(\phi_2) \begin{pmatrix} -kx_2 \\ T_0 \end{pmatrix} + \mathcal{O}(d^{-2}). \quad (7.30)$$

Because our setup is symmetric, the second helix evolves according to exactly the same equations with the indices swapped around.

Guided by observations from the numerical simulation of the system, and in accordance with the wider literature on the topic of hydrodynamic synchronisation, we assume that there is a separation of time scales between the fast time  $t$  for the rotation of the helix, and the slower time  $\tau = d^{-1}t$  on which the phase difference changes (the time scale for synchronisation). This separation of time scales allows us to analyse Eq. (7.30) using the method of multiple scales [84].

We express the independent variables in our system as

$$x_j(t) = x_j^{(0)}(t, \tau) + d^{-1}x_j^{(1)}(t, \tau) + \mathcal{O}(d^{-2}), \quad (7.31)$$

$$\phi_j(t) = \phi_j^{(0)}(t, \tau) + d^{-1}\phi_j^{(1)}(t, \tau) + \mathcal{O}(d^{-2}), \quad (7.32)$$

with time derivatives

$$\dot{x}_j(t) = \frac{\partial x_j^{(0)}}{\partial t} + d^{-1} \left( \frac{\partial x_j^{(0)}}{\partial \tau} + \frac{\partial x_j^{(1)}}{\partial t} \right) + \mathcal{O}(d^{-2}), \quad (7.33)$$

$$\dot{\phi}_j(t) = \frac{\partial \phi_j^{(0)}}{\partial t} + d^{-1} \left( \frac{\partial \phi_j^{(0)}}{\partial \tau} + \frac{\partial \phi_j^{(1)}}{\partial t} \right) + \mathcal{O}(d^{-2}). \quad (7.34)$$

To leading order, Eq. (7.30) gives the dynamical system

$$\begin{pmatrix} \partial x_1^{(0)} / \partial t \\ \partial \phi_1^{(0)} / \partial t \end{pmatrix} = \tilde{\mathbf{S}}^{-1}(\phi_1^{(0)}) \begin{pmatrix} -kx_1^{(0)} \\ T_0 \end{pmatrix}, \quad (7.35)$$

which we have solved in Section 7.2.4 for a single time scale. The second time scale can be incorporated into our solution from Eq. (7.22) by letting the constant of integration,  $\phi_j(0)$ , vary on the slow time scale,  $\tau$ , which leads to

$$\phi_j^{(0)}(t, \tau) = \hat{\phi}_j(\tau) + \Omega_0 t. \quad (7.36)$$

The one-way coupling between lateral displacement and phase angle is preserved, at leading order, so

$$x_j^{(0)}(t, \tau) \approx \rho(K) \cos(\hat{\phi}_j^{(0)} - \mathbf{v}(K)), \quad (7.37)$$

once the initial transients have decayed exponentially.

### 7.2.6 Kinematic perturbation due to hydrodynamic interactions

The process of synchronisation relies on the intrinsic kinematics of the filaments being perturbed by hydrodynamic interactions. Hence, we must consider the first-order terms in Eq. (7.30), which give the dynamical system

$$\begin{aligned} \begin{pmatrix} \partial x_1^{(0)}/\partial \tau + \partial x_1^{(1)}/\partial t \\ \partial \phi_1^{(0)}/\partial \tau + \partial \phi_1^{(1)}/\partial t \end{pmatrix} &= \tilde{\mathbf{S}}^{-1}(\phi_1^{(0)}) \begin{pmatrix} -kx_1^{(1)} \\ 0 \end{pmatrix} + \phi_1^{(1)} \frac{\partial \tilde{\mathbf{S}}^{-1}}{\partial \phi}(\phi_1^{(0)}) \begin{pmatrix} -kx_1^{(0)} \\ T_0 \end{pmatrix} \\ &\quad - \tilde{\mathbf{S}}^{-1}(\phi_1^{(0)}) [d\tilde{\mathbf{C}}(\phi_1^{(0)}, \phi_2^{(0)})] \tilde{\mathbf{S}}^{-1}(\phi_2^{(0)}) \begin{pmatrix} -kx_2^{(0)} \\ T_0 \end{pmatrix}. \end{aligned} \quad (7.38)$$

Due to the one-way coupling between the lateral displacement and the phase angle, we can eliminate the variables  $x_1^{(0)}$  and  $x_2^{(0)}$  from this system using Eq. (7.37), to find that

$$\begin{aligned} \begin{pmatrix} 1 & -\rho \sin(\phi_1^{(0)} - \nu) \\ 0 & 1 \end{pmatrix} \begin{pmatrix} \partial x_1^{(1)}/\partial t \\ \partial \phi_1^{(0)}/\partial \tau \end{pmatrix} + \begin{pmatrix} 0 \\ \partial \phi_1^{(1)}/\partial t \end{pmatrix} \\ = \tilde{\mathbf{S}}^{-1}(\phi_1^{(0)}) \begin{pmatrix} -kx_1^{(1)} \\ 0 \end{pmatrix} + \phi_1^{(1)} \frac{\partial \tilde{\mathbf{S}}^{-1}}{\partial \phi}(\phi_1^{(0)}) \begin{pmatrix} -k\rho \cos(\phi_1^{(0)} - \nu) \\ T_0 \end{pmatrix} \\ - \tilde{\mathbf{S}}^{-1}(\phi_1^{(0)}) [d\tilde{\mathbf{C}}(\phi_1^{(0)}, \phi_2^{(0)})] \tilde{\mathbf{S}}^{-1}(\phi_2^{(0)}) \begin{pmatrix} -k\rho \cos(\phi_2^{(0)} - \nu) \\ T_0 \end{pmatrix}. \end{aligned} \quad (7.39)$$

This system is under-determined since we have two coupled equations with three unknown functions to solve for:  $\phi_1^{(0)}$ ,  $x_1^{(1)}$  and  $\phi_1^{(1)}$ . A standard way to resolve this is to invoke a solvability condition that ensures our asymptotic expansion from Eqs. (7.31)-(7.32) remains valid at large times. In other words, we need to ensure that the first-order correction  $\phi_1^{(1)}$  remains bounded for large time  $t$ .

In Appendix 7.B, we provide the full derivation of the solvability condition which says that the terms proportional to  $\phi_1^{(1)}$  in Eq. (7.39) must vanish. Therefore, we arrive at a two-dimensional system of equations for  $\phi_1^{(0)}$  and  $x_1^{(1)}$  only,

$$\begin{aligned} \begin{pmatrix} 1 & -\rho \sin(\phi_1^{(0)} - \nu) \\ 0 & 1 \end{pmatrix} \begin{pmatrix} \partial x_1^{(1)}/\partial t \\ \partial \phi_1^{(0)}/\partial \tau \end{pmatrix} &= \tilde{\mathbf{S}}^{-1}(\phi_1^{(0)}) \begin{pmatrix} -kx_1^{(1)} \\ 0 \end{pmatrix} \\ &\quad - \tilde{\mathbf{S}}^{-1}(\phi_1^{(0)}) [d\tilde{\mathbf{C}}(\phi_1^{(0)}, \phi_2^{(0)})] \tilde{\mathbf{S}}^{-1}(\phi_2^{(0)}) \begin{pmatrix} -k\rho \cos(\phi_2^{(0)} - \nu) \\ T_0 \end{pmatrix}. \end{aligned} \quad (7.40)$$

As previously done for the matrix  $\tilde{\mathbf{S}}^{-1}(\phi)$  in Section 7.2.4, we calculate  $\tilde{\mathbf{S}}^{-1}(\phi_1)\tilde{\mathbf{C}}(\phi_1, \phi_2)\tilde{\mathbf{S}}^{-1}(\phi_2)$  as a series expansion in the small parameter  $(\pi N)^{-1}$ ,

$$\tilde{\mathbf{S}}^{-1}(\phi_1) [d\tilde{\mathbf{C}}(\phi_1, \phi_2)] \tilde{\mathbf{S}}^{-1}(\phi_2) = \mathbf{M}_2(\phi_1, \phi_2) + \mathbf{M}_0(\phi_1, \phi_2) + \mathcal{O}((\pi N)^{-1}), \quad (7.41)$$

with the first two coefficients equal to

$$\mathbf{M}_2(\phi_1, \phi_2) = -\frac{1}{8\pi\mu} \begin{pmatrix} 0 & 0 \\ 0 & B_{33}^2 D_{33}^{-2} \end{pmatrix}, \quad (7.42)$$

$$\mathbf{M}_0(\phi_1, \phi_2) = -\frac{1}{8\pi\mu} \begin{pmatrix} 2 & 0 \\ 0 & B_{23}^2 D_{33}^{-2} \cos(\phi_1) \cos(\phi_2) \end{pmatrix}. \quad (7.43)$$

The full derivation of these terms is provided in Appendix 7.C.

After substituting the results of Eqs. (7.18)-(7.20) and Eqs. (7.41)-(7.43) into Eq. (7.40), we find that

$$\begin{pmatrix} 1 & -\rho \sin(\phi_1^{(0)} - \nu) \\ 0 & 1 \end{pmatrix} \begin{pmatrix} \partial x_1^{(1)}/\partial t \\ \partial \phi_1^{(0)}/\partial \tau \end{pmatrix} = -\frac{k}{A_0} x_1^{(1)} \begin{pmatrix} 1 \\ B_{23} D_{33}^{-1} \sin(\phi_1^{(0)}) \end{pmatrix} \\ + \frac{1}{8\pi\mu} \begin{pmatrix} -2k\rho \cos(\phi_2^{(0)} - \nu) \\ B_{33}^2 D_{33}^{-2} T_0 + B_{23}^2 D_{33}^{-2} T_0 \cos(\phi_1^{(0)}) \cos(\phi_2^{(0)}) \end{pmatrix} + \mathcal{O}((\pi N)^{-1}). \quad (7.44)$$

Next, after inverting on the left-hand side, we have

$$\begin{pmatrix} \partial x_1^{(1)}/\partial t \\ \partial \phi_1^{(0)}/\partial \tau \end{pmatrix} \approx \begin{pmatrix} 1 & \rho \sin(\phi_1^{(0)} - \nu) \\ 0 & 1 \end{pmatrix} \\ \times \begin{pmatrix} -kA_0^{-1} x_1^{(1)} - \frac{k}{4\pi\mu} \rho \cos(\phi_2^{(0)} - \nu) \\ -\frac{kB_{23}}{A_0 D_{33}} x_1^{(1)} \sin(\phi_1^{(0)}) + \frac{B_{33}^2 T_0}{8\pi\mu D_{33}^2} + \frac{B_{23}^2 T_0}{8\pi\mu D_{33}^2} \cos(\phi_1^{(0)}) \cos(\phi_2^{(0)}) \end{pmatrix}, \quad (7.45)$$

where the  $\times$  sign represents standard matrix-vector multiplication in this case. From this we obtain immediately the slow evolution of the phase,

$$\frac{\partial \phi_1^{(0)}}{\partial \tau} = \frac{B_{33}^2 T_0}{8\pi\mu D_{33}^2} - \frac{kB_{23}}{A_0 D_{33}} x_1^{(1)} \sin(\phi_1^{(0)}) + \frac{B_{23}^2 T_0}{8\pi\mu D_{33}^2} \cos(\phi_1^{(0)}) \cos(\phi_2^{(0)}). \quad (7.46)$$

The equation for the lateral displacement involves more terms, but not all of them are essential. From Appendix 7.A, we know how all the terms scale with the number of helical

turns of the filament,

$$A_0 = \mathcal{O}((\pi N)^0), \quad B_{33} = \mathcal{O}((\pi N)^{-1}), \quad B_{23}, D_{33} = \mathcal{O}((\pi N)^{-2}), \quad (7.47)$$

so the first term on the right hand side of Eq. (7.46) is dominant, being of  $\mathcal{O}((\pi N)^2)$ . Furthermore, from Eqs. (7.28) and (7.47), we deduce that  $\rho = \mathcal{O}((\pi N)^{-2})$ .

Hence, from Eq. (7.45), the fast evolution of the lateral displacement is

$$\frac{\partial x_1^{(1)}}{\partial t} = -\frac{k}{A_0}x_1^{(1)} - \frac{k}{4\pi\mu}\rho \cos(\phi_2^{(0)} - \nu) - \frac{B_{33}^2 T_0}{8\pi\mu D_{33}^2}\rho \sin(\phi_1^{(0)} - \nu), \quad (7.48)$$

up to and including  $\mathcal{O}((\pi N)^0)$  terms. The general solution of this equation has the form

$$x_1^{(1)}(t, \tau) = \hat{x}_1(\tau)e^{-kt/A_0} + \gamma \sin(\phi_1^{(0)}) + \delta \cos(\phi_1^{(0)}) + \zeta \sin(\phi_2^{(0)}) + \eta \cos(\phi_2^{(0)}), \quad (7.49)$$

and is obtained by multiplying the differential equation by an integrating factor,  $\exp(kt/A_0)$ , and then integrating the right-hand side by parts using the fact that  $\partial\phi_j^{(0)}/\partial t \approx T_0 D_{33}^{-1}$  to leading order.

### 7.2.7 Evolution of phase difference

To obtain the evolution of the phase difference, we subtract the two versions of Eq. (7.46) with the indices swapped around to get

$$\frac{\partial}{\partial \tau} (\phi_1^{(0)} - \phi_2^{(0)}) = -\frac{kB_{23}}{A_0 D_{33}} (x_1^{(1)} \sin(\phi_1^{(0)}) - x_2^{(1)} \sin(\phi_2^{(0)})) \quad (7.50)$$

Then, by substituting the solution for  $x_j^{(1)}$  from Eq. (7.49) and neglecting the transient term, since it does not affect the long-time dynamics, we get that

$$\begin{aligned} \frac{\partial}{\partial \tau} (\phi_1^{(0)} - \phi_2^{(0)}) = & -\frac{kB_{23}}{A_0 D_{33}} \left[ \gamma (\sin^2(\phi_1^{(0)}) - \sin^2(\phi_2^{(0)})) \right. \\ & \left. + \delta (\sin(\phi_1^{(0)}) \cos(\phi_1^{(0)}) - \sin(\phi_2^{(0)}) \cos(\phi_2^{(0)})) + \eta \sin(\phi_1^{(0)} - \phi_2^{(0)}) \right]. \end{aligned} \quad (7.51)$$

The first two terms on the right-hand side of the equation are equivalent to

$$\sin^2(\phi_1^{(0)}) - \sin^2(\phi_2^{(0)}) = \sin(\Delta\phi) \sin(2\bar{\phi}), \quad (7.52)$$

$$\sin(\phi_1) \cos(\phi_1) - \sin(\phi_2) \cos(\phi_2) = \sin(\Delta\phi) \cos(2\bar{\phi}). \quad (7.53)$$

Note that the phase difference  $\Delta\phi = \phi_1^{(0)} - \phi_2^{(0)}$  only varies on the slow time scale, while the mean phase  $\bar{\phi} = (\phi_1^{(0)} + \phi_2^{(0)})/2 \approx T_0 D_{33}^{-1} t$  increases linearly on the fast time scale, to leading order. Therefore, the first two terms on the right-hand side of Eq. (7.51) average out to zero when integrated over the fast time scale.

Hence, the average phase difference evolves according to the equation

$$\frac{\partial \Delta\phi}{\partial \tau} = -\frac{kB_{23}\eta}{A_0 D_{33}} \sin(\Delta\phi). \quad (7.54)$$

This is the classic Adler's equation [2]

$$\frac{\partial \Delta\phi}{\partial \tau} = -\frac{1}{\tau_{\text{sync}}} \sin(\Delta\phi), \quad (7.55)$$

with solution

$$\Delta\phi(\tau) = 2 \tan^{-1} \left[ \tan \left( \frac{\Delta\phi_0}{2} \right) \exp \left( -\frac{\tau}{\tau_{\text{sync}}} \right) \right]. \quad (7.56)$$

Hence, the long-time behaviour of the system is that the helices synchronise to an in-phase configuration with  $\Delta\phi \rightarrow 0$  as  $\tau \rightarrow \infty$ .

## 7.2.8 Time scale for synchronisation

To determine the time scale of synchronisation, we must find the coefficient  $\eta$  from Eq. (7.49). This coefficient comes from the integration by parts of the term

$$\int^t e^{ks/A_0} \cos(\phi_2^{(0)}(s, \tau) - \nu) ds = e^{kt/A_0} \frac{kA_0^{-1} \cos(\phi_2^{(0)} - \nu) + T_0 D_{33}^{-1} \sin(\phi_2^{(0)} - \nu)}{k^2 A_0^{-2} + T_0^2 D_{33}^{-2}}, \quad (7.57)$$

giving us

$$\eta = -\frac{k\rho}{4\pi\mu} \times \frac{kA_0^{-1} \cos(\nu) - T_0 D_{33}^{-1} \sin(\nu)}{k^2 A_0^{-2} + T_0^2 D_{33}^{-2}}. \quad (7.58)$$

Using the definitions of  $\rho$  and  $\nu$  from Eq. (7.28), and  $K$  from Eq. (7.26), we simplify this result as

$$\eta = \frac{B_{23}K^2}{2\pi\mu(K^2 + 1)^2}. \quad (7.59)$$

Finally, by combining Eqs. (7.54), (7.55) and (7.59), we identify the dimensionless time scale for synchronisation,  $t_{\text{sync}} = d\tau_{\text{sync}}$ , as

$$t_{\text{sync}} = \frac{2\pi\mu d D_{33}^2}{B_{23}^2 T_0} \lambda(K), \quad \lambda(K) = \frac{(K^2 + 1)^2}{K^3}. \quad (7.60)$$

Note that the time scale for synchronisation is linearly proportional to the distance between the filaments, and is non-monotonic in the dimensionless parameter  $K$ . The function  $\lambda(K)$  has a global minimum at  $K = \sqrt{3}$ , and behaves asymptotically as  $\lambda(K) \sim K^{-3}$  for small  $K$  and  $\lambda(K) \sim K$  for large  $K$ .

Using the RFT expressions for the resistance coefficients  $A_0$ ,  $B_{23}$  and  $D_{33}$ , listed in Appendix 7.A, we derive a closed-form analytical expression for the synchronisation time scale of two hydrodynamically-coupled rotating helices

$$t_{\text{sync}}^{\text{RFT}} = \frac{2\pi\mu d}{T_0} \left( \frac{\sin(\psi)}{\sin(\pi N)} \right)^2 \frac{(K_{\text{RFT}}^2 + 1)^2}{K_{\text{RFT}}^3}, \quad (7.61)$$

where

$$K_{\text{RFT}} = \frac{2(\cos^2 \psi c_{\perp} + \sin^2 \psi c_{\parallel})}{(1 + \cos^2 \psi) c_{\perp} + \sin^2 \psi c_{\parallel}} \left( \frac{\sin(\psi)}{\pi N} \right)^2 \frac{k}{T_0}. \quad (7.62)$$

Notably, the synchronisation time diverges at integer number of helical turns, when  $\sin(\pi N) = 0$ . A physical explanation of this divergence is provided in Section 7.3.

We make the result of Eq. (7.61) dimensional by using the length scale  $\tilde{L}/2$  and time scale  $\tilde{\mu}\tilde{L}^3/8\tilde{T}_0$  which we had used to non-dimensionalise our problem. In dimensional form, the synchronisation time can be written as a function of the filament length as

$$\tilde{t}_{\text{sync}}^{\text{RFT}} = \frac{\pi\tilde{\mu}\tilde{d}\tilde{L}^2}{2\tilde{T}_0} \left( \frac{\sin(\psi)}{\sin(\pi N)} \right)^2 \frac{(K_{\text{RFT}}^2 + 1)^2}{K_{\text{RFT}}^3}, \quad (7.63)$$

and

$$K_{\text{RFT}} \approx \left( \frac{2 + 2\cos^2 \psi}{3 + \cos^2 \psi} \right) \frac{\tilde{k}\tilde{R}^2}{\tilde{T}_0}, \quad (7.64)$$

using the fact that the perpendicular drag coefficient is roughly twice as large as the parallel drag coefficient,  $c_{\perp} \approx 2c_{\parallel}$  (see Eq. (7.94)).

### 7.2.9 Unequal driving torques

We next consider the situation when the two helices are driven by unequal torques,  $\mathbf{T}_j = T_0(1 + \alpha(-1)^j)\mathbf{e}_z$ , where the index  $j$  identifies the helix. The leading order equation for the evolution of the phase, Eq. (7.35), is hence modified to

$$\begin{pmatrix} \partial x_j^{(0)}/\partial t \\ \partial \phi_j^{(0)}/\partial t \end{pmatrix} = \tilde{\mathbf{S}}^{-1}(\phi_1^{(0)}) \begin{pmatrix} -kx_j^{(0)} \\ T_0(1 + \alpha(-1)^j) \end{pmatrix}, \quad (7.65)$$

which means that the phases evolve according to the equivalent of Eq. (7.36),

$$\phi_j^{(0)}(t, \tau) \approx \tilde{\phi}_j(\tau) + T_0 D_{33}^{-1} (1 + \alpha(-1)^j) t. \quad (7.66)$$

Assuming that the system settles into a long-term equilibrium (i.e.  $\tilde{\phi}_j(\tau)$  tends to a constant value), the helices tend towards a steady state of rotation with a fixed phase difference,  $\Delta\phi_\infty$ , such that

$$\lim_{\tau \rightarrow \infty} \phi_j^{(0)}(t, \tau) = (-1)^j \frac{\Delta\phi_\infty}{2} + T_0 D_{33}^{-1} [1 + \alpha(-1)^j] t, \quad (7.67)$$

$$\lim_{\tau \rightarrow \infty} \frac{\partial \Delta\phi}{\partial t} = -2\alpha T_0 D_{33}^{-1}. \quad (7.68)$$

Substituting these expressions into Eq. (7.55), we obtain

$$2\alpha T_0 D_{33}^{-1} = \frac{\sin(\Delta\phi_\infty)}{t_{\text{sync}}}. \quad (7.69)$$

Physically, Eq. (7.69) is saying that, in order to maintain a stable equilibrium, the rate at which the faster helix is moving ahead (the left-hand side of the equation) must equal the rate at which the slower helix is catching up (the right-hand side of the equation). For  $\alpha \neq 0$ , the equilibrium phase difference is positive and the helices can no longer synchronise in-phase.

When the helices are driven by constant but unequal torques, they synchronise to a fixed phase difference  $\Delta\phi_\infty$  that satisfies

$$\sin(\Delta\phi_\infty) = 2\alpha \frac{t_{\text{sync}}}{t_{\text{rot}}}, \quad (7.70)$$

where we have introduced the leading-order time scale of rotation  $t_{\text{rot}} = D_{33}/T_0$ . The condition is that the fractional torque difference between the two filaments is not too large,

$$|\alpha| < \frac{t_{\text{rot}}}{2t_{\text{sync}}} \equiv \alpha_c. \quad (7.71)$$

As the parameter  $\alpha$  is increased past the critical value,  $\alpha_c$ , the system undergoes a saddle-node bifurcation where the unstable branch (starting from  $\Delta\phi = \pi$  at  $\alpha = 0$ ) and the stable branch (starting from  $\Delta\phi = 0$  at  $\alpha = 0$ ) collide and disappear. For  $|\alpha| > \alpha_c$  there are no steady states towards which the helices can synchronise, so the faster helix slips periodically past the slower one.

The result of Eq. (7.71) is consistent with previous computational studies, where rotating helical filaments would slip out of phase with each other if the difference in driving torques

is greater than a critical value that decays with increasing distance between the filaments [177]. Here as well, we find that  $\alpha_c \sim d^{-1}$  through its dependence on the time scale for synchronisation.

## 7.3 Physical mechanism for synchronisation

In this section we provide, with the help of diagrams, an intuitive explanation for the physical mechanism that leads to the synchronisation of two hydrodynamically-coupled and elastically-tethered helices rotating about their axes.

### 7.3.1 Preliminary considerations

We consider a slightly modified setup where the axes of the helices are allowed to move in both the  $x$  and the  $y$  directions. This helps to illustrate the physical mechanism more clearly, without the need to project quantities onto the  $x$  axis at every step. In contrast, the one-dimensional elastic trap is more convenient for analytical calculations since it reduces the number of equations to be solved, which is why this setup was preferred in the previous section. Note that we have compared the two setups by way of numerical simulations (data not shown) to confirm that the physical mechanisms are identical, the only difference being a 50% increase in the rate of synchronisation when the helices are allowed to move in the  $y$  direction as well. This suggests that oscillations along  $x$  contribute twice as much to synchronisation as do oscillations along  $y$ , which is consistent with the anisotropy of hydrodynamic interactions (the Oseen tensor is proportional to  $\mathbf{I} + \mathbf{e}_x \mathbf{e}_x$  at leading order).

Since the dynamics that lead to synchronisation happen in the plane perpendicular to the axes of the helices, we can explain the physical mechanism for synchronisation by considering only the projection of the helical filaments onto the horizontal plane. After discarding full circles, over which the forces balance out by symmetry, the helical filaments are thus reduced to the shape of a circular arc rotating about its centre in the horizontal plane. We call this shape a “horseshoe”.

### 7.3.2 Intrinsic dynamics of a helical filament

In order to understand the dynamics by which two rotating helices synchronise through hydrodynamic interactions, we must first understand the intrinsic dynamics of a single helix in the absence of hydrodynamic interactions. We explain the intrinsic dynamics of an elastically-tethered rotating helix using the reduced horseshoe model introduced above

and the diagrams in Fig. 7.2. Along the way, we point out the key features that lead to synchronisation in the physical mechanism considered in this chapter.

The first of these features is that there exists a net viscous force on the horseshoe due to its rotation about its centre. In Fig. 7.2 (a), we show the local velocity of the fluid relative to a rotating horseshoe (short straight arrows). Because the velocity is always tangent to the filament, this leads to a local fluid drag in the same direction. When integrating the local drag over the entire filament, the components parallel to  $\mathbf{e}_r(\phi)$  cancel out by symmetry, where the phase  $\phi$  of the horseshoe is the angle between the midpoint of the horseshoe and the  $x$  axis. However, symmetry is lost in the  $\mathbf{e}_\phi(\phi)$  direction unless the horseshoe is a complete circle (equivalent to a helical filament with an integer number of turns). Therefore, a horseshoe rotating CCW about its centre experiences a net fluid drag in the negative  $\mathbf{e}_\phi(\phi)$  direction. The mechanism for synchronisation depends on the existence of this net viscous drag due to rotation, which explains why the time scale for synchronisation from Eq. (7.61) diverges when the helices have an integer number of turns. The consequence of the net viscous drag due to rotation is that the elastically-tethered horseshoe performs oscillations around its tethering point, and the radius of this orbit depends crucially on the elastic compliance of the tether, as we now proceed to explain.

Since the horseshoe is force-free, it must orbit around the centre of the elastic trap in order to balance the viscous drag due to rotation (or, in the 1D version version of the problem, it will oscillate around  $x = 0$ , as seen in the previous section). When the elastic tether is very flexible (Fig. 7.2 (b)), the viscous drag due to rotation is balanced out primarily by the viscous drag due to translation, so  $\dot{\mathbf{x}} \parallel -\mathbf{e}_\phi(\phi)$ . This means that the orbiting motion of the centre of the horseshoe,  $\mathbf{x}$ , lags behind the phase  $\phi$  by an angle slightly less than  $\pi$ . At the opposite end of the spectrum, when the elastic tether is very stiff (Fig. 7.2 (c)), the viscous drag due to the rotation of the horseshoe is balanced out primarily by the elastic restoring force, and hence the centre of the horseshoe lags behind the rotation phase  $\phi$  by an angle slightly greater than  $\pi/2$ . Note that the orbit occupied by the centre of the horseshoe reduces in amplitude as the strength of elastic tethering is increased (c.f. Eqs. (7.27) and (7.28)). This information is summarised in Fig. 7.2 (d), where we depict by green arrows the possible positions  $\mathbf{x}$  of the centre of the horseshoe for varying elastic tethering strength.

The net hydrodynamic force exerted by the horseshoe on the fluid, which ultimately leads to hydrodynamic interactions with the second horseshoe, is equal to the elastic restoring force applied to the horseshoe by the elastic tether,  $-k\mathbf{x}$ . This is also depicted on Fig. 7.2 (d) as orange arrows. Because the centre of the horseshoe lags behind the phase  $\phi$  by an angle between  $\pi/2$  and  $\pi$  (c.f. Eqs. (7.27) and (7.28)), this means that the net force exerted by the filament on the fluid has positive components in both the  $\mathbf{e}_r(\phi)$  and  $\mathbf{e}_\phi(\phi)$  directions. Notably,

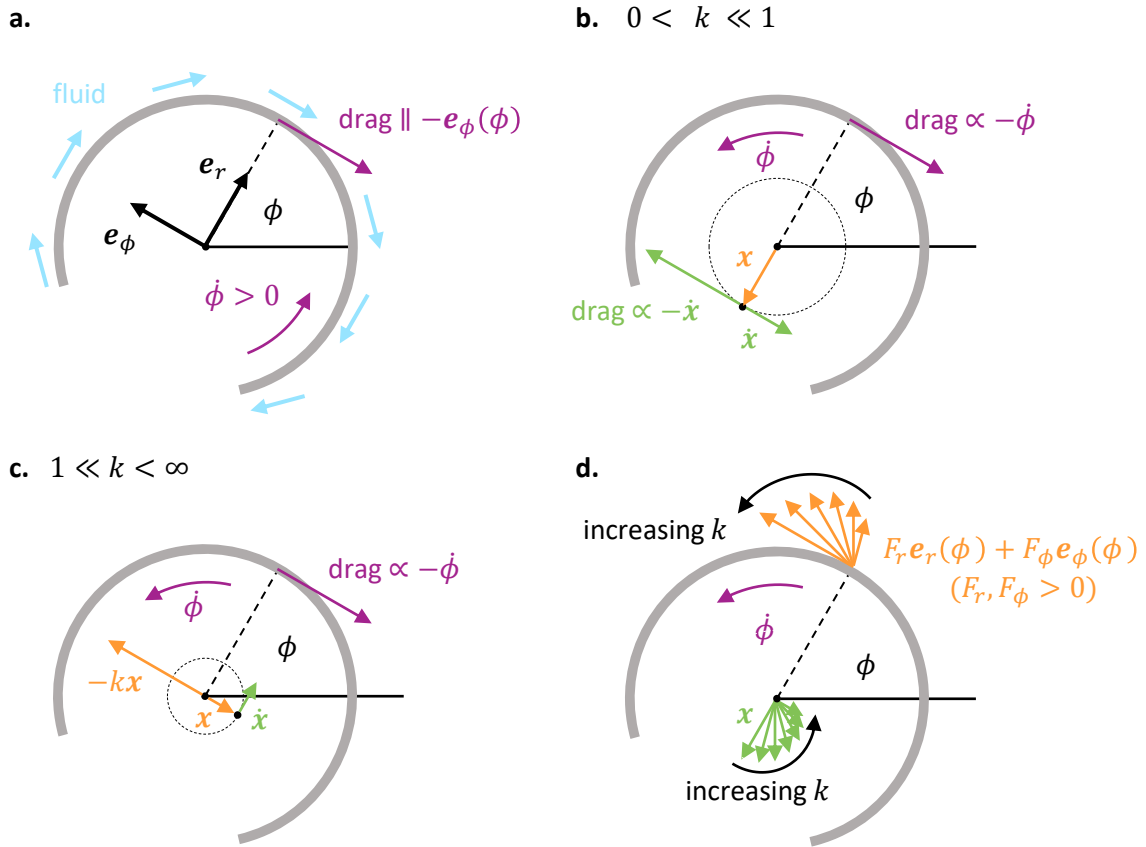


Fig. 7.2 Intrinsic dynamics of a rotating horseshoe in the absence of hydrodynamic interactions. (a) When a horseshoe with phase  $\phi$  rotates CCW relative to the fluid, it feels a net drag from the fluid in the negative  $e_\phi(\phi)$  direction. If placed in an elastic trap, the rotating horseshoe will oscillate about the centre of the trap in order to balance this viscous drag. (b) When the elastic restoring force is very weak ( $0 < k \ll 1$ ), the viscous drag on the horseshoe due to rotation is balanced out primarily by the viscous drag due to translation. Therefore, the centre of the horseshoe,  $\mathbf{x}$ , lags behind the phase  $\phi$  by an angle  $\pi$ . (c) When the elastic restoring force is very strong ( $1 \ll k < \infty$ ), the viscous drag on the horseshoe due to rotation is balanced out primarily by the elastic restoring force. Therefore, the centre of the horseshoe lags behind the rotation phase  $\phi$  only by an angle  $\pi/2$ . (d) For  $0 < k < \infty$ , the centre of the horseshoe lags behind the phase  $\phi$  by an angle between  $\pi/2$  and  $\pi$ , and the amplitude of the orbit decreases with increasing  $k$ . In this way, the net force exerted by the horseshoe on the fluid,  $\mathbf{F}_h = -k\mathbf{x}$ , has a positive component in the  $e_r(\phi)$  direction, and this component is largest for intermediate values of  $k$ .

the  $\mathbf{e}_r(\phi)$  component vanishes for both  $k = 0$  (because there is no elastic restoring force), and for  $k \rightarrow \infty$  (because the force is parallel to  $\mathbf{e}_\phi(\phi)$ ), and it is largest for intermediate values of  $k$ . As we later explain, the  $\mathbf{e}_r(\phi)$  component of the hydrodynamic force is crucial for synchronisation. This is why the time scale for synchronisation from Eq. (7.60) is minimised at intermediate values of the elastic tethering strength  $k$ , because the radial component of the force exerted by the filament on the fluid is largest.

### 7.3.3 Dynamics of synchronisation

Having understood how each horseshoe behaves at leading order, i.e. its intrinsic dynamics in the absence of hydrodynamic interactions, we now illustrate in Fig. 7.3 how the net hydrodynamic forces exerted by the horseshoes on the fluid affect their respective kinematics.

In the far-field, the flow exerted by the first horseshoe is that of a Stokeslet of strength  $\mathbf{F}_1$ , which at the position of the second filament manifests itself, to leading-order, as a uniform flow in the direction  $(\mathbf{I} + \mathbf{e}_x \mathbf{e}_x) \cdot \mathbf{F}_1$ . We first explain how a horseshoe responds to a generic uniform background flow, as shown in Fig. 7.3 (a) and (b). If the flow is parallel to  $\mathbf{e}_r(\phi)$ , then the forces are balanced by symmetry and the horseshoe does not rotate. If, however, the flow is in the positive (or negative)  $\mathbf{e}_\phi(\phi)$  direction, then the horseshoe speeds up (or slows down) due to the force exerted on it by the fluid. Therefore, when looking at the hydrodynamic interaction of two rotating horseshoes, it is the  $\mathbf{e}_\phi(\phi)$  component of the induced flow that determines whether they synchronise or not.

Finally, in Fig. 7.3 (c) we bring together our understanding of the net force exerted by each filament on the fluid, and the way in which each filament responds to a uniform background flow, in order to deduce that hydrodynamic interactions lead to in-phase synchronisation. We consider the hydrodynamic interactions coming from the radial component of the net hydrodynamic force,  $F_r \mathbf{e}_r(\phi_j)$ , and then the azimuthal component,  $F_\phi \mathbf{e}_\phi(\phi_j)$ .

If the leftmost horseshoe is more advanced (by at most an angle  $\pi$ ), then  $F_r \mathbf{e}_r(\phi_2)$  points in the negative  $\mathbf{e}_\phi(\phi_1)$  direction since  $F_r > 0$ . Hence, the flow induced by the rightmost horseshoe in the  $+\mathbf{e}_r(\phi_2)$  direction, indicated by purple arrows on the left of Fig. 7.3 (c), makes the leftmost horseshoe slow down. Likewise, the flow induced by the leftmost filament in the  $+\mathbf{e}_r(\phi_1)$  direction makes the rightmost filament speed up, and the two horseshoes synchronise in-phase. There is, of course, a second contribution to the background flow proportional to  $F_r \mathbf{e}_x(\mathbf{e}_x \cdot \mathbf{e}_r(\phi_1))$ , but we do not show it on the diagram because its effect is more subtle. The rightmost horseshoe can either speed up or slow down due to this component of the flow, based on the sign of  $F_r(\mathbf{e}_\phi(\phi_2) \cdot \mathbf{e}_x)(\mathbf{e}_x \cdot \mathbf{e}_r(\phi_1)) = -F_r \sin \phi_2 \cos \phi_1$ . However, the angular velocity of the rightmost horseshoe relative to the leftmost one is proportional to  $F_r(\sin \phi_1 \cos \phi_2 - \sin \phi_2 \cos \phi_1) = F_r \sin(\phi_1 - \phi_2)$ , so the rightmost horseshoe

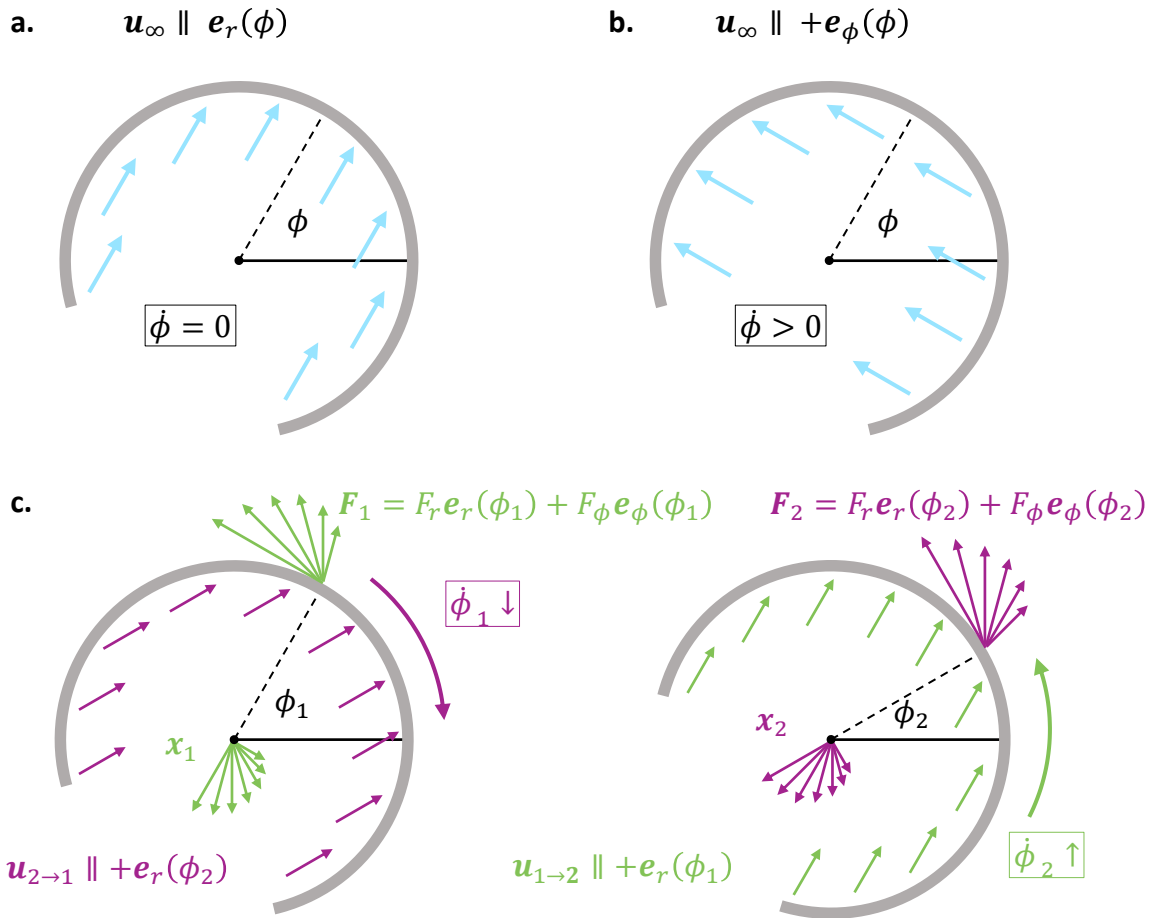


Fig. 7.3 Physical mechanism for the synchronisation of two hydrodynamically-coupled rotating horseshoes. (a) A horseshoe with phase  $\phi$  neither speeds up, nor slows down if placed in a background flow parallel to  $\mathbf{e}_r(\phi)$ . (b) The horseshoe speeds up/slow down if placed in a background flow with positive/negative  $\mathbf{e}_\phi(\phi)$  component. (c) Two interacting horseshoes. To leading order, the centre of rotation of each horseshoe undergoes circular periodic motion around its reference position, due to the unbalanced geometry of the horseshoe - see Fig. 7.2. Each exerts a net force on the fluid with positive components along  $\mathbf{e}_r(\phi)$  and  $\mathbf{e}_\phi(\phi)$ . As explained in the text, the azimuthal component of the force does not affect the relative rotation rate of the horseshoes so, for clarity of the diagram, we do not depict its contribution to hydrodynamic interactions. The contribution of the radial component of the force is illustrated by small green/purple arrows for the flow induced by the leftmost/rightmost horseshoe. The horseshoes respond to the background flow according to the principles described in (a) and (b). Because the leftmost horseshoe is more advanced, it is slowed down by the flow induced by the other filament. Likewise, the rightmost horseshoe speeds up due to hydrodynamic interactions, leading to in-phase synchronisation. The rate of synchronisation is proportional to the radial component of the leading-order force, which is largest in magnitude for intermediate values of the elastic tethering strength - see Fig. 7.2.

catches up from behind if  $0 < \phi_1 - \phi_2 < \pi$ . Therefore, both contributions to the background flow coming from the radial force,  $F_r \mathbf{e}_r(\phi)$ , have the effect of reducing the phase difference between the filaments.

In contrast, the  $F_\phi \mathbf{e}_\phi(\phi)$  component of the hydrodynamic force does not contribute to synchronisation, since it leads to a symmetric effect proportional to  $F_\phi \mathbf{e}_\phi(\phi_1) \cdot (\mathbf{I} + \mathbf{e}_x \mathbf{e}_x) \cdot \mathbf{e}_\phi(\phi_2)$  on both filaments, which makes them both speed up or slow down by the same amount. This justifies our earlier statement that the radial component of the hydrodynamic force is the one crucial for synchronisation.

## 7.4 Numerical simulations

In this section, we compare the theoretical predictions of Section 7.2 against numerical simulations, in order to verify that the two asymptotic steps in our calculations are justified (the multiple scales expansion in a slow and a fast time variable, and the series expansion of the mobility matrices in powers of the number of helical turns of the filament).

### 7.4.1 Computational method

In the simulations, we compute the instantaneous hydrodynamic forces on the two filaments using Johnson's slender-body theory (SBT) [105], and then we step forward in time using the classic Runge–Kutta method (RK4).

For the calculation of instantaneous forces, we solve an integral equation relating the velocity along the filament centreline,  $\mathbf{u}(\mathbf{r}_j(s))$ , and the force densities along the two filaments,  $\mathbf{f}_1(s)$  and  $\mathbf{f}_2(s)$ , via

$$8\pi\mu\mathbf{u}(\mathbf{r}_1(s)) = \mathcal{L}[\mathbf{f}_1(s)] + \mathcal{K}[\mathbf{f}_1(s')] + \mathcal{J}[\mathbf{f}_2(s'), \mathbf{d}], \quad (7.72)$$

where the first operator represents local effects

$$\mathcal{L}[\mathbf{f}_1(s)] = \left[ 2 \left( \ln \left( \frac{2}{\varepsilon} \right) + \frac{1}{2} \right) \mathbf{I} + 2 \left( \ln \left( \frac{2}{\varepsilon} \right) - \frac{3}{2} \right) \hat{\mathbf{t}}_1(s) \hat{\mathbf{t}}_1(s) \right] \cdot \mathbf{f}_1(s), \quad (7.73)$$

and the second operator represents non-local effects

$$\begin{aligned} \mathcal{K}[\mathbf{f}_1(s')] = \int_{-1}^{+1} \left[ \frac{\mathbf{I} + \hat{\mathbf{R}}_0(s, s') \hat{\mathbf{R}}_0(s, s')}{|\mathbf{R}_0(s, s')|} - \frac{\mathbf{I} + \hat{\mathbf{t}}_1(s) \hat{\mathbf{t}}_1(s)}{|s' - s|} \right] \cdot \mathbf{f}_1(s') ds' \\ + (\mathbf{I} + \hat{\mathbf{t}}_1(s) \hat{\mathbf{t}}_1(s)) \cdot \int_{-1}^{+1} \frac{\mathbf{f}_1(s') - \mathbf{f}_1(s)}{|s' - s|} ds', \end{aligned} \quad (7.74)$$

where  $\mathbf{R}_0(s, s') = \mathbf{r}_1(s) - \mathbf{r}_1(s')$ . Finally, the third operator represents interactions between the two filaments, as previously modelled by Tornberg and Shelley [205],

$$\mathcal{J}[\mathbf{f}_2(s'), \mathbf{d}] = \int_{-1}^{+1} \left[ \frac{\mathbf{I} + \hat{\mathbf{R}}_d(s, s')\hat{\mathbf{R}}_d(s, s')}{|\mathbf{R}_d(s, s')|} + \frac{\varepsilon^2 \mathbf{I} - 3\hat{\mathbf{R}}_d(s, s')\hat{\mathbf{R}}_d(s, s')}{2|\mathbf{R}_d(s, s')|^3} \right] \cdot \mathbf{f}_2(s') ds', \quad (7.75)$$

where  $\mathbf{R}_d(s, s') = \mathbf{d} + \mathbf{r}_2(s') - \mathbf{r}_1(s)$ . The two terms in the interaction operator,  $\mathcal{J}$ , represent Stokeslet and source dipole contributions, respectively.

We solve Eq. (7.72) numerically using a Galerkin method, whereby we decompose the velocities,  $\mathbf{u}(\mathbf{r}_j(s))$ , and force densities,  $\mathbf{f}_j(s)$ , into Legendre polynomial modes. The system is then truncated to a finite number of modes,  $N_{\text{Legendre}}$ , and inverted numerically to find the net forces and torques exerted by the filaments,  $(\mathbf{F}_1, \mathbf{T}_1; \mathbf{F}_2, \mathbf{T}_2)$ , for any given rigid body motion of the filaments,  $(\mathbf{U}_1, \boldsymbol{\Omega}_1; \mathbf{U}_2, \boldsymbol{\Omega}_2)$ . This is equivalent to finding the extended resistance matrix from Eq. (7.3) by computational means.

Our computational method for evaluating the instantaneous forces is identical to that from Chapter 6. We refer the reader to §6.3.1 for further details of the numerical implementation. All numerical results presented in this chapter, with the exception of the data from Fig. 7.6 (e-f) and Fig. 7.7 (c), were obtained by truncating the solution to  $N_{\text{Legendre}} = 15$  Legendre polynomial modes. This cutoff was chosen based on self-convergence tests for the resistance matrix of a single filament with the geometry of the normal polymorphic form (i.e. solving Eq. (7.72) without the interaction term,  $\mathcal{J}$ ). The SBT computations used in Fig. 7.6 (e-f) and Fig. 7.7 (c) were obtained with a higher number of Legendre polynomial modes,  $N_{\text{Legendre}} = 24$ , to account for the fact that the curly I and II polymorphic forms have more helical turns per unit length of the filament.

To obtain the time evolution of the rotating filaments, we solve the dynamical system

$$\dot{\mathbf{X}} = \mathbf{R}(\mathbf{X})^{-1} \mathbf{F}(\mathbf{X}), \quad (7.76)$$

where  $\mathbf{X}$  is the generalised configuration of the two filaments, i.e. the orientations of both filaments and the positions of their centres, and  $\mathbf{F}$  encapsulates the overall dynamics, i.e. the forces and torques on both filaments, and may depend on the instantaneous configuration. The linear relationship between the two is provided by the extended resistance matrix,  $\mathbf{R}(\mathbf{X})$ , calculated from Eq. (7.72), as described above.

We integrate Eq. (7.76) numerically using the classic Runge–Kutta method (RK4), within the conditions prescribed by the minimal model of synchronisation introduced in Section 7.2.1. Therefore, we impose the condition that  $\dot{\mathbf{X}} = 0$  in all components except for the four degrees of freedom of the system,  $x_{1,2}$  and  $\phi_{1,2}$ . In these four degrees of freedom, we

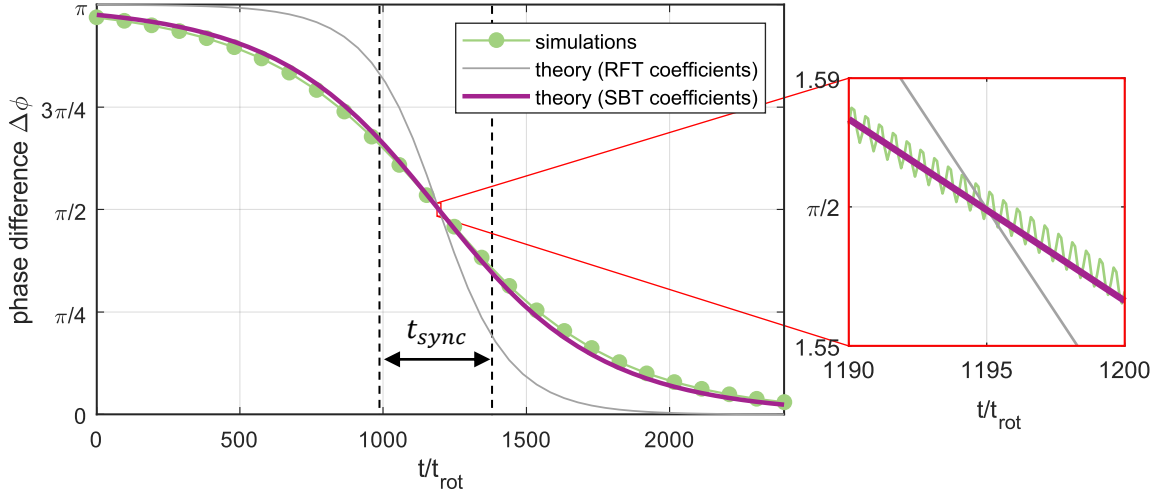


Fig. 7.4 In-phase synchronisation of two hydrodynamically-coupled helices. On a large time scale (left) the phase difference decays like the solution of Adler’s equation, Eq. (7.56), while on a short time scale (right) the phase difference oscillates with twice the frequency of rotation of the helices. We define the time scale for synchronisation as the inverse rate of synchronisation in the linear regime around  $\Delta\phi = \pi/2$ . Simulation parameters:  $d = 2L$ ,  $K = 300$ ,  $N = 2.5$ ,  $\psi = 0.5$ ,  $\varepsilon = 0.0038$ .

prescribe a constant driving torque,  $T_0\mathbf{e}_z$ , and an elastic restoring force,  $-kx_j\mathbf{e}_x$ , for each filament. The initial conditions for the dependent variables are

$$\phi_1(0) = 0, \quad \phi_2(0) = \frac{\pi}{2}, \quad x_1(0) = \rho \cos(\nu), \quad x_2(0) = \rho \sin(\nu), \quad (7.77)$$

where the conditions for  $x_{1,2}$  are informed by our knowledge of the intrinsic dependence of the lateral displacement on the phase angle, Eq. (7.27). The only exception is the numerical simulation shown in Fig. 7.4, where the phase difference  $\Delta\phi = \phi_2 - \phi_1$  starts close to  $\pi$ .

Note that the time step must be smaller than the period of rotation, so that we capture the dynamics on the fast time scale of rotation as well. The time step chosen for our integration is  $t_{\text{step}} = t_{\text{rot}}/20$ , where the intrinsic time scale for rotation  $t_{\text{rot}} = T_0/D_{33} = D_{33}^{-1}$  is estimated from the SBT resistance matrix of a single filament (derived by solving Eq. (7.72) without the interaction term,  $\mathcal{I}$ ). The only exception is the long-time simulation shown in Fig. 7.4, where we use a smaller time step,  $t_{\text{step}} = t_{\text{rot}}/10$ .

## 7.4.2 Comparison with theory

In Fig. 7.4 (left), we show the time evolution of the phase difference over the slow time scale of synchronisation. We compare the results obtained from numerical simulations (see

Section 7.4.1) with the analytical results from the multiple scales analysis of the system (see Eqs. (7.56) and (7.60)). The theory with RFT/SBT coefficients means that we compute the time scale for synchronisation by substituting into Eq. (7.60) the coefficients of the resistance matrix,  $A_{ij}, B_{ij}, D_{ij}$ , obtained from RFT/SBT. Analytical expressions for the RFT coefficients are provided in Appendix 7.A, while the SBT coefficients are calculated numerically by solving Eq. (7.72) without the interaction term,  $\mathcal{I}$ .

The results of Fig. 7.4 demonstrate perfect agreement between the theory with SBT coefficients and the numerical simulations, which are also based on SBT, thus validating our multiple scales analysis of the dynamical system. The theory with RFT coefficients captures the qualitatively features of synchronisation, and the correct order of magnitude for the time scale of synchronisation. Note that the mismatch between RFT and SBT is expected, since RFT does not take into account the full hydrodynamic interactions between points along the slender filament, which are incorporated in SBT through the non-local term,  $\mathcal{K}$ , in Eq. (7.72).

In Fig. 7.4 (right), we zoom in on a short time interval around phase difference  $\Delta\phi = \pi/2$  to illustrate the evolution of the phase difference on the fast time scale. Note that the phase difference oscillates with twice the frequency of rotation (twenty peaks on a time interval of ten periods of rotation). The amplitude of oscillations, relative to the mean phase difference, does not depend at leading order on the distance between the filaments,  $d$ , as one might expect. It is not the effect of hydrodynamic interactions, but of the imbalance of the helical filament that produces these oscillations. From the numerical simulations in Fig. 7.5, we measure that the amplitude of oscillations decreases with increasing elastic tethering strength,  $k$ , and vanishes when the helix has an integer number of turns,  $N$  (plots not shown). To obtain an analytical expression for the amplitude of oscillations, one would have to solve the intrinsic evolution of the phase angles, Eq. (7.13), to higher order and go beyond the leading-order solution, at  $\mathcal{O}((\pi N)^2)$ , provided in Eq. (7.22).

### 7.4.3 Extracting the time scale for synchronisation

To reduce computation time, we do not compute the full evolution of the phase difference for every set of parameters. Note that the solution to Adler's equation, Eq. (7.56), is linear near its inflection point,  $\Delta\phi = \pi/2$ , since

$$\Delta\phi(\tau) \approx \frac{\pi}{2} - \frac{\tau - \tau_0}{\tau_{\text{sync}}}, \quad (7.78)$$

when expanded around the point  $(\tau, \Delta\phi) = (\tau_0, \pi/2)$ .

Except for the long-time simulation in Fig. 7.4, we initialise the simulations with a phase difference  $\Delta\phi = \pi/2$  (see Eq. (7.77)) and let the system evolve for ten periods of rotation (equivalent to the time interval in the right panel of Fig. 7.4). From this shorter simulation, we estimate the time scale for synchronisation by applying a linear fit to the mean phase difference. The slope of the linear fit near phase difference  $\Delta\phi = \pi/2$  is equivalent to the rate of synchronisation, or the inverse of the time scale for synchronisation.

#### 7.4.4 Variation of parameters

In Fig. 7.5 (a)-(c) we show the dependence of the time scale for synchronisation on the three most important parameters in the model: the distance between the tethering points,  $d$ , the strength of the elastic restoring force,  $k$ , and the number of helical turns in the filament,  $N$ .

First, in Fig. 7.5 (a), we confirm that synchronisation is due to hydrodynamic effects and, as such, the rate of synchronisation,  $1/t_{\text{sync}}$ , is linearly proportional to the hydrodynamic coupling between the filaments, which decays like  $1/d$  in the far field. The value predicted by theory is in excellent agreement with numerical simulations down to an inter-filament distance equal to the contour length of the filaments.

Secondly, in Fig. 7.5 (b), we illustrate the non-monotonic dependence of the time scale for synchronisation on the strength of the elastic restoring force,  $k$ , with a global minimum at  $K^* = \sqrt{3}$  equivalent to  $k^* = \sqrt{3}A_0T_0/D_{33}$ . The fact that the rate of synchronisation decreases for very small  $k$  is a novel observation, since previous studies on synchronisation had only considered the regime of large elastic restoring strength.

Finally, in Fig. 7.5 (c), we confirm that the divergence of the time scale of synchronisation at integer number of helical turns, Eq. (7.61), is not merely an artefact of RFT. The time scale for synchronisation estimated from numerical simulations based on SBT also increases by orders of magnitude as we approach integer values of  $N$ . Numerical simulations carried out at exact integers show that the phase difference between the filaments oscillates with constant amplitude and does not drift. At integer values of  $N$ , the rate of synchronisation is zero to arithmetic precision (data outside the range of Fig. 7.5 (c)).

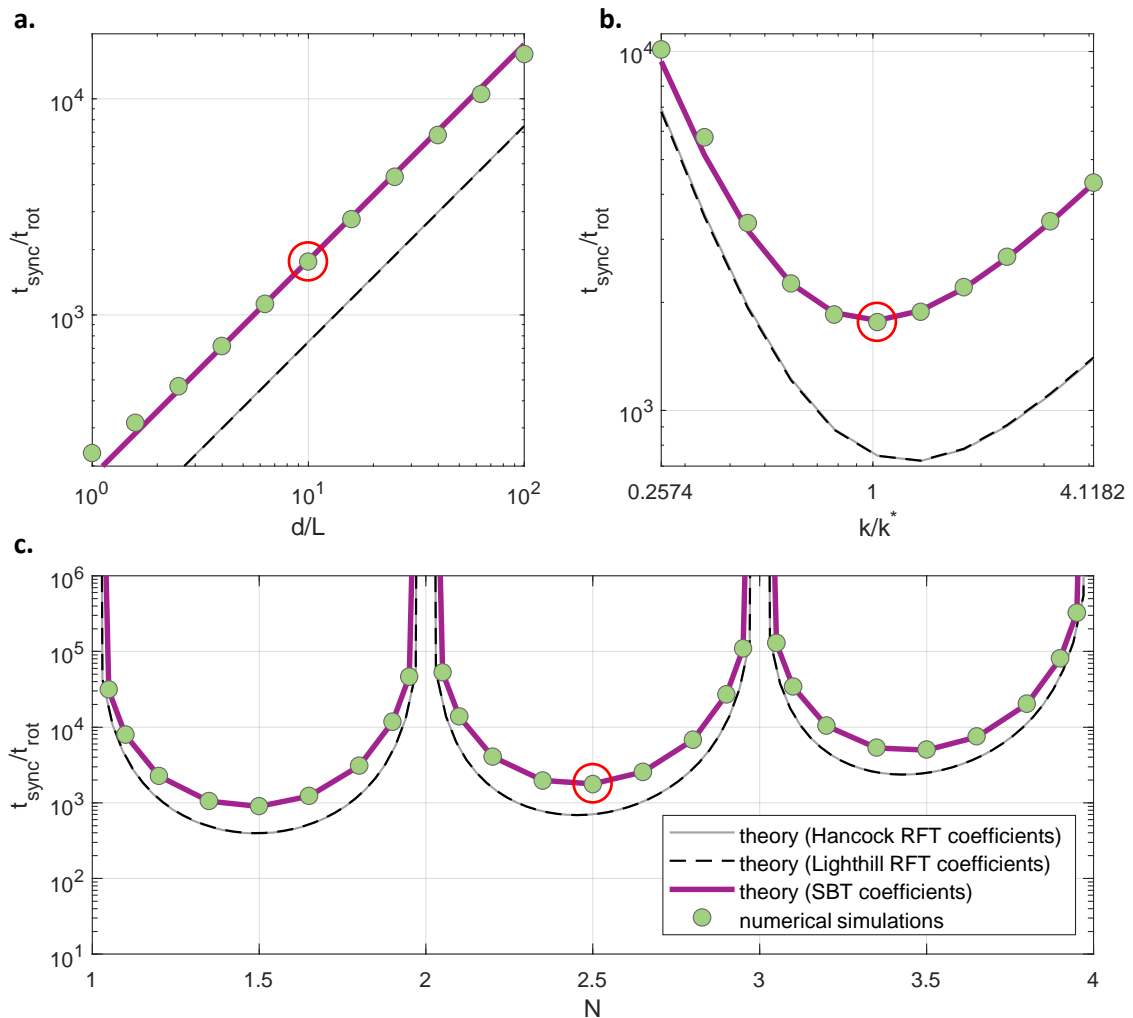


Fig. 7.5 Effect of the variation of parameters on the time scale for synchronisation, which (a) is linearly proportional to the distance between the filaments, (b) has a global minimum at intermediate values of the dimensionless elastic tethering strength, and (c) diverges at integer numbers of helical turns of the filament. The three data points circled in red correspond to the same set of input parameters:  $d = 10L$ ,  $k \approx k^*$ ,  $N = 2.5$ ,  $\psi = 0.4459$ ,  $\varepsilon = 0.0038$ . This corresponds to a normal polymorphic form with pitch  $\tilde{p} = 2.3 \mu\text{m}$  and amplitude  $\tilde{r} = 0.175 \mu\text{m}$ , a filament of length  $\tilde{L} = 6.4 \mu\text{m}$  and cross-sectional radius  $\tilde{\varepsilon} = 0.012 \mu\text{m}$ .

## 7.5 Biophysical insights

In this section, we take a step forward from dimensionless to dimensional results, in order to make theoretical predictions about the time scale on which bacterial flagella synchronise. We also discuss how the physical principles governing our minimal setup of synchronisation relate to the real bacterial flagellum. In doing so, we address all three components of the flagellum: the rotary motor which provides the torque, the hook which provides elasticity, and the polymorphic shapes of the flagellar filament which govern its hydrodynamic response.

### 7.5.1 Time scale for synchronisation

The most important comparison to be made is between the time scale for synchronisation and the typical duration of a run, at the end of which the filaments leave the bundle and the cell changes orientation. If the flagellar filaments inside a bundle are to synchronise, they must be able to do so before the run interval is over.

From the experimental measurements referenced in Table 7.1, we note that a run typically lasts about one hundred periods of rotation of the filaments, so  $\tilde{t}_{\text{run}}/\tilde{t}_{\text{rot}} \approx 100$ . This is considerably lower than the ratio  $\tilde{t}_{\text{sync}}/\tilde{t}_{\text{rot}}$  plotted in Fig. 7.5 (a), which furthermore corresponds to an elastic tethering strength very close to optimum (so the values could not be reduced by choosing a different  $k$ ). However, the data in Fig. 7.5 (a) represents the far-field regime where the inter-filament separation is greater than the contour length of the filaments.

The fact that the bacterial flagellar filament is much longer than the typical width of the cell body (see Table 7.1) is a limiting factor in the application of our theory. The data from Fig. 7.6 (e-f) shows that, when the filaments are  $10 \mu\text{m}$  apart, the time scale for synchronisation can fall below 10 s for appropriate values of the elastic compliance. However, it is not possible to extrapolate and predict a synchronisation time below one second, i.e. the duration of the run, when the filaments are only  $1 \mu\text{m}$  apart, i.e. close to the width of the cell body. This is because, once we reach the near-field, the time scale of synchronisation may not decay linearly with distance as it does in the far-field. Note that the lower end of the data spectrum in Fig. 7.5 (a) sees the time scale for synchronisation rise above the far-field trend.

### 7.5.2 Comparison of different polymorphic forms

In contrast to previous studies on synchronisation, our model accounts for the full helical geometry of the filament, which gives us the opportunity to explore how the polymorphic forms of the bacterial flagellum compare to each other in terms of synchronisation.

Parameter	Symbol	Value	Source
Helical diameter	$2\tilde{R}$		
normal		0.35 $\mu\text{m}$	[209]
semicoiled		0.50 $\mu\text{m}$	[209]
curly I		0.25 $\mu\text{m}$	[209]
curly II		0.16 $\mu\text{m}$	[209]
Helical pitch	$\tilde{p}$		[209]
normal		2.3 $\mu\text{m}$	[209]
semicoiled		1.1 $\mu\text{m}$	[209]
curly I		1.0 $\mu\text{m}$	[209]
curly II		0.9 $\mu\text{m}$	[209]
Cross-sectional radius	$\tilde{\epsilon}$		
filament		12 nm	[222]
Contour length			
hook	$\tilde{h}$	59 nm	[188]
filament	$\tilde{L}$	$7.1 \pm 1.8 \mu\text{m}$	[40]
Cell body width	$\tilde{w}$	0.88 $\mu\text{m}$	[40]
bending rigidity	$\tilde{EI}$		
hook		$1.6 \times 10^{-4} \text{ pN } \mu\text{m}^2$	[188]
filament		$3.5 \text{ pN } \mu\text{m}^2$	[39]
Motor torque	$\tilde{T}_0$	0.4 – 0.8 pN $\mu\text{m}$	[42]
Dynamic viscosity	$\tilde{\mu}$		
water (20° C)		$1.0 \times 10^{-3} \text{ pN } \mu\text{m}^{-2} \text{ s}$	
Time scales			
rotation	$\tilde{t}_{\text{rot}}$	0.08 s	[40]
run interval	$\tilde{t}_{\text{run}}$	1 s	[209]

Table 7.1 Geometric, dynamic, and kinematic parameters relevant to the synchronisation of bacterial flagella, with references to experimental measurements.

### Getting around the issue of divergence

One geometric parameter, the number of helical turns in the filament, has a particularly strong influence on the time scale of synchronisation, as seen in Fig. 7.5, to the extent that the synchronisation time diverges at integer values of  $N$ . Therefore, we cannot use Eq. (7.60) directly to compare different filament geometries against each other, because for any given length of the filament,  $\tilde{L}$ , there will be some geometries  $(2\pi\tilde{R}, \tilde{p})$  that fit an exact integer number of turns into that length, although it does not mean that filaments with that circumference and pitch cannot synchronise. In order to make a meaningful comparison between different filament geometries, we consider a wider distribution of filament lengths and compute the statistics of the time scale for synchronisation over that distribution.

### Definition of median synchronisation time

Suppose that the filament length is a random variable with probability density function  $g(\tilde{L})$ . From the distribution of filament lengths, we aim to derive a distribution of synchronisation times for different filament geometries. Let  $\tilde{t}_{\text{sync}}(\tilde{L})$  be our theoretical prediction for the time scale of synchronisation as a function of the filament length. We write down the cumulative distribution function for the synchronisation time as

$$F(\tilde{t}) \equiv P(\tilde{t}_{\text{sync}} < \tilde{t}) = \int_0^{\infty} H(\tilde{t} - \tilde{t}_{\text{sync}}(\tilde{L}))g(\tilde{L})d\tilde{L}, \quad (7.79)$$

where  $H(x)$  is the Heaviside step function ( $H(x) = 1$  for  $x \geq 0$ ,  $H(x) = 0$  for  $x < 0$ ). The cumulative distribution function,  $F(\tilde{t})$  represents the total probability that the length of the filament is such that the synchronisation time is less than  $\tilde{t}$ , all other things being fixed.

From this we determine the median synchronisation time,  $\tilde{t}_{\text{median}}$ , defined implicitly by

$$F(\tilde{t}_{\text{median}}) = \frac{1}{2}. \quad (7.80)$$

Note that the median synchronisation time is always finite, since  $F \rightarrow 1$  as  $\tilde{t} \rightarrow \infty$ , in contrast with the mean synchronisation time

$$\tilde{t}_{\text{mean}} = \int_0^{\infty} \tilde{t}_{\text{sync}}(\tilde{L})g(\tilde{L})d\tilde{L}, \quad (7.81)$$

which diverges for any biologically relevant probability density function,  $g(\tilde{L})$ , of filament lengths (it is not physical to assume a probability distribution that vanishes at integer number of turns, in order to keep  $\tilde{t}_{\text{mean}}$  finite). By computing the median synchronisation time, we have a meaningful quantity against which to compare different filament geometries.

### Comparison of median synchronisation time

Since the theory with RFT coefficients is faster to evaluate but less quantitative than the theory with SBT coefficients, we use RFT to make a relative comparison of filament geometries over a larger parameter space, and SBT to make an absolute comparison for a selected number of geometries (the normal, semicoiled, curly I and II polymorphic forms).

For the RFT part of the analysis, we solve Eq. (7.80) iteratively using the function  $\tilde{t}_{\text{sync}}^{\text{RFT}}$  from Eq. (7.63). For the filament length, we choose to model  $g(\tilde{L})$  as a lognormal distribution, which ensures the filament length is always positive. The values used for the mean and SD of filament lengths are provided in Table 7.1. The results are shown in Fig. 7.6 (a-d), where the median synchronisation time is rescaled by the value for the normal polymorphic form. The symbols overlaid on the contour plots represents the geometries of the four most common polymorphic forms, with data taken from two experimental papers on *Salmonella* [88, 106], an experimental paper on *E. coli* [209] and two theoretical papers [20, 81].

For the SBT part of the analysis, we derive not only the median synchronisation time, but also the statistics of the distribution around it ("minimum", first quartile, median, third quartile, "maximum"). For the clarity of the diagram, we do not depict outliers since they extend too far up the vertical axis. We obtain the statistics for synchronisation time by sampling 10,000 points from a lognormal distribution of filament lengths. The synchronisation time at each point is estimated by interpolating against a data set of fifty equally spaced filament lengths between  $\tilde{L} = 3 \mu\text{m}$  and  $\tilde{L} = 12 \mu\text{m}$ , obtained using the theory with SBT coefficients. The results are shown in Fig. 7.6 (e,f). Any parameters not referenced in the caption are taken from Table 7.1, including the mean and SD of the filament length.

The key observation from Fig. 7.6 (a-f) is that the normal and semicoiled polymorphic forms synchronise faster than curly filament, but the ratio between normal and semicoiled depends on the dimensionless elastic tethering strength,  $k$ . For very flexible tethering (small  $k$ ) semicoiled synchronises faster, while normal does better in stiffer elastic traps (large  $k$ ). In terms of the parameter space from Fig. 7.6 (a-d), we observe that the pitch of the helical geometry does not have a strong effect on the synchronisation time for small values of  $k$ , but the circumference does. For larger values of  $k$ , the contours begin to bend and we observe that for any given pitch, there is an optimum value of helix circumference which leads to the fastest synchronisation time. This is explained by the fact that the optimum  $k^* = \sqrt{3}A_0T_0D_{33}^{-1} \sim R^{-2}$  depends strongly on the helical amplitude, as later seen in Fig. 7.7 (b). The relationship can be reversed to say that, for a fixed  $k$ , there is an optimum helical amplitude that minimises the synchronisation time, which is what we see in Fig. 7.6 (c-d). The optimum  $R^*$  exists for any value of  $k$ , but for small  $k$  it lies outside the range plotted in Fig. 7.6 (a-b). The physical interpretation of this observation is that, to maximise the rate

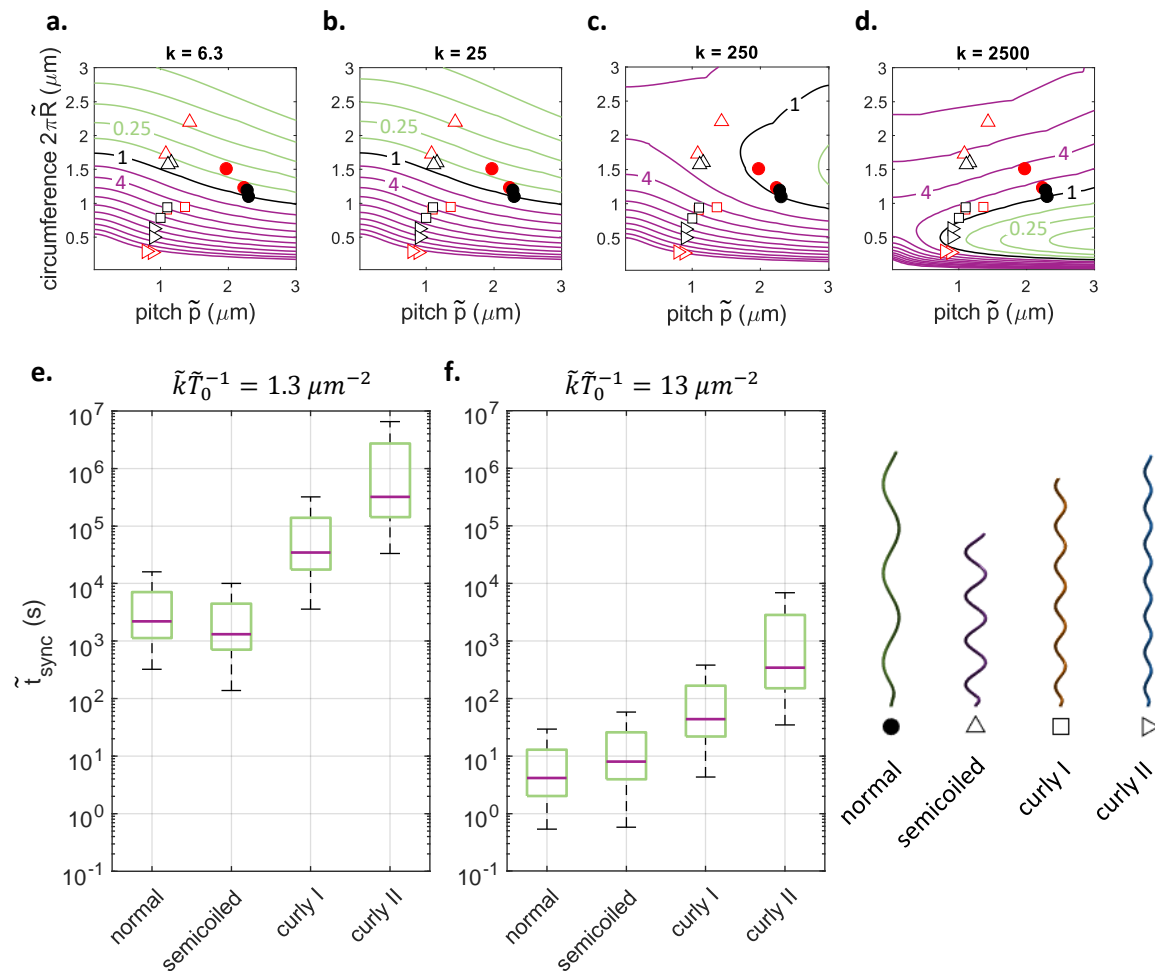


Fig. 7.6 Direct comparison of polymorphic forms. (a-d) Contour plots of the median synchronisation time predicted by the theory with RFT coefficients, for different values of the dimensionless elastic tethering strength,  $k$ , in a parameter space of filaments with helical circumference and pitch ( $2\pi\tilde{R}, \tilde{p}$ ). The values are normalised by the median synchronisation time of the normal polymorphic form. Symbols represent experimental measurements (black) and theoretical predictions (red) of the geometry of the four most common polymorphic forms (data sources in the text). Green contours correspond to sub-unitary values, decreasing by factors of two, while purple contours correspond to supra-unitary values, increasing by factors of two. (e-f) Box-and-whisker plots of the synchronisation time predicted by the theory with SBT coefficients for two filaments tethered at a distance  $\tilde{d} = 10 \mu\text{m}$  apart and driven by a constant torque  $\tilde{T}_0 = 0.6 \text{ pN } \mu\text{m}$ . Methodology explained in the text.

of synchronisation, the helical filament should have a large enough amplitude to generate lateral displacements around the tethering point, but not so large as to respond slowly to the hydrodynamic flows induced by the second filament.

Note that the values of  $\tilde{k}\tilde{T}_0^{-1}$  from Fig. 7.6 (e,f) are not chosen at random, but as representative of the case when the elastic compliance,  $\tilde{k}$ , comes primarily from the deformation of the hook or the flagellar filament. On that note, we move on to discussing the role of elastic compliance in the synchronisation of rotating bacterial flagella.

### 7.5.3 Optimal elastic tethering strength

In Fig. 7.7 (a), we illustrate the dimensional scaling argument that leads to our estimate of the elastic restoring strength,  $\tilde{k}$ , according to the scaling

$$\tilde{k} \sim \frac{\tilde{E}\tilde{I}}{\tilde{h}^3}, \quad (7.82)$$

where  $\tilde{E}\tilde{I}$  is the bending rigidity and  $\tilde{h}$  is the length of the element that provides the elastic compliance. Furthermore, we refer to the group of variables  $\tilde{k}\tilde{T}_0^{-1}$  as the ‘‘actuation dynamics’’ because, as suggested by Fig. 7.7 (a), it captures the entire external mechanism that is actuating the flagellar filament.

In order to model the elastic restoring force as linear in the lateral displacement of the filament, the deformation of the elastic link should be much smaller than its length,  $\tilde{h}$ . From Eq. (7.28), we estimate the dimensional amplitude of oscillations to be at most  $\tilde{\rho}_{\max} \approx 0.02 \mu\text{m}$  for a flagellar filament of length  $7 \mu\text{m}$  in one of the four most common polymorphic forms. Hence, the amplitude of lateral displacements is smaller than the length of the hook by a factor of three, suggesting that we are at the edge of the linear regime, and that the flagellar filament may have to deform as well to allow for the sideways displacements imposed by the hydrodynamic forces on the flagellum.

The values of  $\tilde{k}\tilde{T}_0^{-1}$  from Fig. 7.6 (e) and (f) are based on estimates of the elastic tethering strength coming from the dimensional scaling argument in Eq. (7.82), and assuming linear deformations for either the hook or the flagellar filament. Both estimates correspond to a motor torque  $\tilde{T}_0 = 0.6 \text{ pN } \mu\text{m}$ , in the middle of the range referenced in Table 7.1. The smaller value of  $\tilde{k}\tilde{T}_0^{-1} = 1.3 \mu\text{m}^{-2}$  from Fig. 7.6 (e) is estimated from the length and bending rigidity of the hook referenced in Table 7.1. The larger value  $\tilde{k}\tilde{T}_0^{-1} = 13 \mu\text{m}^{-2}$  from Fig. 7.6 (f) corresponds to the case when the elastic compliance comes not from the hook, but from a section of flagellar filament with length  $0.75 \mu\text{m}$  and bending rigidity from Table 7.1. Here, we implicitly make the simplifying assumption that most of the flagellar filament rotates

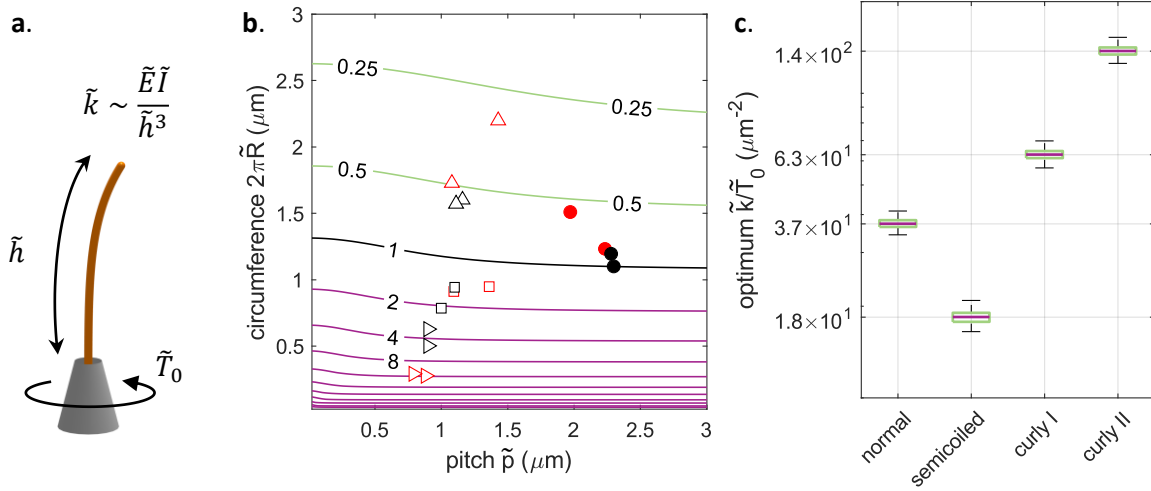


Fig. 7.7 Optimum actuation dynamics for synchronisation in the far field. (a) Dimensional argument for the actuation dynamics. The strength of the elastic restoring force,  $\tilde{k}$ , is estimated from the bending rigidity,  $\tilde{E}\tilde{I}$ , and the length,  $\tilde{h}$ , of the elastic link connecting the motor and the rigidly rotating part of the flagellar filament. (b) Contour plot of the optimum  $\tilde{k}\tilde{T}_0^{-1}$  predicted by the theory with RFT coefficients, in a parameter space of filaments with helical circumference and pitch ( $2\pi\tilde{R}, \tilde{p}$ ). The values are normalised by the optimum  $\tilde{k}\tilde{T}_0^{-1}$  for the normal polymorphic form. The symbols indicate the geometries of the four most common polymorphic forms (legend in Fig. 7.6, data sources in the text). (c) Box-and-whisker plot of the optimum  $\tilde{k}\tilde{T}_0^{-1}$  predicted by the theory with SBT coefficients (methodology explained in the text).

rigidly, maintaining the helical geometry of the polymorphic shape used in our simulations, and that only a section at the base of the filament deforms and exerts an elastic restoring force on the rest of the filament. The synchronisation times are significantly smaller for the larger value of  $\tilde{k}\tilde{T}_0^{-1}$ , suggesting that the flagellar filament, although less flexible than the hook, may in fact contribute more to this particular mechanism for synchronisation.

One of the most important biophysical insights in the current chapter comes from the novel observation that the time scale for synchronisation is minimised at intermediate values of the elastic tethering strength. The minimum of Eq. (7.60) is achieved for an optimal  $K^* = \sqrt{3}$ . We now consider the physical meaning of the parameter  $K$ , whose definition is copied below from Eq. (7.26),

$$K = \frac{kD_{33}}{A_0T_0}. \quad (7.83)$$

Note that  $A_0/k$  is the time scale of elastic relaxation of the filament, since  $A_0$  is the leading-order drag coefficient of the helical filament perpendicular to the helical axis. Meanwhile,  $D_{33}/T_0$  is the leading-order time scale of rotation identified in Eq. (7.22). Hence, the

parameter  $K$  is the ratio between the rotation time scale and the elastic relaxation time scale the flagellar filament.

Previous models of ciliary synchronisation work on the assumption that  $K = t_{\text{rot}}/t_{\text{elast}}$  is very large [159, 171]. While this is suitable for eukaryotic flagella, the dynamical properties of bacterial flagella are qualitatively different. Crucially, the bacterial flagellum has two components, the hook and the flagellar filament, with bending rigidities separated by four orders of magnitude - see Table 7.1. Based on a simple dimensional scaling argument, Eq. (7.82), we estimate that  $K \approx 0.05$  if the elastic compliance comes primarily from the hook. This is significantly below the optimum  $K^* = \sqrt{3}$  and gives  $t_{\text{sync}}/t_{\text{opt}} = \mathcal{O}(10^3)$  due to the rapid increase of  $\lambda(K) \sim K^{-3}$  for small  $K$ . However, the finite size of the hook likely requires that the proximal end of the flagellar filament deforms as well, as discussed above. For a length scale of deformation in the range  $h = 0.1 - 1 \mu\text{m}$ , we estimate that the flagellar filament gives  $K = 0.2 - 200$ , a range which straddles the optimum. The time scale for synchronisation increases more slowly when  $K$  is larger than the optimum,  $t_{\text{sync}} \sim K$  for large  $K$ , which suggest that it is more robust to have a relatively rigid elastic coupling, i.e. the one provided by the flagellar filament.

To obtain a more faithful estimate, an in-depth analysis of the elasto-hydrodynamics of the entire bacterial flagellum would be required, including the dynamic stiffening of the flagellar hook [162] and the elastic deformation of the helical flagellar filament modelled via Kirchhoff rod theory [112, 217]. Nevertheless, we continue our analysis of the optimal conditions for synchronisation within the framework of our minimal setup for synchronisation. In Fig. 7.7 we provide estimates of the optimum  $\tilde{k}\tilde{T}_0^{-1}$  derived from the theory with (b) RFT coefficients and (c) SBT coefficients.

The contour plot in Fig. 7.7 (b) is based on Eq. (7.63). After putting the dimensions back in and substituting the RFT coefficients from Appendix 7.A, we get

$$\left(\frac{\tilde{k}}{\tilde{T}_0}\right)_{\text{opt}} = \frac{4A_0K^*}{D_{33}\tilde{L}^2} = \frac{\sqrt{3}}{2\tilde{R}^2} \frac{(1 + \cos^2 \psi)c_{\perp} + \sin^2 \psi c_{\parallel}}{\cos^2 \psi c_{\perp} + \sin^2 \psi c_{\parallel}}, \quad (7.84)$$

where we have also used the fact that  $\tilde{L} \sin \psi = 2\pi\tilde{R}N$ . Finally, with the approximation  $c_{\perp} \approx 2c_{\parallel}$ , we arrive at

$$\left(\frac{\tilde{k}}{\tilde{T}_0}\right)_{\text{opt}} = \frac{\sqrt{3}(3 + \cos^2 \psi)}{2(1 + \cos^2 \psi)} \tilde{R}^{-2}. \quad (7.85)$$

Note that the pitch angle  $\psi$  of the helix does not affect the result very much, since  $2 < (3 + \cos^2 \psi)/(1 + \cos^2 \psi) < 3$ . This is why the contour lines in Fig. 7.7 (b) are almost flat. The greater variation comes from  $(\tilde{k}\tilde{T}_0^{-1})_{\text{opt}} \sim \tilde{R}^{-2}$ , meaning that helices with smaller amplitude synchronise faster when the elastic tethering strength is larger. In particular, curly

I and II prefer a value around two to four times larger than the normal, while the semicoiled optimum is about half of the normal optimum.

In Fig. 7.7 (c), we make the comparison between polymorphic forms more quantitative by using the theory with SBT coefficients. The statistics for the optimum  $\tilde{k}\tilde{T}_0^{-1}$  are obtained by sampling 10,000 points from a lognormal distribution of filament lengths (mean and SD from Table 7.1). The optimum  $\tilde{k}\tilde{T}_0^{-1}$  at each sampling point is estimated by interpolating against a set of SBT computations at fifty equally spaced filament lengths between  $\tilde{L} = 3 \mu\text{m}$  and  $\tilde{L} = 12 \mu\text{m}$ . The optimum actuation dynamics for the normal polymorphic form is  $\tilde{k}\tilde{T}_0^{-1} = 37\mu\text{m}^{-2}$ , which is closer to the estimate using the bending rigidity of the flagellar filament, rather than the hook (see discussion of Fig. 7.6 (e-f)).

## 7.6 Signs of multisynchrony in the near-field

Motivated by our understanding of the role played by elastic compliance in the far-field synchronisation of rotating bacterial flagella, we extend our investigation into the near-field regime using the computational method described in §7.4.1. If the far-field rate of in-phase synchronisation goes to zero for very small elastic tethering strength,  $k$ , could this be related to a loss of stability of the in-phase configuration as the filaments are brought closer together? Indeed, our findings suggest that when the filaments are rotating in close proximity to each other, the in-phase configuration is stable for larger values of  $k$ , while the anti-phase configuration is stable for smaller values of  $k$ .

Our numerical results on the multisynchrony of bacterial flagella in the near field are presented in Fig. 7.8. These results are obtained by short-interval numerical simulations where we sample the instantaneous rate of change of the phase difference,  $\frac{d\Delta\phi}{dt}$ , at discrete points in the interval  $\Delta\phi \in (0, \pi)$ , which are then extended to the full interval  $(0, 2\pi)$  by symmetry. The initial conditions imposed on the filaments are the same as in Eq. (7.77). In other words, the filaments follow their intrinsic kinematics until time  $t = 0$ , at which point we turn on the hydrodynamic interactions between the filaments and observe the average rate of change of their phase difference over five periods of rotation. The stability of the in-phase and anti-phase configurations is then deduced from the sign of  $\frac{d\Delta\phi}{dt}$  as a function of  $\Delta\phi$ , as shown in Fig. 7.8.

In panels (a-c) of Fig. 7.8, we observe that the lowest value of elastic tethering strength considered in our simulations,  $k/k^* = 0.25$ , is the first one to undergo a transition (blue data points). In panels (b) and (c), there is a coexistence of stable in-phase and anti-phase solutions depending on the elastic compliance of the filaments, and there are signs of an approaching transition for the  $k/k^* = 0.5$  curve as well. In panels (d-g) we investigate in more detail the

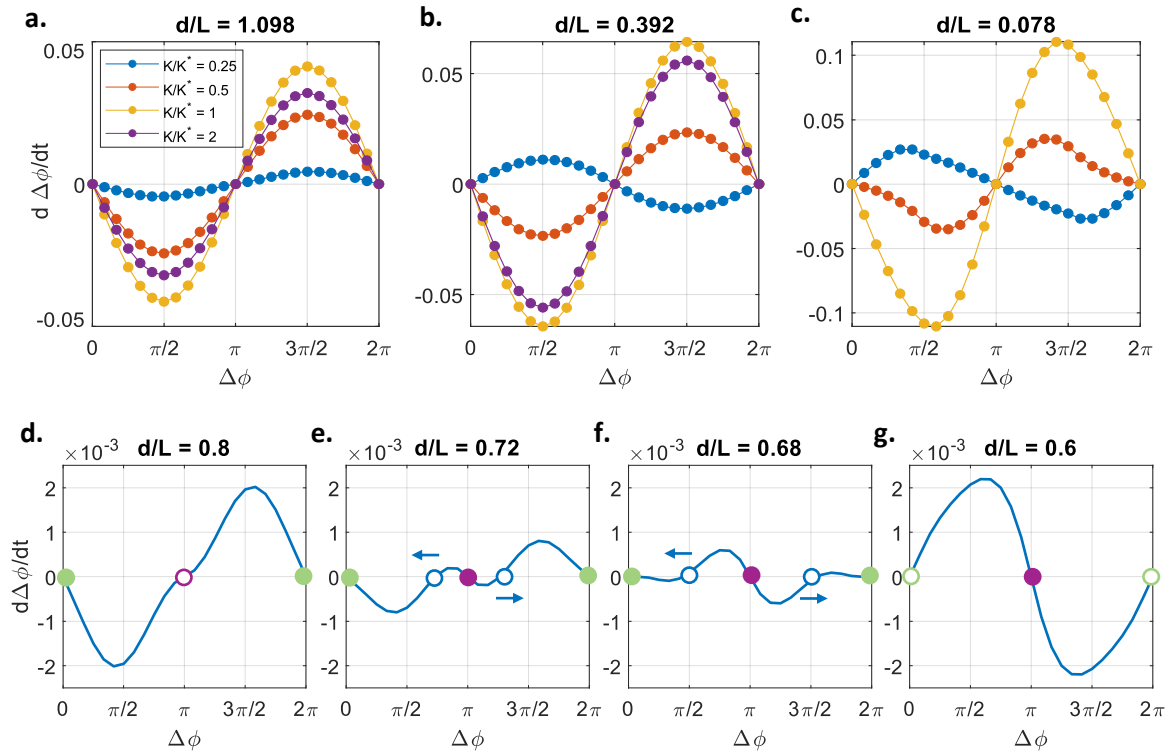


Fig. 7.8 Numerical observations of multisynchrony in hydrodynamically-coupled helical filaments rotating nearby. The stability of the fixed points is determined by the rate of change of the phase difference,  $\frac{d\Delta\phi}{dt}$ , as a function of the phase difference,  $\Delta\phi$ . In panels (a-c), we observe that helical filaments may synchronise either in-phase or anti-phase depending on the value of the elastic compliance. In panels (d-g), we explore in more detail the exchange of stability on the blue curve,  $k/k^* = 0.25$ , between panels (a) and (b). The anti-phase configuration becomes stable around  $d/L = 0.76$  through a subcritical pitchfork bifurcation, after which the in-phase configuration loses stability around  $d/L = 0.68$ . In all seven panels, the filament geometry corresponds to a normal shape filament with  $N = 2.5$  helical turns. For comparison, the width of a bacterial cell body is  $w/L \approx 0.3$ .

way in which the in-phase/anti-phase configuration loses/gains stability for the  $k/k^* = 0.25$  curve, between the values of inter-filament separation from panels (a) and (b). We find that the anti-phase configuration gains stability around  $d/L = 0.76$  through a subcritical pitchfork bifurcation. Afterwards, the newly-created unstable fixed points migrate towards the in-phase configuration, which loses stability through another subcritical pitchfork bifurcation around  $d/L = 0.68$ . On the diagram, the stable solutions are depicted by filled circles, while the unstable solutions are represented as empty circles. Note that these observations are based on short-interval simulations to determine the instantaneous rate of change of the phase difference. Longer simulations are required in order to confirm the global stability of the fixed points.

Why are these results important for the swimming of multiflagellated bacteria? The stability of the in-phase configuration is crucial for the smooth operation of a bundle of flagellar filaments, especially when the filaments are rotating close to each other, since excluded-volume interactions and the helical geometry of the filaments impose restrictions on the phase difference between the filaments, as discussed in Chapter 5. The potential stability of the anti-phase configuration presents a novel challenge for our understanding of how bundling and unbundling works. While previous studies have suggested that a difference in the motor torque driving the filaments generates intermittent unbundling of the filaments [176, 177], the possibility of anti-phase synchronisation when the filaments are driven by the same motor torque has not been fully explored. Furthermore, the fact that in-phase synchronisation first loses stability at lower values of elastic tethering strength,  $k$ , reinforces the idea that elastic compliance plays a crucial role in the synchronisation of bacterial flagella. We come back to the issue of near-field mutisynchrony in our discussion from Chapter 9.

## 7.7 Discussion

In this chapter, we have proposed a novel analytical model for the synchronisation of rotating helical filaments through hydrodynamic interactions. Our minimal setup for synchronisation constitutes an idealised model of the bacterial flagellum, where the action of the motor is represented by a constant driving torque along the axis of the filaments, and the deformation of the hook is modelled by a linear elastic spring. We have solved the reduced dynamical system using a multiple scales analysis that exploits the separation of time scales between the rotation of the filaments and the hydrodynamic synchronisation. The theoretical solution from the multiple scales analysis is in perfect agreement with numerical simulations of the fully-coupled hydrodynamic problem of two filaments rotating next to each other. We have also provided a diagrammatic explanation of the physical mechanism underlying synchronisation,

and we have used our theoretical results to derive valuable biophysical insights about the role played by the flagellar geometry and the elasticity of the hook and flagellar filament in the synchronisation of bacterial flagella. In the final section, we have extended our numerical simulations to small inter-filament separations in order to investigate the stability of in-phase synchronisation, which is the only stable configuration in the far field.

The main novelty in this work is the tether-compliance physical mechanism for synchronisation which is qualitatively different from previous mechanisms based on orbital compliance [159] (in our setup, the rotating filament is rigid and does not change its radius) or phase-dependent forcing [211, 212] (in our setup, the actuation mechanism provides a constant driving torque). The fact that the intrinsic kinematics of the filament consists of two different motions on the fast time scale of the problem (i.e. the rotation about the axis, and the sideways oscillation of the axis itself) seems to provide scope for a new type of dynamical behaviour, where the time scale for synchronisation varies non-monotonically with the strength of elastic compliance. Our setup is similar to the shaft-compliance mechanism in Qian et al. [171] in terms of the conditions prescribed for elastic compliance, but the resulting dynamics of synchronisation are qualitatively different due to the specific hydrodynamic resistance of a helical filament.

Importantly, we find that the optimal elastic compliance for the synchronisation of rotating bacterial flagella does not depend on the distance between the filaments, so long as they are in the far field. Based on a simple dimensional scaling argument, we estimate that the elastic compliance provided by the hook is significantly below the optimum value for synchronisation, while the elastic compliance provided by the flagellar filament covers a wider range, falling on either side of the optimum. Surprisingly, this suggests that the flagellar filament, although more rigid than the hook, may play a more important role in the synchronisation of bacterial flagella. A more comprehensive analysis of the elasto-hydrodynamics of the bacterial flagellum would be required in order to address this point, including the dynamic stiffening of the flagellar hook [162] and the deformation of the flagellar filament due to external flow and rotation about its axis [101, 112, 217].

The important role played by elastic compliance is further emphasised in this chapter through our numerical observations of stable anti-phase synchronisation when the filaments are sufficiently close to each other, and the elastic tethering strength is sufficiently weak. Our findings suggest once again that a larger elastic tethering strength, such as the one provided by the flagellar filament, is more robust since it favours the stability of in-phase synchronisation in bundles of flagellar filaments.

The analytical model presented in the chapter can be extended to allow for a two-dimensional elastic trap, or to consider a tilting of the filament axis from side to side, rather

than a lateral displacement. It can also be used to investigate other potential mechanisms for synchronisation, such as the torque-speed relationship of the bacterial motor [196]. Another possible extension is to include multiple interacting filaments placed in a circular arrangement, as an idealised model of a bundle of bacterial flagella. This may lead to different dynamics than the array configurations typically used in studies of many interacting cilia.

We made a number of simplifications in order to keep the model analytically tractable. In computational studies, these restrictions could be relaxed in order to allow multiple degrees of freedom for the motion of the filaments, to include more than two filaments, or to account for hydrodynamic interactions with the cell body. In contrast to eukaryotic organisms, not much is known about the role of the cell body in the synchronisation of a bundle of bacterial flagellar filaments.

The analytical framework that we have used to describe the hydrodynamic interactions between filaments, derived in Chapter 6, is valid when the distance between the filaments is greater than the filament length,  $d > L$ . The multiple scales analysis makes this restriction stronger, requiring in principle that  $d \gg L$ , although the results presented in Section 7.4 suggest that the theory is able to capture the dynamics of synchronisation down  $d \approx L$ . Hence, the current theory is not suitable for making quantitative predictions about the time scale for synchronisation in bundles of bacterial flagella, although it can inform our physical understanding of the mechanisms underlying the synchronisation of rotating helical filaments. The theory may also be used to predict the synchronisation between bacterial flagella on different cells, which do not have non-hydrodynamic mechanisms for synchronisation such as being elastically coupled through the cell wall, or individually coupled to the motion of the cell body.

## Appendix 7.A Resistance matrix coefficients obtained from RFT

In this appendix, we provide a list of analytical expressions for those components of the resistance matrix which are necessary in our model of synchronisation.

$$A_{11} = 2c_{\perp} + (c_{\parallel} - c_{\perp}) \sin^2 \psi \left( 1 - \frac{\sin(2\pi N)}{2\pi N} \right), \quad (7.86)$$

$$A_{22} = 2c_{\perp} + (c_{\parallel} - c_{\perp}) \sin^2 \psi \left( 1 + \frac{\sin(2\pi N)}{2\pi N} \right), \quad (7.87)$$

$$A_0 = (1 + \cos^2 \psi) c_{\perp} + \sin^2 \psi c_{\parallel}, \quad (7.88)$$

$$\Delta A = \frac{(c_{\perp} - c_{\parallel}) \sin^2 \psi \sin(2\pi N)}{2\pi N} \quad (7.89)$$

$$A_{23} = \sigma \frac{\sin(2\psi) \sin(\pi N)}{\pi N} (c_{\parallel} - c_{\perp}), \quad (7.90)$$

$$B_{23} = \frac{2 \sin(\psi) (\cos^2 \psi c_{\perp} + \sin^2 \psi c_{\parallel}) \sin(\pi N)}{(\pi N)^2}, \quad (7.91)$$

$$B_{33} = \sigma \frac{\sin(\psi) \sin(2\psi)}{\pi N} (c_{\parallel} - c_{\perp}), \quad (7.92)$$

$$D_{33} = \frac{2 \sin(\psi) (\cos^2 \psi c_{\perp} + \sin^2 \psi c_{\parallel}) \sin(\psi)}{(\pi N)^2}. \quad (7.93)$$

These expressions were derived in Chapter 6 using resistive-force theory (RFT). The perpendicular and parallel drag coefficients from Gray and Hancock's RFT [69, 79] are

$$c_{\perp} = \frac{4\pi\mu}{\ln(2/\varepsilon) + 1/2}, \quad c_{\parallel} = \frac{2\pi\mu}{\ln(2/\varepsilon) - 1/2}. \quad (7.94)$$

## Appendix 7.B Derivation of solvability condition

The dynamical system from Eq. (7.39), copied below,

$$\begin{aligned} & \begin{pmatrix} 1 & -\rho \sin(\phi_1^{(0)} - \nu) \\ 0 & 1 \end{pmatrix} \begin{pmatrix} \partial x_1^{(1)}/\partial t \\ \partial \phi_1^{(1)}/\partial \tau \end{pmatrix} + \begin{pmatrix} 0 \\ \partial \phi_1^{(1)}/\partial t \end{pmatrix} \\ &= \tilde{\mathbf{S}}^{-1}(\phi_1^{(0)}) \begin{pmatrix} -kx_1^{(1)} \\ 0 \end{pmatrix} + \phi_1^{(1)} \frac{\partial \tilde{\mathbf{S}}^{-1}}{\partial \phi}(\phi_1^{(0)}) \begin{pmatrix} -k\rho \cos(\phi_1^{(0)} - \nu) \\ T_0 \end{pmatrix} \\ & \quad - \tilde{\mathbf{S}}^{-1}(\phi_1^{(0)}) [d\tilde{\mathbf{C}}(\phi_1^{(0)}, \phi_2^{(0)})] \tilde{\mathbf{S}}^{-1}(\phi_2^{(0)}) \begin{pmatrix} -k\rho \cos(\phi_2^{(0)} - \nu) \\ T_0 \end{pmatrix}. \end{aligned} \quad (7.95)$$

is over-determined. In order for the asymptotic expansion, Eq. (7.32), to remain valid for large times  $t$ , the first-order correction  $\phi_1^{(1)}$  must remain bounded. Hence, we separate all terms dependent on  $\phi_1^{(1)}$ , and we write

$$\begin{pmatrix} 0 \\ \partial \phi_1^{(1)}/\partial t \end{pmatrix} - \phi_1^{(1)} \frac{\partial \tilde{\mathbf{S}}^{-1}}{\partial \phi}(\phi_1^{(0)}) \begin{pmatrix} -k\rho \cos(\phi_1^{(0)} - \nu) \\ T_0 \end{pmatrix} = \begin{pmatrix} f(t, \tau) \\ g(t, \tau) \end{pmatrix}, \quad (7.96)$$

where the unknown functions  $f(t, \tau)$  and  $g(t, \tau)$  represent all the terms dependent on  $\phi_1^{(0)}, \phi_2^{(0)}$  and  $x_1^{(1)}$  from Eq. (7.95).

Using the expansion of the matrix  $\tilde{\mathbf{S}}^{-1}$  from Eqs. (7.18)-(7.20), we determined that

$$\frac{\partial \tilde{\mathbf{S}}^{-1}}{\partial \phi} = \frac{B_{23} \cos(\phi)}{A_0 D_{33}} \begin{pmatrix} 0 & 1 \\ 1 & 2B_{23} D_{33}^{-1} \sin(\phi) \end{pmatrix}, \quad (7.97)$$

to leading order. Hence, writing out each line of Eq. (7.96) separately, we have

$$f(t, \tau) = -\frac{T_0 B_{23}}{A_0 D_{33}} \cos(\phi_1^{(0)}) \phi_1^{(1)}, \quad (7.98)$$

$$g(t, \tau) = \frac{\partial \phi_1^{(1)}}{\partial t} - \phi_1^{(1)} \frac{B_{23} \cos(\phi_1^{(0)})}{A_0 D_{33}} \left( -k\rho \cos(\phi_1^{(0)} - \nu) + \frac{2T_0 B_{23}}{D_{33}} \sin(\phi_1^{(0)}) \right) \quad (7.99)$$

If the function  $f(t, \tau)$  is non-zero, then  $\phi_1^{(1)}$  is non-zero as well, to satisfy Eq. (7.98). The function  $\phi_1^{(1)}$  is also a solution of the linear ODE from Eq. (7.99), so it can be expressed as a linear superposition of the complementary function,  $\phi_{\text{CF}}$ , and a particular solution dependent on  $g(t, \tau)$ .

The complementary function is the solution of the homogeneous equation

$$\frac{\partial \phi_{\text{CF}}}{\partial t} - \frac{B_{23} \cos(\phi_1^{(0)})}{A_0 D_{33}} \left( -k\rho \cos(\phi_1^{(0)} - \nu) + \frac{2T_0 B_{23}}{D_{33}} \sin(\phi_1^{(0)}) \right) \phi_{\text{CF}} = 0. \quad (7.100)$$

Since the complementary function is non-zero by definition, we can divide through by it and integrate with respect to the fast time variable,  $t$ ,

$$\begin{aligned} \int \frac{d\phi_{\text{CF}}}{\phi_{\text{CF}}} &= \frac{B_{23}}{A_0 D_{33}} \int \cos(\phi_1^{(0)}) \left( -k\rho \cos(\phi_1^{(0)} - \nu) + \frac{2T_0 B_{23}}{D_{33}} \sin(\phi_1^{(0)}) \right) dt, \\ &= \frac{B_{23}}{A_0 D_{33}} \int -\frac{1}{2} k\rho \left( \cos \nu (1 + \cos(2\phi_1^{(0)})) + \sin \nu \sin(2\phi_1^{(0)}) \right) + \frac{T_0 B_{23}}{D_{33}} \sin(2\phi_1^{(0)}) dt. \end{aligned} \quad (7.101)$$

We integrate this using the fact that  $\dot{\phi}_1^{(0)} = \Omega_0 = T_0/D_{33}$  at leading order, and we find

$$\begin{aligned} \ln \phi_{\text{CF}} - \ln A &= \frac{B_{23}}{A_0 D_{33}} \left( -\frac{k\rho \cos \nu}{2} t - \frac{k\rho \cos \nu}{4\Omega_0} \sin(2\phi_1^{(0)}) \right. \\ &\quad \left. + \frac{k\rho \sin \nu}{4\Omega_0} \cos(2\phi_1^{(0)}) - \frac{B_{23}}{2} \cos(2\phi_1^{(0)}) \right), \end{aligned} \quad (7.102)$$

so for large times  $t$  we have

$$\phi_{\text{CF}} \sim \exp \left( -\frac{B_{23} k\rho \cos \nu t}{2A_0 D_{33}} \right). \quad (7.103)$$

Using the definitions of  $\rho$  and  $\nu$  from Eq. (7.28), we rewrite this as

$$\phi_{\text{CF}} \sim \exp \left( \frac{B_{23}^2 k t}{2A_0^2 (K^2 + 1) D_{33}} \right). \quad (7.104)$$

Hence, the complementary function grows exponentially over time since both  $k$  and  $D_{33}$  are positive. The only way to suppress this exponential growth is if the functions  $f(t, \tau)$  and  $g(t, \tau)$  are both identically zero, leading to the trivial solution  $\phi_1^{(1)} = 0$ .

## Appendix 7.C Series expansions for the matrices $\tilde{\mathbf{S}}^{-1}$ and $\tilde{\mathbf{S}}^{-1}\tilde{\mathbf{C}}\tilde{\mathbf{S}}^{-1}$

To keep the analytical model simple, we work in the regime  $\pi N \gg 1$  so that we can write the matrices  $\tilde{\mathbf{S}}^{-1}(\phi)$  and  $\tilde{\mathbf{S}}^{-1}(\phi_1)\tilde{\mathbf{C}}(\phi_1, \phi_2)\tilde{\mathbf{S}}^{-1}(\phi_2)$  as asymptotic series in the small parameter  $(\pi N)^{-1}$ . First, we remind the reader that

$$\tilde{\mathbf{S}}(\phi) = \begin{pmatrix} S_{11}(\phi) & S_{16}(\phi) \\ S_{16}(\phi) & S_{66}(\phi) \end{pmatrix}, \quad \tilde{\mathbf{C}}(\phi_1, \phi_2) = \begin{pmatrix} C_{11}(\phi_1, \phi_2) & C_{16}(\phi_1, \phi_2) \\ C_{61}(\phi_1, \phi_2) & C_{66}(\phi_1, \phi_2) \end{pmatrix}. \quad (7.105)$$

Because the single-helix resistance matrix  $\mathbf{S}(\phi)$  is obtained from the reference matrix  $\mathbf{S}_0 = (\mathbf{A}, \mathbf{B}; \mathbf{B}^T, \mathbf{D})$  through a rotation by angle  $\phi$ , i.e.

$$\mathbf{S}(\phi) = \begin{pmatrix} \mathbf{Q}(\phi)\mathbf{A}\mathbf{Q}(\phi)^T & \mathbf{Q}(\phi)\mathbf{B}\mathbf{Q}(\phi)^T \\ \mathbf{Q}(\phi)\mathbf{B}^T\mathbf{Q}(\phi)^T & \mathbf{Q}(\phi)\mathbf{D}\mathbf{Q}(\phi)^T \end{pmatrix}, \quad \mathbf{Q}(\phi) = \begin{pmatrix} \cos \phi & -\sin \phi & 0 \\ \sin \phi & \cos \phi & 0 \\ 0 & 0 & 1 \end{pmatrix}, \quad (7.106)$$

we know that

$$S_{11}(\phi) = A_0 + \Delta A \cos(2\phi) \quad (7.107)$$

$$S_{16}(\phi) = -B_{23} \sin(\phi) \quad (7.108)$$

$$S_{66} = D_{33}, \quad (7.109)$$

where we have introduced the notation  $A_0 = (A_{11} + A_{22})/2$  and  $\Delta A = (A_{11} - A_{22})/2$ .

We also need the elements

$$S_{12}(\phi) = S_{21}(\phi) = \Delta A \sin(2\phi) \quad (7.110)$$

$$S_{13}(\phi) = S_{31}(\phi) = -A_{23} \sin(\phi) \quad (7.111)$$

$$S_{26}(\phi) = S_{62}(\phi) = B_{23} \cos(\phi) \quad (7.112)$$

$$S_{36} = S_{63} = B_{33}, \quad (7.113)$$

because the cross-resistance matrix  $\mathbf{C}(\phi_1, \phi_2)$  is defined, to  $\mathcal{O}(d^{-1})$ , as

$$C_{ij}(\phi_1, \phi_2) = -\frac{1}{8\pi\mu d} S_{ip}(\phi_1) (\delta_{pq} + \hat{d}_p \hat{d}_q) S_{qj}(\phi_2), \quad (7.114)$$

with the indices  $p, q$  summed from 1 to 3. In our setup we have  $\mathbf{d} = d\mathbf{e}_x$ , so

$$C_{ij}(\phi_1, \phi_2) = -\frac{2S_{i1}(\phi_1)S_{1j}(\phi_2) + S_{i2}(\phi_1)S_{2j}(\phi_2) + S_{i3}(\phi_1)S_{3j}(\phi_2)}{8\pi\mu d}. \quad (7.115)$$

Now that we have expressions for all the components of matrices  $\tilde{\mathbf{S}}(\phi)$  and  $\tilde{\mathbf{C}}(\phi_1, \phi_2)$ , we can begin to sort the terms order by order. From the analytical expressions in Appendix 7.A, we gain the key insight that

$$A_0 = \mathcal{O}(1), \quad (7.116)$$

$$\Delta A, A_{23}, B_{33} = \mathcal{O}((\pi N)^{-1}), \quad (7.117)$$

$$B_{23}, D_{33} = \mathcal{O}((\pi N)^{-2}). \quad (7.118)$$

Based on this, we calculate the inverse matrix

$$\tilde{\mathbf{S}}^{-1}(\phi) = \frac{1}{S_{11}(\phi)S_{66} - S_{16}(\phi)^2} \begin{pmatrix} S_{66} & -S_{16}(\phi) \\ -S_{16}(\phi) & S_{11}(\phi) \end{pmatrix}, \quad (7.119)$$

starting with the determinant

$$S_{11}(\phi)S_{66} - S_{16}(\phi)^2 = A_0 D_{33} + \Delta A D_{33} \cos(2\phi) - B_{23}^2 \sin^2(\phi), \quad (7.120)$$

which means that

$$\begin{aligned} (S_{11}(\phi)S_{66} - S_{16}(\phi)^2)^{-1} &= \frac{1}{A_0 D_{33}} - \frac{\Delta A}{A_0^2 D_{33}} \cos(2\phi) \\ &+ \left[ \frac{\Delta A^2}{A_0^3 D_{33}} \cos^2(2\phi) + \frac{B_{23}^2}{A_0^2 D_{33}^2} \sin^2(\phi) \right] + \mathcal{O}((\pi N)^{-1}). \end{aligned} \quad (7.121)$$

Using the information above, we can expand the expression for

$$\begin{aligned} \tilde{\mathbf{S}}^{-1}(\phi) &= \left( \frac{1}{A_0 D_{33}} - \frac{\Delta A}{A_0^2 D_{33}} \cos(2\phi) \right. \\ &+ \left. \left[ \frac{\Delta A^2}{A_0^3 D_{33}} \cos^2(2\phi) + \frac{B_{23}^2}{A_0^2 D_{33}^2} \sin^2(\phi) \right] + \dots \right) \begin{pmatrix} D_{33} & B_{23} \sin(\phi) \\ B_{23} \sin(\phi) & A_0 + \Delta A \cos(2\phi) \end{pmatrix}, \end{aligned} \quad (7.122)$$

to obtain the asymptotic series

$$\tilde{\mathbf{S}}^{-1}(\phi) = \hat{\mathbf{S}}_2(\phi) + \hat{\mathbf{S}}_0(\phi) + \mathcal{O}((\pi N)^{-1}), \quad (7.123)$$

because the  $\mathcal{O}((\pi N)^1)$  terms cancel out, and

$$\hat{\mathbf{S}}_2 = \begin{pmatrix} 0 & 0 \\ 0 & D_{33}^{-1} \end{pmatrix}, \quad (7.124)$$

$$\hat{\mathbf{S}}_0 = A_0^{-1} \begin{pmatrix} 1 & B_{23}D_{33}^{-1} \sin(\phi) \\ B_{23}D_{33}^{-1} \sin(\phi) & B_{23}^2 D_{33}^{-2} \sin^2(\phi) \end{pmatrix}. \quad (7.125)$$

Coming back to the components of matrix  $\tilde{\mathbf{C}}(\phi_1, \phi_2)$ , we have that

$$\begin{aligned} C_{11}(\phi_1, \phi_2) &= -\frac{2S_{11}(\phi_1)S_{11}(\phi_2) + S_{12}(\phi_1)S_{21}(\phi_2) + S_{13}(\phi_1)S_{31}(\phi_2)}{8\pi d} \\ &= -\frac{2(A_0 + \Delta A \cos(2\phi_1))(A_0 + \Delta A \cos(2\phi_2)) + \Delta A^2 \sin(2\phi_1) \sin(2\phi_2)}{8\pi\mu d} \\ &\quad + \frac{A_{23}^2 \sin(\phi_1) \sin(\phi_2)}{8\pi\mu d}, \end{aligned} \quad (7.126)$$

$$\begin{aligned} C_{16}(\phi_1, \phi_2) = C_{61}(\phi_2, \phi_1) &= -\frac{2S_{11}(\phi_1)S_{16}(\phi_2) + S_{12}(\phi_1)S_{26}(\phi_2) + S_{13}(\phi_1)S_{36}(\phi_2)}{8\pi d} \\ &= -\frac{-2(A_0 + \Delta A \cos(2\phi_1))B_{23} \sin(\phi_2) + \Delta AB_{23} \sin(2\phi_1) \cos(\phi_2) - A_{23}B_{33} \sin(\phi_1)}{8\pi\mu d}, \end{aligned} \quad (7.127)$$

$$\begin{aligned} C_{66}(\phi_1, \phi_2) &= -\frac{2S_{61}(\phi_1)S_{16}(\phi_2) + S_{62}(\phi_1)S_{26}(\phi_2) + S_{63}(\phi_1)S_{36}(\phi_2)}{8\pi d} \\ &= -\frac{2B_{23}^2 \sin(\phi_1) \sin(\phi_2) + B_{23}^2 \cos(\phi_1) \cos(\phi_2) + B_{33}^2}{8\pi\mu d}. \end{aligned} \quad (7.128)$$

The terms can be sorted into a finite asymptotic series

$$\tilde{\mathbf{C}}(\phi_1, \phi_2) = \hat{\mathbf{C}}_0(\phi_1, \phi_2) + \hat{\mathbf{C}}_{-1}(\phi_1, \phi_2) + \hat{\mathbf{C}}_{-2}(\phi_1, \phi_2) + \hat{\mathbf{C}}_{-3}(\phi_1, \phi_2) + \hat{\mathbf{C}}_{-4}(\phi_1, \phi_2), \quad (7.129)$$

where

$$\hat{\mathbf{C}}_0 = -\frac{1}{8\pi\mu d} \begin{pmatrix} 2A_0^2 & 0 \\ 0 & 0 \end{pmatrix}, \quad (7.130)$$

$$\hat{\mathbf{C}}_{-1} = -\frac{1}{8\pi\mu d} \begin{pmatrix} 2A_0\Delta A(\cos(2\phi_1) + \cos(2\phi_2)) & 0 \\ 0 & 0 \end{pmatrix}, \quad (7.131)$$

$$\hat{\mathbf{C}}_{-2} = -\frac{1}{8\pi\mu d} \begin{pmatrix} 2\Delta A^2 \cos(2\phi_1) \cos(2\phi_2) + \Delta A^2 \sin(2\phi_1) \sin(2\phi_2) & -2A_0 B_{23} \sin(\phi_2) \\ +A_{23}^2 \sin(\phi_1) \sin(\phi_2) & -A_{23} B_{33} \sin(\phi_1) \\ -2A_0 B_{23} \sin(\phi_1) - A_{23} B_{33} \sin(\phi_2) & B_{33}^2 \end{pmatrix}, \quad (7.132)$$

$$\hat{\mathbf{C}}_{-3} = -\frac{1}{8\pi\mu d} \begin{pmatrix} 0 & -2\Delta A B_{23} \cos(2\phi_1) \sin(\phi_2) \\ -2\Delta A B_{23} \cos(2\phi_2) \sin(\phi_1) & +\Delta A B_{23} \sin(2\phi_1) \cos(\phi_2) \\ +\Delta A B_{23} \sin(2\phi_2) \cos(\phi_1) & 0 \end{pmatrix}, \quad (7.133)$$

$$\hat{\mathbf{C}}_{-4} = -\frac{1}{8\pi\mu d} \begin{pmatrix} 0 & 0 \\ 0 & 2B_{23}^2 \sin(\phi_1) \sin(\phi_2) + B_{23}^2 \cos(\phi_1) \cos(\phi_2) \end{pmatrix}. \quad (7.134)$$

Thanks to the sparse structure of the matrices, we deduce that

$$\hat{\mathbf{S}}_2 \hat{\mathbf{C}}_0 = \hat{\mathbf{C}}_0 \hat{\mathbf{S}}_2 = \hat{\mathbf{S}}_2 \hat{\mathbf{C}}_{-1} = \hat{\mathbf{C}}_{-1} \hat{\mathbf{S}}_2 = \hat{\mathbf{S}}_2 \hat{\mathbf{C}}_{-3} \hat{\mathbf{S}}_2 = 0. \quad (7.135)$$

After expanding out the product

$$\begin{aligned} \tilde{\mathbf{S}}^{-1}(\phi_1) \tilde{\mathbf{C}}(\phi_1, \phi_2) \tilde{\mathbf{S}}^{-1}(\phi_2) &= (\hat{\mathbf{S}}_2(\phi_1) + \hat{\mathbf{S}}_0(\phi_1) + \dots) \\ &(\hat{\mathbf{C}}_0(\phi_1, \phi_2) + \hat{\mathbf{C}}_{-1}(\phi_1, \phi_2) + \hat{\mathbf{C}}_{-2}(\phi_1, \phi_2) + \hat{\mathbf{C}}_{-3}(\phi_1, \phi_2) + \hat{\mathbf{C}}_{-4}(\phi_1, \phi_2)) \\ &(\hat{\mathbf{S}}_2(\phi_2) + \hat{\mathbf{S}}_0(\phi_2) + \dots), \end{aligned} \quad (7.136)$$

we find that the asymptotic expansion for  $\tilde{\mathbf{S}}^{-1}(\phi_1) \tilde{\mathbf{C}}(\phi_1, \phi_2) \tilde{\mathbf{S}}^{-1}(\phi_2)$  has no terms of order  $\mathcal{O}(d^{-1}(\pi N)^4)$ ,  $\mathcal{O}(d^{-1}(\pi N)^3)$  or  $\mathcal{O}(d^{-1}(\pi N)^1)$  because of the vanishing combinations of terms detailed in Eq. (7.135), meaning that

$$\tilde{\mathbf{S}}^{-1}(\phi_1) [d\tilde{\mathbf{C}}(\phi_1, \phi_2)] \tilde{\mathbf{S}}^{-1}(\phi_2) = \mathbf{M}_2(\phi_1, \phi_2) + \mathbf{M}_0(\phi_1, \phi_2) + \mathcal{O}((\pi N)^{-1}), \quad (7.137)$$

where the matrices

$$\mathbf{M}_2(\phi_1, \phi_2) = d\hat{\mathbf{S}}_2(\phi_1) \hat{\mathbf{C}}_{-2}(\phi_1, \phi_2) \hat{\mathbf{S}}_2(\phi_2), \quad (7.138)$$

$$\begin{aligned} \mathbf{M}_0(\phi_1, \phi_2) &= d\hat{\mathbf{S}}_2(\phi_1) \hat{\mathbf{C}}_{-4}(\phi_1, \phi_2) \hat{\mathbf{S}}_2(\phi_2) + d\hat{\mathbf{S}}_2(\phi_1) \hat{\mathbf{C}}_{-2}(\phi_1, \phi_2) \hat{\mathbf{S}}_0(\phi_2) \\ &+ d\hat{\mathbf{S}}_0(\phi_1) \hat{\mathbf{C}}_{-2}(\phi_1, \phi_2) \hat{\mathbf{S}}_2(\phi_2) + d\hat{\mathbf{S}}_0(\phi_1) \hat{\mathbf{C}}_0(\phi_1, \phi_2) \hat{\mathbf{S}}_0(\phi_2). \end{aligned} \quad (7.139)$$

It is easy to see from the above that

$$\mathbf{M}_2(\phi_1, \phi_2) = -\frac{1}{8\pi\mu} \begin{pmatrix} 0 & 0 \\ 0 & B_{33}^2 D_{33}^{-2} \end{pmatrix}, \quad (7.140)$$

but the second matrix requires more work. The first product is simply

$$\hat{\mathbf{S}}_2(\phi_1) \hat{\mathbf{C}}_{-4}(\phi_1, \phi_2) \hat{\mathbf{S}}_2(\phi_2) = -\frac{1}{8\pi\mu d} \begin{pmatrix} 0 & 0 \\ 0 & D_{33}^{-2} (2B_{23}^2 \sin(\phi_1) \sin(\phi_2) + B_{23}^2 \cos(\phi_1) \cos(\phi_2)) \end{pmatrix}, \quad (7.141)$$

and the second is

$$\hat{\mathbf{S}}_2(\phi_1) \hat{\mathbf{C}}_{-2}(\phi_1, \phi_2) \hat{\mathbf{S}}_0(\phi_2) = -\frac{1}{8\pi\mu d} \left( \frac{-2B_{23} \sin(\phi_1)}{D_{33}} + \frac{B_{33}(B_{23}B_{33} - A_{23}D_{33}) \sin(\phi_2)}{A_0 D_{33}^2} \right) \begin{pmatrix} 0 & 0 \\ 1 & \frac{B_{23} \sin(\phi_2)}{D_{33}} \end{pmatrix}. \quad (7.142)$$

In RFT, the combination  $B_{23}B_{33} - A_{23}D_{33} = 0$  (see analytical expressions in Appendix 7.A). Hence, the previous expression simplifies to

$$\hat{\mathbf{S}}_2(\phi_1) \hat{\mathbf{C}}_{-2}(\phi_1, \phi_2) \hat{\mathbf{S}}_0(\phi_2) = \frac{B_{23}D_{33}^{-1} \sin(\phi_1)}{4\pi\mu d} \begin{pmatrix} 0 & 0 \\ 1 & B_{23}D_{33}^{-1} \sin(\phi_2) \end{pmatrix}, \quad (7.143)$$

and by symmetry,

$$\hat{\mathbf{S}}_0(\phi_1) \hat{\mathbf{C}}_{-2}(\phi_1, \phi_2) \hat{\mathbf{S}}_2(\phi_2) = \frac{B_{23}D_{33}^{-1} \sin(\phi_2)}{4\pi\mu d} \begin{pmatrix} 0 & 1 \\ 0 & B_{23}D_{33}^{-1} \sin(\phi_1) \end{pmatrix}. \quad (7.144)$$

The fourth term is again easy to compute as

$$\hat{\mathbf{S}}_0(\phi_1) \hat{\mathbf{C}}_0(\phi_1, \phi_2) \hat{\mathbf{S}}_0(\phi_2) = -\frac{1}{4\pi\mu d} \begin{pmatrix} 1 & B_{23}D_{33}^{-1} \sin(\phi_2) \\ B_{23}D_{33}^{-1} \sin(\phi_1) & B_{23}^2 D_{33}^{-2} \sin(\phi_1) \sin(\phi_2) \end{pmatrix}. \quad (7.145)$$

Finally, by adding the four contributions and noticing the cancellation of terms, we obtain the matrix

$$\mathbf{M}_0(\phi_1, \phi_2) = -\frac{1}{8\pi\mu} \begin{pmatrix} 2 & 0 \\ 0 & B_{23}^2 D_{33}^{-2} \cos(\phi_1) \cos(\phi_2) \end{pmatrix}, \quad (7.146)$$

which completes our asymptotic series to the first non-trivial order.

# Chapter 8

## Hydrodynamics of multiflagellar propulsion

In this chapter, we investigate the link between the number of flagellar filaments and the swimming speed of a peritrichous bacterium via numerical computations and a minimal model for the swimming bacterium. Our model incorporates the hydrodynamic interactions (HIs) within the bundle, as captured by a distribution of Stokeslets and source dipoles along the centrelines of the filaments, but the HIs between the flagellar bundle and the cell body are not included. Furthermore, we include in our model the full torque-speed relationship of the bacterial flagellar motor (BFM), which leads to qualitatively novel observations about the swimming speed of the cell. Specifically, we observe that the swimming speed reaches a maximum and then decays after a critical number of filaments, due to a transition from the high-load regime to the low-load regime of the motors actuating the filaments. Therefore, hydrodynamics predicts an optimal number of flagella for propulsion, and this number is within the biologically relevant range.

The work presented in this chapter is a summary of ongoing research as of the date of submission of this dissertation.

### 8.1 Motivation

The instantaneous speed of a bacterium is one of the key parameters defining its motility, including the way in which peritrichous bacteria actively diffuse via run-and-tumble [8]. It is known from both experiments [146, 156] and theoretical studies [107, 158] that the swimming speed of a bacterium depends on the number of flagella, although the details of this dependence have not been fully elucidated.

While previous theoretical studies have reported a monotonic increase in swimming speed with the number of flagella, experiments with flagellar mutant strains of *Bacillus subtilis* have suggested that the swimming speed is largest for the wild-type strain which has a mid-range value for the number of filaments [156]. In this aforementioned study, the flagellar deficient mutants had an average of 10 flagella, while the hyperflagellated mutants had up to 40, compared to the wild-type *B. subtilis* which exhibited around 26 flagella. On the other hand, experiments with flagellar mutants of *Helicobacter pylori* found that a relatively small change in the number of flagella, from three to only four flagella, could lead to an increase of 19% in the swimming speed of the cell [146]. *H. pylori* is a polarly-flagellated bacterium with multiple flagella protruding from one end of the cell body, so is very different to the highly-flagellated peritrichous bacterium *B. subtilis*. In this chapter, the model organism that we have in mind is *Escherichia coli*, which sits in between the two extremes, typically having three to five flagella distributed uniformly across the cell body [9]. This comparison helps us to identify the regime that we are interested in: a bundle made up of relatively few flagellar filaments, no more than ten, and a bundle radius on the same order as the width of the cell body, since the flagella are coming from all directions not just one end of the cell.

In the introduction, §1.3, we discussed a simple argument based on a force balance along the direction of motion of the bacterium to argue that the swimming speed of the cell,

$$U(N_f) = -\frac{N_f B_{33} \Omega}{N_f A_{33} + A_{\text{body}}}, \quad (8.1)$$

is bounded above by the limiting speed of each of its helical propellers,  $B_{33} \Omega / A_{33}$ . This calculation, proposed by Nguyen and Graham [158], assumes that the drag and thrust exerted by each filament does not depend on the number of filaments in the bundle, hence there are no HIs within the bundle or between the cell body and the bundle. Nguyen and Graham [158] found that this simple argument could explain relatively well the sub-linear increase in swimming speed observed in their full elastohydrodynamic simulations, in which the hydrodynamics of the filaments were modelled using the framework of regularised Stokeslets.

A separate numerical study by Kanehl and Ishikawa [107], using the boundary element method (BEM), also found that the swimming of the cell increases monotonically with the number of flagella, but reported a logarithmic increase with number of flagella. It has been suggested that the hydrodynamic resistance of a bundle with  $N_f$  helical filaments of thickness  $\varepsilon$  could be captured by a single filament with an effective radius of  $\varepsilon \sqrt{N_f}$ , such that the total cross-sectional area of the helix is the same as the sum over its constituent filaments [40]. Since the resistive drag coefficients on a slender filament, Eqs. (2.24)-(2.25), vary

logarithmically with the aspect ratio of the filament, Kanehl and Ishikawa [107] found this to be a reasonable approximation of their numerical results.

In this chapter, we use our computational method based on slender-body theory (SBT), which was introduced in Chapter 6, to further investigate the question of swimming with a bundle of helical flagellar filaments. We focus in particular on the HIs inside the bundle, and we investigate how these depend on the number of filaments and the radius of the bundle. A previous numerical study using the BEM also found that the distance between filaments affects the dynamics of a bacterium with only two flagella, with the cell body rotating more slowly and swimming faster when the two filaments were placed further apart [193].

## 8.2 Theoretical model

In this section, we describe the modelling assumptions of this investigation, and we define the key physical quantities through which we compare the hydrodynamic performance of bundles with different radii and number of filaments. Finally, we discuss briefly the computational method used to model the full HIs within the bundle, and refer the reader to §6.3.1 for further details of the numerical implementation.

### 8.2.1 Geometric and hydrodynamic setup

We consider a minimal model of a bundle of bacterial flagellar filaments, where  $N_f$  identical helical filaments are placed in a regular polygonal arrangement inscribed in a circle of radius  $R_b$ , the radius of the bundle. The setup is shown in Fig. 8.1 for the case of  $N_f = 5$  filaments, where the position of filament  $k$  relative to the centre of the bundle,

$$\mathbf{x}_k = R_b \cos\left(\frac{2\pi k}{N_f}\right) \mathbf{e}_x + R_b \sin\left(\frac{2\pi k}{N_f}\right) \mathbf{e}_y, \quad (8.2)$$

is indicated by a blue arrow for one filament in the bundle ( $k = 4$ ).

The kinematics of the filaments are prescribed under the conditions of rotational symmetry around the bundle, so that each filament translates and rotates rigidly with the same velocity components  $(U_r, U_\phi, U_z)$  and  $(\Omega_r, \Omega_\phi, \Omega_z)$ . For each filament, the  $r$  components of the linear and angular velocities point from the central axis of the bundle towards the axis of the filament, as illustrated by the yellow arrows in Fig. 8.1. Likewise, the  $\phi$  components point counter-clockwise around the bundle, in the direction of increasing azimuthal angle around the central axis of the bundle.

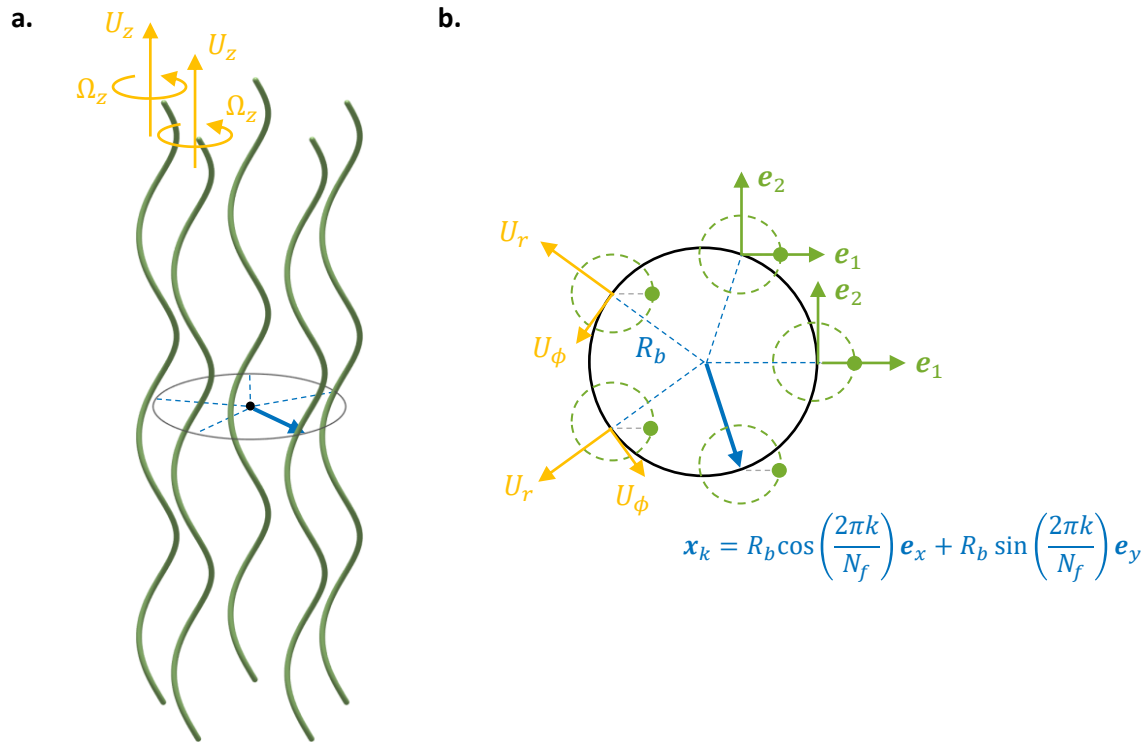


Fig. 8.1 Geometrical and kinematic setup for investigating the hydrodynamics of a circular bundle of filaments. (a) Side view of the bundle consisting of  $N_f$  identical helical filaments, whose axes are aligned with the  $z$  direction. (b) Horizontal cross-section through the bundle, illustrating the placement of the helical axes at regular intervals around a circle of radius  $R_b$ . The filled green circle is the cross-section through the filament, while the dashed green circle indicates the locus of the filament as it rotates about its axis. The kinematics of the filaments satisfy rotational symmetry around the bundle, so that all filaments translate with the same vertical velocity  $U_z$ , the same radial velocity  $U_r$  outward from the central axis of the bundle, and the same circumferential velocity  $U_\phi$  around the bundle. Likewise for rotational velocities,  $\Omega_{z,r,\phi}$ . The velocities are indicated by yellow arrows on a selection of filaments from the bundle. Furthermore, the filaments rotate in phase with each other, so that the instantaneous orientation is the same for all filaments,  $\{\mathbf{e}_1, \mathbf{e}_2, \mathbf{e}_2\}$ , indicated by green arrows on a selection of filaments.

For simplicity, we assume that the axes of the helices remain parallel over time, such that  $\Omega_r = \Omega_\phi = 0$ , and that the radius of the bundle is fixed, so  $U_r = 0$ . The remaining degrees of freedom allow the filaments to rotate about their own axis,  $\Omega_z$ , to translate along the same axis,  $U_z$ , and to rotate around the central axis of the bundle,  $U_\phi$ . Later, when we couple the bundle with the cell body, the last two conditions allow us to capture the forward propulsion of the cell and the counter-rotations of the cell body.

We further assume that the filaments rotate in-phase with each other, so that the absolute phase angle of each filament is the same,  $\Phi_k = \phi_k + \chi_k = \Phi$ . In other words, we are assuming that the filaments have had sufficient time to synchronise through hydrodynamic interactions (see Chapter 7) and that the bundle has reached a steady state. Therefore, the body-fixed vectors  $\{\mathbf{e}_1^{(k)}, \mathbf{e}_2^{(k)}, \mathbf{e}_3^{(k)}\}$  are the same for all the filaments, so we may drop the filament label. These are depicted by green arrows on Fig. 8.1 for two filaments amongst the bundle.

Finally, we non-dimensionalise the physical variables in such a way that the length of the filament is  $L = 2$ , and the dynamic viscosity of the fluid is  $\mu = 1$  in dimensionless terms, just as in Chapter 6. Since we later consider the full torque-speed relationship of the BFM, not just a constant torque applied to the filaments, we non-dimensionalise forces and torques such that the maximum torque, also known as the stall torque of the motor, is  $T_{\text{stall}} = 1$  in dimensionless terms. The time scale resulting from these three choices is  $\tilde{\tau} = \tilde{\mu} \tilde{L}^3 / 8 \tilde{T}_{\text{stall}}$ .

### 8.2.2 Extended resistance matrix for a circular bundle of filaments

Just as we have done in Chapter 6, when considering the HIs between two rigid filaments, we express the relationship between the dynamics and the kinematics of multiple hydrodynamically-coupled filaments through an extended resistance matrix,

$$\begin{pmatrix} \mathbf{F}_1 \\ \mathbf{T}_1 \\ \mathbf{F}_2 \\ \mathbf{T}_2 \\ \vdots \\ \mathbf{F}_{N_f} \\ \mathbf{T}_{N_f} \end{pmatrix} = \begin{pmatrix} \mathbf{S}_1 & \mathbf{C}_{2 \rightarrow 1} & \cdots & \mathbf{C}_{N_f \rightarrow 1} \\ \mathbf{C}_{1 \rightarrow 2} & \mathbf{S}_2 & \cdots & \mathbf{C}_{N_f \rightarrow 2} \\ \vdots & \vdots & \ddots & \vdots \\ \mathbf{C}_{1 \rightarrow N_f} & \mathbf{C}_{2 \rightarrow N_f} & \cdots & \mathbf{S}_{N_f} \end{pmatrix} \begin{pmatrix} \mathbf{U}_1 \\ \boldsymbol{\Omega}_1 \\ \mathbf{U}_2 \\ \boldsymbol{\Omega}_2 \\ \vdots \\ \mathbf{U}_{N_f} \\ \boldsymbol{\Omega}_{N_f} \end{pmatrix}, \quad (8.3)$$

where  $\mathbf{F}_k$  and  $\mathbf{T}_k$  are the forces and torques exerted by filament  $k$  on the fluid, and  $\mathbf{U}_k$  and  $\boldsymbol{\Omega}_k$  are the rigid body translation and rotation of the filaments relative to the fluid. The resistance matrices  $\mathbf{S}_k$  measure the self-induced dynamics of each filament, while the resistance matrices  $\mathbf{C}_{j \rightarrow k}$  capture the hydrodynamic effects induced by the motion of filament  $j$  on filament  $k$ .

Under our notation convention from the rest of the dissertation, the self-induced matrices  $\mathbf{S}_k$  and the cross-interaction matrices  $\mathbf{C}_{j \rightarrow k}$  are expressed relative to the laboratory frame  $\{\mathbf{e}_x, \mathbf{e}_y, \mathbf{e}_z\}$ .

To account for the rotational symmetry in our setup, we introduce some new notation,  $\mathbf{S}_k^{\text{cb}}$  and  $\mathbf{C}_{j \rightarrow k}^{\text{cb}}$ , where the superscript stands for ‘‘circular bundle’’. These resistance matrices provide the linear relationship between the dynamics and kinematics of the filaments expressed in radial, azimuthal and vertical components relative to the central axis of the bundle, i.e.  $\mathbf{\Gamma}_k^{\text{cb}} = (\Gamma_r, \Gamma_\phi, \Gamma_z)$ , where  $\Gamma$  is a generic placeholder for a force, torque or velocity.

The conversion between  $\mathbf{S}_k$ ,  $\mathbf{C}_{j \rightarrow k}$  and  $\mathbf{S}_k^{\text{cb}}$ ,  $\mathbf{C}_{j \rightarrow k}^{\text{cb}}$  is achieved by a change of basis,

$$\mathbf{S}_k^{\text{cb}} = \begin{pmatrix} \mathbf{Q}_k^T & \mathbf{0} \\ \mathbf{0} & \mathbf{Q}_k^T \end{pmatrix} \mathbf{S}_k \begin{pmatrix} \mathbf{Q}_k & \mathbf{0} \\ \mathbf{0} & \mathbf{Q}_k \end{pmatrix}, \quad \mathbf{C}_{j \rightarrow k}^{\text{cb}} = \begin{pmatrix} \mathbf{Q}_k^T & \mathbf{0} \\ \mathbf{0} & \mathbf{Q}_k^T \end{pmatrix} \mathbf{C}_{j \rightarrow k} \begin{pmatrix} \mathbf{Q}_j & \mathbf{0} \\ \mathbf{0} & \mathbf{Q}_j \end{pmatrix}, \quad (8.4)$$

$$\mathbf{Q}_k = \begin{pmatrix} \cos\left(\frac{2\pi k}{N_f}\right) & -\sin\left(\frac{2\pi k}{N_f}\right) & 0 \\ \sin\left(\frac{2\pi k}{N_f}\right) & \cos\left(\frac{2\pi k}{N_f}\right) & 0 \\ 0 & 0 & 1 \end{pmatrix}, \quad (8.5)$$

where the matrix  $\mathbf{Q}_k$  represents a rotation by angle  $2\pi k/N_f$  about the  $z$  axis.

### 8.2.3 Average resistance coefficients

Since the time scale of rotation of bacterial flagellar filaments is much faster than the time scale on which bacteria swim in a straight line with their flagellar filaments gathered in a bundle [40], we are interested in the mean hydrodynamic resistance of the bundle averaged over a period of rotation of the filaments.

We define the effective drag coefficient

$$A_{33}^{\text{fcb}}(R_b, N_f) = \langle (\mathbf{S}_k^{\text{cb}})_{33} + \sum_{j \neq k} (\mathbf{C}_{j \rightarrow k})_{33} \rangle, \quad (8.6)$$

as an average of all the hydrodynamic effects in the bundle over one period of the phase angle,  $\langle \dots \rangle = 1/(2\pi) \int_0^{2\pi} \dots d\Phi$ . The drag coefficient  $A_{33}^{\text{fcb}}$  measures the average resistance of a ‘‘filament in a circular bundle’’ (fcb) to translation along its own axis. Due to rotational symmetry around the bundle, the drag coefficient is the same for any filament label  $k$ . However, we have made it explicit in our notation that the resistance coefficient depends on the radius of the bundle and the number of filaments in the bundle.

Likewise, we define the effective thrust coefficient

$$B_{33}^{\text{fcb}}(R_b, N_f) = \langle (\mathbf{S}_k^{\text{cb}})_{36} + \sum_{j \neq k} (\mathbf{C}_{j \rightarrow k})_{36} \rangle, \quad (8.7)$$

which measures the average propulsion generated by a helix through its rotation about its own axis, and the effective torque coefficient

$$D_{33}^{\text{fcb}}(R_b, N_f) = \langle (\mathbf{S}_k^{\text{cb}})_{66} + \sum_{j \neq k} (\mathbf{C}_{j \rightarrow k})_{66} \rangle, \quad (8.8)$$

which measures the average torque that must be applied to the filament in order to sustain its rotation against viscous drag from the fluid. For a single filament, the quantities from Eqs. (8.6)-(8.8) are equivalent to the resistance coefficients  $A_{33}$ ,  $B_{33}$  and  $D_{33}$  previously computed by RFT in Appendix 6.A.

Finally, since we later include the motion of the filaments due to the counter-rotations of the cell body, we also need to define the resistance coefficients

$$A_{32}^{\text{fcb}}(R_b, N_f) = \langle (\mathbf{S}_k^{\text{cb}})_{32} + \sum_{j \neq k} (\mathbf{C}_{j \rightarrow k})_{32} \rangle, \quad (8.9)$$

$$B_{32}^{\text{fcb}}(R_b, N_f) = \langle (\mathbf{S}_k^{\text{cb}})_{62} + \sum_{j \neq k} (\mathbf{C}_{j \rightarrow k})_{62} \rangle, \quad (8.10)$$

which describe the effective force and torque exerted on the fluid by a filament due to its circumferential velocity  $U_\phi$  around the bundle (see Fig. 8.1 (c)).

## 8.2.4 Computational method for hydrodynamic interactions

Since our goal is to capture the hydrodynamics of a circular bundle of filaments across a range of length scales, including bundle radii  $R_b$  of order  $\mathcal{O}(L)$ , we need to resort to numerical computations in order to quantify the full HIs within the bundle. We use the same computational method as in Chapter 6, which is based on Johnson's SBT [105] with HIs between the filaments modelled using the framework of Tornberg and Shelley [205]. We extend Eq. (6.60) to multiple interacting filaments,

$$8\pi\mu\mathbf{u}(\mathbf{r}_k(s)) = \mathcal{L}[\mathbf{f}_k(s)] + \mathcal{H}[\mathbf{f}_k(s')] + \sum_{j \neq k} \mathcal{I}[\mathbf{f}_j(s'), \mathbf{d}_{j \rightarrow k}], \quad (8.11)$$

where  $\mathbf{d}_{j \rightarrow k} = \mathbf{x}_k - \mathbf{x}_j$  is the distance between filaments  $j$  and  $k$ , and  $\mathbf{f}_k$  is the force density along filament  $k$ . The linear and integral operators  $\mathcal{L}$  and  $\mathcal{H}$  come from SBT, and the

integral operator  $\mathcal{J}$  models the HIs between filaments through the Stokeslet and source dipole flows they each induce.

We invert Eq. (8.11) using the same Galerkin method described in §6.3.1, from which we derive the extended resistance matrix of Eq. (8.3). Afterwards, we carry through with the calculations as described in this section.

## 8.3 Results and biophysical insights

After introducing the key assumptions of our model and the computational method used in this investigation, we now present our results and explain their significance in a biophysical context. We start by considering the effective hydrodynamic resistance of a circular bundle of filaments, and then we couple the bundle with a spheroidal cell body through a force and torque balance on the entire cell. This allows us to calculate the swimming speed of a multiflagellated bacterium as a function of the number of filaments in the bundle. In this final part, the full HIs between the filaments are included, but the HIs between the bundle and the cell body are not.

### 8.3.1 Hydrodynamic resistance of a bundle of flagellar filaments

All the results provided in this subsection correspond to flagellar filaments in the normal polymorphic shape, with measurements for the helical pitch and amplitude, and the contour length of the filament taken from Darnton et al. [40]. In dimensional terms, the control parameters used in our simulation are  $\tilde{R} = 0.195 \mu\text{m}$ ,  $\tilde{p} = 2.22 \mu\text{m}$ ,  $\tilde{\varepsilon} = 0.012 \mu\text{m}$  and  $\tilde{L} = 8.3 \mu\text{m}$ .

The first physical quantities we look at are the total drag, thrust and torque exerted by a circular bundle as a function of the number of filaments, shown in Fig. 8.2 (a-c). All of these quantities are averaged over the phase angle of the filaments so they cannot be fully separated from the idea that the filaments are rotating about their axes, but the drag pertains specifically to the force induced by the translation of the filaments as they are rotating, while the thrust and torque pertain to the actual rotation - see diagrams on the left of Fig. 8.2.

For large bundle radii, the total forces and torque exerted by the filaments increase linearly with the number of filaments, as expected, since HIs do not affect the dynamics of the individual filaments very much. For small bundle radii, we find that HIs significantly decrease the total drag, thrust and torque, leading to a sub-linear increase with the number of filaments, and even an initial decrease going from one to two filaments when the radius of

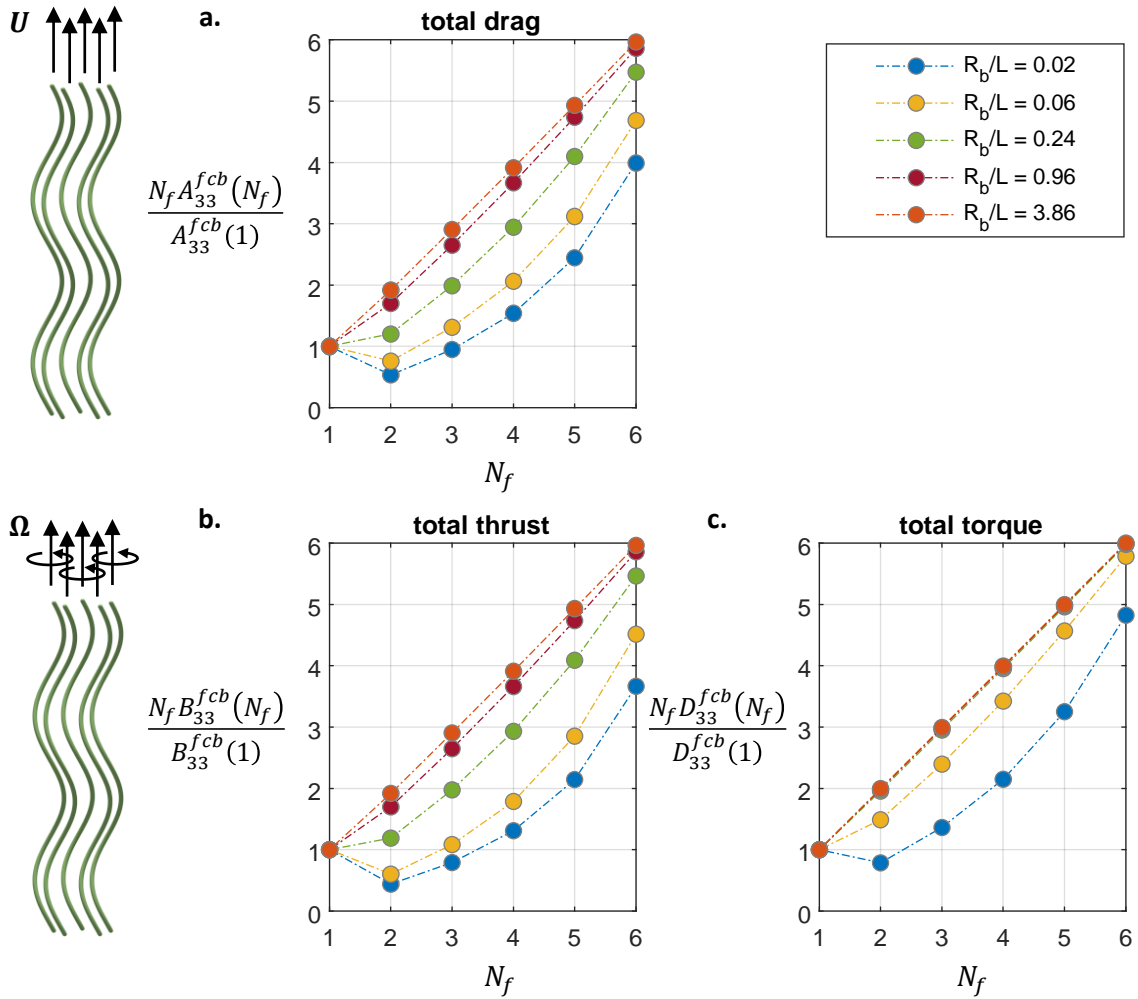


Fig. 8.2 Total drag, thrust and torque exerted by a circular bundle of hydrodynamically-coupled filaments, calculated numerically using the computational method described in §6.3.1 and extended to multiple filaments in Eq. (8.11). The effective drag, thrust and torque coefficients  $A_{33}^{fcb}$ ,  $B_{33}^{fcb}$ ,  $D_{33}^{fcb}$  are defined in Eqs. (8.6)-(8.8).

the bundle is sufficiently small. This is most noticeable for the forces exerted by the bundle in Fig. 8.2 (a) and (b), and less so for the torque.

To understand where the sublinear increase in total drag, thrust and torque comes from, we now focus on the deficit in these quantities for a single filament in the bundle. In Fig. 8.3 (a), we plot the relative difference in the thrust exerted by a filament rotating in a circular bundle of  $N_f$  filaments compared to the thrust that the same filament would exert if actuated on its own. We repeat for the drag and torque in Fig. 8.3 (b) and (c), respectively. The circles represent numerical computations, while the solid lines are far-field asymptotics based on our calculations from Chapter 6.

Recall the far-field deficit in thrust and torque was explicitly calculated in §6.4 for the case of two helices rotating in parallel. The result of Eq. (6.89) tells us that the deficit due to pairwise HIs between two helices rotating in phase, at distance  $d$  away from each other, is

$$\langle \Delta F_z \rangle = -\frac{\Omega_z}{8\pi d} \left( A_{33} B_{33} + \frac{3}{2} A_{23} B_{23} \right) + \mathcal{O}(d^{-2}). \quad (8.12)$$

Summing over all pairwise interactions in a circular bundle of large radius,  $R_b \gg L$ , we obtain the following asymptotic expression for the deficit in thrust on a filament in a circular bundle, relative to the thrust coefficient  $B_{33}$  for an isolated helix,

$$B_{33}^{\text{fcb}}(R_b, N_f) - B_{33} \approx -\frac{1}{16\pi R_b} \left( A_{33} B_{33} + \frac{3}{2} A_{23} B_{23} \right) \sum_{k=1}^{N_f-1} \frac{1}{\sin(k\pi/N_f)} + \mathcal{O}(R_b^{-2}). \quad (8.13)$$

Similarly, we obtain the deficit in torque by extending the result of Eq. (6.91) into

$$D_{33}^{\text{fcb}}(R_b, N_f) - D_{33} \approx -\frac{1}{16\pi R_b} \left( B_{33}^2 + \frac{3}{2} B_{23}^2 \right) \sum_{k=1}^{N_f-1} \frac{1}{\sin(k\pi/N_f)} + \mathcal{O}(R_b^{-2}). \quad (8.14)$$

Although not explicitly calculated in §6.4, the deficit in drag is easily obtained as

$$A_{33}^{\text{fcb}}(R_b, N_f) - A_{33} \approx -\frac{1}{16\pi R_b} \left( A_{33}^2 + \frac{3}{2} A_{23}^2 \right) \sum_{k=1}^{N_f-1} \frac{1}{\sin(k\pi/N_f)} + \mathcal{O}(R_b^{-2}). \quad (8.15)$$

The asymptotic expressions from Eqs. (8.13)-(8.15) are in excellent agreement with the numerical data when the bundle radius is sufficiently large - see Fig. 8.3 (a-c).

As we decrease the radius of the bundle, we observe that the deficit in thrust and drag grows more slowly in the near field than in the far field, while the opposite is true for the torque. In all cases, however, the thrust, drag and torque exerted by a filament in a circular bundle is significantly reduced compared to the way it would operate in the absence of HIs.

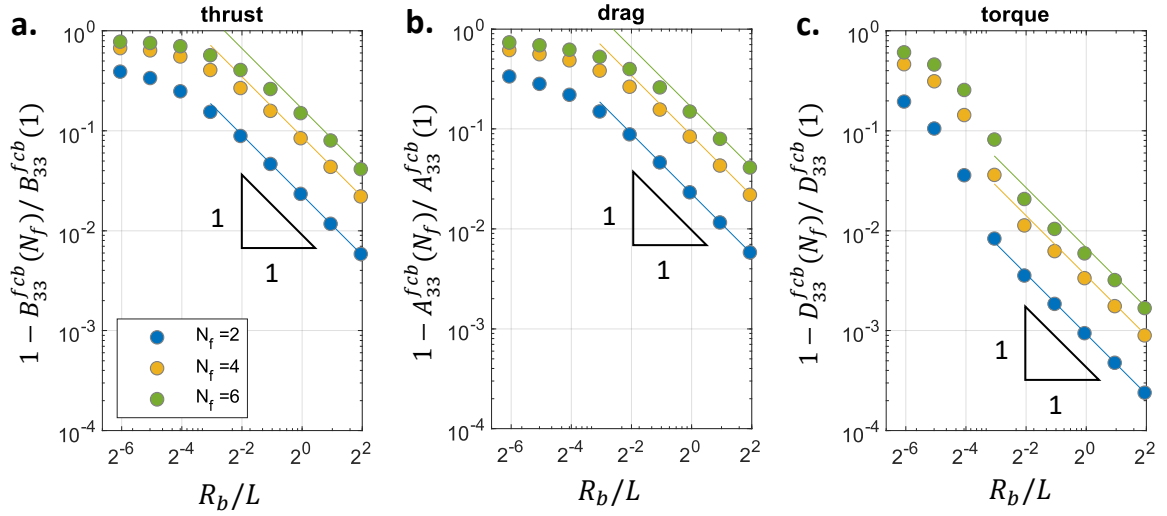


Fig. 8.3 Deficit in drag, thrust and torque on an individual filament operating inside a circular bundle. The numerical data (circles) is shown alongside the far-field asymptotic expressions (solid lines) from Eqs. (8.13)-(8.15). For reference, the typical width of a bacterial cell body is  $w/L \approx 0.1$ , so our numerical results span a range between  $R_b/w = 0.14$  and  $R_b/w = 36$ .

The fact that a filament rotating within a bundle requires much less torque to be actuated at the same angular velocity is very important later on, when we consider how the torque-speed relationship of the BFM affects the swimming speed of the cell.

We also remind the reader that the physical origin of the thrust deficit was illustrated in Fig. 6.11 based on the far-field hydrodynamic interactions between the filaments. The flows induced by the force density along each filament are expected to have the same qualitative features in the near-field, although the magnitude of hydrodynamic effects increases. When the separation between the filaments becomes comparable to the thickness of the filaments, the force moments induced by the rotation of the filament about its own centreline are expected to become important. The numerical results presented in this section go down to a dimensionless bundle radius  $R_b = 0.02$ , much larger than the cross-sectional radius of the filaments,  $\varepsilon = 0.003$ , so we do not included the effect of force moments in our computational method.

### 8.3.2 Swimming speed of a multiflagellated bacterium

Now that we have a better understanding of the hydrodynamic resistance of a circular bundle of filaments, we want to use our results to gain physical insights about the swimming speed of a multiflagellated bacterium.

We model the cell body as a prolate spheroid with length,  $l$ , and width,  $w$ , as shown in Fig. 8.4 (a). As a starting point, we consider a “dry” coupling where there are no HIs between the bundle and the cell body, but the two are coupled through a force and torque balance on the entire bacterium

$$N_f \begin{pmatrix} A_{33}^{\text{fcb}} & B_{33}^{\text{fcb}} \\ B_{33}^{\text{fcb}} & D_{33}^{\text{fcb}} \end{pmatrix} \begin{pmatrix} U \\ \Omega \end{pmatrix} + N_f \begin{pmatrix} A_{32}^{\text{fcb}} \\ B_{32}^{\text{fcb}} \end{pmatrix} R_b \Omega_{\text{body}} + \begin{pmatrix} A_{\parallel} & 0 \\ 0 & D_{\parallel} \end{pmatrix} \begin{pmatrix} U \\ \Omega_{\text{body}} \end{pmatrix} = 0. \quad (8.16)$$

The first term represents the forces and torques exerted by the filaments due to rotation and translation about their own axes. The second term represents the vertical forces and torques exerted by the filaments due to their linear velocity around the circumference of the bundle,  $U\phi = R_b\Omega_{\text{body}}$ , which comes from the fact that the anchoring points of the filaments rotate together with the cell body. The final term represents the forces and torques exerted by the spheroidal cell body along its major axis, where  $A_{\parallel}$  and  $D_{\parallel}$  are the resistance coefficients for a prolate spheroid defined in Eqs. (2.29)-(2.30).

To close the system, we need a third condition for the dynamic actuation of the filaments. The modelling assumption commonly used in the literature is that the motors apply a constant torque to the flagellar filaments [107, 158]. Here, we consider the full torque-speed relationship of the BFM, which was previously described in §1.2.3. Our choice is motivated by our previous understanding of the hydrodynamic resistance of a bundle of flagellar filaments, from Fig. 8.3, where we have seen that HIs within the bundle can reduce the effective torque coefficient  $D_{33}^{\text{fcb}}$  by up to 60% in the parameter space considered in our numerical simulations.

Motivated by experimental measurements on the rotary motors of *E. coli*, which have been summarised in the review article by Sowa and Berry [196], we model the torque-speed relationship of the BFM as a piecewise linear function,

$$T = \begin{cases} 1 - \alpha(\Omega - \Omega_{\text{body}}) & \text{if } \Omega - \Omega_{\text{body}} \leq \Omega_{\text{knee}}, \\ \gamma - \beta(\Omega - \Omega_{\text{body}} - \Omega_{\text{knee}}) & \text{if } \Omega - \Omega_{\text{body}} > \Omega_{\text{knee}}, \end{cases} \quad (8.17)$$

as shown by the black solid line in Fig. 8.4 (b). The angular velocity at the knee is such that the function is continuous,  $\Omega_{\text{knee}} = (1 - \gamma)/\alpha$ . Note that the maximum torque applied by the BFM is  $T_{\text{stall}} = 1$  in our dimensionless units.

We extract the parameters  $\alpha, \beta, \gamma$  by fitting the scatter plots provided by Xing et al. [227], which are themselves a summary of experimental data [25, 60]. We fit the relative torque at the knee as  $\gamma = 0.85$ , and the dimensional slopes  $\tilde{\alpha} = 1 \times 10^{-4}$  s, and  $\tilde{\beta} = 22 \times 10^{-4}$  s. The dimensionless slopes  $\alpha$  and  $\beta$  are obtained after rescaling by the time scale  $\tilde{\tau} = \tilde{\mu}\tilde{L}^3/8\tilde{T}_{\text{stall}}$ .

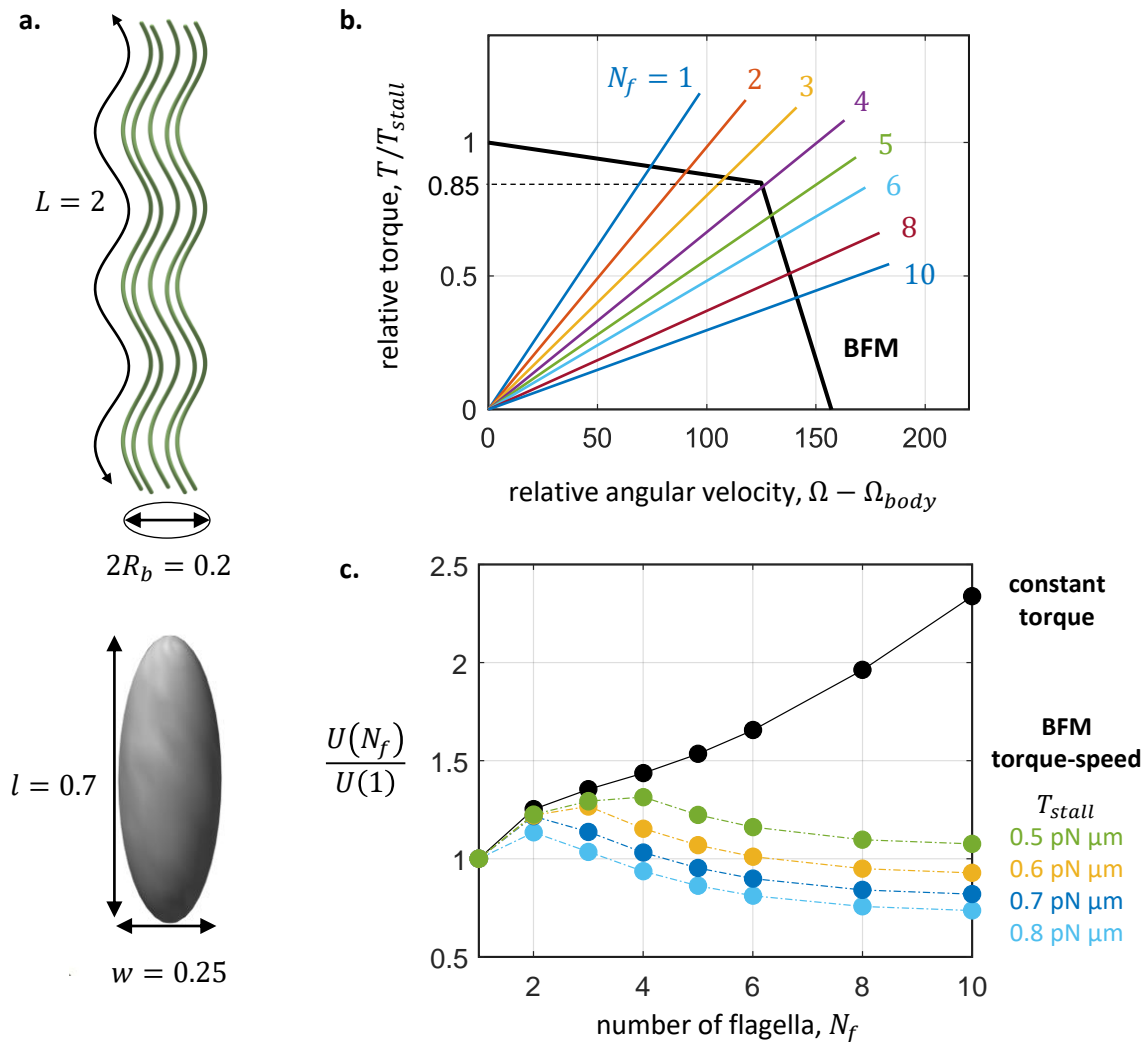


Fig. 8.4 Swimming with a bundle of flagellar filaments. (a) Our minimal model of a swimming multiflagellated bacterium consists of a bundle of parallel helical filaments and a spheroidal cell body. The “dry” coupling between the bundle and cell body consists of a force and torque balance on the entire bacterium, Eq. (8.16). (b) Piecewise linear model for the torque-speed relationship of the BFM (black) and viscous “load lines” (colour) for a single filament that operates as part of a circular bundle of  $N_f$  filaments. For  $N_f > 4$ , the bundle enters the low-load regime of the BFM, because the hydrodynamic resistance of a filament to rotation about its own axis is greatly reduced when the filament is part of a bundle. The torque-speed curve displayed in this figure corresponds to a motor stall torque of  $\tilde{T}_{stall} = 0.5 \text{ pN } \mu\text{m}$ . (c) The torque-speed relationship of the BFM has a significant effect on the swimming speed of a multiflagellated bacterium. The swimming speed of the cell starts to decay when the motors actuating the filaments enter the low-load regime, which happens when the number of filaments in the bundle is sufficiently large.

However, the values reported in the literature for the stall torque of the BFM vary by a considerable amount [12, 40, 42]. For the results presented in Fig. 8.4 (b) we non-dimensionalise using a stall torque of  $\tilde{T}_{\text{stall}} = 0.5 \text{ pN } \mu\text{m}$ , together with the viscosity of water at  $20^\circ\text{C}$ ,  $\tilde{\mu} = 1 \text{ cP}$ , and a filament length of  $\tilde{L} = 7.1 \text{ } \mu\text{m}$  [40]. In Fig. 8.4 (c) we consider a few different values for the stall torque, selected from the mid-range of values reported in the literature [12, 40, 42].

Finally, we equate the torque applied by the BFM to each filament, Eq. (8.17), to the average torque exerted by each flagellar filament on the fluid,

$$T = B_{33}^{\text{fcb}}U + D_{33}^{\text{fcb}}\Omega. \quad (8.18)$$

Note that the torque applied by the motor to the flagellar filament depends on the relative angular velocity of the filament with respect to the cell body,  $\Omega - \Omega_{\text{body}}$ , while the torque exerted by the filament on the fluid depends on its absolute angular velocity in the laboratory frame,  $\Omega$ .

Our model for the swimming of a multiflagellated bacterium consists of the coupled system of equations from Eqs. (8.16)-(8.18). We solve these equations using the effective resistance coefficients  $A_{33}^{\text{fcb}}$ ,  $B_{33}^{\text{fcb}}$ ,  $D_{33}^{\text{fcb}}$  calculated via our computational method. The final results are shown in Fig. 8.4 (b) and (c).

The torque at which the motors operate is given by the intersection between the intrinsic torque-speed curve of the BFM (black solid line) and the viscous ‘‘load line’’ for a filament (coloured solid lines) on Fig. 8.4 (b). As the number of filaments in the bundle increases, the effective hydrodynamic resistance of the filament to rotation about its own axis decreases, which is reflected by the decreasing slope of the load lines. After a certain point, which in this case happens to be  $N_f = 4$ , the rotary motors enter the low-load regime where the torque falls rapidly with increasing angular speed.

When considering the overall swimming speed of the cell, in Fig. 8.4 (c), the change from the high-load to the low-load regime is manifested by a local maximum, after which the swimming speed of the cell starts to decay.

## 8.4 Conclusion

In this chapter, we have investigated the hydrodynamic resistance of a circular bundle of filaments by computational means, and we have identified the dependence of key quantities (the drag, thrust and torque exerted by the filaments) on the radius of the bundle and the number of filaments. We have also used our understanding of how the torque exerted by

the filaments is reduced through HIs to propose a model of a swimming multiflagellated bacterium which incorporates the torque-speed relationship of the BFM. Our findings suggest that the swimming speed of the cell may depend in a fundamental way on the torque-speed relationship of the BFM, since we observe strong effects within the biologically relevant range of two to six flagellar filaments [208, 209].

Our model does not yet include two important hydrodynamic effects: the HIs between the cell body and the bundle, and the HIs within the bundle due to the rotation of the filaments around their own centreline. We expect that including HIs between the cell body and the bundle would delay the transition into the low-load regime, and hence the number of filaments at which the maximum swimming velocity is achieved. This is because the angular velocity of the cell body would be reduced in magnitude due to HIs with the bundle, and hence the relative angular velocity  $\Omega - \Omega_{\text{body}}$  would be less. However, even if the rotation rate of the cell body were to remain constant, the slope of the load lines would still decrease with increasing number of filaments due to HIs within the bundle. Eventually, it is reasonable to expect a maximum in swimming speed at some larger number of filaments.

The one hydrodynamic aspect that could prevent the monotonic decrease of the load lines in Fig. 8.4 (b) and the transition to the low-load regime, are the hydrodynamic moments generated by the rotation of the filaments about their own centreline. These moments are negligible in the parameter range explored in this chapter, as explained at the end of §8.3.1, but as the number of filaments is further increased and the distance between the filaments goes down, the effects due to hydrodynamic moments may become important. This suggests a fruitful avenue for future research into the hydrodynamics of flagellar bundles.



# Chapter 9

## Summary and perspectives

In this dissertation, we have proposed a series of novel theoretical models for the dynamics of a bundle of rotating helical filaments, such as the ones used by multiflagellated bacteria for swimming. We have considered two types of interactions between the flagellar filaments: “dry” interactions in the form of excluded-volume effects, which depend in an essential way on the helical geometry of flagellar filaments, and hydrodynamic interactions (HIs) mediated by the fluid flow generated by each filament as it rotates and translates.

Our mathematical models have revealed a series of interesting biophysical results, which we now summarise very briefly. In Chapter 3, we have seen that the polymorphic transformation of bacterial flagellar filaments during a tumbling event may contribute to the re-bundling of the filaments, since the right-handed geometry of the semicoiled and curly I/II polymorphs allows them to intertwine in a counter-clockwise direction around normal-shape filaments, as imposed by HIs. We have also found, in Chapter 4, that the typical number of flagellar filaments owned by peritrichous bacteria like *Escherichia coli* and *Salmonella typhimurium* is sufficiently small for these bacteria to be able to form tangle-free bundles robustly. In the final chapter on geometry, Chapter 5, we have characterised the conditions under which rotating helical filaments may come together to form a bundle without colliding into each other, and identified the rate of synchronisation required by the geometry through excluded-volume effects. This final chapter regarding the geometric constraints on synchronisation makes the connection with the second half of the dissertation, in which we consider the HIs between bacterial flagellar filaments.

In order to investigate the topic of hydrodynamic synchronisation between bacterial flagella, we first needed to develop some analytical tools for describing the HIs between filaments, and to implement a computational method against which to validate our analytical calculations. This has been done in Chapter 6 and used in the following two chapters to explore the elastohydrodynamic synchronisation of two bacterial flagella, and then the

propulsion of a bacterium by a circular bundle of multiple filaments. The key biophysical insight gained in Chapter 7 is that the elastic compliance provided by the hook and the flagellar filament plays a crucial role in the synchronisation of bacterial flagella. In the far field, we have found that there is an optimum elastic compliance which maximises the rate of in-phase synchronisation, while our near-field numerical observations suggest that elastic compliance is fundamentally linked to multisynchrony and the exchange of stability between in-phase and anti-phase synchronisation. This has significant implications for the stability of bacterial flagellar bundles, and for the understanding of the onset of unbundling events. In the last chapter on hydrodynamics, Chapter 8, we have used our physical understanding of inter-filament HIs in order to identify the essential role played by the bacterial flagellar motor (BFM) in the propulsion of a cell by a circular bundle of flagellar filaments. Specifically, our findings suggest that there is an optimum number of flagella at which the swimming speed of the cell is maximised. Above this optimum number, the hydrodynamic resistance of the filaments to rotation about their own axis is reduced so much by the HIs inside the bundle that the BFMs enter the low-load regime, which reduces the torque applied to each filament and hence the swimming speed of the cell.

We conclude this chapter and this thesis by suggesting a few directions for future research which are directly connected to the work presented in this dissertation.

### **Geometrical requirements vs. hydrodynamic mechanism for synchronisation**

One way in which the geometrical and the hydrodynamic results of this dissertation can be combined is through the rate of synchronisation. By comparing the rate of synchronisation required by excluded-volume effects, Chapter 5, and the rate of synchronisation enabled by hydrodynamic interactions, Chapter 7, it should in principle be possible to determine operational constraints on the bundle, such as the maximum number of filaments or the maximum torque difference between the motors to ensure the smooth operation of the bundle.

### **From one to many: synchronisation in a bundle**

Having understood how two bacterial flagella synchronise via the elastohydrodynamic mechanism proposed in Chapter 7, a natural step forward would be to extend the current model to the synchronisation of multiple flagella. While previous theoretical studies have considered the synchronisation of beating eukaryotic cilia arranged in a regular two-dimensional lattice [52, 73], not much is known about synchronisation in a circular array of oscillators, which is the relevant geometry for bacterial flagellar bundles. Just as we have seen in Chapter 5,

---

where the dominant effect came from excluded-volume interactions with either the nearest neighbour or the filament directly across the bundle, it is reasonable to expect that there is a distinction between these two regimes in the case of hydrodynamic interactions as well. The consequence that this might have on the synchronisation of bacterial flagella organised in circular bundles remains to be explored.

### **Near-field multisynchrony of bacterial flagella**

Another way in which the synchronisation of bacterial flagella is qualitatively different from eukaryotic flagella are the features observed for multisynchrony in the near field. A theoretical study by Man and Kanso [141] on the synchronisation of active microfilaments found that the anti-phase configuration loses stability through a supercritical pitchfork bifurcation, whereby two stable fixed points are created at nontrivial phase lag. In contrast, our preliminary numerical observations have shown that the anti-phase configuration gains stability through a subcritical pitchfork bifurcation, so the newly created fixed points with nontrivial phase lag are unstable. Therefore, the coexistence of stable configurations where the flagella rotate in-phase, anti-phase or with a nontrivial phase difference to each other may be qualitatively different for bacterial flagella, and this could be linked to the motility of the cell. In summary, the near-field multisynchrony of rotating flagella is likely to be important for the run-and-tumble motility of peritrichous bacteria and should be investigated more systematically.

### **Alternative mechanisms for bacterial flagellar synchronisation**

The framework for hydrodynamic interactions and the multiple-scales analysis of synchronisation presented in Chapters 6 and 7, respectively, provide us with a methodology to explore alternative mechanisms for the synchronisation of bacterial flagella, other than the elastic tethering mechanism considered in this dissertation.

A first possibility is to assume that the axis of each filament remains fixed, but to allow the helical shape of the filament to deform in a quasi-steady fashion due to the flows induced by the other filament along its axis. The elastic deformations of helical filaments have previously been modelled in the context of bacterial dynamics using Kirchhoff rod theory [39, 40, 112, 124, 217]. Since bacterial flagellar filaments are semi-rigid, these deformations would modulate the hydrodynamic resistance of the filament on a slow time scale, much larger than the period of rotation, and may lead to in-phase synchronisation in a similar way as the orbital-compliance mechanism proposed by Niedermayer et al. [159] in their minimal model of synchronisation between spherical beads.

A second direction to be explored, inspired by our work on the propulsion of multi-flagellated bacteria, is to consider the torque-speed relationship of the BFM. It is easy to deduce from the symmetry of the governing equations that the torque-speed relationship of the BFM, on its own, cannot lead to synchronisation if the motors always operate in either the high-load or the low-load regime. However, it may be possible to achieve synchronisation by coupling the filaments to the counter-rotations of the cell body, since there is evidence from eukaryotic swimmers that the feedback between the beating of the flagella and the swaying of the cell body contributes to synchronisation [62]. Alternatively, the filaments may be able to synchronise without the cell body if the BFM operates in the non-linear “knee” region of the torque-speed curve. If synchronisation in this way were mathematically feasible, it would remain open for debate whether such fine-tuning of the BFM near the knee value is a robust mechanism for synchronisation in real bundles of bacterial flagella.

Other synchronisation mechanisms can be investigated by expanding or modifying the degrees of freedom for the kinematics of the filaments. In this dissertation, the rotating filaments were assumed to remain vertical and the entire axes of the filaments swayed left and right. An alternative approach is to give the filaments a rotational degree of freedom whereby the axes of the filaments are allowed to swing about the vertical direction. In this case, the restoring mechanism could either be due to the elastic force applied by the hook at the basal end of the filament, or due to the advection of the filaments under the flow generated by the cell body.

### **The effect of HIs with the cell body on multiflagellar swimming**

Finally, our minimal model for a swimming multi-flagellated bacterium remains to be extended to include the HIs between the cell body and the bundle of helical filaments, following the method used by Higdon [82, 83] to include the HIs between a spherical cell body and a single filament. The flows generated by the force density along each filament will be modified in accordance with the solution for a point force outside a rigid sphere [115]. Whether these hydrodynamic effects can sufficiently alter our observations of how the swimming speed depends on the number of flagella, and whether they can move the optimum number outside the biologically relevant range, is to be determined.

# References

- [1] Adhyapak, T. C. and Stark, H. (2015). Zipping and entanglement in flagellar bundle of *E. coli* : Role of motile cell body. *Phys. Rev. E*, 92:052701.
- [2] Adler, R. (1946). A study of locking phenomena in oscillators. *Proc. IRE*, 34(6):351–357.
- [3] Aizawa, S.-I. (2014). Topic 4. Flagellin size. In *The Flagellar World*, pages 54–55. Academic Press.
- [4] Alouges, F., DeSimone, A., Giraldi, L., Or, Y., and Wiesel, O. (2019). Energy-optimal strokes for multi-link microswimmers: Purcell's loops and Taylor's waves reconciled. *New J. Phys.*, 21:043050.
- [5] Asakura, S., Eguchi, G., and Iino, T. (1964). Reconstitution of bacterial flagella in vitro. *J. Mol. Biol.*, 10(1):42–IN9.
- [6] Becker, L. E., Koehler, S. A., and Stone, H. A. (2003). On self-propulsion of micro-machines at low Reynolds number: Purcell's three-link swimmer. *J. Fluid Mech.*, 490:15–35.
- [7] Bennett, R. R. and Golestanian, R. (2013). Phase-dependent forcing and synchronization in the three-sphere model of *Chlamydomonas*. *New J. Phys.*, 15:75028.
- [8] Berg, H. C. (1983). *Random Walks in Biology*. Princeton University Press, Princeton, N.J.
- [9] Berg, H. C. (2004). *E. coli in motion*. Springer-Verlag, New York.
- [10] Berg, H. C. and Anderson, R. A. (1973). Bacteria swim by rotating their flagellar filaments. *Nature*, 245:380–382.
- [11] Berg, H. C. and Brown, D. A. (1972). Chemotaxis in *Escherichia coli* analysed by three-dimensional tracking. *Nature*, 239:500–504.
- [12] Berry, R. M. and Berg, H. C. (1997). Absence of a barrier to backwards rotation of the bacterial flagellar motor demonstrated with optical tweezers. *Proc. Natl. Acad. Sci. USA*, 94(26):14433–14437.
- [13] Bottone, E. J. (2004). *An atlas of the clinical microbiology of infectious diseases*. Encyclopedia of visual medicine series. Parthenon, Boca Raton ; London.
- [14] Bray, D. (2000). *Cell movements : From molecules to motility*. Garland Science.

- [15] Brennen, C. and Winet, H. (1977). Fluid mechanics of propulsion by cilia and flagella. *Annu. Rev. Fluid Mech.*, 9(1):339–398.
- [16] Brumley, D. R., Polin, M., Pedley, T. J., and Goldstein, R. E. (2012). Hydrodynamic synchronization and metachronal waves on the surface of the colonial alga *Volvox carterii*. *Phys. Rev. Lett.*, 109:268102.
- [17] Brumley, D. R., Wan, K. Y., Polin, M., and Goldstein, R. E. (2014). Flagellar synchronization through direct hydrodynamic interactions. *eLife*, 3:e02750.
- [18] Buchmann, A., Fauci, L. J., Leiderman, K., Strawbridge, E., and Zhao, L. (2018). Mixing and pumping by pairs of helices in a viscous fluid. *Phys. Rev. E*, 97:023101.
- [19] Butler, J. E. and Shaqfeh, E. S. G. (2002). Dynamic simulations of the inhomogeneous sedimentation of rigid fibres. *Journal of Fluid Mechanics*, 468:205–237.
- [20] Calladine, C. R. (1976). Design requirements for the construction of bacterial flagella. *J. Theor. Biol.*, 57:469–489.
- [21] Calladine, C. R. (1978). Change of waveform in bacterial flagella: The role of mechanics at the molecular level. *J. Mol. Biol.*, 118(4):457–479.
- [22] Chakrabarti, B. and Saintillan, D. (2019). Hydrodynamic synchronization of spontaneously beating filaments. *Phys. Rev. Lett.*, 123:208101.
- [23] Chamolly, A. and Lauga, E. (2020). Direct versus indirect hydrodynamic interactions during bundle formation of bacterial flagella. *Phys. Rev. Fluids*, 5:123102.
- [24] Chelakkot, R., Hagan, M. F., and Gopinath, A. (2021). Synchronized oscillations, traveling waves, and jammed clusters induced by steric interactions in active filament arrays. *Soft Matter*, 17:1091.
- [25] Chen, X. and Berg, H. C. (2000). Torque-speed relationship of the flagellar rotary motor of *Escherichia coli*. *Biophysical J.*, 78(2):1036–1041.
- [26] Chwang, A. T. and Wu, T. Y.-T. (1975). Hydromechanics of low-Reynolds-number flow. Part 2. Singularity method for Stokes flows. *J. Fluid Mech.*, 67:787–815.
- [27] Cichocki, B., Felderhof, B., and Schmitz, R. (1988). Hydrodynamic interactions between two spherical particles. *Physico Chem. Hyd.*, 10:383–403.
- [28] Cichocki, B., Felderhof, B. U., Hinsen, K., Wajnryb, E., and Bławdziewicz, J. (1994). Friction and mobility of many spheres in Stokes flow. *J. Chem. Phys.*, 100:3780–3790.
- [29] Collins, J. J. and Richmond, S. A. (1994). Hard-wired central pattern generators for quadrupedal locomotion. *Biol. Cybern.*, 71(5):375–385.
- [30] Collins, J. J. and Stewart, I. N. (1993). Coupled nonlinear oscillators and the symmetries of animal gaits. *J. Nonlinear Sci.*, 3:349–392.
- [31] Coombs, D., Huber, G., Kessler, J. O., and Goldstein, R. E. (2002). Periodic chirality transformations propagating on bacterial flagella. *Phys. Rev. Lett.*, 89:118102.

- [32] Cox, R. G. (1970). The motion of long slender bodies in a viscous fluid Part 1. General theory. *J. Fluid Mech.*, 44(4):791–810.
- [33] Czeszumski, A., Eustergerling, S., Lang, A., Menrath, D., Gerstenberger, M., Schuberth, S., Schreiber, F., Rendon, Z. Z., and König, P. (2020). Hyperscanning: A valid method to study neural inter-brain underpinnings of social interaction. *Front. Hum. Neurosci.*, 14:39.
- [34] Dabroś, T. (1985). A singularity method for calculating hydrodynamic forces and particle velocities in low-Reynolds-number flows. *J. Fluid Mech.*, 156:1–21.
- [35] Dai, L., He, G., Zhang, X., and Zhang, X. (2018). Stable formations of self-propelled fish-like swimmers induced by hydrodynamic interactions. *J. R. Soc. Interface*, 15(147):20180490.
- [36] Dang, H. (2020). Grand challenges in microbe-driven marine carbon cycling research. *Front. Microbiol.*, 11:1039.
- [37] Danis, U., Rasooli, R., Chen, C.-Y., Dur, O., Sitti, M., and Pekkan, K. (2019). Thrust and hydrodynamic efficiency of the bundled flagella. *Micromachines*, 10(7):449.
- [38] Darnton, N., Turner, L., Breuer, K., and Berg, H. C. (2004). Moving fluid with bacterial carpets. *Biophys. J.*, 86:1863–1870.
- [39] Darnton, N. C. and Berg, H. C. (2007). Force-extension measurements on bacterial flagella: Triggering polymorphic transformations. *Biophys. J.*, 92:2230–2236.
- [40] Darnton, N. C., Turner, L., Rojevsky, S., and Berg, H. C. (2007). On torque and tumbling in swimming *Escherichia coli*. *J. Bacteriol.*, 189:1756–1764.
- [41] Darnton, N. C., Turner, L., Rojevsky, S., and Berg, H. C. (2010). Dynamics of bacterial swarming. *Biophys. J.*, 98:2082–2090.
- [42] Das, D. and Lauga, E. (2018). Computing the motor torque of *Escherichia coli*. *Soft Matter*, 14(29):5955–5967.
- [43] Dauparas, J., Das, D., and Lauga, E. (2018). Helical micropumps near surfaces. *Biomicrofluidics*, 12:014108.
- [44] Di Leonardo, R., Búzás, A., Kelemen, L., Vizsnyiczai, G., Oroszi, L., and Ormos, P. (2012). Hydrodynamic synchronization of light driven microrotors. *Phys. Rev. Lett.*, 109:034104.
- [45] Drescher, K., Dunkel, J., Cisneros, L. H., Ganguly, S., and Goldstein, R. E. (2011). Fluid dynamics and noise in bacterial cell-cell and cell-surface scattering. *Proc. Natl. Acad. Sci. USA*, 108:10940–10945.
- [46] Drescher, K., Goldstein, R. E., Michel, N., Polin, M., and Tuval, I. (2010). Direct measurement of the flow field around swimming microorganisms. *Phys. Rev. Lett.*, 105:168101.
- [47] Drescher, K., Leptos, K. C., Tuval, I., Ishikawa, T., Pedley, T. J., and Goldstein, R. E. (2009). Dancing *Volvox*: Hydrodynamic bound states of swimming algae. *Phys. Rev. Lett.*, 102:1168101.

- [48] du Roure, O., Lindner, A., Nazockdast, E. N., and Shelley, M. J. (2019). Dynamics of flexible fibers in viscous flows and fluids. *Annu. Rev. Fluid Mech.*, 51:539–572.
- [49] Eisenstecken, T., Hu, J., and Winkler, R. G. (2016). Bacterial swarmer cells in confinement: a mesoscale hydrodynamic simulation study. *Soft Matter*, 12:8316–8326.
- [50] Elfring, G. J. and Lauga, E. (2011a). Passive hydrodynamic synchronization of two-dimensional swimming cells. *Phys. Fluids*, 23(1):011902.
- [51] Elfring, G. J. and Lauga, E. (2011b). Synchronization of flexible sheets. *J. Fluid Mech.*, 674:163–173.
- [52] Elgeti, J. and Gompper, G. (2013). Emergence of metachronal waves in cilia arrays. *Proc. Natl. Acad. Sci. USA*, 110(12):4470–4475.
- [53] Elgeti, J., Winkler, R., and Gompper, G. (2015). Physics of microswimmers—single particle motion and collective behavior: a review. *Rep. Prog. Phys.*, 78:056601.
- [54] Fàbrega, A. and Vila, J. (2013). *Salmonella enterica* serovar typhimurium skills to succeed in the host: virulence and regulation. *Clin. Microbiol. Rev.*, 26:308–341.
- [55] Fauci, L. J. and Dillon, R. (2005). Biofluidmechanics of Reproduction. *Annu. Rev. Fluid Mech.*
- [56] Felderhof, B. (1977). Hydrodynamic interaction between two spheres. *Physica A*, 89(2):373 – 384.
- [57] Flores, H., Lobaton, E., Méndez-Diez, S., Tlupova, S., and Cortez, R. (2005). A study of bacterial flagellar bundling. *Bull. Math. Biol.*, 67:137–168.
- [58] Forterre, Y. and Dumais, J. (2011). Generating helices in nature. *Science*, 333:1715–1716.
- [59] Fujii, M., Shibata, S., and Aizawa, S.-I. (2008). Polar, peritrichous, and lateral flagella belong to three distinguishable flagellar families. *J. Mol. Biol.*, 379:273–283.
- [60] Gabel, C. V. and Berg, H. C. (2003). The speed of the flagellar rotary motor of *Escherichia coli* varies linearly with protonmotive force. *Proc. Natl. Acad. Sci. USA*, 100(15):8748–8751.
- [61] Gadêlha, H., Hernández-Herrera, P., Montoya, F., Darszon, A., and Corkidi, G. (2020). Human sperm uses asymmetric and anisotropic flagellar controls to regulate swimming symmetry and cell steering. *Sci. Adv.*, 6:eaba5168.
- [62] Geyer, V. F., Jülicher, F., Howard, J., and Friedrich, B. M. (2013). Cell-body rocking is a dominant mechanism for flagellar synchronization in a swimming alga. *Proc. Natl. Acad. Sci. USA*, 110:18058–18063.
- [63] Goddard, B. D., Mills-Williams, R. D., and Sun, J. (2020). The singular hydrodynamic interactions between two spheres in stokes flow. *Phys. Fluids*, 32(6):062001.
- [64] Goldman, A., Cox, R., and Brenner, H. (1966). The slow motion of two identical arbitrarily oriented spheres through a viscous fluid. *Chem. Eng. Sci.*, 21:1151–1170.

- [65] Goldstein, R. E., Lauga, E., Pesci, A. I., and Proctor, M. R. E. (2016). Elastohydrodynamic synchronization of adjacent beating flagella. *Phys. Rev. Fluids*, 1:073201.
- [66] Goldstein, R. E., Polin, M., and Tuval, I. (2009). Noise and synchronization in pairs of beating eukaryotic flagella. *Phys. Rev. Lett.*, 103:168103.
- [67] Götz, T. (2000). *Interactions of fibers and flow: asymptotics, theory and numerics*. PhD thesis, University of Kaiserslautern.
- [68] Götz, I. O. and Gompper, G. (2010). Mesoscale simulations of hydrodynamic squirmer interactions. *Phys. Rev. E*, 82:041921.
- [69] Gray, J. and Hancock, G. J. (1955). The propulsion of sea-urchin spermatozoa. *J. Exp. Biol.*, 32(4):802–814.
- [70] Gu, H., Boehler, Q., Cui, H., Secchi, E., Savorana, G., De Marco, C., Gervasoni, S., Peyron, Q., Huang, T. Y., Pane, S., Hirt, A. M., Ahmed, D., and Nelson, B. J. (2020). Magnetic cilia carpets with programmable metachronal waves. *Nat. Commun.*, 11:1–10.
- [71] Guazzelli, É. and Hinch, J. (2011). Fluctuations and instability in sedimentation. *Annu. Rev. Fluid Mech.*, 43(1):97–116.
- [72] Gueron, S., Levit-Gurevich, K., Liron, N., and Blum, J. J. (1997). Cilia internal mechanism and metachronal coordination as the result of hydrodynamical coupling. *Proc. Natl. Acad. Sci. USA*, 94:6001–6006.
- [73] Guirao, B. and Joanny, J.-F. (2007). Spontaneous creation of macroscopic flow and metachronal waves in an array of cilia. *Biophys. J.*, 92:1900 – 1917.
- [74] Guo, H., Fauci, L., Shelley, M., and Kanso, E. (2018). Bistability in the synchronization of actuated microfilaments. *J. Fluid Mech.*, 836:304–323.
- [75] Guo, H., Man, Y., Wan, K. Y., and Kanso, E. (2021). Intracellular coupling modulates biflagellar synchrony. *J. R. Soc. Interface*, 18(174):20200660.
- [76] Guttenplan, S. B., Shaw, S., and Kearns, D. B. (2013). The cell biology of peritrichous flagella in *Bacillus subtilis*. *Mol. Microbiol.*, 87:211–229.
- [77] Gyrya, V., Aranson, I. S., Berlyand, L. V., and Karpeev, D. (2010). A model of hydrodynamic interaction between swimming bacteria. *Bull. Math. Biol.*, 72(1):148–183.
- [78] Hamilton, E. and Cicuta, P. (2018). Interpreting the synchronisation of driven colloidal oscillators via the mean pair interaction. *New J. Phys.*, 20:093028.
- [79] Hancock, G. (1953). The self-propulsion of microscopic organisms through liquids. *Proc. R. Soc. A*, 217:96–121.
- [80] Harisa, G. I., Sherif, A. Y., Youssof, A. M. E., Alanazi, F. K., and Salem-Bekhit, M. M. (2020). Bacteriosomes as a promising tool in biomedical applications: Immunotherapy and drug delivery. *AAPS PharmSciTech*, 21:168–168.
- [81] Hasegawa, K., Yamashita, I., and Namba, K. (1998). Quasi- and nonequivalence in the structure of bacterial flagellar filament. *Biophys. J.*, 74:569–575.

- [82] Higdon, J. J. L. (1979a). A hydrodynamic analysis of flagellar propulsion. *J. Fluid Mech.*, 90(4):685–711.
- [83] Higdon, J. J. L. (1979b). The hydrodynamics of flagellar propulsion: helical waves. *J. Fluid Mech.*, 94:331–351.
- [84] Hinch, E. J. (1991). *Perturbation Methods*. Cambridge Texts in Applied Mathematics. Cambridge University Press.
- [85] Hocking, L. M. (1964). The behaviour of clusters of spheres falling in a viscous fluid Part 2. Slow motion theory. *J. Fluid Mech.*, 20:129—139.
- [86] Hooke, R. (1667). *Micrographia*. The Royal Society, London.
- [87] Hotani, H. (1976). Light microscope study of mixed helices in reconstituted *Salmonella* flagella. *J. Mol. Biol.*, 106:151–166.
- [88] Hotani, H. (1982). Micro-video study of moving bacterial flagellar filaments: III. Cyclic transformation induced by mechanical force. *J. Mol. Biol.*, 156:791–806.
- [89] Huang, C., Wang, Z., Quinn, D., Suresh, S., and Hsia, K. J. (2018). Differential growth and shape formation in plant organs. *Proc. Natl. Acad. Sci. USA*, 115(49):12359–12364.
- [90] Hughes, K. T. (2017). Flagellum length control: How long is long enough? *Curr. Biol.*, 27(11):R413–R415.
- [91] Iino, T. (1974). Assembly of *Salmonella* flagellin *in vitro* and *in vivo*. *J. Supramol. Struct.*, 2:372–384.
- [92] Iino, T., Oguchi, T., and Kuroiwa, T. (1974). Polymorphism in a flagellar-shape mutant of *Salmonella typhimurium*. *J. Gen. Microbiol.*, 81:37–45.
- [93] Iino, T., Oguchi, T., and Kutsukake, K. (1987). Flagellation of *Salmonella typhimurium* treated with nalidixic acid. *J. Gen. Microbiol.*, 133:779–782.
- [94] Ishikawa, T. (2009). Suspension biomechanics of swimming microbes. *J. R. Soc. Interface*, 6(39):815–834.
- [95] Ishikawa, T., Pedley, T. J., Drescher, K., and Goldstein, R. E. (2020). Stability of dancing *Volvox*. *J. Fluid. Mech.*, 903:A11.
- [96] Ishikawa, T., Sekiya, G., Imai, Y., and Yamaguchi, T. (2007). Hydrodynamic interactions between two swimming bacteria. *Biophys. J.*, 93:2217–2225.
- [97] Ishimoto, K. and Lauga, E. (2019). The N-flagella problem: Elastohydrodynamic motility transition of multi-flagellated bacteria. *Proc. R. Soc. A*, 475:20180690.
- [98] Jalaal, M., Schramma, N., Dode, A., de Maleprade, H., Raufaste, C., and Goldstein, R. E. (2020). Stress-induced dinoflagellate bioluminescence at the single cell level. *Phys. Rev. Lett.*, 125:028102.
- [99] Jalife, J. (1984). Mutual entrainment and electrical coupling as mechanisms for synchronous firing of rabbit sino-atrial pace-maker cells. *J. Physiol.*, 356(1):221–243.

- [100] Janssen, P. J. A. and Graham, M. D. (2011). Coexistence of tight and loose bundled states in a model of bacterial flagellar dynamics. *Phys. Rev. E*, 84:011910.
- [101] Jawed, M. K., Khouri, N. K., Da, F., Grinspun, E., and Reis, P. M. (2015). Propulsion and instability of a flexible helical rod rotating in a viscous fluid. *Phys. Rev. Lett.*, 115:168101.
- [102] Jayaweera, K. O. L. F., Mason, B. J., and Slack, G. W. (1964). The behaviour of clusters of spheres falling in a viscous fluid Part 1. Experiment. *J. Fluid Mech.*, 20:121—128.
- [103] Jeffery, G. B. (1915). On the steady rotation of a solid of revolution in a viscous fluid. *Proc. Lond. Math. Soc.*, 14:327–338.
- [104] Jiao, N., Herndl, G. J., Hansell, D. A., Benner, R., Kattner, G., Wilhelm, S. W., Kirchman, D. L., Weinbauer, M. G., Luo, T., Chen, F., and Azam, F. (2010). Microbial production of recalcitrant dissolved organic matter: Long-term carbon storage in the global ocean. *Nat. Rev. Microbiol.*, 8:593–599.
- [105] Johnson, R. E. (1980). An improved slender-body theory for Stokes flow. *J. Fluid Mech.*, 99(2):411–431.
- [106] Kamiya, R. and Asakura, S. (1976). Helical transformations of *Salmonella* flagella *in vitro*. *J. Mol. Biol.*, 106:167–186.
- [107] Kanehl, P. and Ishikawa, T. (2014). Fluid mechanics of swimming bacteria with multiple flagella. *Phys. Rev. E*, 89:042704.
- [108] Keller, J. B. and Rubinow, S. I. (1976). Slender-body theory for slow viscous flow. *J. Fluid Mech.*, 75(4):705–714.
- [109] Khan, S. and Macnab, R. M. (1980). The steady-state counterclockwise/clockwise ratio of bacterial flagellar motors is regulated by protonmotive force. *J. Mol. Biol.*, 138:563–597.
- [110] Kim, M. and Breuer, K. (2008). Microfluidic pump powered by self-organizing bacteria. *Small*, 4:111–118.
- [111] Kim, M. and Powers, T. R. (2004). Hydrodynamic interactions between rotating helices. *Phys. Rev. E*, 69:061910.
- [112] Kim, M. and Powers, T. R. (2005). Deformation of a helical filament by flow and electric or magnetic fields. *Phys. Rev. E*, 71:021914.
- [113] Kim, M. J., Bird, J. C., Van Parys, A. J., Breuer, K. S., and Powers, T. R. (2003). A macroscopic scale model of bacterial flagellar bundling. *Proc. Natl. Acad. Sci. USA*, 100(26):15481–15485.
- [114] Kim, M. J., Kim, M. J., Bird, J. C., Park, J., Powers, T. R., and Breuer, K. S. (2004). Particle image velocimetry experiments on a macro-scale model for bacterial flagellar bundling. *Exp. Fluids*, 37:782–78.

- [115] Kim, S. and Karrila, S. J. (1991). *Microhydrodynamics : principles and selected applications*. Butterworth-Heinemann series in Chemical Engineering. Courier Corporation.
- [116] Kim, S. and Mifflin, R. T. (1985). The resistance and mobility functions of two equal spheres in low-Reynolds-number flow. *Phys. Fluids*, 28:2033–2045.
- [117] Koens, L. and Lauga, E. (2016). Slender-ribbon theory. *Phys. Fluids*, 28(1):013101.
- [118] Koens, L. and Lauga, E. (2018). The boundary integral formulation of stokes flows includes slender-body theory. *J. Fluid Mech.*, 850:R1.
- [119] Koens, L. M. (2016). *The Hydrodynamics of Complex Microswimmers: An exploration of slender filaments and ribbons*. PhD thesis, University of Cambridge.
- [120] Kotar, J., Leoni, M., Bassetti, B., Lagomarsino, M. C., and Cicuta, P. (2010). Hydrodynamic synchronization of colloidal oscillators. *Proc. Natl. Acad. Sci. USA*, 107(17):7669–7673.
- [121] Lauga, E. (2015). Bacterial hydrodynamics. *Annu. Rev. Fluid Mech.*, 48(1):105–130.
- [122] Laurell, T., Petersson, F., and Nilsson, A. (2007). Chip integrated strategies for acoustic separation and manipulation of cells and particles. *Chem. Soc. Rev.*, 36:492–506.
- [123] Lawrence, J. D. (1972). *A catalog of special plane curves*. Dover Publications.
- [124] Lee, W., Kim, Y., Griffith, B. E., and Lim, S. (2018). Bacterial flagellar bundling and unbundling via polymorphic transformations. *Phys. Rev. E*, 98:052405.
- [125] Leifson, E. (1960). *Atlas of bacterial flagellation*. Academic Press, New York.
- [126] Leifson, E., Cosenza, B. J., Miurichelano, R., and Cleverdon, I. C. (1964). Motile marine bacteria. *J. Bacteriol.*, 87:652–666.
- [127] Li, G., Ostace, A., and Ardekani, A. M. (2016). Hydrodynamic interaction of swimming organisms in an inertial regime. *Phys. Rev. E*, 94:053104.
- [128] Li, M. (2010). *Experimental study of swimming flagellated bacteria and their collective behaviour in concentrated suspensions*. PhD thesis, The University of Edinburgh.
- [129] Liao, Q., Subramanian, G., DeLisa, M., Koch, D., and Wu, M. (2007). Pair velocity correlations among swimming *Escherichia coli* bacteria are determined by force-quadrupole hydrodynamic interactions. *Phys. Fluids*, 19:061701.
- [130] Liao, W. and Lauga, E. (2021). Energetics of synchronization for model flagella and cilia. *Phys. Rev. E*, 103:042419.
- [131] Lighthill, J. (1976). Flagellar hydrodynamics—The John von Neumann lecture, 1975. *SIAM Rev.*, 18:161–230.
- [132] Lighthill, J. (1996). Helical distributions of stokeslets. *J. Eng. Math.*, 30:35–78.
- [133] Liu, B. and Gonzalez, J. (2020). Bundled slender-body theory for elongated geometries in swimming bacteria. *Phys. Rev. Fluids*, 5:053102.

- [134] Lo, C. J., Sowa, Y., Pilizota, T., and Berry, R. M. (2013). Mechanism and kinetics of a sodium-driven bacterial flagellar motor. *Proc. Natl. Acad. Sci. USA*, 110:E2544–E2551.
- [135] Luckey, T. D. (1972). Introduction to intestinal microecology. *Am. J. Clin. Nutr.*, 25(12):1292–1294.
- [136] Machemer, H. (1972). Ciliary activity and the origin of metachrony in *Paramecium*: effects of increased viscosity. *J. Exp. Biol.*, 57(1):239–259.
- [137] Mackaplow, M. B. and Shaqfeh, E. S. (1996). A numerical study of the rheological properties of suspensions of rigid, non-Brownian fibres. *J. Fluid Mech.*, 329:155–186.
- [138] Macnab, R. M. (1977). Bacterial flagella rotating in bundles: a study in helical geometry. *Proc. Natl. Acad. Sci. USA*, 74:221–225.
- [139] Macnab, R. M. (2003). How bacteria assemble flagella. *Annu. Rev. Microbiol.*, 57(1):77–100.
- [140] Macnab, R. M. and Han, D. P. (1983). Asynchronous switching of flagellar motors on a single bacterial cell. *Cell*, 32:109–117.
- [141] Man, Y. and Kanso, E. (2020). Multisynchrony in active microfilaments. *Phys. Rev. Lett.*, 125:148101.
- [142] Man, Y., Koens, L., and Lauga, E. (2016). Hydrodynamic interactions between nearby slender filaments. *Europhys. Lett.*, 116(2):24002.
- [143] Mandadapu, K. K., Nirody, J. A., Berry, R. M., Oster, G., and Berg, H. C. (2015). Mechanics of torque generation in the bacterial flagellar motor. *Proc. Natl. Acad. Sci. USA*, 112:E4381–E4389.
- [144] Marchetti, M. C., Joanny, J. F., Ramaswamy, S., Liverpool, T. B., Prost, J., Rao, M., and Simha, R. A. (2013). Hydrodynamics of soft active matter. *Rev. Mod. Phys.*, 85:1143–1189.
- [145] Martindale, J. D. and Fu, H. C. (2017). Autonomously responsive pumping by a bacterial flagellar forest: A mean-field approach. *Phys. Rev. E*, 96:033107.
- [146] Martínez, L. E., Hardcastle, J. M., Wang, J., Pincus, Z., Tsang, J., Hoover, T. R., Bansil, R., and Salama, N. R. (2016). *Helicobacter pylori* strains vary cell shape and flagellum number to maintain robust motility in viscous environments. *Mol. Microbiol.*, 99(1):88–110.
- [147] Maxian, O., Mogilner, A., and Donev, A. (2021). Integral-based spectral method for inextensible slender fibers in Stokes flow. *Phys. Rev. Fluids*, 6:014102.
- [148] Meister, M., Lowe, G., and Berg, H. C. (1987). The proton flux through the bacterial flagellar motor. *Cell*, 49:643–650.
- [149] Meurer, K. P. and Vögtle, F. (1985). Helical molecules in organic chemistry. In *Organic Chemistry*, pages 1–76, Berlin, Heidelberg. Springer Berlin Heidelberg.

- [150] Michaels, D. C., Matyas, E. P., and Jalife, J. (1987). Mechanisms of sinoatrial pacemaker synchronization: a new hypothesis. *Circ. Res.*, 61(5):704–714.
- [151] Mirollo, R. E. and Strogatz, S. H. (1990). Synchronization of pulse-coupled biological oscillators. *SIAM J. Appl. Math.*, 50(6):1645–1662.
- [152] Moens, S. and Vanderleyden, J. (1996). Functions of bacterial flagella. *Crit. Rev. Microbiol.*, 22:67–100.
- [153] Molina, J. J., Nakayama, Y., and Yamamoto, R. (2013). Hydrodynamic interactions of self-propelled swimmers. *Soft Matter*, 9:4923–4936.
- [154] Morales, A. J., Vavilala, V., Benito, R. M., and Bar-Yam, Y. (2017). Global patterns of synchronization in human communications. *J. R. Soc. Interface*, 14(128):20161048.
- [155] Najafi, J., Altegoer, F., Bange, G., and Wagner, C. (2019). Swimming of bacterium *Bacillus subtilis* with multiple bundles of flagella. *Soft Matter*, 15:10029–10034.
- [156] Najafi, J., Shaebani, M. R., John, T., Altegoer, F., Bange, G., and Wagner, C. (2018). Flagellar number governs bacterial spreading and transport efficiency. *Sci. Adv.*, 4:eaar6425.
- [157] Nasserri, S. and Phan-Thien, N. (1997). Hydrodynamic interaction between two nearby swimming micromachines. *Comp. Mech.*, 20:551–559.
- [158] Nguyen, F. T. M. and Graham, M. D. (2018). Impacts of multiflagellarity on stability and speed of bacterial locomotion. *Phys. Rev. E*, 98:042419.
- [159] Niedermayer, T., Eckhardt, B., and Lenz, P. (2008). Synchronization, phase locking, and metachronal wave formation in ciliary chains. *Chaos*, 18:037128.
- [160] Nirody, J. A., Berry, R. M., and Oster, G. (2016). The Limiting Speed of the Bacterial Flagellar Motor. *Biophys. J.*, 111:557–564.
- [161] Nirody, J. A., Nord, A. L., and Berry, R. M. (2019). Load-dependent adaptation near zero load in the bacterial flagellar motor. *J. R. Soc. Interface*, 16:20190300.
- [162] Nord, A. L., Biquet-Bisquert, A., Abkarian, M., Pigaglio, T., Seduk, F., Magalon, A., and Pedaci, F. (2021). Dynamic stiffening of the flagellar hook. arXiv:2106.15435.
- [163] Olson, S. D. and Fauci, L. J. (2015). Hydrodynamic interactions of sheets vs filaments: Synchronization, attraction, and alignment. *Phys. Fluids*, 27:121901.
- [164] Pan, Y. and Dong, H. (2020). Computational analysis of hydrodynamic interactions in a high-density fish school. *Phys. Fluids*, 32(12):121901.
- [165] Parsons, S. P. and Huizinga, J. D. (2020). Modulation of contractions in the small intestine indicate desynchronization via supercritical Andronov–Hopf bifurcation. *Sci. Rep.*, 10:15099.
- [166] Ping, L. (2010). The asymmetric flagellar distribution and motility of *Escherichia coli*. *J. Mol. Biol.*, 397:906–916.

- [167] Polin, M., Tuval, I., Drescher, K., Gollub, J. P., and Goldstein, R. E. (2009). Chlamydomonas swims with two “gears” in a eukaryotic version of run-and-tumble locomotion. *Science*, 325(5939):487–490.
- [168] Powers, T. R. (2002). Role of body rotation in bacterial flagellar bundling. *Phys. Rev. E*, 65:040903.
- [169] Pozrikidis, C. (1992). *Boundary Integral and Singularity Methods for Linearized Viscous Flow*. Cambridge Texts in Applied Mathematics. Cambridge University Press.
- [170] Purcell, E. M. (1977). Life at low reynolds number. *Am. J. Phys.*, 45:3–11.
- [171] Qian, B., Jiang, H., Gagnon, D. A., Breuer, K. S., and Powers, T. R. (2009). Minimal model for synchronization induced by hydrodynamic interactions. *Phys. Rev. E*, 80:061919.
- [172] Qu, Z., Temel, F., Henderikx, R., and Breuer, K. S. (2018). Changes in the flagellar bundling time account for variations in swimming behavior of flagellated bacteria in viscous media. *Proc. Natl. Acad. Sci. USA*, 115:1707–1712.
- [173] Quaranta, G., Aubin-Tam, M.-E., and Tam, D. (2015). Hydrodynamics versus intracellular coupling in the synchronization of eukaryotic flagella. *Phys. Rev. Lett.*, 115:238101.
- [174] Ramaswamy, S. (2010). The mechanics and statistics of active matter. *Annu. Rev. Condens. Matter Phys.*, 1:323–345.
- [175] Reichert, M. and Stark, H. (2005). Synchronization of rotating helices by hydrodynamic interactions. *Eur. Phys. J. E*, 17:493–500.
- [176] Reigh, S. Y., Winkler, R. G., and Gompper, G. (2012). Synchronization and bundling of anchored bacterial flagella. *Soft Matter*, 8:4363–4372.
- [177] Reigh, S. Y., Winkler, R. G., and Gompper, G. (2013). Synchronization, slippage, and unbundling of driven helical flagella. *PLoS ONE*, 8:e70868.
- [178] Renault, T. T., Abraham, A. O., Bergmiller, T., Paradis, G., Rainville, S., Charpentier, E., Guet, C. C., Tu, Y., Namba, K., Keener, J. P., Minamino, T., and Erhardt, M. (2017). Bacterial flagella grow through an injection-diffusion mechanism. *eLife*, 6.
- [179] Reynolds, O. (1895). Iv. on the dynamical theory of incompressible viscous fluids and the determination of the criterion. *Philos. Trans. R. Soc. A*, 186:123–164.
- [180] Riley, E. E., Das, D., and Lauga, E. (2018). Swimming of peritrichous bacteria is enabled by an elastohydrodynamic instability. *Sci. Rep.*, 8:10728.
- [181] Rodenborn, B., Chen, C.-H., Swinney, H. L., Liu, B., and Zhang, H. P. (2013). Propulsion of microorganisms by a helical flagellum. *Proc. Natl. Acad. Sci. USA*, 110:E338–E347.
- [182] Rodrigues, M. F. V., Lisicki, M., and Lauga, E. (2021). The bank of swimming organisms at the micron scale (boso-micro).

- [183] Rosenblum, D., Joshi, N., Tao, W., Karp, J. M., and Peer, D. (2018). Progress and challenges towards targeted delivery of cancer therapeutics. *Nat. Commun.*, 9:1410–12.
- [184] Saha, S., Ramaswamy, S., and Golestanian, R. (2019). Pairing, waltzing and scattering of chemotactic active colloids. *New J. Phys.*, 21:063006.
- [185] Saintillan, D., Darve, E., and Shaqfeh, E. S. G. (2005). A smooth particle-mesh Ewald algorithm for stokes suspension simulations: The sedimentation of fibers. *Physics of Fluids*, 17(3):033301.
- [186] Schoeller, S. F., Holt, W. V., and Keaveny, E. E. (2020). Collective dynamics of sperm cells. *Philos. Trans. R. Soc. B*, 375:20190384.
- [187] Schuhmacher, J. S., Thormann, K. M., and Bange, G. (2015). How bacteria maintain location and number of flagella? *FEMS Microbiol. Rev.*, 39:812–822.
- [188] Sen, A., Nandy, R. K., and Ghosh, A. N. (2004). Elasticity of flagellar hooks. *J. Electron Microsc.*, 53:305–309.
- [189] Sender, R., Fuchs, S., and Milo, R. (2016). Revised Estimates for the Number of Human and Bacteria Cells in the Body. *PLoS Biology*, 14(8):e1002533.
- [190] Shaqfeh, E. S. and Fredrickson, G. H. (1990). The hydrodynamic stress in a suspension of rods. *Phys. Fluids A*, 2(1):7–24.
- [191] Sharifi-Mood, N., Mozaffari, A., and Córdova-Figueroa, U. M. (2016). Pair interaction of catalytically active colloids: from assembly to escape. *J. Fluid Mech.*, 798:910–954.
- [192] Sherman, A., Rinzal, J., and Keizer, J. (1988). Emergence of organized bursting in clusters of pancreatic beta-cells by channel sharing. *Biophys. J.*, 54(3):411–425.
- [193] Shum, H. (2019). Microswimmer propulsion by two steadily rotating helical flagella. *Micromachines*, 10:65.
- [194] Smith, H. M. (1935). Synchronous flashing of fireflies. *Science*, 82(2120):151–152.
- [195] Son, K., Guasto, J. S., and Stocker, R. (2013). Bacteria can exploit a flagellar buckling instability to change direction. *Nat. Phys.*, 9:494–498.
- [196] Sowa, Y. and Berry, R. M. (2008). Bacterial flagellar motor. *Q. Rev. Biophys.*, 41:103–132.
- [197] Spagnolie, S. E. and Lauga, E. (2011). Comparative hydrodynamics of bacterial polymorphism. *Phys. Rev. Lett.*, 106:058103.
- [198] Spöring, I., Martinez, V. A., Hotz, C., Schwarz-Linek, J., Grady, K. L., Nava-Sedeño, J. M., Vissers, T., Singer, H. M., Rohde, M., Bourquin, C., Hatzikirou, H., Poon, W. C. K., Dufour, Y. S., and Erhardt, M. (2018). Hook length of the bacterial flagellum is optimized for maximal stability of the flagellar bundle. *PLoS Biology*, 16:e2006989.
- [199] Srigiriraju, S. V. and Powers, T. R. (2005). Continuum model for polymorphism of bacterial flagella. *Phys. Rev. Lett.*, 94(24):1–4.

- [200] Srigiriraju, S. V. and Powers, T. R. (2006). Model for polymorphic transitions in bacterial flagella. *Phys. Rev. E*, 73:011902.
- [201] Stimson, M. and Jeffery, G. B. (1926). The motion of two spheres in a viscous fluid. *Proc. R. Soc. Lond. A*, 111:110—116.
- [202] Stocker, R. and Seymour, J. R. (2012). Ecology and Physics of Bacterial Chemotaxis in the Ocean. *Microbiol. Mol. Biol. Rev.*, 76:792–812.
- [203] Tanasijević, I. and Lauga, E. (2021). Hydrodynamic synchronization in strong confinement. *Phys. Rev. E*, 103:022403.
- [204] Taylor, G. I. (1951). Analysis of the swimming of microscopic organisms. *Proc. R. Soc. A*, 209:447–461.
- [205] Tornberg, A. K. and Shelley, M. J. (2004). Simulating the dynamics and interactions of flexible fibers in Stokes flows. *J. Comp. Phys.*, 196(1):8–40.
- [206] Tătulea-Codrean, M. and Lauga, E. (2020). Geometrical constraints on the tangling of bacterial flagellar filaments. *Sci. Rep.*, 10:8406.
- [207] Tătulea-Codrean, M. and Lauga, E. (2021). Asymptotic theory of hydrodynamic interactions between slender filaments. *Phys. Rev. Fluids*, in press.
- [208] Turner, L., Ping, L., Neubauer, M., and Berg, H. C. (2016). Visualizing flagella while tracking bacteria. *Biophys. J.*, 111:630–639.
- [209] Turner, L., Ryu, W. S., and Berg, H. C. (2000). Real-time imaging of fluorescent flagellar filaments. *J. Bacteriol.*, 182:2793–2801.
- [210] Turner, L., Stern, A. S., and Berg, H. C. (2012). Growth of flagellar filaments of *Escherichia coli* is independent of filament length. *J. Bacteriol.*, 194:2437–2442.
- [211] Uchida, N. and Golestanian, R. (2011). Generic conditions for hydrodynamic synchronization. *Phys. Rev. Lett.*, 106:058104.
- [212] Uchida, N. and Golestanian, R. (2012). Hydrodynamic synchronization between objects with cyclic rigid trajectories. *Eur. Phys. J. E*, 35(12):1–14.
- [213] Varma, A. and Michelin, S. (2019). Modeling chemo-hydrodynamic interactions of phoretic particles: A unified framework. *Phys. Rev. Fluids*, 4:124204.
- [214] Varma, A., Montenegro-Johnson, T. D., and Michelin, S. (2018). Clustering-induced self-propulsion of isotropic autophoretic particles. *Soft Matter*, 14:7155–7173.
- [215] Vicsek, T. and Zafeiris, A. (2012). Collective motion. *Phys. Rep.*, 517:71 – 140.
- [216] Vilfan, A. and Jülicher, F. (2006). Hydrodynamic flow patterns and synchronization of beating cilia. *Phys. Rev. Lett.*, 96:058102.
- [217] Vogel, R. and Stark, H. (2013). Rotation-induced polymorphic transitions in bacterial flagella. *Phys. Rev. Lett.*, 110(15):1–5.

- [218] Wakiya, S. (1967). Slow motions of a viscous fluid around two spheres. *J. Phys. Soc. Japan*, 22(4):1101–1109.
- [219] Walker, T. J. (1969). Acoustic synchrony: Two mechanisms in the snowy tree cricket. *Science*, 166(3907):891–894.
- [220] Wan, K. Y. and Goldstein, R. E. (2016). Coordinated beating of algal flagella is mediated by basal coupling. *Proc. Natl. Acad. Sci. USA*, 113:E2784–E2793.
- [221] Wan, K. Y., Leptos, K. C., and Goldstein, R. E. (2014). Lag, lock, sync, slip: the many phases of coupled flagella. *J. R. Soc. Interface*, 11:20131160.
- [222] Wang, F., Burrage, A., Postel, S., Clark, R. E., Orlova, A., Sundberg, E. J., Kearns, D. B., and Egelman, E. H. (2017). A structural model of flagellar filament switching across multiple bacterial species. *Nat. Commun.*, 8:960.
- [223] Watari, N. and Larson, R. G. (2010). The hydrodynamics of a run-and-tumble bacterium propelled by polymorphic helical flagella. *Biophys. J.*, 98:12–17.
- [224] Watson, J. D. and Crick, F. H. C. (1953). Molecular Structure of Nucleic Acids: A Structure for Deoxyribose Nucleic Acid. *Nature*, 171:737–738.
- [225] Weihs, D. (1973). Hydromechanics of Fish Schooling. *Nature*, 241(5387):290–291.
- [226] Wollin, C. and Stark, H. (2011). Metachronal waves in a chain of rowers with hydrodynamic interactions. *Eur. Phys. J. E*, 34:1–10.
- [227] Xing, J., Bai, F., Berry, R. M., and Oster, G. (2006). Torque–speed relationship of the bacterial flagellar motor. *Proc. Natl. Acad. Sci. USA*, 103:1260–1265.
- [228] Yoon, B. J. and Kim, S. (1987). Note on the direct calculation of mobility functions for two equal-sized spheres in Stokes flow. *J. Fluid Mech.*, 185:437–446.